POLITECNICO DI TORINO

Dipartimento di Ingegneria Meccanica e Aerospaziale

MA.Sc. Thesis in Automotive Engineering

Finite element simulation of the Offset-Deformable Barrier Euro NCAP crash test reproduction on a HYGE sled for assessing ten-year-old child safety

Academic advisor:
Prof. Giovanni BELINGARDI

Graduate student:
Paolo LORUSSO

ACADEMIC YEAR   2019 – 2020

Finite element simulation of the Offset-Deformable Barrier Euro NCAP crash test reproduction on a HYGE sled for assessing ten-year-old child safety

by

Paolo Lorusso

APPROVED BY:

_____
D. Green
Department of Mechanical, Automotive & Materials Engineering

_____
J. Johrendt
Department of Mechanical, Automotive & Materials Engineering

_____
N. Zamani, Advisor
Department of Mechanical, Automotive & Materials Engineering

October 15, 2019

DECLARATION OF ORIGINALITY

I hereby certify that I am the sole author of this thesis and that no part of this thesis has been published or submitted for publication.

I certify that, to the best of my knowledge, my thesis does not infringe upon anyone's copyright nor violate any proprietary rights and that any ideas, techniques, quotations, or any other material from the work of other people included in my thesis, published or otherwise, are fully acknowledged in accordance with the standard referencing practices. Furthermore, to the extent that I have included copyrighted material that surpasses the bounds of fair dealing within the meaning of the Canada Copyright Act, I certify that I have obtained a written permission from the copyright owner(s) to include such material(s) in my thesis and have included copies of such copyright clearances to my appendix.

I declare that this is a true copy of my thesis, including any final revisions, as approved by my thesis committee and the Graduate Studies office, and that this thesis has not been submitted for a higher degree to any other University or Institution.

ABSTRACT

This research focuses on the definition of the guidelines to simulate a sled test which reproduces the ODB Euro NCAP crash test, using LS-DYNA Finite Element code. In addition, the last sections are based on the validation of the model, comparing numerical results with those of an experimental sled test performed with the same equipment in late 2018, and on a sensitivity study on the friction coefficient of a virtual slip ring.

Several FE models have been utilized, to represent vehicle body, seats and restraint system with LS-DYNA. The subject of the test is a ten-year-old child dummy (Q-series Q10), placed on a booster seat in the second-row seat of the vehicle. Both experimental and numerical dummies were provided by Humanetics®.

All the pre-processing steps needed to perform this kind of simulation have been described throughout this thesis. The most investigated step was the generation and calibration of the virtual restraint system, built utilising ANSA by BetaCAE. The LS-DYNA pretensioner and retractor were calibrated using different data from the experimental test as reference.

The model was verified and validated computing cumulative error and validation metric. The head accelerations showed values of V equal to 78, 79 and 76% respectively, reasonably predicting the trend of the experimental curves. Additionally, the $HICs$ have been well predicted, with coincident time instants and peak relative error below 15%.

Chest and pelvis accelerations were predicted with an average V equal to 85%, constituting the areas of highest performance of the FE model. Upper neck forces and moments displayed an acceptable level of prediction, with V at least equal to 70%, whereas the lower neck showed the lowest correlation of the results, mostly on x and z-moments.

It is important to underline that all biomechanical data in this thesis document were normalized for confidentiality reasons.

Lastly, a sensitivity study on the influence of the dynamic friction coefficient FC of the lower LS-DYNA slip ring on the dummy injury responses was performed, obtaining a more correlated operation of the belt with respect to the experimental setting. The analysis was performed comparing all values of E and V among the different configurations, concluding that the most correlated setting has FC = 0.4, with an increase in V of 10% in the upper neck region.

ACKNOWLEDGMENTS

Paolo e Giuseppe, non mi dimentico di voi. Semplicemente compagni di vita. Grazie per tutto il supporto che mi avete dato durante questi anni di crescita personale.

Inoltre, voglio ringraziare coloro che mi hanno affiancato durante questa avventura in Canada, Stefano e Carlo. Siete stati entrambi fonte di crescita personale per me e dopo aver passato un intero anno insieme mi conoscete alla perfezione. Le ore passate a giocare a "Call of Duty" e a parlare dei nostri interessi mi hanno sempre permesso di distrarmi dagli impegni universitari, allentando un po' la presa. Spero di rivedervi presto una volta tornati tutti in Italia.

Moreover, I would like to thank Mike, Daniel and my housemates James and Luka. You all made this year easier since its beginning, and every evening spent with you has been a lot special and funny. Also, I want to thank Ewon, Stephen and Max, my friends from the DIMD program. I look forward to meeting with you in Torino.

Lastly, thank you to my new friends from the Exchange group: Alessio, Federico, Jorge, Aanjan, Julia, Lucie, and Julia. The nights all together have been a great occasion to know other cultures and new awesome people!

TABLE OF CONTENTS

LIST OF TABLES

LIST OF FIGURES

LIST OF APPENDICES

LIST OF ABBREVIATIONS

ABS	Anti-Blocking System
AEB	Advanced Emergency Braking
AIS	Abbreviated Injury Scale
ANCAP	Australia and New Zealand New Car Assessment Program
ANPRM	Advanced Notice of Proposed Rule Making
ATD	Anthropomorphic Test Device
BIORID	Biofidelic Rear Impact Dummy
BioSID	Biofidelic Small Side Impact Dummy
CAD	Computer-Aided Design
CARE	Community database on Accidents on the Roads in Europe
CMVSS	Canadian Motor Vehicle Safety Standard
COTR	Contractive Officer's Technical Representative
CRABI	Child restraint/Air Bag Interaction
CRS	Child Restraint System
DLT	Dynamic Locking Tongue
DOT	Department of Transportation
ECE	Economic Commission for Europe
ESC	Electronic Stability Control
ETSC	European Transport Safety Council
Euro NCAP	European New Car Assessment Program
EuroSID	Small Side Impact Dummy for European tests
FARS	Fatality Analysis Reporting System
FC	Friction Coefficient
FE	Finite Element
FEM	Finite Element Method
FFCRS	Forward Facing Child Restraint System

FMVSS	Federal Motor Vehicle Safety Standard
FTSS	First Technology Safety Systems
HIC	Head Injury Criterion
IC	Injury Criterion
IS	Injury Severity
Istat	Istituto Nazionale di Statistica
LATCH	Lower Anchors and Tethers for Children
LSTC	Livermore Software Technology Corporation
MDB	Mobile Deformable Barrier
NCAP	New Car Assessment Program
NHTSA	National Highway Traffic Safety Administration
NPRM	Notice of Proposed Rule Making
NTSB	National Transportation Safety Board
ODB	Offset-Deformable Barrier
OEM	Original Equipment Manufacturer
PCSI	Pediatric Cervical Spine Injury
PMHS	Post-Mortem Human Subjects
Q10	Q-series 10-year-old child dummy
Q6	Q-series 6-year-old child dummy
RFCRS	Rearward Facing Child Restraint System
RID	Rear Impact Dummy
SAE	Society of Automotive Engineers
SID	Small Side Impact Dummy
THOR	Test device for Human Occupant Restraint
THUMS	Total Human Model for Safety
UK	United Kingdom
UMTRI	University of Michigan Transportation Research Institute

UN	United Nations
USA	United States of America
VBV	Velocity of Bullet Vehicle
VIP	Very Important People
VRU	Vulnerable Road User

NOMENCLATURE

t_1	First Time instant
t_2	Last Time instant
$a(t)$	Acceleration as function of time
HIC_{MAX}	Maximum Head Injury Criterion
a_x	Acceleration x-component
a_y	Acceleration y-component
a_z	Acceleration z-component
$a_{resultant}$	Resultant Acceleration
Nij	Neck Injury Criterion
F_z	Force z-component/Axial Force
F_{zc}	Critical Axial Force
M_y	Moment y-component/Bending Moment
M_{yc}	Critical Bending Moment
C	Amplitude factor
β	Shape factor
V_0	Initial Velocity
V_i	Intermediate Velocity
V_f	Final Velocity
m	Mass
$F(t)$	Force as function of time
t_0	Initial Time instant
t_f	Final Time instant
V_D	Dummy Velocity
V_V	Vehicle Velocity
$D_{chest}(t)$	Chest Deflection as function of time
D_{chest}	Chest Deflection

V	Validation metric
E	Cumulative Error
$y(x)$	Measured value
$Y(x)$	Expected value
L	Range of the independent variable
$error(x)$	Relative Error
E_{kin}	Kinetic Energy
E_{int}	Internal Energy
E_{sli}	Sliding Energy
E_{rw}	Rigid Wall Energy
E_{damp}	Damping Energy
E_{hg}	Hourglass Energy
E_{tot}	Total Energy
E_{kin}^{0}	Initial Kinetic Energy
E_{int}^{0}	Initial Internal Energy
W_{ext}	External Work
$w_{DUMMY_{NUMERICAL}}$	Numerical Dummy Weight
$w_{DUMMY_{EXPECTED}}$	Expected Dummy Weight
$w_{CRS_{NUMERICAL}}$	Numerical CRS Weight
$w_{CRS_{EXPECTED}}$	Expected CRS Weight
r_{ISOFIX}	ISOFIX Reaction load

1. INTRODUCTION

Nowadays, vehicles are essential for everyday life. They are used in every city to do the most common actions of a family or by an employee to go to work and, sometimes, to actually travel. Therefore, safety of all types of occupants (male, female, adult and child) while traveling in cars has been analyzed and improved in the last decades. The identification of the injury mechanisms has been shown to be essential to design both adult and child restraint systems, which can help to reduce the risk of death and serious injuries.

In 2006, in Europe, the average number of car accidents was equal to 21,000. Ten years later, in 2015, it was decreased to 12,000 [1]. In addition, Transport Canada registered a lowering of the number of personal injuries from 140,700 (in 1997) to 115,000 (in 2016), hence a decrease of 21% [3]. Moreover, the Centers for Disease Control and Prevention evidenced a decrease of vehicle crashes in the United States from 237 car accidents per 100,000 citizens (in 2005) to 129 car accidents per 100000 citizens (in 2015).

The utilization of a correct and improved restraint system is surely one of the most contributing factors to these reductions. The use of child safety seats, for example, reduced fatal injury by more than 50% for both infants and toddlers from 2005 to 2015, in North America [19]. In Europe, the rate of fatality for children of the last decade had also decreased. [22].
In 1997, the European New Car Assessment Program (Euro NCAP) was founded in the UK. For the first time, a rating test of child safety in vehicles was introduced and the improvement of child restraint systems (CRS) has been called for. Since 2009, Euro NCAP performs rating tests divided among three different main test areas; one of these is completely related to child safety, and to assess the performance of both vehicles and CRSs in static and dynamic conditions.

Consequently, vehicle manufacturers always try to improve safety performance of their product and child occupant protection had become one of the most investigated fields. This is critical because of the weaker body of such occupants and the need for absolutely safeguard the passengers.

To verify the effects of the modifications of vehicle body and restraint system to improve occupant safety, many crash tests are performed by all car companies, spending almost millions of dollars every year to assess their products' performance. To minimize the costs of this process, sled tests (which are more conservative) and Finite Element simulations are performed, to reduce the number of destructive tests to execute. This is the reason why nowadays car companies invest more resources in the so-called "virtual safety area".

2. LITERATURE REVIEW

2.1 Automotive crash statistics

2.1.1 Europe

The Community database on Accidents on the Roads in Europe (CARE) is a collection of road accident data and subsequent statistics; only the crashes resulting in death or injury are considered.

Additionally, all the European national data sets are integrated into the CARE database in their original structure and definitions, in order to provide a total analysis of accidents and injuries on the whole continent.

In 2015, in Europe, the average number of car accidents was equal to about 12,000; this value represents a decrease of car crash in the last 10 years since, in 2006, the crashes had been around 21,000 [1], as shown in Figure 1.
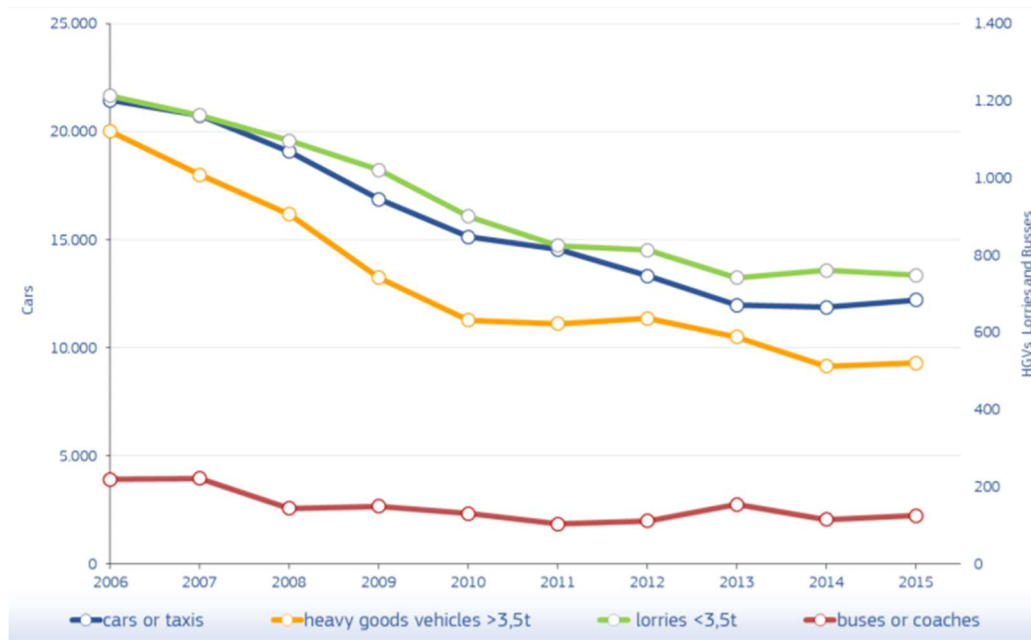
Figure 1 – Car accidents classified per type of vehicle from 2006 to 2015 [1]

This constant reduction of accidents cannot be associated with a decrease in number of operating vehicles given that this statistic increased in the last years: as shown by the European Automobile Manufacturers Association in Table 1 and Figure 2. The passenger car registrations increased by 6.2% in only one year, from 2017 to 2018, and by 31.2% in eleven years, from 2007 to 2018 [2].

	August '18	August '17	%Change 18/17	Jan - Aug '18	Jan - Aug '17	%Change 18/17
						19/09/2018
AUSTRIA	34,227	26,058	+31.3	258,564	240,350	+7.6
BELGIUM	54,437	35,517	+53.3	428,577	394,446	+8.7
BULGARIA	2,887	2,344	+23.2	23,685	19,556	+21.1
CROATIA	3,190	2,410	+32.4	47,188	38,480	+22.6
CYPRUS	719	703	+2.3	9,508	9,347	+1.7
CZECH REPUBLIC	27,830	21,192	+31.3	193,252	185,292	+4.3
DENMARK	20,741	15,313	+35.4	157,969	154,318	+2.4
ESTONIA	2,655	1,984	+33.8	18,982	17,087	+11.1
FINLAND	12,004	9,672	+24.1	91,197	82,978	+9.9
FRANCE	150,390	107,449	+40.0	1,513,932	1,390,234	+8.9
GERMANY	316,405	253,680	+24.7	2,473,284	2,323,786	+6.4
GREECE	7,718	5,134	+50.3	79,154	63,911	+23.9
HUNGARY	12,931	8,915	+45.0	95,724	73,099	+31.0
IRELAND	5,925	5,729	+3.4	119,929	124,651	-3.8
ITALY	91,551	83,638	+9.5	1,365,947	1,366,881	-0.1
LATVIA	1,613	1,469	+9.8	12,080	11,491	+5.1
LITHUANIA	3,308	2,087	+58.5	22,049	16,674	+32.2
LUXEMBOURG	4,187	3,429	+22.1	39,773	36,904	+7.8
NETHERLANDS	41,355	29,093	+42.1	330,471	287,501	+14.9
POLAND	56,701	34,505	+64.3	376,031	318,350	+18.1
PORTUGAL	15,281	11,937	+28.0	169,827	156,695	+8.4
ROMANIA	25,546	12,001	+112.9	100,824	68,344	+47.5
SLOVAKIA	10,595	7,265	+45.8	71,202	64,158	+11.0
SLOVENIA	5,636	4,492	+25.5	53,559	48,834	+9.7
SPAIN	107,692	72,410	+48.7	973,542	849,851	+14.6
SWEDEN	24,670	29,915	-17.5	262,717	248,167	+5.9
UNITED KINGDOM	94,094	76,433	+23.1	1,571,986	1,640,241	-4.2
EUROPEAN UNION	1,134,288	864,774	+31.2	10,860,953	10,231,626	+6.2
EU15[2]	980,677	765,407	+28.1	9,836,869	9,360,914	+5.1
EU12[3]	153,611	99,367	+54.6	1,024,084	870,712	+17.6
ICELAND	1,464	1,521	-3.7	15,028	17,048	-11.8
NORWAY	14,524	13,415	+8.3	100,880	102,874	-1.9
SWITZERLAND	21,484	23,160	-7.2	204,877	206,963	-1.0
EFTA	37,472	38,096	-1.6	320,785	326,885	-1.9
EU + EFTA	1,171,760	902,870	+29.8	11,181,738	10,558,511	+5.9
EU15 + EFTA	1,018,149	803,503	+26.7	10,157,654	9,687,799	+4.8

Table 1 – Growth of car sales from 2017 to 2018 in EU countries [2]
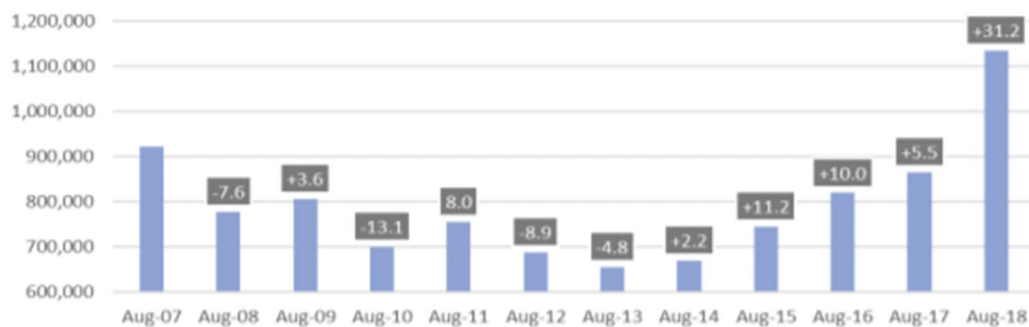
Figure 2 – Growth of car sales from 2007 to 2018 in the European Union [2]

2.1.2 North America

In the last years, the number of car accidents in North America has decreased as well. As a matter of fact, Transport Canada registered a reduction of the number of personal injuries from 140,700 (in 1997) to 115,000 (in 2016), hence a decrease of 21% [3].

Moreover, the Centers for Disease Control and Prevention evidenced a decrease of vehicle crashes in the United States number from 237 car accidents per 100000 citizens (in 2005) to 129 car accidents per 100000 citizens (in 2015), even if the US represents the slowest country in number of crashes decrease per year [4]. Figure 3 displays the trend in the U.S., evidencing the lowest decrease of deaths in car accidents per 100,000 citizens in thirteen years.
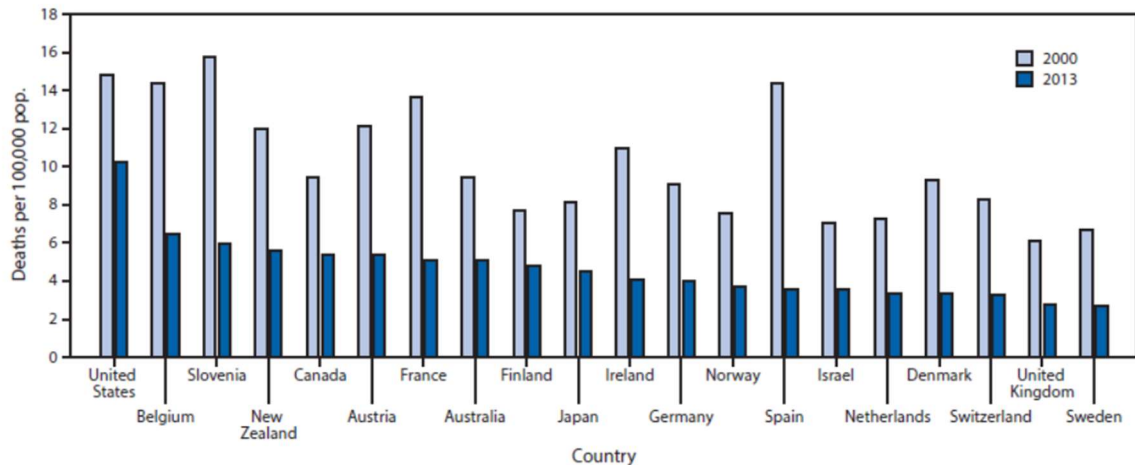
Figure 3 – Deaths in car accidents per 100,000 citizens in different world countries [4]

Additionally, the Figure above confirms that most countries have revealed a decisive lowering in car accident casualties during those years.

2.2 Active, passive and preventive safety of vehicles

2.2.1 Active safety

The term active safety (or primary safety) refers to automobile safety systems that help to avoid a crash. These include braking and steering systems and every device which can improve their response and performance: brake assist, traction control systems, anti-lock braking system (ABS) and electronic stability control systems are all micro-systems that interpret signals from many sensors placed in the vehicle to help the driver's control. Such improvements are mostly based on the analysis of the braking maneuver and the consequent vertical load transfer from the rear to the front axle [5].

2.2.2 Passive safety

It is defined as "all designs that minimize losses when an accident occurs". Therefore, all the systems that protect the driver from the worst consequences of an accident are considered passive safety instruments. Since they are the most important devices for the topic of this thesis it is important to describe them more precisely:

- *Airbag*, flexible fabric bag or a cushion designed to inflate rapidly during a collision. Its function is to soften the occupant impact during a crash when they could hit vehicle parts such as the steering wheel or the cockpit. Modern vehicles comprise of multiple airbag modules in different side and frontal locations of the passenger seating positions which offer maximum protection during a collision;
- *Seat belt*, safely belts installed on all seats of a vehicle to secure the occupant against harmful movements that may result due to collision, jerk or sudden braking;
- *Whiplash protection*, a seat device where the entire backrest is designed to protect the front occupant's neck in case of a rear impact. Such a system utilizes a specially designed hinge-mount that attaches the backrest to the seat bottom, which has a pre-determined rate of rearward movement in the event of certain types of rear impacts;
- *Child Safety System*, specifically designed seats that protect children from injury or death during collisions. Generally, such seats are installed based on end-user requirements [6].

To conclude, the whole vehicle structure, with its stiffness and layout, can be considered a passive safety instrument as well [7].

2.2.3 Preventive safety

This safety field includes all the systems that can communicate to the driver the likely presence of danger. The only difference with respect to active safety systems is the possibility to only warn the driver about a possible hazard, without any active device to avoid it or to minimize the damages in the worst cases [7].

Given this definition, preventive safety most common instruments are:

- Systems of communication and warnings in case of danger or obstacle detection;
- Systems for the detection of the physical and health conditions of the driver;
- Driver general warning and assistance;
- Traffic signals and information panels;
- Road surface and indications [7].

The last two points indicate that preventive safety does not regard only the vehicle itself but also the environment in which it is driven; each type of road has its own dangers and advantages.

2.3 Passive safety

2.3.1 Biomechanical approach

In this type of approach, the safety concept takes into consideration the mitigation of injuries to the occupant of a vehicle that may result from a collision against an external obstacle or another vehicle. In this way, such a concept assumes both the possibility that a collision may occur and the probability of injuries arising due to the collision itself.

Accepting this assumption implies that the safety concept is associated with probability. Thus, rather than pursuing the design of a totally safe vehicle, the approach taken is to consider vehicle safety issues regarding certain types of accidental events. Additionally, the main method is not to seek damage avoidance but instead reasonable mitigation of damage to the vehicle and, above all, injury to the occupants [9].

Originally, the passive safety of a car was associated with the maintenance of cockpit integrity. In this way, the car body was considered like a shell that can protect the occupants, but which can deform, in defined situations of static and dynamic loads, within certain geometric limits. In this way, the car body can offer a good degree of protection for the occupants in case of impact [9].

This approach to safety is here identified as the *geometric approach*. Due to this method, a series of regulations were created for the car structure and geometry and some of these are still in force today; for example, during a front impact test on a car, the backward movement of the steering wheel must be less than 12.7 cm, while, in the case of side impacts, intrusion must not exceed specific geometric values.

Several years ago, this approach started to be considered as incomplete since it is not linked with the human tolerance limits of traumas due to accidents. Hence, it became evident the need to evaluate the safety of a car with biomechanical criteria requiring the need to verify, in case of a crash, that the stresses suffered by the occupants are lower than the human tolerance limits. This approach became known as the so-called *biomechanical approach*: the logical scheme to define safety standards according to this methodology is multi-disciplinary, and it is shown in Figure 4 [9].
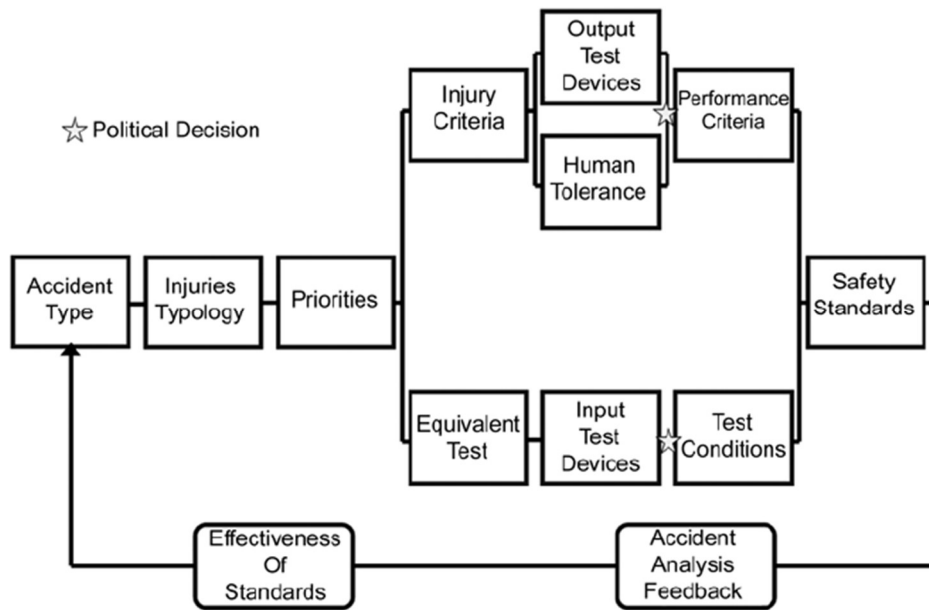
Figure 4 – The biomechanical approach [9]

For examining this representation, it is necessary to clarify the meaning of different terms:

- *Lesion*: a lesion is a physiological change arising from mechanical stress. The detection of lesions and the attribution of different severity limits concerns the first-aid doctors;

- *Injury criterion*: this is a physical parameter (acceleration, force, deformation, etc.) which indicates the extent of damage to the human body, with respect to the severity of the lesion for the body segment of interest. To identify injury criteria and attribute human tolerance levels, it is necessary to conduct tests on cadavers. Thus, this type of activity is mainly done within Forensic Medicine Institutes or selected universities (for example, the Wayne State University of Detroit, MI);

- *Performance criterion*: this is the value of the injury criterion which is obtained from the biomechanical process and must not be exceeded. It is measured with a dummy positioned inside a car in an impact test. The selection of performance criteria concerns the legislator;

- *Injury mechanism*: the logic of the biomechanical approach assumes that, for each body segment, an absolute injury criterion can be determined independently of how the injury occurs. This is not possible when the injuries can be created by different mechanisms; today it has been understood that for a body segment it is necessary to determine as many criteria as there are causes of injury. The interaction between these mechanisms will determine different values for each single injury criterion. How to identify the consequences of interactions between different injury mechanisms is one of the main issues currently being addressed in biomechanics.

Therefore, the biomechanical approach combines three typologies of activities and knowledge which contribute to the formulation of a regulation relating to biomechanics specifications, called *Safety Standards*:

1. *Accident analysis*, to determine in which types of accident injuries or deaths occur, the parameters that characterize the severity of the impact and how the occupants are injured; this analysis must provide the priority of action and verify, over time, the validity of the regulation issued. Its results are summarized in Figure 5.
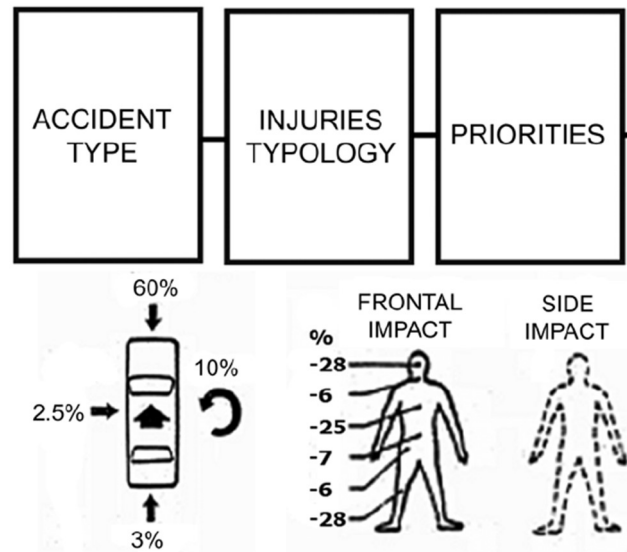
Figure 5 – Schematic representation of accident analysis [9]

2. The definition of *test conditions*, so that the car body is submitted to the same stress levels as in a real accident. A schematic example is shown in Figure 6.
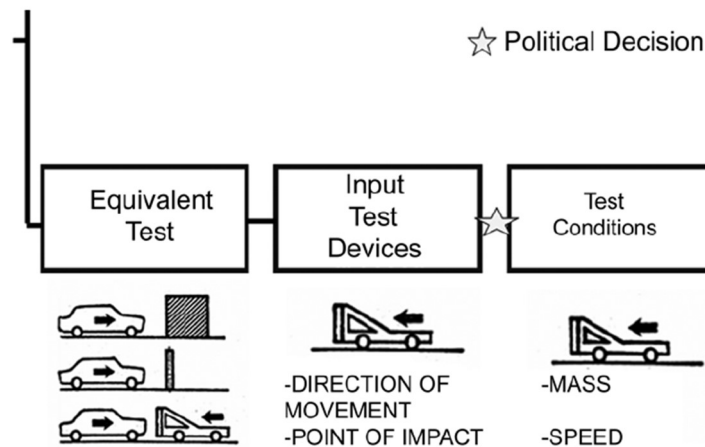
Figure 6 – Test conditions [9]

3. The definition of performance criteria, which are expressed in biomechanical terms. More accurately, the determination of measurable physical parameters (injury criterion, IC) for each part of the human body, which are linked to the injury severity (IS). Once the injury criterion has been defined, it is necessary to proceed to determine the maximum values that can be applied to the human body (H = Human tolerance level). These values must be correlated with an injury scale (AIS = Abbreviated Injury Scale). In parallel, it is necessary to develop a conformity anthropomorphic instrument that can measure the injury criterion during the impact. These instruments may be complex, such as dummies, which will be analyzed in more detail in section 2.9, or relatively simple, like an impactor with anthropomorphic characteristics of head used in pedestrian crash tests [9].

When a new Safety Standard is defined, its effectiveness is verified through feedback on the accident analysis. Consequently, the standard can be modified where necessary, constituting the loop cycle shown in Figure 4.

2.3.2 Injury criteria

2.3.2.1 Head

The Head Injury Criterion (*HIC*) is the injury criterion universally known for the head. It is based on the resultant acceleration on the centre of gravity of the head. Its expression is

$$HIC_{max} = \left\{ \left[\frac{1}{t_2 - t_1} \int_{t_1}^{t_2} a(t)dt \right]^{2.5} (t_2 - t_1) \right\} < 1000 \tag{1}$$

where *a(t)* is the temporal progress of resultant acceleration, expressed in g,

$$a_{resultant} = \sqrt{a_x^2 + a_y^2 + a_z^2} \tag{2}$$

while t_1 and t_2 are two instants that define the width of a temporal window along with the time interval encompassing the acceleration impulse measured on the head [10].

On the *a(t)* curve, a mobile temporal window (in blue in Figure 7) with variable width is applied along the time axis. For each window configuration, a correspondent *HIC* value is obtained: the maximum value obtained in this way represents the definitive *HIC*.
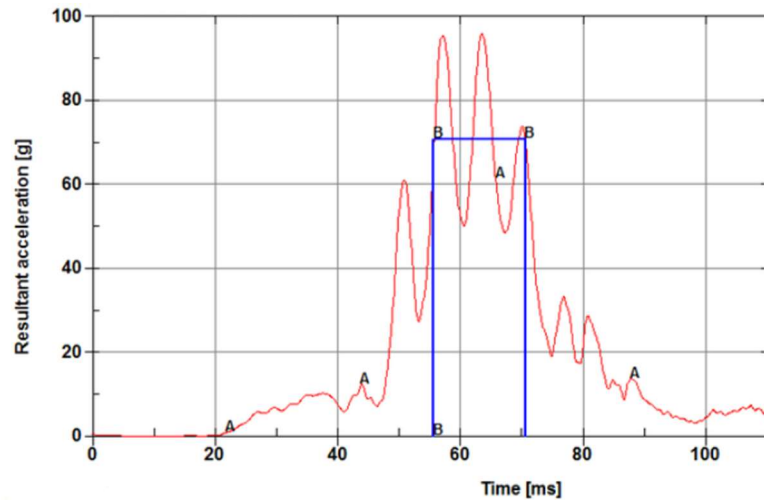
Figure 7 – HIC criterion calculation [11]

Moreover, it is important to specify that the integral contained in the definition of *HIC* yields an average value over the $t_2 - t_1$ window: in this way, the influence of peaks is reduced.

Additionally, the limit value of 1000 is tied to a straight-line equation that represents the trend line of the border zone between the absence and presence of a linear fracture of the skull. This straight line is positioned on a logarithmic diagram with time on the abscissa and acceleration on the ordinate. This was obtained with the experimental test mentioned previously.

Currently, for the calculation of the *HIC* required by the standard CMVSS208 and FMVSS 213, mobile windows with a width of $t_2 - t_1 \leq 36$ ms are used [12].

2.3.2.2   Neck

Serious injuries to the neck, in adult occupants, occur only during high severity impact and are usually associated to serious injuries to other body segments (for example head or chest), while minor injuries to the neck occur mainly with low severity impacts and are often not associated to other injuries.

Neck injuries, despite not being a priority from the perspective of injury seriousness, have remarkable importance from an economic standpoint due to their frequent occurrence. In addition, child occupants are much more exposed to this type of injury, which can be highly dangerous for them. For these reasons, even a small reduction of medium and minor neck injuries has significant importance.

As concerns most of the injury criteria, the situation has not yet been consolidated and today there are no fixed regulations.

The calculation of the *Nij* injury criterion required by the most important Safety Standards (UN-ECE, FMVSS, and CMVSS) to calculate the neck injury risks of child occupants during vehicle crashes is based on Equation 3:

$$Nij = \left(\frac{F_z}{F_{zc}}\right) + \left(\frac{M_y}{M_{yc}}\right) \tag{3}$$

where F_z and M_y are the actual values of axial force and bending moment exerted during the event, whereas F_{zc} and M_{yc} are the critical values, equal to 2120 N (in both tension and compression) and 68 Nm (in the forward direction) or 27 Nm (in the backward direction), respectively. The value of these parameters should not exceed unity, which indicates severe neck injuries.

Moreover, the standard CMVSS 208 collects limit values for different forces and moments which could be applied to the neck (Figure 8a): more precisely, the shear force F_x and the axial force F_z must respect some limit curves, while the bending moment M_y must not exceed 57 Nm in extension [13].

As concerns the accepted limit value of force, these curves are cumulative, therefore for each value of force, the curves indicate the maximum time for which they may be applied. These are shown in Figure 8b.

(a)

(b)
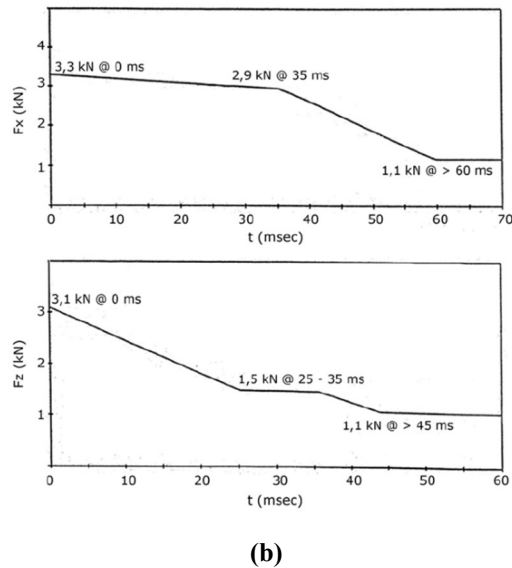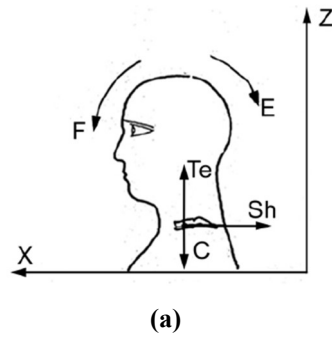
Figure 8 – Trend of performance criteria as a function of time. Shear criterion above, tension criterion below [9]

2.3.3 Simplified models for crash

The definition of simple models to analyze a crash case can be useful for understanding the trend of main physical parameters such as time, force and acceleration.

Firstly, a time interval between the start of a crash (time instant t_1) and the end of a crash (time instant t_2, when the vehicle is fully stopped) must be considered; at this point, it is important to observe the transmitted force and acceleration during the time interval just defined, thus during the crash itself.

2.3.3.1 Crash against a rigid barrier of infinite mass

Let us consider a single vehicle which is impacting against a rigid barrier of infinite mass. The force transmitted during this type of crash can be measured by instrumenting the barrier with load cells, and the results will be a sequence of peaks during the folding of the

structures followed by abrupt valleys caused by bending and collapse of some parts with other contributions due to the impact of the parts in the engine compartment [9], as shown in Figure 9 and 10; in the former, the reduction of the distance *d* between the center of gravity of the vehicle and the barrier due to the folding of its front end can be noticed; in the latter, the trend of speed of the center of gravity *VBV* (velocity of the bullet vehicle) and of the distance *d* can be observed.
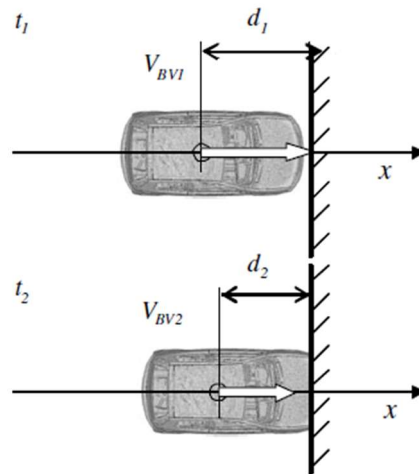
Figure 9 – Crash against a rigid barrier of infinite mass [9]
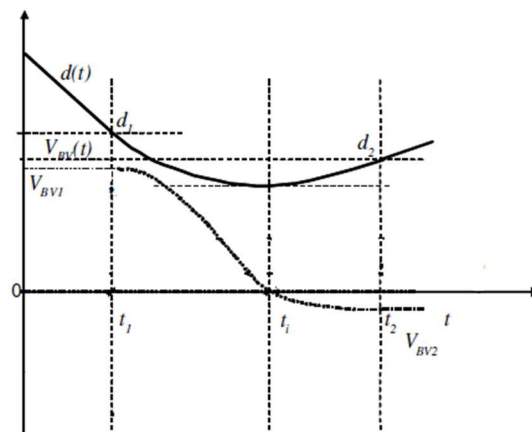
Figure 10 – Speed of the vehicle centre of gravity and distance with respect to the barrier [9]

A similar behaviour can be found measuring the acceleration on a part of the vehicle that is not directly involved in the crash, for example, the seat rail. Figure 11 shows the qualitative shape of this acceleration (curve a). Curve b represented on the same diagram is obtained by the best fit interpolation of the experimental data (curve a) by the McMillan curve

which is simply a semi-empirical expression that represents the low-frequency content of the acceleration:

$$a(t) = C\frac{t}{t_2}\left(1 - \frac{t}{t_2}\right)^{\beta}$$

(4)

where coefficient C is the amplitude factor and exponent β is the shape factor that can be identified by curve-fitting the experimental data with Equation 4 [9].
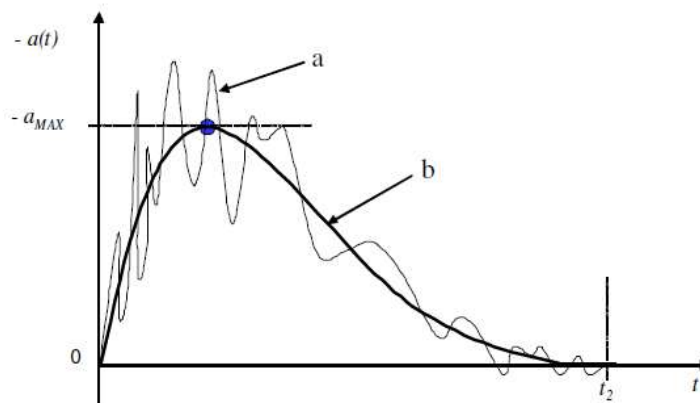
Figure 11 – Qualitative behaviour of the acceleration measured on the seat rail during a frontal crash against a barrier [9]

2.3.3.2 Role of the restraint system

The role played by the restraint system is a crucial object of the study of crash scenarios and it is useful to refer to two different decelerations of the same vehicle, of mass m, from the same initial speed. In the first case, the driver acts on the brake pedal until the vehicle stops within a distance X. in the second case, instead, the vehicle crashes against a rigid wall, as shown in Figures 12 and 13 respectively.
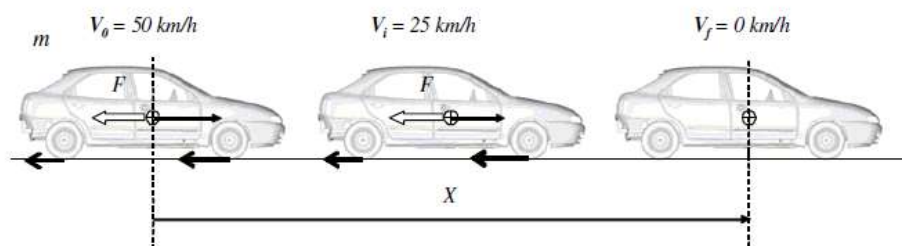
Figure 12 – Deceleration from 50 km/h to full stop by braking [9]
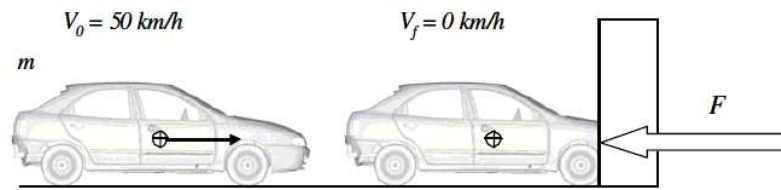
Figure 13 – Deceleration from 50 km/h by crash against a rigid barrier [9]

The kinetic energy of the vehicle at the beginning and at the end of the deceleration is the same in the two cases; nevertheless, the process of reaching a full stop differs significantly. In the first case, the use of brakes generates forces with resultant F between the tire and the road surface that acts to reduce the vehicle speed.

Due to Newton's second law, the variation of the momentum is equal to the impulse, which can be computed as the time integral of the resultant force F between the start t_0 and the final time t_f of the deceleration:

$$m(V_0 - V_f) = \int_{t_0}^{t_f} F(t)\, dt \qquad (5)$$

As these forces move with the vehicle, the corresponding work reduces the kinetic energy until the vehicle comes to a full stop.

In the second case, the vehicle crashes against a fixed barrier reaching a full stop almost instantly. As in the previous case, the time integral of the force transmitted from the barrier to the vehicle is the same, with the difference that, due to the much shorter time interval, the force is correspondingly higher.

Therefore, the first difference between a crash and normal braking lies in the time interval needed to stop the vehicle from a certain speed. Looking at Equation 5, since the impulse is the same, normal braking involves a relatively long time and, consequently, the forces lower are lower than in the case of a crash which occurs in a very short time interval.

The second difference corresponds to how the kinetic energy of the vehicle is dissipated; during normal braking, the forces between the tires and the road surface dissipate all the kinetic energy. On the other hand, during a crash against a rigid barrier, the force acting on the vehicle does not dissipate energy as the surface of the barrier is not moving at all. The kinetic energy will then be dissipated by the vehicle with the plastic deformation of its front structure [9].

The same considerations can be applied to the occupants: during normal braking, each occupant is subject to several forces transmitted by the seat, belts (the restraint system), feet and all other elements of the body in contact with some part of the vehicle. These forces move their

points of application over the braking space. Therefore, at the occupant level, many forces are transmitted to the cabin, to dissipate the kinetic energy. If the kinetic energy is not transformed into internal energy of the occupant body, but elsewhere, no damage to the occupant will occur in this process.

During a crash, if the occupant is restrained, energy is dissipated by the forces developed by the restraint system; in this case, there may not be a substantial difference in the energy dissipation with respect to the case of the normal braking, apart from the loads applied to its body.

Conversely, a completely different scenario emerges if the occupant is not restrained: in this case when the vehicle reduces its speed by plastic deformation of its structure, the occupant continues its motion until impacting the interior surfaces (dashboard or steering wheel for the front occupants). The very short time involved in a crash (in the order of a tenth of a second) makes any conscious or unconscious reaction by the occupant impossible and the speed of the impact of people inside the vehicle will be almost equal to the initial one. Consequently, the high stiffness of the interior surfaces stops the occupant in a very short time and with very little deformation of the surface itself. The kinetic energy of the occupant is then transformed into internal energy, causing significant injuries [14].

Correspondingly, it can be easily understood that the main role of the restraint system is to reduce the kinetic energy of the occupant with forces that act during the deformation of the vehicle due to an impact. The motion of their points of application avoids the transformation into internal energy of the body and the relative consequences in terms of physical injury. The main positions assumed by a restrained occupant during a crash can be observed in Figure 14.
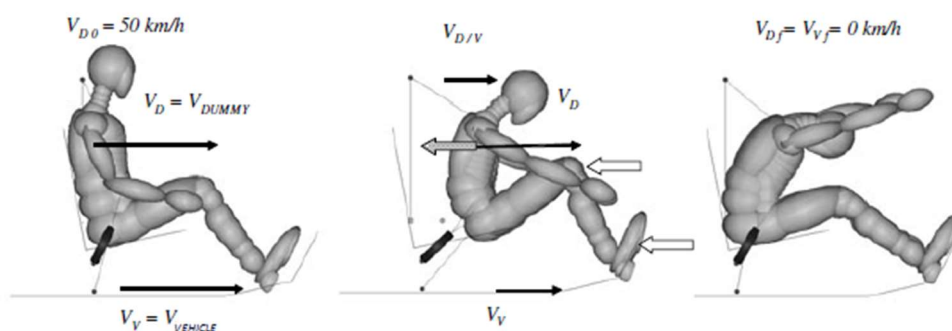
Figure 14 – Restrained occupant during a crash [9]

2.3.4 The seat belt mechanism

The three-point seat belt (the safety belt) has been in use in cars for more than fifty years and no other safety product has saved as many lives of car occupants. Other products as frontal and side airbags have been successfully implemented to further enhance car occupant protection. However, these new restraint systems complement the three-point seat belt, without replacing it. As a matter of fact, seat belts are mandatory in vehicles since 1968, thanks to the Federal Motor Vehicle Safety Standard 208 [67]. A schematic of the standard safety belt is shown in Figure 15.

Figure 15 – The standard three-point seat belt [15]

The first generation of the three-point safety belt, the static belt, was a very good restraint provided it was well adjusted with only a small amount of slack present. However, such an operation was not completely appreciated. One major reason for this was probably that people wanted a loose belt for optimal comfort. Another common reason was that for example, a husband and his wife used the same car. The belt was often adjusted for one of them, but it was inconvenient for the other to readjust when using the same one.

Therefore, during the 1960s, the first improvement of the three-point belt was the inertia-reel, today normally called the retractor (shown in Figure 16). It is installed in the lower part of the B-pillar of the vehicle and is composed of a spool and spring mechanism, which is rotated when the seat belt is tight. Consequently, it exploits the elastic force of the spring to return to the original position [15]. Nevertheless, the rewinding spring force must be rather weak otherwise the belt will be too uncomfortable to wear but, at the same time, the rewinding capacity of the retractor has to be sufficient to tighten the belt, when it is un-buckled.

Figure 16 – The seat belt retractor [15]

Thus, the retractor allows every occupant to adapt the seat belt to his/her body dimensions, however sacrificing some restraining ability in the early phase of a frontal crash, to get the belt comfortable in the daily usage.

Successively, the retractor pretensioner eliminated this weakness: a small pyrotechnic charge generates gas very quickly with a high pressure that acts upon a pulling mechanism to immediately rewind the retractor spool. Depending on the amount of slack present, up to 150-200 mm of webbing can be pulled in. The retractor pretensioner is fired by an electronic control unit sensing the vehicle crash pulse, so tightening up the belt significantly before the occupant has moved more than a few centimeters forward relative to the car during a frontal crash [15].

If people wear a lot of clothing, a considerable amount of slack can be present in the belt system and especially in the lap belt, increasing the risk of belt slipping. In order to further improve the pre-tensioning of the lap belt, a buckle pretensioner (a pretensioner mounted on the seat belt buckle) was developed. The first generation was fully mechanical with a strong and fast-acting spring. Nowadays, the actuators of the buckle pretensioners are pyrotechnically driven.

The last improvement made so far in the three-point seat belt restraining system is represented by the Dynamic Locking Tongue (DLT) [16]. It consists of a seat belt tongue (the plate which fastens into the buckle) with a rotating cam and a concealed spring. It allows webbing to pass freely through the tongue when buckling and in normal seat belt use to ensure comfort and convenience for everyday use. However, in the event of hard braking or a crash resulting in a force greater than a defined limit on the belt, the DLT clamps the webbing and collaborates with the pretensioners helping to reduce both loads on the occupant's chest and pelvis displacement.

2.4 Traffic safety facts for children

Based on the 2015 National Highway Traffic Safety Administration (NHTSA) report on Traffic Safety Facts [17], 32,166 crashes occurred in North America, where 22,441 occupants died. Of these occupants, 775 (3%) were children aged 0 through 14 years old. Moreover, the Istat 2017 report affirms that 23,636 occupants were killed in motor crashes in Europe during that year and 1.4% of these were children aged 0 through 9 years old [18].

In the last ten years, the way to correctly use the restraint system has spread through families and drivers; nowadays, crashes are caused mostly by driving distractions, such as the use of smartphones, rather than by the improper use of safety and restraint systems. However, misuse of restraint systems for children is still present in today's drivers and parents, and each of these acts could lead to fatal consequences [19].

2.4.1 Fatalities and injuries in frontal and side impact crashes

The number of fatalities and injuries which child occupants are exposed to had shown a decline in the recent years, while some differences can be noticed in the changes of front versus rear seat fatalities and injuries.

2.4.1.1   Fatality data

As shown in Figure 17, the 2015 NHTSA report on Traffic Safety Facts for children [17] affirms that child motor vehicle traffic fatalities have continuously decreased between 2006 and 2015, in North America.
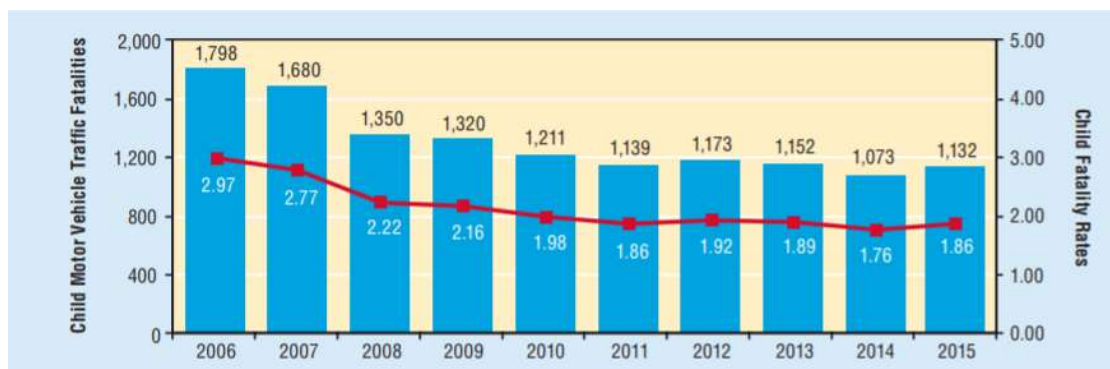
Figure 17 – Child motor vehicle traffic fatalities and child fatalities rates per 100,000 child population, 2006 - 2015 [17]

Moreover, Figure 18 divides such fatalities by age group, underlining that children aged 8 through 12 years old are the principal victims of fatal crashes. This may happen because children of that age start to use normal seat belts as a restraint system, even if their body is still weaker and smaller than an adult one.
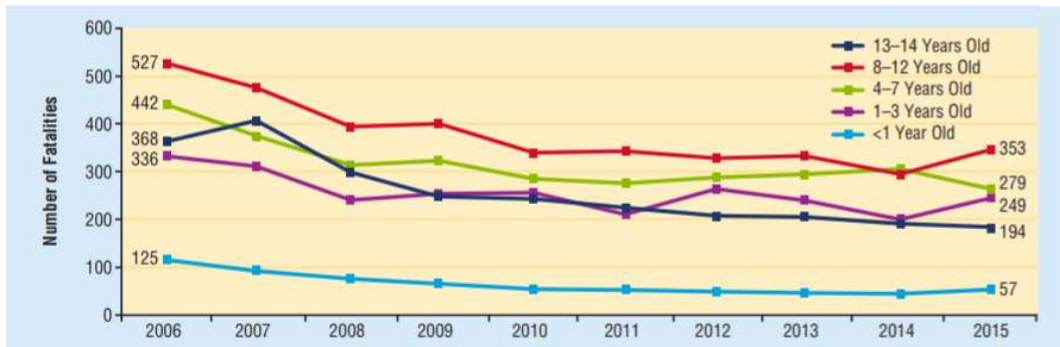
Figure 18 – Child motor vehicle traffic fatalities, by age group, 2006 – 2015 [17]

Child safety seats have been shown to reduce fatal injury by 71% for infants (under 1-year-old) and by 54% for toddlers (1 to 4 years old) in passenger cars [20]. Additionally, lap/shoulder seat belts, when used, reduce the risk of fatal injury to front-seat occupants of passenger cars ages 5 and older by 45 percent and the risk of moderate-to-critical injury by 50 percent [21].

Among the 775 child passengers killed in motor vehicle crashes in 2015, 274 (39%) were unrestrained and of the 38,152 passenger vehicle occupants who survived in fatal crashes, 4,516 (12%) were children and 608 (14%) of them were unrestrained [19].

Regarding Europe, the 12th Annual Road Safety Performance Index (PIN) report of the European Transport Safety Council (ESTC) affirms that 630 children were killed in motor crashes in 2016 and this value represents a decrease in mortality of 7.3% with respect to 2006. Moreover, child road safety improved more than adult road safety in these 10 years, since the adult mortality had decreased only by 5.8%. In Italy, the number of fatal crashes for children decreased by 8.2% and by 3% for adults between 2006 and 2016 [22].

Analyzing the Fatality Analysis Reporting System (FARS) Encyclopedia, a public web database provided by NHTSA, it can be noticed that, regardless of whether the child was seated in the front or in the rear seat, frontal and side crashes accounted for most child occupant fatalities.

In 2007, the total number of crashes in which a 0-to-14-year-old child died in the USA was equal to 604; in 2017, this number decreased to 444 [23].

Moreover, in 2007, 48.5% of the fatal crashes in the USA for children aged 0 through 14 years old was a frontal impact and 38.9% was a side or angled impact.

In 2017, instead, 45.3% of the fatal crashes in the USA for children aged 0 through 14 years old was a frontal impact and 52.5% was a side or angled impact [23]. The remaining 2.2% includes rear-to-side or rear-to-rear crashes, which are much less dangerous and usually happen at lower velocities; on the other hand, the high percentages of front and side crashes, even after 10 years, lets us understand why it is so important to analyze both, simulating them in crash tests and creating restraint systems to limit the number of injuries.

Figure 19 shows three histograms regarding the number of crashes (a), fatality data (b) and injury data (c) registered using the FARS.

(a)

(b)

(c)
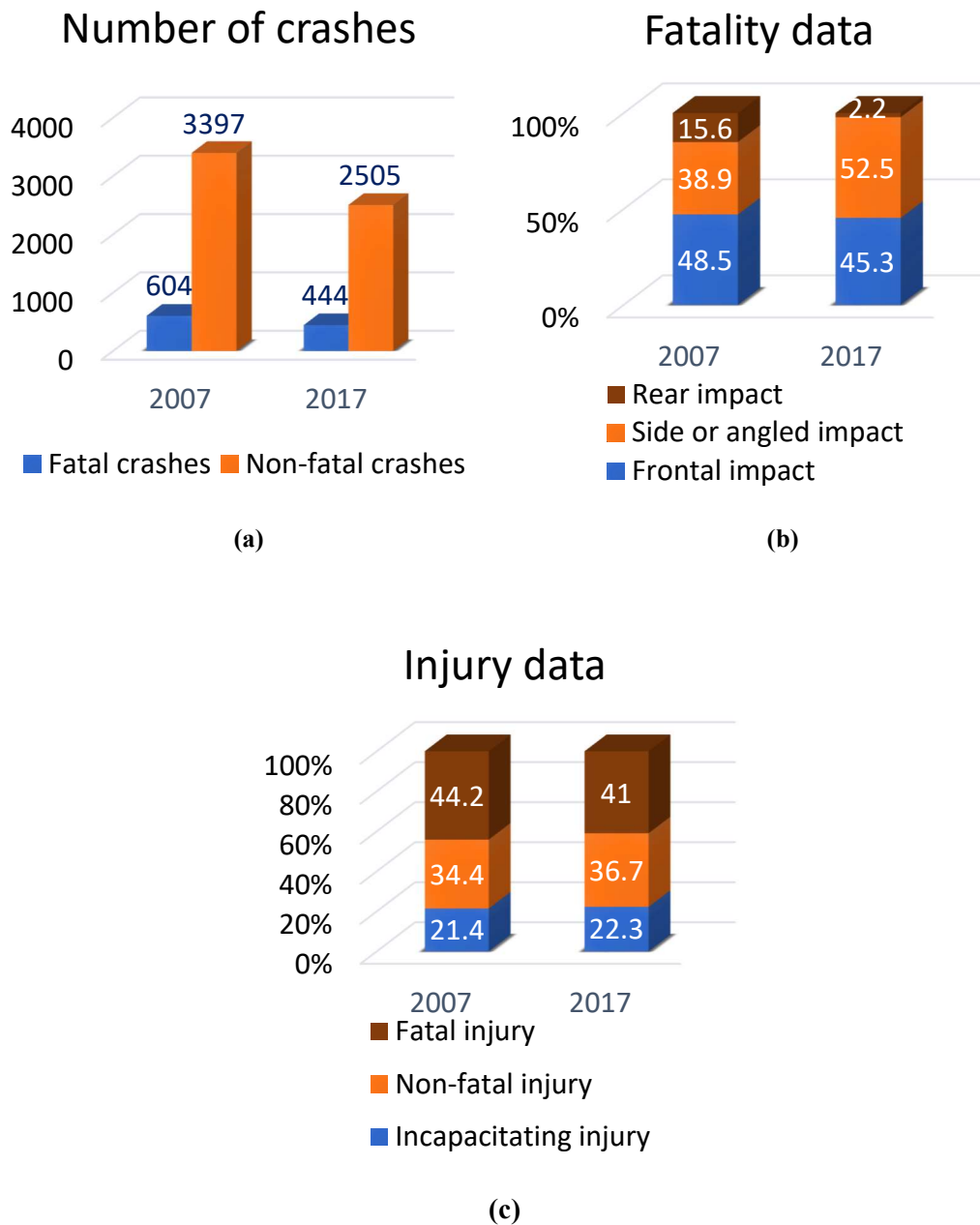
Figure 19 – Number of crashes (a), fatality data (b) and injury data (c) collected from FARS about 2007 and 2017 [23]

2.4.1.2   Injury data

The number of fatal crashes is not the only one to consider in road safety, mostly when studying impact cases regarding children, since every type of injury could lead to serious consequences.

Using the FARS, it can be noticed that 55.8% of injuries of 2007 crashes involving 0-14 years old children were non-fatal, but 21.4% includes incapacitating injuries, which must be absolutely avoided for a child.

In 2017, instead, the number of crashes leading to non-fatal injuries decreased from 3,397 to 2,505, a relevant improvement in road safety. To conclude, the percentage of incapacitating injuries remained almost the same, equal to 22.3% [23], indicating that a certain impact case in which a child can be severely injured can still occur, due to the intensity of the impact or to the misuse or the malfunctioning of the child restraint system.

2.5 Child restraint system

Children are the most vulnerable road users; hence parents should always use a proper restraint system when traveling with their sons/daughters in motor vehicles. A child safety seat (more technically, a child restraint system) is designed specifically to protect children from injuries or death during vehicle collisions. Most commonly, these seats are purchased by car owners and nowadays car manufacturers prefer to integrate them directly into their vehicle's design, providing anchorages and ensuring seat belt compatibility.

The first design of a child restraint system is dated 1962, when Leonard Rivkin, in Denver, Colorado, designed a forward-facing child seat with a metal frame to protect the baby. It must be noticed that standard seat belts were not default equipment in automobiles until the end of the 1960s [24].

When the FMVSS 208 established the mandatory use of seat belts in vehicles in 1968, child restraint systems consequently started to be equipped with different restraining configurations, as shown in Figure 20.
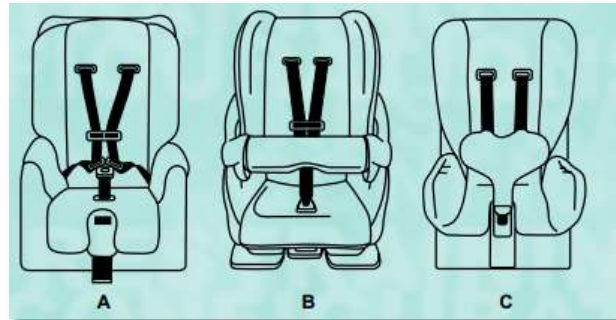
Figure 20 – Restraining configurations: (a) 5-point harness, (b) tray shield, (c) T-shield [35]

Child restraint systems can be distinguished between two main categories:

- Forward-facing child restraint systems (FFCRS), in which children face the direction of travel of the vehicle (Figure 21a);
- Rearward-facing child restraint systems (RFCRS), in which children face the opposite direction with respect to the vehicle travel (Figure 21b).

(a)　　　　　　　　　　　　　　　　　　　(b)

Figure 21 – Forward (a) and rearward (b) child restraint systems [45]

Furthermore, children older than 8 years old, due to the excessive increase of their torso width and height, are often no more able to fit an FFCRS. To ensure their maximum safety in vehicles, before letting them use the standard seat belt, a booster cushion should be used, which can exploit the lower anchorages of each CRS standard. A common booster is substantially composed by the only lower section of a forward-facing CRS and its functioning and advantages will be described in Section 2.6.2.

2.5.1 Installation systems of child restraints

In the early 1990s, the initial development of standardized anchorage devices to be mounted in cars for the CRS began in Europe so that, in 1999, the ISOFIX system was standardized.

Transport Canada originally developed a system called CANFIX, which contributed to the ISOFIX development. In the USA, instead, a system called LATCH (Lower Anchors and Tethers for Children), based on the ISOFIX, has been developed and made obligatory since September 2002. With both ISOFIX and LATCH, seats are secured with a single attachment at the top (top tether) and two attachments at the base of each side of the seat, as shown in Figure 22.
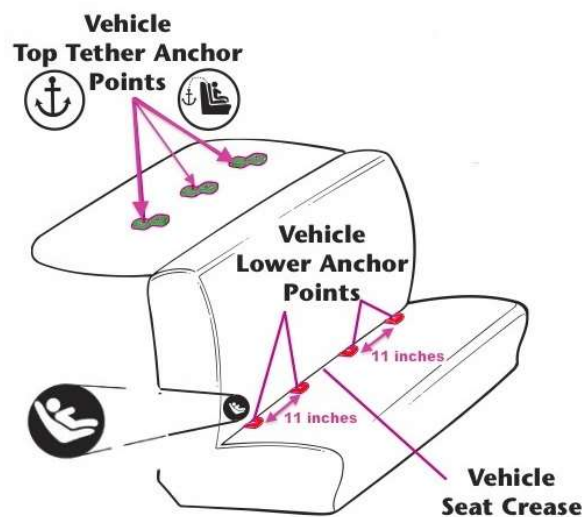
Figure 22 – Anchorage system of LATCH and ISOFIX [35]

In addition, in the European standard, there are various installation categories: "universal" and "vehicle-specific". The main difference is that "universal" represents the use of a top tether strap with the ISOFIX anchorage, whereas "vehicle-specific" characterizes the usage of ISOFIX anchorage without the top tether in specified vehicles only. Figure 23 shows the anchorages of both ISOFIX (a) and LATCH (b).

<div align="center">(a)   (b)</div>
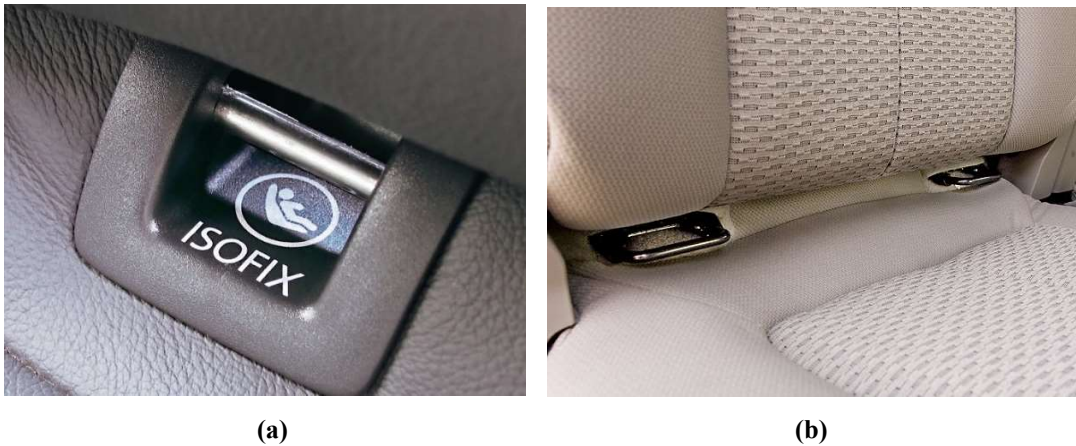
Figure 23 – ISOFIX (a) and LATCH (b) anchorages [28]

2.6 Injury mechanisms for child occupants in motor vehicle accidents

The way a child gets injured in a crash obviously depends, first, on the type of crash. For instance, if it is characterized by a frontal or a side impact. From the analysis of the FARS reassumed in the previous chapter, it can be noticed that most injuries in 2017 are reported after side crashes.

Additionally, in this type of impact, vehicle intrusion appeared to be a contributing factor to injury [28], either direct intrusion of the lateral door structure or indirect intrusion of other vehicle interior parts into the occupant space of the child. Therefore, most side impacts involve children seated near the crash region, which appears to be the more hazardous: information from FARS, for the period 1999-2008, shows that 61% of side impact fatalities involved children seated near the side of impact, while only 20% involved children seated opposite to the crash side [26]. The most common body region reporting injuries after these impacts are the head, face and lower extremities [27]. The variety of crash cases that can lead to different types of injury indicates the need to study the anatomy of a child and relating a proper injury model.

2.6.1 Child anatomy and related injury model

Children differ from adults not only in size but also in the proportion of their body segments proportions and anatomy; these, in fact, change during the child's growth [28]. Observing Figure 24, it can be noticed that, mostly during the first 6 years of life, the head of a child occupies a higher volume in proportion to the rest of the body. This different anatomy is a

cause of the fragility of the neck of children, which must support a disproportionate head, also being not as robust as an adult one.

One of the major causes of pediatric cervical spine injury (PCSI) is vehicle crashes [29]. This is a consequence of the rushing of the head with no direct impact during automotive crashes [30], worse by its disproportionate size, which increases the relative moment of inertia per unit of acceleration, and it is also due to the underdeveloped cervical spine of children [31]. Additionally, the spine's bony links are less well developed, which allow additional movement that can place stresses on the spine ligaments and, thus, lead to spinal damages [28].
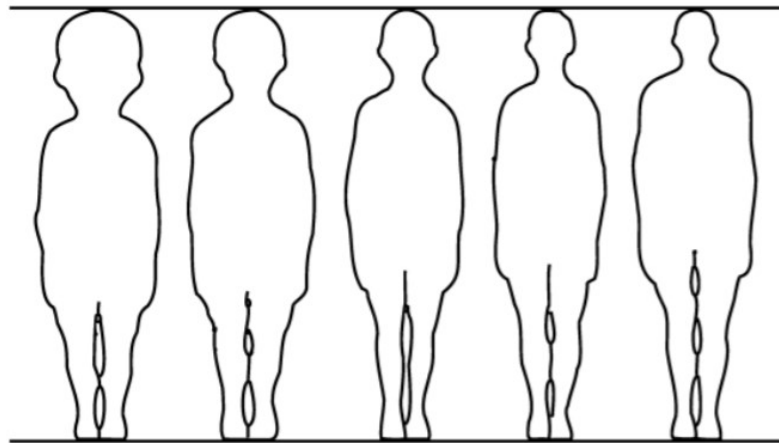
Figure 24 – Proportion of the human body at different ages. From left to right: new-born infant, 2 years old child, 6 years old child, 12 years old child and 25 years old adult [28]

There is also a fundamental difference between a child and adult hip bone, since the anterior superior iliac spine, which is important for the use of a lap belt, is absent up to the age of 10. This is the reason why the belts used in child seats are completely different from the adult and standard ones: the need for different restraint points.

The difference in body segment proportions is also reflected by a higher center of gravity in the child, which may affect the body kinematics in the event of an accident. Moreover, the injury pattern in children is quite different from the one in adults since, in the former, most injuries are reported to the head and those in other parts of the body are relatively rare, whereas in adults the pattern is substantially reversed [28].

2.6.2 Child restraint use and associated injury risk

Child safety seats offer the best protection for children in the event of a vehicle crash and when they are used correctly in the second row, their effectiveness in preventing fatalities is at least equal to 60% [26].

They are designed to limit and control the body's rate of deceleration during a crash, thus reducing the forces acting on the body surface to minimize the differential motion between the skeleton and the internal organs [31]. For this reason, since 1971, every child safety seat and all the other types of child restraint system must meet the minimum performance standards detailed in the standard FMVSS 213 [32].

Researchers investigating child safety seat performance and related injury patterns highlight the two most important issues that nowadays require special attention: constant misuse of a CRS and the number of injuries due to a side impact, or a frontal impact collision [33].

2.6.2.1 Mechanisms of restraint associated injury

The main injury mechanism is related to head injuries typically caused by contact with the vehicle interior [34]. These head contacts generally occur when there is excessive head displacement because of poor upper body restraint, due to misuse of a safety system, or when there is vehicle intrusion [25].

Head injuries due to intrusion occur to inappropriately restrained children in frontal, side and rollover crashes. Additionally, head injuries include both contact-induced injuries as well as inertia injuries. Injuries such as skull fracture, epidural hematoma, and frontal lobe contusion are contact injuries [32] that are most likely due to excursion of the head and subsequent impact with the vehicle interior.

Usually, children in FFCRS sustained inertial injuries (thus, non-contact injuries) to the head such as subdural hematomas [32]. Also, lower leg fractures in children in FFCRS were described by Uphold, Harvey et al. [35], who identified two case reports of children in FFCRS with bilateral fractures to the proximal tibia. On the other hand, cervical spine injuries are very rare in children involved in motor vehicle crashes [36]; neck injuries, although rare, are of concern due to the high likelihood of functional impairment of fatality [37].

Alternatively, an RFCRS can be used with children up to 6 years old, but it can be 5 times safer than FFCRS [38] since, for a frontal impact using a forward-facing child seat, a child's neck is subjected to a higher force than the one which displays on the same child but seated on a RFCRS, which provides cushioning for the head and neck, giving to the child's back a greater surface area where force is distributed [39].

However, both FFCRS and RFCRS must be correctly installed to partially or totally avoid injuries due to misuse: in fact, different crash cases reported child injuries only due to the incorrect setting of the CRS [41], especially in low-speed crashes, where an efficient restraint system can make a real difference. Among all vehicle crashes involving children in the USA in 2017, only 33% of them were correctly restrained, whereas 32% of them were restrained in a CRS without the LATCH top tether strap correctly buckled and 35% of them were completely unrestrained [42].

Weber et al. [41] found several consequences of misuse of child restraint systems: the use of a top tether keeps the child's head from traveling beyond a safe limit in a frontal crash, thus its neglect can lead to a substantial increase of the risk of head contact-injuries, as shown in Figure 25, where the excursion of the rearmost child dummy is evidently higher.

Figure 25 – Head excursion of children with tethered (front) and untethered (rear) top strap of the LATCH [41]

In addition, Weber et al. [41] concluded that, in the absence of lower anchorages, the whole child seat moves forward with higher acceleration, leading to the increase of the value of the head injury criterion. Spinal injuries, instead, which mostly occur in the cervical and thoracic spine, are associated with poor fit of the seat belt, poor pre-crash posture or misuse

[34]. To avoid this type of injury, the use of a system such as a high back booster that adequately corrects poor belt fit and assists in maintaining an acceptable pre-crash posture is recommended.

Furthermore, the careless use of restraint systems, such as the premature use of adult seat belts for children, generally leads to a greater head excursion, putting both the head and spinal regions at greater risk of injury [41].

In fact, interaction of vulnerable child body parts, such as the abdomen and neck, with the adult belt and the standard vehicle seat, displayed in Figure 26a, gives rise to abdominal and cervical spine injuries [43], hence must be absolutely avoided. Instead, a child restraint system must be correctly installed and used. This notion is schematized in Figure 26b, which evidences that the use of a booster seat shifts the child relative to the belt so that it is no more installed against the neck.

(a)   (b)
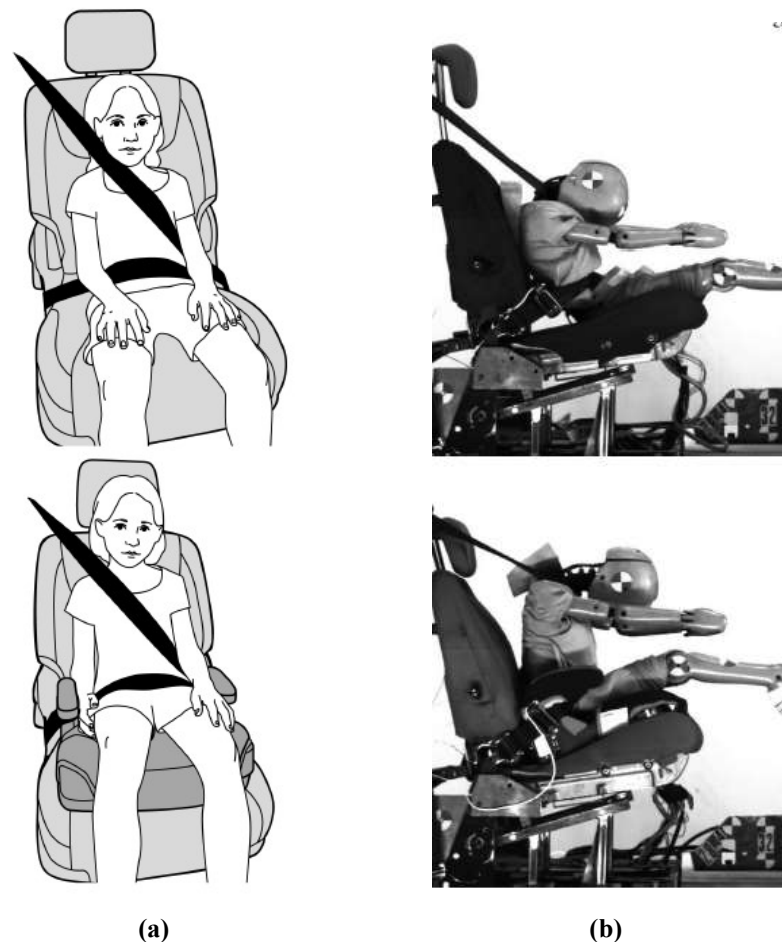
Figure 26 – (a) Front impact crash simulation with (bottom) and without (top) a booster. The higher abdomen load on the top figure can be noticed. (b) An 8-year-old child seated on the vehicle seat (top) and on an additional booster seat (bottom) [41]

On the other hand, the use of a booster seat could lead to the slipping of the upper belt webbing over the child's shoulder, due to the excessive lifting of the child's torso. Consequently, the chest of the child would be completely unrestrained during a crash. This is the reason why the interaction between a booster seat and the standard three-point seat belt in restraining children is always analyzed in greater detail, through both experimental and numerical analyses.

2.6.2.2   Side impact crashes and related injury pattern

The front structures of vehicles are designed to crush during frontal crashes, thereby absorbing a portion of the crash energy and allowing the passenger compartment to stop over a greater distance and longer time. In other crash directions, the occupant motion is primarily toward the point of vehicle impact. Although side impacts usually have a lower change in velocity than frontal impacts, there is much less vehicle structure available to absorb energy between the occupant and the striking object [44].

To analyze the injuries due to a side impact event, it is better to describe, in detail, a crash of this type:

1. The nearside door is impacted by the bullet vehicle and will start intruding laterally into the passenger compartment;

2. Once the bullet vehicle engages with the door sill, the whole vehicle will experience a lateral movement as a result of being pushed by the bullet vehicle itself. During this phase, the occupant tends to move towards the intruding structure;

3. If the speed of the bullet vehicle is sufficiently high at the instant of impact and mostly if the occupant is seated near the struck side, there will be an imminent contact between the occupant and the intruding structure; this is the reason why the severity of the injury is correlated to the relative velocity between the occupant and the vehicle structure [46];

4. The intruding door usually interacts with the pelvis and thorax forcing the head to rotate towards the struck side of the vehicle;

Another parameter to define and classify is the bullet vehicle intrusion: according to Arbogast et al. [47], to compare crush over a variety of vehicle sizes, the width of the vehicle can be divided into 8 zones, as shown in Figure 27. The first seven are equidistant and across the impact half of the interior compartment, whereas the eighth zone represents the other half of the vehicle.
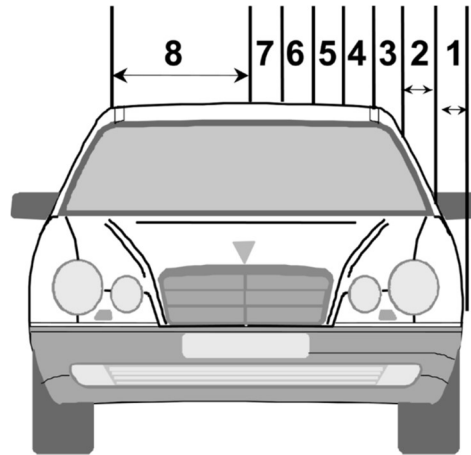
Figure 27 – Defined crush zones in side impact crashes [47]

Then, different kinds of intrusion can be defined, depending on the occupied zones:

- zones 0-2: no or minor intrusion;

- zones 3-4: moderate intrusion;

- zones 5-8: severe intrusion.

Additionally, Arbogast analyzed 32 side impact crashes, with children from 12 to 47 months old and extrapolated different results, including the body region distribution of AIS 2+injuries[1] (Figure 28) and the distribution of crush zone among all the considered cases (Figure 29).
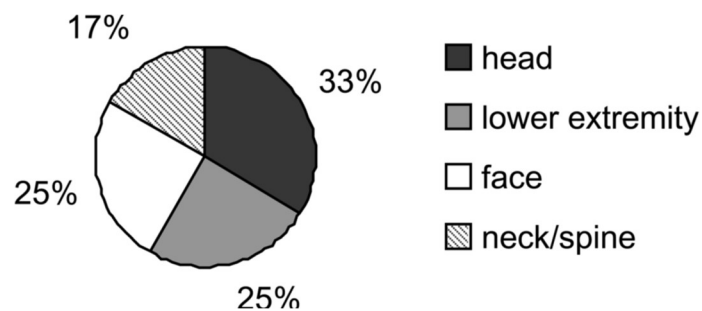
Figure 28 – Body region distribution of AIS 2+ injuries in children 12 to 47 months old restrained in CRS in side impact cases [47]

---

[1] Abbreviated Injury Scale, an anatomical-based coding system created by the Association of the Advancement of Automotive Medicine to classify and describe the severity of injuries. AIS 2+ indicates that the injured person unconscious for at least 2 hours after the impact.
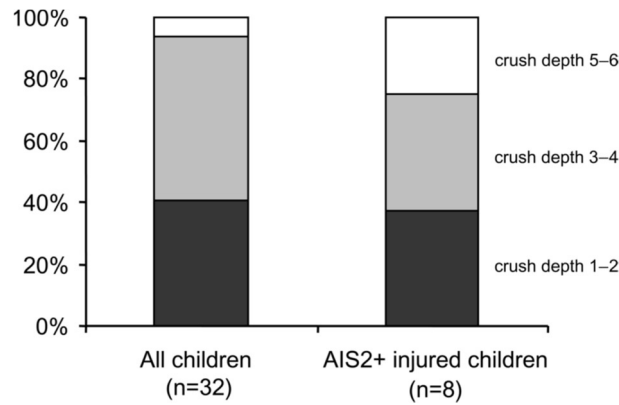
Figure 29 – Distribution of crush zone in the overall and injured study sample [47]

Observing Figure 28, it can be noticed that the superior extremity of the child is the most subjected to risk during a side crash; instead, Figure 29 demonstrates that injuries occurred to children equally for almost all crush zones, except for zones 7 and 8, which may indicate a very severe crash and hence a higher injury severity.

Sometimes, children seated on CRS with side wings appear to were protected from both thoracic and pelvic injuries in a side impact, compared to children in restraints with no side structures. This study also highlighted the influence of the side in which the child is seated; as shown in Figure 30, the majority of AIS 2+ injuries were found on children seated near the impact side (about 28% on the struck side and approximately 62% on the center of the rear row).
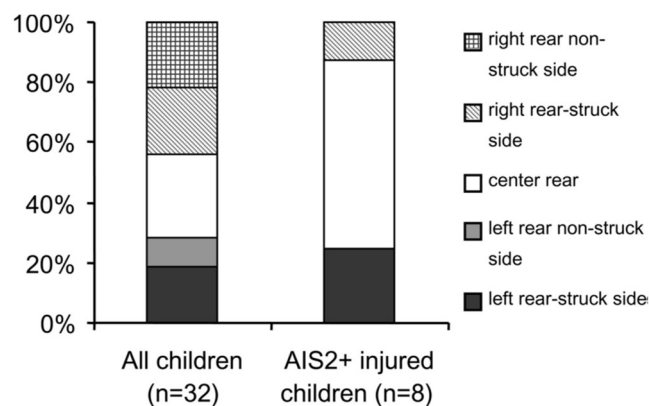
Figure 30 – Distribution of seat position in the overall and injured study sample [47]

As a matter of fact, it has been demonstrated many times that children are at higher risk of sustaining face, head, and lower extremities injuries when seated on the same side of the impact [48, 49, 50]: Starnes and Eigen [50] found out that in children aged 0 to 8 years, 61% of

side-impact deaths involved those seated on the struck side whereas only 20% involved far-seated children.

2.6.2.3   Side airbags and related child injury risk

Side airbags, usually called curtain airbags for their shape, were introduced in 1996 to reduce the impact of lateral crashes on vehicle occupants, and these airbags are designed to protect occupants who are heavier than the fifth-percentile woman (48 kg) [51].

In fact, still nowadays, no child younger than 13 or less than 40 kg should sit in the front seat or in the back seats if they are equipped with passenger-side airbags, according to both the Department of Transportation (DOT) and the National Transportation Safety Board (NTSB) [52]. Thereafter, the safest place for children is in the center of the back seat row, using the appropriate CRS, based on their weight and height [53].

Since airbags inflate in less than $1/20^{th}$ of a second and at high speeds (up to 200 mph), the force generated is enough to kill or cause severe injuries to a child [54], especially if his/her head, neck or chest is near the airbag at the time of deployment [55]. In fact, The American Academy of Pediatrics 2010 guidelines indicate that "side airbags improve safety for adults in side-impact crashes" [56] and also warns parents to never put a rear-facing child seat in a front seat with an airbag; due to the lightweight of an infant, serious injuries may be caused by the deployment of a frontal passenger-side airbag. This is the reason why car manufacturers now install cut-off switches that let drivers turn off an airbag when a child is riding up front [51].

2.7 Vehicle Safety Standards

Among the different countries of the world, there are specific unions and councils which regulate and standardize vehicle safety. All these associations seek to identify and promote effective measures and best practices for a reduction in transport crashes and casualties. Additionally, some of them provide factual and statistical information in the form of scientific reports, mostly yearly published. Obviously, these companies regard child safety with many standards for the construction and validation of child seats; for example, the United Nations – Economic Commission for Europe (UN-ECE) Regulation 44/04 [57] or the FMVSS standard 213 [12]. The most important standards and councils that will be described more deeply in the next sections are:

1. The European Transport Safety Council (ESTC);
2. The Federal Motor Vehicle Safety Standard (FMVSS);
3. The Canadian Motor Vehicle Safety Standard (CMVSS).

2.7.1 The European Transport Safety Council

The ETSC is a Brussels-based independent non-profit making organization dedicated to reducing the number of deaths and injuries in transport in Europe. It was founded in 1993 and it provides an impartial source of expert advice on transport safety matters to the European Commission, the European Parliament, and the Member States [58].

2.7.1.1 The ETSC child safety standards and recent updates

The directive 2003/20/EC of the European Parliament and the Council [59] has mandated the use of child restraint systems in vehicles since May 5th, 2006. Children less than 135 cm (53 in) tall in vehicles must be restrained by an approved child restraint system suitable for the child's size. For a child restraint to be sold or used within any of the 56 UN-ECE member states, it must be approved by the standards of UN-ECE (or ECE) Regulation 44/04. In order to be granted UN-ECE R44 approval, a child restraint must comply with several design, construction, and conformity standards [60]. If the approval is granted, the seat can display an orange label with the approval license number, the type of approval and the details of the manufacturer.

Every year, the ETSC organizes communication briefings to recommend many technology priorities to vehicle manufacturers, hence new safety devices that constructors should install on their new car model, or suggests upgrades to crash test procedures, which may need to be modified depending on drivers and occupants' safety and needs [61]; Figure 31 shows an illustration of statistics about children road deaths and related endorsements to improve their safety.

The most recent briefing [62] introduced the recommendation of fitting all new commercial vehicles with Seat Belt Reminders, Advanced Emergency Braking Systems and Lane Keep Assistance by 2020. Moreover, the council suggested many implementations for Euro NCAP crash tests such as the addition of new testing procedures (for instance, the front small overlap test or the side pole impact test) or the modifications of some instruments, such as the crash barriers.

Figure 31 – Scheme with statistics and recommendations about child road safety [63]

2.7.1.2 United Nations Economic Commission for Europe 44/04 standard: Child restraint system [57]

Such standard applies to child restraint systems which are suitable for installation in power-driven vehicles having three or more wheels, and which are not intended for use with folding (tip-up) or with side-facing seats.

In the first chapter, it defines the child restraint system as "an arrangement of components which may comprise the combination of straps or flexible components with a securing buckle, adjusting devices, attachments and in some cases a supplementary device as a carry-cot, infant carrier, a supplementary chair and/or an impact shield, capable of being anchored to a power-driven vehicle. It is designed so as to diminish the risk of injury to the wearer, in the event of a collision or of abrupt deceleration of the vehicle, by limiting the mobility of the wearer's body" and it also describes other restraint systems such as booster cushion, belt, and infant carrier.

Therefore, it defines five different "mass groups" for child restraints:

1. Group 0 for children of a mass lower than 10 kg;
2. Group 0+ for children of a mass lower than 13 kg;
3. Group I for children of mass from 13 kg to 18 kg;
4. Group II for children of mass from 15 kg to 25 kg;
5. Group III for children of mass from 22 kg to 36 kg.

2.7.1.3   UN-ECE 44/04 standard: Dynamic tests

In chapter 8, the standard defines all requirements about static (corrosion and overturning) and dynamic tests of the child restraint systems.

In the test on trolley and vehicle bodyshell (which is the one that will be studied in this thesis project), a CRS and a related child manikin are placed in a vehicle body for performing a frontal or rear impact crash test, where the vehicle seat and child restraint shall be fitted and shall be placed in a position chosen by the Technical Service[2] conducting approval tests to give the most adverse conditions in respect of strength, compatible with installing the manikin in the vehicle. Furthermore, the position of the vehicle seat-back and child restraint shall be stated in the report. The vehicle seat-back, if adjustable for inclination, shall be locked as specified by the manufacturer or, in the absence of any specification, at an actual seat-back angle as near as possible to 25°.

Unless the instructions for fitting and use require otherwise, the front seat shall be placed in the most forward normally used position for child restraints in the front passenger seat, and in the rearmost normally used position for child restraints in rear seats. In addition, different measurements are made between dummy and vehicle body, as references for the final assessment.

For frontal impact, the trolley shall be so propelled that, during the test, its total velocity change ΔV is $52 + 0 \div 2$ km/h and its acceleration curve is within the hatched area of Figure 32 below and stay above the segment defined by the coordinates (5 g, 10 ms) and (9 g, 20 ms). The start of the impact (t_0) is defined, according to ISO 17 373 for a level of acceleration of 0.5 g.
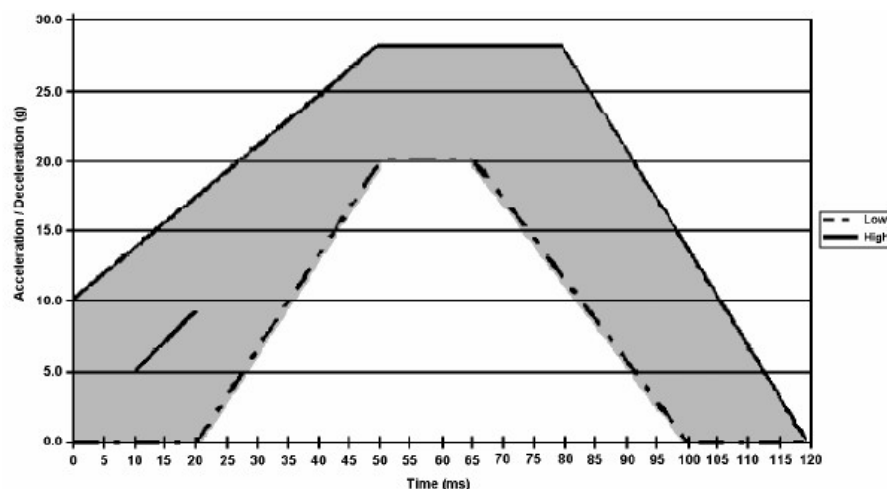
Figure 32 – Low corridor and high corridor curves for the frontal impact test of the child restraint system [57]

---

[2] The technical group which set the vehicle, the CRS and the manikin for executing the test.

2.7.1.4   UN-ECE 44/04 standard: Test manikins

The 8th chapter of the standard also defines different parameters of the manikins used in the tests such as installation, dimensions and construction materials. The series of dummies used in such a test can be either the P-series or the Q-series, due to the influence of R129 [61].

The most important phases of this type of test are the dummy positioning, defined by precise rules and parameters, and the adjustment of friction in the various joints of the manikins, as well as the tension in the lumbar spine and the stiffness of the abdominal insert, in order to achieve realistic and physically congruent results. Before starting the test, the manikin is also equipped with accelerometers for monitoring chest and head motions.

2.7.2 The Federal Motor Vehicle Safety Standard

The FMVSS are U.S. federal regulations specifying design, construction, performance and durability requirements for motor vehicle safety and related components, systems, and design features.

Such standards are issued by the National Highway Traffic Safety Administration (NHTSA), an agency part of the U.S. Department of Transportation founded in 1970, after the passage of the Highway Safety Act of the same year. FMVSS are established and modified through a process of a petition, public notation, public comment, and final ruling. Interested parties can petition NHTSA to act with respect to the FMVSS. Additionally, anyone can submit comments regarding an NHTSA proposal and this one then considers them before issuing a final rule on a proposed change or addition to the FMVSS. If the proposal is preliminary and lacks enough detail to lead directly to a final rule, the notice is typically referred to as an Advanced Notice of Proposed Rule Making (ANPRM). On the other hand, if the notice proposes specific changes or addition to the FMVSS that will likely lead to a final rule, the proposal is typically referred to as Notice of Proposed Rule Making (NPRM). Once NHTSA has made a final decision, the Final Rule can be published [64].

2.7.2.1   Federal Motor Vehicle Safety Standard 213: Child Restraint Systems

This standard specifies requirements for child restraint systems used in motor vehicles and aircraft for the purpose of reducing the number of children killed or injured in motor vehicle crashes and in aircraft. Over the last decades, FMVSS 213 has been modified many times; the most recent Final Rule is dated February 25th, 2014, in which most aspects of a petition for reconsideration of the final rule of February 27th, 2012 were denied [65].

2.7.2.2 FMVSS 213: Final rule [65, 66]

The final rule of February the 27th, 2012 incorporates many additions to the previous final rule:

- It extends the applicability of FMVSS 213 to child restraint systems recommended for use by children weighing 80 lb or less, from the previous criterion of 65 lb or less (Table 2 shows the final rule weight and height categories);

- It adopts the following injury criteria for the Hybrid III-10C[3] in the sled test: chest acceleration = 60 g, head excursion = 813 mm for untethered condition and 720 mm for tethered condition, knee excursion = 915 mm;

- It adopts a procedure for positioning the Hybrid III-6C and Hybrid III-10C dummies in belt-positioning seats based on the procedure developed by UMTRI (University of Michigan Transportation Research Institute) but without the use of the pelvis positioning pad for the Hybrid III-6C dummy;

- It requires a label to be placed on a CRS equipped with an internal harness for which the combined weight of the CRS and the maximum recommended child weight for use with the internal harness exceeds 65 lb. The label informs the consumer that the lower anchors may be used to attach the CRS to the vehicle seat up to a combined child and CRS weight of 65 lb when the child is restrained by the internal harness.

MASS	HEIGHT	DUMM(IES)
≤ 5 kg (11 lb)	≤ 650 mm (26 in.)	Newborn Part 572(K)
> 5 kg 11 lb) and ≤ 10 kg (22 lb)	> 650 mm (26 in.) and ≤ 850 mm (34 in.)	Newborn Part 572(K) and 12-Month-Old Part 572(R)
> 10 kg(22 lb.) and ≤ 18 kg (40 lb)	> 850 mm (34 in.) and ≤ 1100 mm (43 in.)	12-Month-Old Part 572(R)* and 3-Year-Old Part 572(P)
> 18 kg (40 lb) and ≤ 22.7 kg (50 lb)	> 1100 mm (43 in.) and ≤ 1250 mm (49 in.)	6-Year-Old Part 572(I) (Hybrid II) or 6-Year-Old Part 572(N) (Hybrid III)**
> 22.7 kg (50 lb) and ≤ 30 kg (65 lb)	> 1100 mm (43 in.) and ≤ 1250 mm (49 in.)	6-Year-Old Part 572(I)(Hybrid II) or 6-Year-Old Part 572(N)(Hybrid III)**, and 6-Year-Old Part 572(S)(weighted Hybrid III)
> 30 kg (65 lb)	> 1250 mm (49 in.)	10-Year-Old Part 572(T) (Hybrid III)***

*The 12-month-old dummy is not tested in a booster seat.
**Child restraint manufacturer's option to use 6-year-old HII until further notice per 76 FR 55825.
***No HIC measured with 10-year-old HIII.

Table 2 – Final rule weight and height categories [65]

---

[3] The Hybrid III is a particular dummy series which will be described more deeply in Section 2.9.1.1. So far, it is important to know that Hybrid III-6C and 10C represent 6-year-old and 10-year-old child respectively.

2.7.2.3 FMVSS 213: Frontal impact test [67]

The test device used to evaluate the dynamic performance of the add-on child restraint is the standard seat assembly securely attached to a dynamic test platform, also called HYGE sled. The orientation should simulate a vehicle frontal impact and the standard seat has three seating positions. The standard seat assembly is covered by a seat cushion. The seat cushion is constructed of elastic-backed automotive vinyl on the upper surface, which is in contact with the child restraint, backed by a thin layer of nylon-impregnated vinyl.

The specific vehicle shell, if selected for testing, is mounted on a dynamic test platform so that the longitudinal centerline of the shell is parallel to the direction of the test platform travel and so that movement between the base of the shell and the platform is prevented. Adjustable seat backs shall be placed in the manufacturer's nominal design riding position. If such a position is not specified, the seatback is positioned so that the longitudinal centreline of the child test dummy's neck is vertical, and if an instrumented test dummy is used, the accelerometer surfaces in the dummy's head and thorax, as positioned in the vehicle, are horizontal. If the vehicle seat is equipped with adjustable head restraints, each is adjusted to its highest adjustment position.

Different accelerometers are required to perform the test: one for monitoring the impact sled acceleration and deceleration and two triaxial accelerometers packages to be mounted in the head and in the thorax of the dummy.

For such a test, there are two different configurations:

1. Configuration I tests, which shall be conducted at a velocity change of 48 ± 3.2 km/h (30 ± 2 mph);
2. Configuration II tests, which shall be conducted at a velocity change of 32 ± 3.2 km/h (20 ± 2 mph).

The impact sled acceleration function envelopes are shown in Figure 33. As for the UN-ECE regulation, the acceleration value of the sled shall be within the corridor defined through each instant of the test.
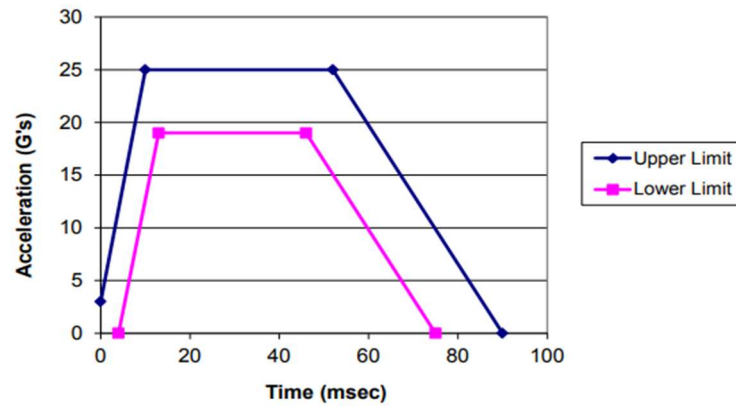
(a)
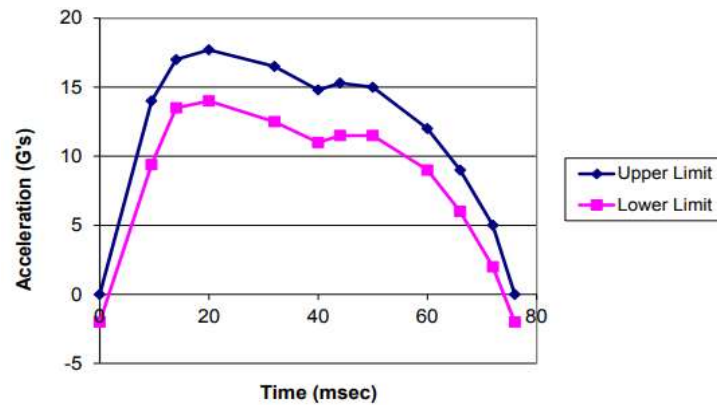
(b)

Figure 33 – Configuration I acceleration function curve [67]

Furthermore, the standard regulates dummy preparation, positioning and installation as well as the adjustment of CRS belts and post-impact evaluations.

2.7.2.4 Federal Motor Vehicle Safety Standard 208: Occupant Crash Protection

This standard specifies performance requirements for the protection of vehicle occupants in crashes. The purpose of this standard is to reduce the number of deaths of vehicle occupants, and the severity of injuries, by specifying vehicle crashworthiness requirements in terms of forces and accelerations measured on anthropomorphic dummies in test crashes, and by specifying equipment requirements for active and passive restraint systems.

In the frontal barrier impact test, the speed of the vehicle is dependent on the speed requested by the Contracting Officer's Technical Representative (COTR) and must be controlled to achieve and maintain the vehicle speed within ± 0.8 km/h [68].

2.7.2.5   Federal Motor Vehicle Safety Standard 214: Side Impact Protection

This standard specifies dynamic and static performance requirements to assure the crashworthiness of vehicle side structures. The purpose of the standard is to reduce the risk of serious and fatal injury to occupants of vehicles involved in side impact crashes. It is divided into 214D (dynamic side impact), 214P (rigid pole side impact) and 214S (static test).

2.7.3 The Canadian Motor Vehicle Safety Standard

The regulations for materials, performance, and duration of CRS in Canada are regulated by Transport Canada, which also tests CRSs on a random basis and may also test specific CRS in response to a concern raised by the public or by manufacturers.
Besides, Transport Canada sets the Canadian Motor Vehicle Safety Standards (CMVSS), which in some cases overlap in content and structure with the FMVSS. The CMVSS are the regulations followed by all manufacturers who offer their products for sale on the Canadian market.

The CMVSS regarding safety of both child and adult occupants is number 208. It is very similar in structure and content to FMVSS 208 (Occupant Crash Protection). One of the biggest differences is represented by the presence of a full vehicle frontal crash test to assess both adult and child occupant safety [69].

2.8 Assessment crash testing

2.8.1 Historical background

Crash testing a car is a procedure that has existed for more than 80 years, when, in 1934, General Motors performed the first frontal barrier crash test. In 1949, instead, the first-ever crash test dummy, Sierra Sam, was created by the Sierra Engineering Co. under a contract with United States Air Force and was used to evaluate aircraft ejection seats on rocket sled tests.

In 1958, the United Nations established the World Forum for Harmonization of Vehicle Regulations, an international standards body dedicated to advancing auto safety and, after 21 years, in 1979, the U.S. NHTSA introduced the New Car Assessment Program (NCAP). The program was established in response to Title II of the Motor Vehicle Information and Cost Savings Act of 1972, to encourage manufacturers to build safer vehicles and consumers to buy them [70]. The agency established a frontal impact test protocol based on the FMVSS 208, except for the frontal impact NCAP test, which is conducted at 56 km/h (35 mph), rather than

48 km/h (30 mph), the crash speed requested by the FMVSS 208 before being modified in 2006 [71].

The European program, the Euro NCAP, was founded in 1997 by Transport Research Laboratory for the UK Department for Transport and backed by several European governments, as well as by the European Union. Nowadays, it is based in Brussels, Belgium and it is an effective benchmark for other countries' programs such as the ANCAP (in Australia and New Zealand) [72].

In 1997, Euro NCAP introduced an additional rating, specifically addressed to the protection of children in the event of a crash. The rating was based on the protection offered in the front and side crash tests to a three-year-old and 18-month-old child seated on the rear seat in restraint of the type recommended by the car manufacturer. The assessment was complemented with firm incentives with regards to communication (handbook instructions and warning labels), availability of ISOFIX attachments and other relevant equipment such as front passenger airbag deactivation switch [73]. The child occupant protection star rating has motivated all car manufacturers to aim good child protection and will be analyzed more deeply in the next pages.

2.8.2 European NCAP ratings

Euro NCAP introduced the overall safety rating in 2009, based on assessment in four important areas:

1. Adult Occupant Protection (for the driver and passenger), which score is determined from two frontal impact tests (Offset Deformable Barrier and Full Width Rigid Barrier), two side impact tests (Side Mobile Barrier and Side Pole), one whiplash test and one Autonomous Emergency Braking (AEB) test;

2. Child Occupant Protection, which scores the protection offered by the child restraint systems in frontal and side impact tests (CRS Performance test), the vehicle's ability to accommodate child restraints of various sizes and designs (CRS Installation Check) and the availability of provisions for safe transport of children in the car (Vehicle Provisions test);

3. Vulnerable Road User (VRU) Protection, in which Euro NCAP tests how well cars protect pedestrians and cyclist, with whom they might collide, performing 5 different tests: three regarding the impact of the front end of the vehicle with head, upper and lower leg of a pedestrian and two concerning the effectiveness of AEB with a pedestrian and a cyclist respectively, introduced in January 2018.

4. Safety Assist, which score is determined from tests to the most important driver-assist technologies that support safe driving to avoid accidents and mitigate injuries. In these 5 tests, Euro NCAP analyses functionality and performance during normal driving and in typical accident scenarios of Electronic Stability Control (ESC), Seat belt Reminders, Speed Assistance, Interurban AEB, and Lane Support.

Additionally, Euro NCAP has created the five-star safety rating system to help consumers, their families and business compare vehicles more easily and to help them identify the safest choice for their needs. The number of stars reflects how well the car performs in Euro NCAP tests, but it is also influenced by the safety equipment the vehicle manufacturer is offering to the market. A car may not be equipped with an AEB system since its presence is not yet mandatory for being commercialized, and obtain zero stars in both AEB tests, but may also obtain the maximum rating in all crash tests of areas 1 and 2 [74].

From the description of the four areas above, it can be noticed that child safety really influences the Euro NCAP rating since it represents a whole test zone, with three different subfields concerning the characteristics of the child restraint system and of the vehicle itself. CRS Performance and Vehicle Provisions tests, introduced in 1997, are older than the CRS Installation Check, which was presented in 2013. This one is aimed to verify the installation procedure of a CRS in the tested vehicle since misuse of a restraint system can be attributed not only to a user error but also to a mismatch between the vehicle and the CRS itself. Therefore, a selection of popular child restraints is installed to assess trouble-free installation: seat belt length, belt buckle location, ISOFIX anchorage accessibility, and CRS stability are the typical vehicle characteristics to be verified. Euro NCAP also encourages rearward facing CRS of toddlers and checks if vehicles are equipped to accommodate such seats.

2.8.3 ODB Frontal Impact and Child Occupant Protection tests

The Offset Deformable Barrier Frontal Impact and Child Occupant Protection Euro NCAP tests are performed simultaneously: the vehicle is examined performing a frontal crash test using four certified or re-certified[4] dummies in total, two Hybrid III adult dummies placed on the driver and on the front passenger seat, a Q6 dummy installed on the 2nd row outboard passenger seat behind the driver and a Q10 dummy fitted on the opposite 2nd row outboard passenger seat, behind the front passenger. Before performing the crash simulation, the vehicle is prepared to pass through different setting phases. The car curb mass, the total weight

---

[4] The certification of a dummy is a process, described in Annex 10 of UN-ECE 94, through which a dummy is qualified as ready for a crash test. A Hybrid III dummy shall be recertified after every three impact tests, if an IC exceeds its normally accepted limit or if any of its parts is broken. This helps understanding how expensive can be performing a crash test.

considering fuel, occupants and luggage compartment and the axle reference loads are calculated; then, the vehicle width and the overlap of the deformable barrier are computed. The overlap distance is measured by determining the width and the center-line of the vehicle, calculating 10% of the vehicle width and marking a line on the front end, on the steering wheel side of the car. In this way, a 40% ± 20 mm overlap quote to correctly place the barrier is obtained, which is one of the main parameters of such test, together with the impact speed, equal to 64 ± 1 km/h (40 ± 1.6 mph), as shown in Figure 34 [75]. The test replicates a crash between two cars of the same weight, both traveling at speed of 50 km/h, where the deformable barrier represents the oncoming vehicle. Moreover, it is important to highlight that an offset frontal crash represents a more dangerous situation for the occupants than a full overlap frontal impact; this is because the vehicle structural elements located on one side do not absorb energy during the impact, forcing the impacted side of the car to dissipate the kinetic energy through bigger deformations, with a consequent increase in the risk of cockpit intrusions, which could cause more severe injuries, especially for lower limbs. Figure 34 represents the impact into a rigid barrier with total superposition with the obstacle (w, full overlap) and with partial superposition (w_{offset}) for the same vehicle, with their consequent deformations.
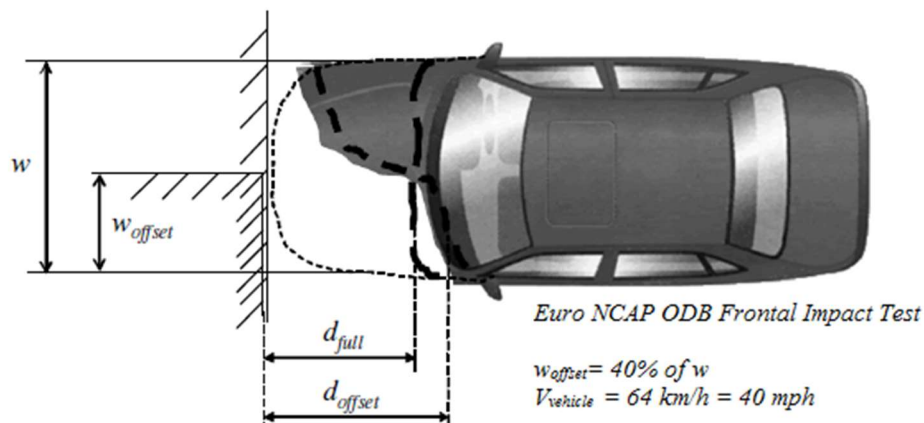
Figure 34 – Impact scheme with total superposition (full overlap) and with partial superposition (offset) [9]

Afterward, the dummies shall be set, installing all the transducers needed to measure accelerations, forces and moments (in total, 30 on the Q10 and 13 on the Q6), and positioned for the dynamic test. In this regard, the child dummies are effectively placed only after the performing of the other two static tests of the Child Occupant Protection area, which are the evaluation of the CRS installation and of vehicle provisions for guaranteeing child safety.

In the dynamic test, the Q6 dummy shall be seated in an appropriate FFCRS for a six-year-old child or a child with a stature of 125 cm; instead, the Q10 dummy shall be seated on a booster cushion only. The booster to be used must be without the backrest and it will be

accepted for use in the test provided that when the Q10 dummy is seated on the booster, no part of the head is higher than 800 mm vertically above a defined point called Cr-point; however, if the booster cushion has UN-ECE R44 approval, it will not need to meet this requirement. Lastly, where a vehicle is equipped with an integrated CRS covering the Q6 and/or Q10 on the rear outboard 2nd row positions, this will be used in the dynamic test [76].

After deciding the CRS to use based on the dummies, six important phases prior to the crash impact test shall be performed:

1. CRS placement;
2. Dummies preparation;
3. Passenger compartment adjusting;
4. Q10 installation;
5. Q10 measurements;
6. Q6 installation.

2.8.3.1   CRS Placement [76]

The standardized procedure is reported as follows:

- The CRS shall be prepared for the installation by lengthening the straps and top-tethers so they are accessible once the CRS is in place;
- Then, the CRS shall be placed passing it through the respective occupant entry door, adjusting the position of the front seat if necessary;
- Where the CRS contains multiple parts, such as base and seat, then both items may be installed sequentially and assessed in the same way;
- When 3-point belts are used, the CRS shall be positioned along the centreline of the chosen seating position and the adult seat belt shall be routed around the CRS in accordance with the instructions on the CRS.

2.8.3.2   Dummy preparation [76]

Many parameters are initialized to prepare the child dummies for the crash test:

a) Stabilized temperature, measured in the chest cavity, of 18°C to 22°C, for at least 1 hour immediately prior to the test;

b) All constant friction joints shall have their stiffness correctly set. The torque on the shoulder screws shall be set to obtain 1 g holding force of the shoulder and elbow; the same holding force value must be reached for the tensioning screw of the knee joint.

The dummy joints shall be set as close as possible to the time of the test and, in any case, not more than 24 hours before the test;

c) Both dummies shall be instrumented with different transducers to measure accelerations, forces, moments and displacements in different body regions (head, neck, shoulder, chest, and pelvis), needed to the post-crash assessment phase.

2.8.3.3 Q10 installation [76]

Firstly, the dummy is prepared attaching a foam pad of 125 x 90 mm with a thickness of 20 ± 2 mm to the rear of the dummy pelvis, outside the suit, using tape to hold it in place. The pad shall be centered on the midsagittal plane with the upper edge at the same height as the top of the pelvis flesh and it shall remain on the dummy for the test unless it can be removed without the need to move the dummy itself.

Then, the CRS shall be placed on the relevant seating position and the fore/aft position on the CRS shall be marked on the side of both CRS and vehicle. Successively, the CRS shall be aligned with the markings on the vehicle seat cushion described in the last paragraph of the previous section and it must be checked that there is no interaction between the CRS and side door when it is closed. Otherwise, if there is some interaction, the CRS may be moved inboard by up to 50 mm. If an ISOFIX CRS is used no markings are needed; in fact, it is enough to align it with the anchorages and engage it with the vehicle.

Sequentially, the Q10 dummy shall be placed in the vehicle:

a) It is placed on the booster cushion and aligned, together with the CRS, with the centreline marked previously, this passage must be repeated every time the CRS is moved;

b) The seat belt shall be buckled. If the buckle is not accessible because of interaction with the CRS, the CRS and dummy shall be moved outboards by the minimum distance (with a maximum of 50 mm) required to get free access to the buckle;

c) The contact between the rear of the CRS and the seatback shall be ensured by pressing the CRS backward against the seat and making sure that the fore/aft markings are still aligned;

d) When applicable, the hip shields shall be placed on the Q10 dummy, ensuring that the distance between the hip shields is no less than 154 mm. If needed, a large gap should be used to establish the best fit;

e) The contact between the dummy's lower back and the vehicle seat back must be ensured bending the dummy's back into an upright position and then rocking the dummy sideways while at the same time pushing the pelvis backward;

f) The correct alignment of the dummy with respect to the CRS shall be ensured, avoiding any rotation about its vertical axis;

g) The dummy's shoulders must be pushed toward the seatback until either the shoulders contact the seat back or the head is in contact with the head restraint;

h) The top of the rear head restraint shall be positioned within ± 20 mm of the top of the dummy head or in the nearest notch above. If it cannot be raised sufficiently to be within 20 mm, it shall be adjusted to the highest position;

i) The femurs shall be positioned straight forward with a distance of 130 ± 5 mm between the centers of the knees. If the CRS prevents this gap from being achieved, the knees must be positioned as close to the target values as possible;

j) Where possible, the lower legs shall rest naturally, the tibias shall be parallel to the vehicle centreline and the feet shall be separated by the same distance as the knees;

k) Interaction between the Q dummy lower legs and feet and the front seat is acceptable;

l) For the belt routing, the slack of the lap belt shall be removed by pulling on the diagonal belt near the buckle with a force of 150 N and it shall be ensured that the belt is not twisted in the guidance of the booster cushion;

m) The upper arms shall be positioned parallel to the chest;

n) The lower arms shall be positioned parallel to the upper legs resting on the booster cushion or armrest as close as possible to the side of the femur;

o) The elbow shall be kept as close as possible to the torso. Where possible, the tip of fingers should be in the *x*-direction in line with the screws of the knee joint.

2.8.3.4   Q10 measurements [76]

The measurements reported in Figure 35 are to be carried out prior to the test but after the completion of the positioning procedure.

A	Top of head to roof (vertically)
B	Head CoG to door/window (horizontal)
C	Shoulder (pivot point) to door/window (horizontal)
D	Lower rib to door (horizontal)
E	Hip joint (femur mounting hole) to door (horizontal)
F	Hip joint (femur mounting hole) to floor (vertical)
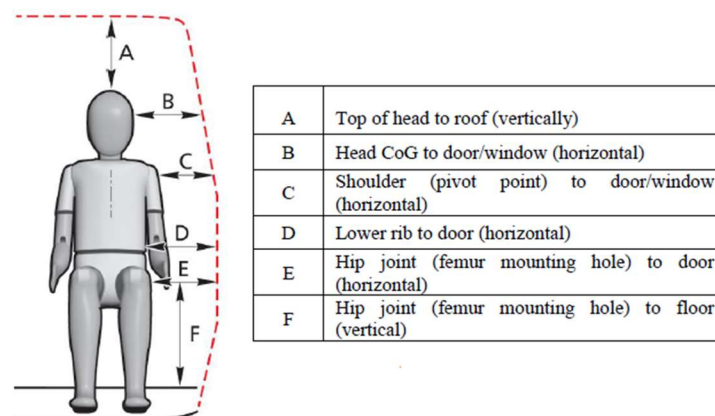
Figure 35 – Q10 dummy measurements [76]

2.8.3.5 Q6 installation [76]

The installation procedure of the Q6 is similar to that reported for the Q10 dummy, except for the absence of the positioning of the foam pad and for the repositioning of the rear head restraints of the rear seats, in order to avoid interference with the Q6 CRS. In some cases, they may be removed if instructed to do so in the vehicle handbook. Once the installation of all dummies is completed, the test can be carried out. After the crash, the assessment of all child dummies for evaluating both the adult occupant protection and child safety performance of the vehicle can be performed, and it will be described in Section 2.8.5.

2.8.4 Side Impact Mobile Deformable Barrier and Child Occupant Protection tests

In the Side Impact MDB test, a deformable barrier is mounted on a trolley and is driven at 50 ± 1 km/h (30 ± 1.6 mph) into the side of the stationary test vehicles at defined angles, in order to evaluate the likely severity of injuries which can be reported after a side crash, characterized by the lower quantity of material that can absorb the impact with respect to the car front end. During this kind of test, a Hybrid III male dummy is put in the driver's seat and Q6 and Q10 dummies are placed in their respective CRS in the rear seats. As a matter of fact, such crash simulation is the second and last one used to evaluate the CRS performance in the Child Occupant Protection test. The ways the vehicle is prepared, and dummies are identical to the way they are prepared before the Frontal Impact ODB test [78]. A representative image of the crash test is reported below, in Figure 36.

When both Side Impact MBD and Frontal Impact ODB tests are completed, the evaluation of the dynamic performance of the CRS can be executed.

Figure 36 – The Euro NCAP Side Impact Mobile Deformable Barrier test [74]

2.8.5 Child Occupant Protection: dynamic performance assessment

The starting point for the dynamic assessment of child occupant protection is the dummy response data recorder in the two different test configurations described in the previous sections. Therefore, individual test scores are computed for both the Q6 and Q10 dummies; a sliding scale scoring system is used to calculate points for each measured criterion where higher and lower performance limits are set. Where a value falls between the two limits, the score is calculated by linear interpolation. Instead, if only a lower performance limit is available for a criterion, this limit is used as a "Pass/Fail" criterion [79].

Different capping limits are applied to both child dummies and exceeding one of them generally indicates an unacceptable high risk of injury. Where a single dummy measurement exceeds a capping limit, the score of that dummy will be 0 points in the impact in which the limit was exceeded. Additionally, if multiple criteria exist for an individual dummy body region, the lowest scoring parameter is used to determine the performance of that region. Furthermore, it is important to know two fundamental directions that influence this evaluation:

1. The injury parameters assessment will not be evaluated during the rebound phase;
2. If the restraint system is unable to keep the child dummy restrained, that dummy will be penalized for its dynamic performance in the impact in which the issue occurred. More precisely:
    a. During the forward movement of the dummy only, if the belt moves below the shoulder joint down the upper arm (slipping of the shoulder), zero points will be awarded to the dummy. This is a crucial argument of analysis for the Q10. Moreover, if the diagonal belt moves into the gap between the clavicle and upper arm with folding of the belt webbing, a penalty of 4 points will be applied to the overall dummy score of the impact in which it occurs;
    b. Situations of dummy ejection, thus where the dummy pelvis does not remain in the booster seat or the CRS does not remain within the same seating position or in no longer correctly restrained by the adult belt, and failures of the restraint system components, such as any breakage or fracturing of a part of the belt system or of a CRS anchorage, will be evaluated by the Technical Team, which will define a penalty scoring.

Table 3 summarizes all available scorings for each dummy, depending on head, upper neck and chest, for the frontal impact simulation test; if there is no hard head contact, the head score is based only on the resultant 3ms acceleration only, thus the resultant acceleration computed as in Equation 2, with $t_f = 3$ ms, otherwise, in presence of high excursion, the head rating can be modified: if the forward excursion of the Q6 head exceeds 550 mm, 4 points will

be subtracted from the final score, instead, if the Q10 head movement exceeds 450 mm or 550 mm, 2 or 4 points will be detracted.

The tension F_z of the upper neck must be included between 1.7 and 2.62 kN, otherwise 2 points will be subtracted from the neck score; in case of head to interior contact, a 2-point penalty can be applied to each dummy if the moment M_y exceeds a limit value. To conclude, the chest scoring is based on the resultant 3 ms acceleration (neglecting the acceleration peaks caused by the firing of seat belt pretensioners early in the loading event) for the Q10 dummy and on the deflection for the Q6 dummy, which computation is shown in Equation 6. The exceeding of either of these values leads to a 2-point penalty.

	Criteria		Performance limits			Available points
			Higher	Lower	Capping	
Head Score	HIC_{15} (with hard contact)		500	700	800	4 points
	Resultant 3ms acceleration		60g	80g	80g	
	Head excursion Q6			550mm	NA	
	Q10		450mm	550mm	NA	
Upper Neck	Tension Fz		1.7kN	2.62kN	(monitoring)	2 points
	Extension My (with head to interior contact) Q6		NA	36Nm	NA	
	Q10		NA	49Nm	NA	
Chest (T4)	Resultant 3ms acceleration* Q6		NA	NA	NA	NA
	Q10		41g	55g	55g	2 points
	Deflection Q6		30mm	42mm	NA	2 points
	Q10		(monitoring)	(monitoring)	NA	NA
Pelvis	ASIS load		NA	NA	NA	
TOTAL						8 points/dummy

*Chest acceleration peaks caused by the firing of seat belt pretensioners early in the loading event will be ignored.

Table 3 – Frontal impact criteria, limits and available points per body region for Q6 and Q10 [79]

$$D_{chest} = \max(D_{chest}(t)) \tag{6}$$

Then, the side impact case is evaluated, with the attribution of 4 points at best for each dummy. Therefore, the double weight of the ODB test, with respect to the side impact one, can

be noticed. To conclude, the contribution of the dynamic performance score to the Child Occupant Protection test area is calculated summing the body points of the relevant regions of Q6 and Q10 in both front and side impact, obtaining 24 points in total at the best.

2.8.6 The HYGE Sled

The HYGE Sled is a test device designed to simulate the effects of a collision, both in acceleration and deceleration. It provides extremely repeatable and reproducible acceleration impulses, thus enabling accurate experimental simulation of crash conditions for the whole passenger compartment, without destroying a vehicle each time.

Systems operational for more than thirty years, with 15,000 tests, declare high levels of repeatability and reproducibility with a scattering of results in the order of 2%. The HYGE Sled is used all over the world by car manufacturers to test devices such as the occupant safety systems, child restraint systems, safety belts, as well as seats, door locking mechanisms, windshields, and fuel tanks. In addition, it is used for performing UN-ECE 44/04 and FMVSS 213 dynamic tests.

The HYGE Sled receives a powerful, reproducible push from the action of two gases at different pressures applied to a piston in a cylinder. Using a runner system, the Sled moves along two rails approximately 30 m long and the entire car, only the body or even just the seat with the belted dummy can be assembled on it [9].

Moreover, the Sled is equipped with a braking system, which can reproduce the longitudinal deceleration conditions which passengers are subjected to in a vehicle involved in a frontal crash; such situations are simulated by moving the system under test in an opposite direction with respect to reality: just before a real impact, the vehicle and its occupant move with constant speed and, at the impact moment, they are stopped very quickly, suffering a deceleration in the opposite direction with respect to the travel one. In the Slide frontal impact test, these conditions are simulated starting from null speed, which represents the traveling vehicle, and accelerating the sled with the elements to be tested assembled in the opposite direction with respect to the HYGE Sled motion. This behavior provides a response comparable to that produced by a quick deceleration by a vehicle initially traveling at constant speed. A schematic of the HYGE Sled test can be observed in Figure 37.

Additionally, when a crash with an offset barrier shall be simulated using the HYGE Sled, the vehicle body must be rotated of a defined angle, in order to reproduce the impact characteristics of a precise offset percentage.
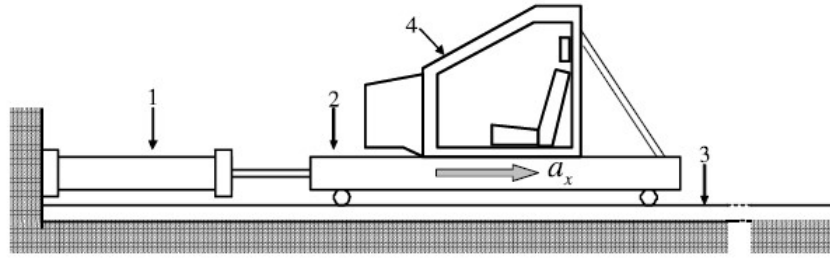
Figure 37 – HYGE Sled scheme. 1) pneumatic hydraulic piston; 2) bogie; 3) rails; 4) element to test [9]

Compared to the destructive tests of a vehicle into a barrier, the HYGE sled tests have several advantages:

- Cost-effectiveness - the test can be repeated many times without extra cost;
- Reproducibility - acceleration profiles are defined very accurately;
- Modularity - the whole car is not required, hence subsystems can be tested at a very early stage.

These are the reasons why such this test is performed by car manufacturers to anticipate the result of a homologation test, such as the ECE check, or of a rating test, such as the Euro NCAP tests.

2.9 Anthropomorphic test devices

Anthropomorphic test devices (ATDs), commonly referred to as dummies, are mechanical surrogates of the human that are used by the automotive industry to evaluate the occupant protection potential of various types of restraint systems in different collision simulations [80]. The first anthropomorphic dummy was realized in 1949 for the US Air Force to evaluate the responses on humans due to accelerations imposed on the spine by ejection seats. Afterward, from the middle of the 1960s, dummies started to develop for applications in the automotive industry and today they play a fundamental role in vehicle safety evaluation being the basis of the homologation and rating testing of vehicles [9].

An ATD is a mechanical system comprising metallic masses, spring, dampers, articulations, and polymeric coverings, aimed to simulate the response of the human body in the considered impact conditions. Inside a dummy, there are sensors (transducers) that enable the measurement of physical quantities, such as accelerations, forces and moments, related to the biological damage that occurs in the real occupant in the same impact conditions. To be a reliable

instrument for measurement during impact tests, it is necessary that a dummy exhibit the following characteristics:

- Biofidelity – the capacity to obtain injury criteria values that would represent correctly the response of the human body to a precise crash situation;
- Repeatability – the same dummy, subject to the same stresses many times, must have equal responses;
- Reproducibility – different dummies of the same type, subject to the same stresses even in different laboratories, must have equal responses;
- Sensitivity – the dummy must be highly sensitive to the variation of the harshness of impact (as the test speed) and to the countermeasures adopted (as the variation of stiffness of the impacted part);
- Long-life – the dummy parts must exhibit physical characteristics which do not vary over time with use;

The definition of correlations between physical quantities detectable on dummies and the corresponding biological damage levels on the human body derives from studies on cadavers (PMHS, Post Mortem Human Subjects), conducted in a limited number of specialized centers in this kind of tests, such as Detroit Wayne State University [9]. The characteristics of dummies depend on the type of impact they are used for and the occupants they represent, such as age, gender, and percentile.

2.9.1 Catalogue of anthropomorphic test devices

A summary of dummies, organized by type of impact and child, is provided in Table 4.

Frontal Impact ATD	Side Impact ATD	Rear Impact ATD	Children ATD
Hybrid III 5th Female	SID-IIs	RID 2	CRABI 6, 12 and 18-Month-Old
Hybrid III 50th Male	BioSID	TRID	Hybrid III 3, 6 and 10-Year-Old
Hybrid III 95th Male	EuroSID-1	BIORID	Hybrid II 6-Year-Old
Hybrid II 50th Male	DOT SID	RID3D	P0.75 9-Month-Old
VIP Test Dummies	ES-2		P1.5 18-Month-Old
TNO-10 Dummy			P3, P6, and P10 (Year-Old)
THOR			Q1.5 18-Month-Old
			Q3, Q6, and Q10 (Year-Old)

Table 4 – Adult and child ATDs [9]

From the table above, it can be noticed that there has been interest in developing reliable models of child dummy over the last years, collecting different series of ATDs (CRABI, Hybrid III, Q, P).

2.9.1.1 The Hybrid III dummy family

The Hybrid III dummy family consists of a small adult (5th percentile) female dummy, a mid-size adult (50th percentile) male dummy, sometimes substituted by a large adult (95th percentile) male dummy, and 3, 6 and 10-year-old child dummies. Figure 38 shows the members of the Hybrid III dummy family.

Figure 38 – The Hybrid III dummy family [9]

Hybrid III was designed to naturally assume the typical posture of a seated man inside a car. The head is made of an aluminum skull onto which a skin is applied having a sufficient thickness to ensure the biomechanical fidelity and response repeatability of the head with respect to impact with hard surfaces; the neck is a flexible component that has stiffness and damping characteristics with good biofidelity both in bending and extension; it is made by three vertebral rigid discs in aluminum with elastomeric elements between them. A single steel cable runs along the neck center to ensure high axial stiffness. Additionally, the transversal section of neck is asymmetric to guarantee high stiffness for the forward head movement (bending), rather than backward (extension), as shown by biomechanical data.

The chest of Hybrid III simulates the spine and rib cage and is covered by a removable protective jacket. The thoracic part is rigid and houses a triaxial accelerometer mounted at the center of gravity. The model of the rib cage allows a maximum deflection of 90 mm and the abdomen, pelvis, and legs were essentially borrowed from the previous version of dummy

(ATD 502) and subject to small alterations in order to obtain a better weight balance of the legs, an improvement of the knee covering and an increase in the reliability of the various components [9].

Due to its excellent biofidelity and measurement capability, General Motors petitioned NHTSA in 1983 to allow the use of Hybrid III mid-size adult male dummy as an alternative test device to the Hybrid II for the FMVSS 208 compliance testing of passive restraints [80], and it was effectively allowed in 1986.

In 1992, the SAE Hybrid III Dummy Family Task Group initiated a program to develop a Hybrid III 3-year-old child dummy [80]. This dummy was designed to have the same level of biofidelity and measurement capabilities as the other Hybrid III type dummies, except for the knee impact requirement and the leg instrumentation, which were omitted from the design requirements since knee impact is an unlikely event for a properly restrained 3-year-old child. Some of the distinguishing characteristics of the Hybrid III 3-year-old child dummy design are biofidelic head, biofidelic segmented neck with a steel cable to limit elongation and biofidelic thorax including ribs made of 1095 steel for increased durability, upper and lower rib guides to limit vertical movement of the ribs and sternum-to-spine bumpers to prevent instrumentation damage caused by metal-to-metal contact in the event of severe chest deflection [9].

This dummy was designed to replace the General Motors 3-year-old "airbag dummy", used for evaluating unrestrained child interactions with deploying passenger airbags and it would also be used to assess the efficiency of child restraints.

2.9.1.2   The Q-series child dummy

In the late 1970s and early 1980s, TNO and other companies developed the P-dummies, a series of child dummies that covers almost the complete child population up to 10 years. The P-series dummies are still test tools for the European regulation ECE 44 and are also adopted by many other standards. In 1993, the International Child Dummy Working Group started with the development of the Q-series of child dummies as successor to the P-series [81].

The Q-series was developed with the aim to be more advanced in terms of biomechanical and anthropometric characteristics and to be used in both front and side impact testing, making it the first "multi-directional" child dummy. This unique behavior has been obtained creating interchangeable instrumentation within the dummy and the entire Q-series. These improvements led the new UN-ECE regulation R129 to require the use of Q dummies instead of P dummies. However, it is yet to be decided if R44 remains in place with modifications or if R129 will replace the R44 after a phase-out period. In case R44 remains in place, the CRS manufacturer can choose whether to follow the R44 or the R129 [61].

Moreover, Euro NCAP has implemented the Q1.5 and Q3 in their January 2013 protocol and began using the Q6 and Q10 in January 2016, replacing the smaller dummies. Q1.5, two Q3, Q6, and Q10 child dummies are shown in Figure 39.

Figure 39 – The Q-series child dummies [80]

Material and construction characteristics of these dummies are very similar to the Hybrid III ones, with the advantage to be used in different kinds of crash simulations.

2.9.1.3   CRABI-series child dummy

The Child Restraint/Air Bag Interaction (CRABI) dummy was designed to be used in rear-facing infant restraint positioned in front of a deploying passenger-side airbag, which can cause, as mentioned in Section 2.6.2.3, severe injuries to children. The head shape is based on scaling down an adult head and such body region is constructed of urethane, with internal steel inserts for attaching it to the neck of the dummy. The latter was originally the same as General Motors 3-year-old airbag dummy neck but was altered to have extra lateral notches to allow for greater amounts of flexion and extension. The spine, instead, consists of a segmented rubber cylinder, spine box, and lumbar load cells. In total, there are three CRABI models that represent 6, 12 and 18-month-old children [9].

2.10 Child safety test simulations using Finite Element Method

A vehicle crash test usually involves hundreds of thousands of dollars, since a car prototype can cost up to 4 times the price of the standard model. In addition, such tests must be repeated to verify the safety performance improvements given by a design modification. This process is mandatory to introduce a new vehicle in the market and forces the company to invest a huge amount of money to develop a different car model.

Therefore, car manufacturers started to use FE codes to simulate a crash test, setting its different parameters at their optimal configuration and then verifying the results performing a real impact simulation. Nowadays, all car manufacturers dispose of a virtual safety area, in which different 3D models are designed and analyzed.

Firstly, Computer-Aided Design (CAD) models are needed, in order to reproduce vehicle, seats and restraint systems in the virtual domain. Afterward, such drawings are discretized (more commonly, meshed), and their material characteristics are added in order to reproduce their real behavior through the software simulation as precisely as possible; the resulting models are then called Finite Element (FE) models. The last part of the pre-processing phase consists of correctly positioning and restraining all FE models and defining all contacts, as well as the integration of external forces which causes the motion and reproduces the real situation to simulate. Afterward, there is the processing phase, where the FE code obtains a numerical solution (further details are described in Appendix 2) and, lastly, all collected results are analyzed in the so-called post-processing stage, in which the outcomes of a real crash test could be predicted.

Usually, each car manufacturer creates its own models of vehicles and safety systems; on the other hand, the FE model of a dummy is often provided by an external company, which is specialized in the reproduction of the biomechanical response of real dummies, such as Hybrid IIIs and Q-series, through virtual ones.

2.10.1 Dummy and Child Restraint System FE models

The advantages of using a FEM simulation to reproduce an impact test can be numerous; for instance, although physical crash test dummies have provided highly valuable data on how human body reacts during impacts and have contributed to improve the design of the structure, a vehicle can be used once for a physical crash test which cannot be repeated exactly in the same way. Moreover, a physical dummy only approximates the response of a human: the sensors installed in a Hybrid III remotely reproduce the number of sensitive elements on a living human, and the simulation of internal organs is still at a rudimentary level [9].

Nowadays, virtual models of dummies used during the experimental test can be created and refined to more accurately reproduce the human physical behavior. In addition to simulating the complete occupant, studies of injuries to single parts can be made with a high level of detail. The consequent advantages are evident: since each variable is under control and each event is repeatable, the cost of physical tests, characterized by dummies, vehicle and sensors replacement, can be significantly reduced.

2.10.1.1 THUMS model

THUMS (Total Human Model for Safety) is an FE model of the mid-size (50th percentile) adult male occupant, developed by Toyota. It consists of all deformable human body parts with anatomical geometry and biomechanical properties, as shown in Figure 40.
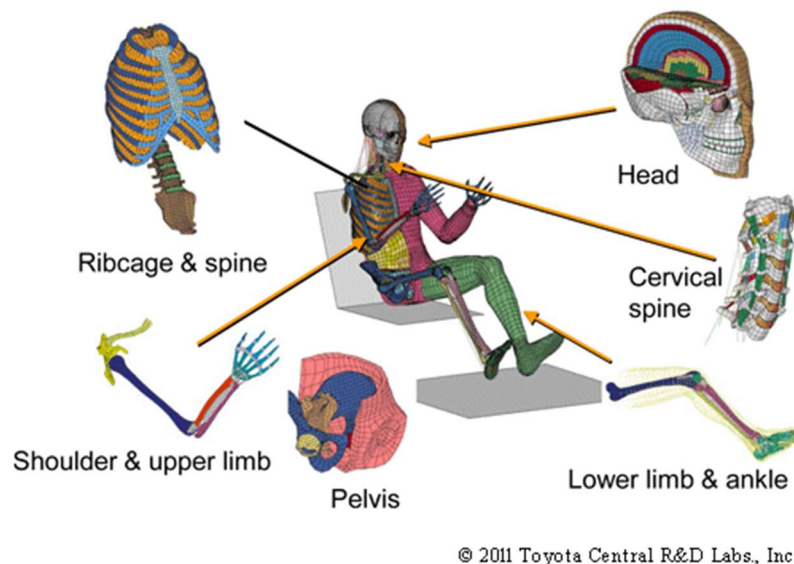
Figure 40 – THUMS Finite Element model [82]

It can be analyzed using the explicit FE analysis code of PAM-CRASH (by ESI GROUP) and LS-DYNA3D (by LSTC) and it can assure reasonable CPU time while using current workstations since it is composed of more than 80,000 total elements [82].

Each bone except the thoracic and lumbar vertebrae consists of outer cortical bone and inner spongy bone and each joint in the whole body was modeled anatomically by bone-to-bone elastic material using membrane of bar elements. In addition, material properties of the density, Young's modulus, Poisson ratio, stress-strain curves in THUMS were based on available databases [82]. Therefore, THUMS can simulate deformations of every part of the human body in a vehicle crash, with the aim to reduce the cost and improve the precision of real crash tests in Toyota.

2.10.1.2 3-year-old child dummy FE models

The research conducted by Mizuno et al. [83] was one of the first in which an FE model of a child dummy was developed, scaling a THUMS model for developing a 3-year-old child dummy FE model, obtaining dimensions very similar to the 3-year-old child anthropometric data. The size scale factors of this model were determined for each body region such as the head, neck, torso, pelvis, and extremities. Such factors were developed in three directions (λ_x, λ_y and λ_z) and a scale factor in a superior-inferior direction was mainly used since the priority was given to the height of the child. The responses of the child finite element model were compared to those of the Hybrid III 3-year-old child dummy in the ECE R44 tests: they were very similar in neck flexion, thorax impact, and lumbar spine flexion. Moreover, it was concluded that the spinal flexion mode of the model was closer to the human one than that of the physical Hybrid III dummy.

Additionally, a Hybrid III 3-year-old dummy FE model was developed by First Technology Safety Systems (FTSS) [84]. A distinctive characteristic of such a model is the presence of zero-length beam elements and nodes in specific areas of the body used to provide numerical observations comparable to the experimental load cells and accelerometers equipped in the physical dummy. Such model is completely deformable and is a complex combination of various material characteristics, joints, masses and element formulations. This FE model is shown in Figure 41, where an FE model of a child safety seat can be noticed, too.

Figure 41 – Hybrid III 3-year-old child dummy FE model developed by FTSS [85]

2.10.1.3   Child seat FE model

Obviously, when simulating a car crash with children, the reproduction of the appropriate CRS is essential. Turchi et al. [85] developed a child seat FE model for 3-year-old child dummies, by which they investigated the injury potential of children in forward and rearward-facing child restraint seats in frontal collisions. Such model reproduced a CRS with a five-point safety belt, used for performing experimental sled tests of the FMVSS 213 dynamic test, using a Hybrid III 3-year-old dummy; the model of the seat only had the pertinent surfaces of the CRS which might have contact with the dummy, in order to study the effectiveness of the CRS in preserving the occupant during a crash.

The seat was modeled using a rigid material model (material type 20, *MAT_RIGID, in LS-DYNA) as the deformation of the CRS was observed to be negligible during the experimental sled testing. Additionally, the eight slots, which the seat belts travel through, were also incorporated into the FE model and the values for the density, elastic modulus, and Poisson's ratio, indicated for the material characterization, were based on typical standards of the polypropylene CRS material. The CRS FE model is shown in Figure 42, where the eight seat belt slots can be noticed.

(a)   (b)
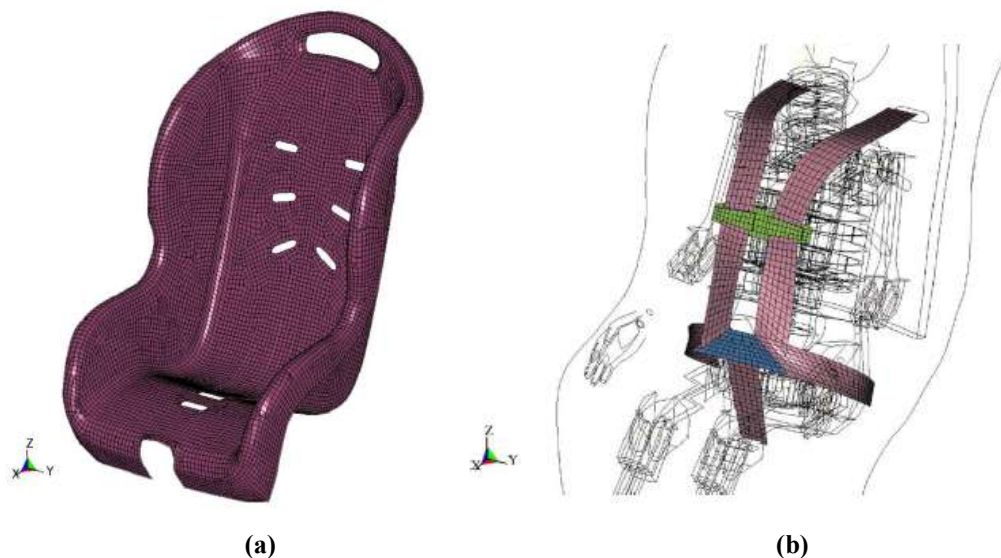
Figure 42 – Isometric view of the FE model of child safety seat (a) and restraint system (b) developed by Turchi [85]

Moreover, the seat belt needed to be modeled: Turchi designed it to fit around the FE child dummy model in a similar way as the experimental setup and modeled the length of the seat belt only up to the mesh of the CRS to simplify the difficulties associated with belt wrap and motion through the slots. The material card chosen to simulate the characteristics of the seat belt webbing was *MAT_FABRIC, which also invokes a shell element formulation

(Belytschko-Tsay membrane element) that is better suited to the large deformations experienced by fabrics. An "automatic surface to surface" contact algorithm was used to model sliding contact between the belt and the torso clasp; both the waist and torso clasps were modelled using a rigid material definition identical to the one of the CRS. The FE model of the restraint system is shown in Figure 46.

Furthermore, a foam pad, which is inserted in between the polypropylene shell and the seat fabric of the CRS, was also incorporated into the FE model. 1200 solid elements were used to discretize the foam pad and the material behavior was defined using material type 57 in LS-DYNA (*MAT_LOW_DENSITY_FOAM), commonly used to simulate polymeric foams; the stress/strain relationship (obtained through experimental tests on specimens) was also implemented into the material model of the foam and, lastly, the hysteretic unloading factor and the shape factor, needed to characterize the energy absorption behavior of the foam during unloading, were determined through a trial and error approach.

Another material model option for a foam pad could be the material type 63 (*MAT_CRUSHABLE_FOAM), which can utilize strain rate dependent compression information but does not account for the tension behavior or the actual recovery characteristics [86].

Furthermore, the solid element formulation to be used for representing polymeric foams is another important parameter to select when working on this type of material; solid elements can be classified into first order or second order and into hexahedral or tetrahedral elements. Generally, second-order elements are computationally expensive and unstable for complex contact problems. Therefore, these elements are not used in full vehicle simulations [86]. Two first-order tetrahedral element formulations which can be used in this type of analysis are the element formulation 10 (ELFORM10), only applicable for foams with Poisson's ratio $\nu = 0$, thus generally not recommended, and ELFORM13, characterized by 1-point constant stress with nodal pressure averaging, implemented for many common material cards and suitable for materials with Poisson's ratio greater than 0 [87].

2.10.2 Finite Element Method simulations for child safety research

After the completion of the pre-processing phase, a crash test can be simulated running the Finite Element code. The reproduction can be very accurate, mostly if the CRS and the child dummy are modeled correctly since motion data such as the acceleration pulse of a standard test can be easily imported from the accelerometers mounted in the vehicle during the experimental crash test. An example of this type of process is given by Kapoor et al., where Hybrid III 3-year-old [88, 89] and Q3 child dummies [87, 90] FE models were positioned into the CRS FE model described in the previous section and used to simulate an FMVSS 213 and a CMVSS 208

sled tests. Before running the simulations using LS-DYNA, experimental sled tests were completed, to successively compare the results.

Once the numerical simulations were completed, the output data were analyzed, beginning the post-processing phase. The main parameters observed using LS-PrePost were the resultant head acceleration, used for computing the HIC_{36}, the chest resultant acceleration, the resultant neck forces and moments and the neck injury criteria, which were also collected by transducers placed in the experimental dummy. The head and neck injury criteria were computed using Equation 1, 2 and 3. Afterward, Kapoor et al. performed a qualitative comparison of numerical and experimental data, analyzing the child dummy motion in both types of simulation and comparing the time plots of all the parameters collected.

In reference [88], the side views of the numerical and experimental child dummies in the crash at different time situations were compared and it was observed that the experimental results had an acceptable correlation to the numerical findings. There appeared to be a slight shift in time between the two kinds of results; this was due to the acceleration pulse, measured by the accelerometers positioned in the vehicle but applied to the seat for the numerical tests. The time difference between these two testing methods was estimated to be no greater than 50 ms. This comparison is shown in Figure 43.

$t1 = 0$ ms
$t2 = 0$ ms

$t1 = 33$ ms
$t2 = 60$ ms

$t1 = 60$ ms
$t2 = 90$ ms

$t1 = 83$ ms
$t2 = 127$ ms

(a)　　　　　　　　　　　　　　(b)
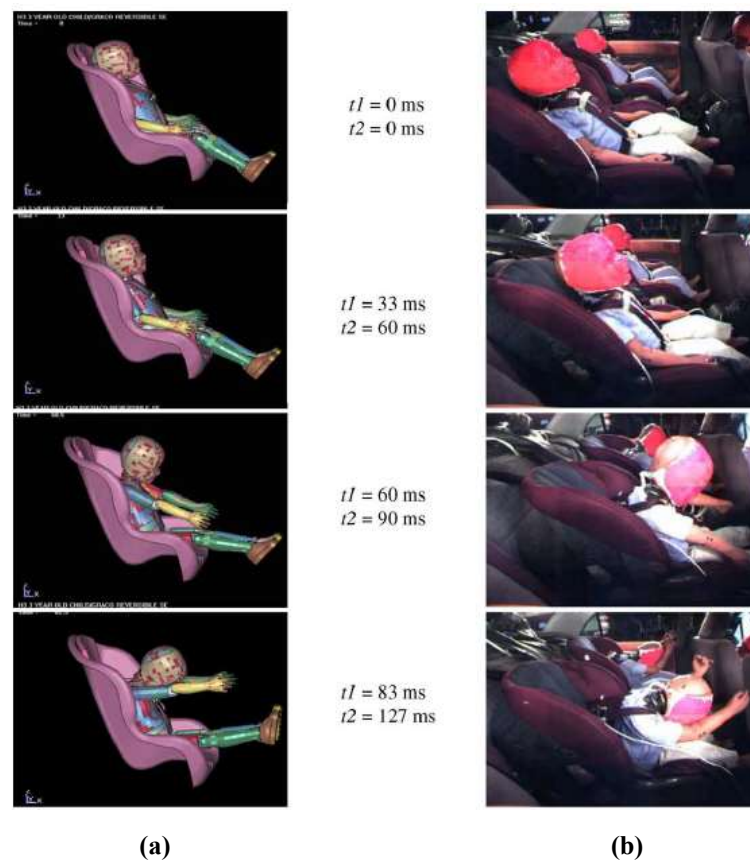
Figure 43 – Numerical (a) and experimental (b) observations (side view) at different time intervals [88]

The objective of such research project was to find the difference in injury potential between forward-facing and rearward facing CRS, hence, after verifying that the model was quite accurate through the comparison with the experimental data, Kapoor et al. performed an FE simulation with the same dummy and CRS, but using a rearward configuration, concluding that placing a child in a RFCRS can be safer than using a FFCRS. Both the verification of the accuracy of the model and comparison between the two different configurations were performed not only matching different instants of the respective motions of children but mostly comparing many plots representing the progress in time of the parameters mentioned before. For instance, Figure 44 shows a comparison between numerical (D1) and experimental (D2) trend of the lower neck moment in the y-direction, which magnitude is very similar, and Figure 45 displays a relation between upper (a) and lower (b) neck forces in the x-direction for FFCRS and RCCRS configurations.
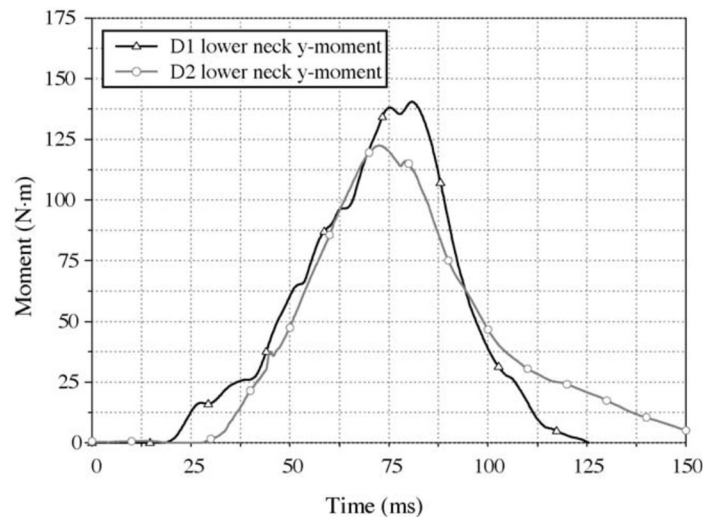
Figure 44 – Experimental and numerical local lower neck moment in the y-direction [88]

| (a) | (b) |
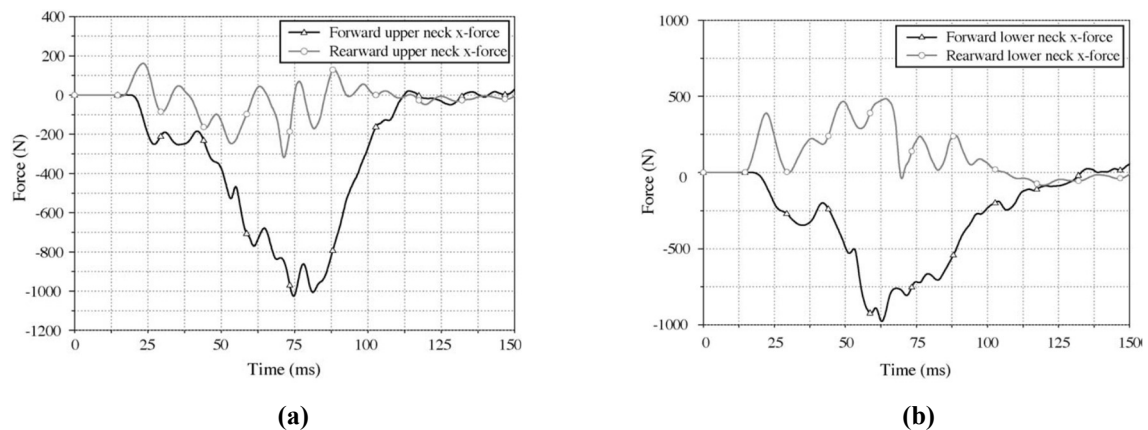
Figure 45 – Upper (a) and lower (b) neck x-force in forward and rearward facing CRS configuration [88]

Observing Figure 45, the much higher magnitude of the x-force in the forward configuration can be noticed and such trend was present also in plots regarding the HIC_{36} and Nij, confirming the lower injury potential of the rearward configuration, as mentioned by Arbogast et al. [38] and Isaksson et al. [39]. The thesis of Weber et al. [36, 41] was numerically confirmed, too. As a matter of fact, Kapoor et al. [89] numerically analyzed the consequences of CRS misuse, conducting simulations for frontal and side impact tests in accordance with FMVSS 213 in the absence of the top tether strap of LATCH. In conclusion, increases by approximately 30% and 70% were registered in HIC and head excursion respectively. A comparison between the child body excursion in the different cases is shown in Figure 46.
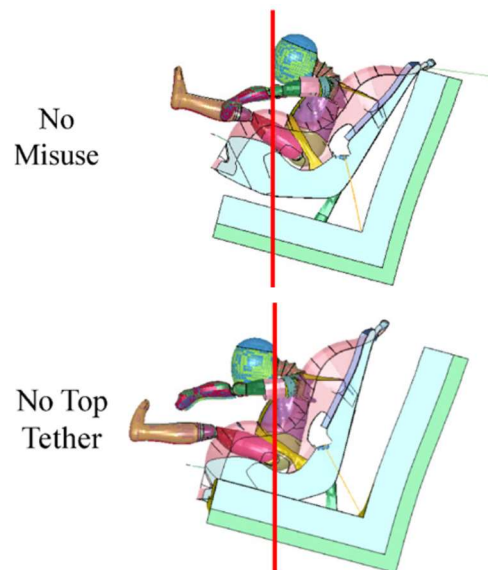
Figure 46 – Side displacement comparison between absence and presence of top tether in CRS [89]

Kapoor et al. [91] also evaluated an implementation of a load-limiting behaviour into the upper tether and lower LATCH anchors of the CRS, in order to reduce the neck injury criteria allowing a greater head excursion of the child, since previous works [89, 90] illustrated that, despite the former being significantly less than the FMVSS 213 limit of 720 mm, values of the latter exceeded the protection reference value (0.33 beyond the first 30 ms of the impact). Therefore, the objective of this research was to exploit the head excursion of the child using a load limit on LATCH tether and anchors, to reduce the Nij.

The simulations were performed on three different validated child FE model: a Hybrid III 3-year-old child model [88], a Q3 model [88, 90] and, lastly, a child FE model developed at Nagoya University by Mizuno et al. [83]; the input acceleration pulse was the same as that in reference [88, 90], representing the FMVSS 213 dynamic frontal impact test. The results showed a higher head excursion when limiting the load of the LATCH tethers and anchors, which never exceeded the limit of 720 mm imposed by the FMVSS 213. On the other hand, the

load on the neck has been reduced of approximately 40% using this method: this reduction led to a decrease of the *Nij*, even if it remained higher than the FMVSS 213 limit.

2.10.2.1 FE model validation

Nowadays, Finite Element simulations cannot completely substitute physical tests; as a matter of fact, FEM results must always be correlated to experimental data. The comparison between FE and experimental model is called validation and it is aimed to authorize the use of an FE simulation even without an experimental correlation, only if the type of test simulated in the FE model does not change at all.

For example, Kapoor et al. [92] validated a Hybrid-III 3-year-old child dummy FE model used for analyzing LATCH performance in near-side impact crashes; the validation was quantitative, thus effectuated through a comparison of different plots from experimental and numerical tests. Figure 47 shows this comparison for head acceleration (a) and chest acceleration (b).

(a)   **(b)**
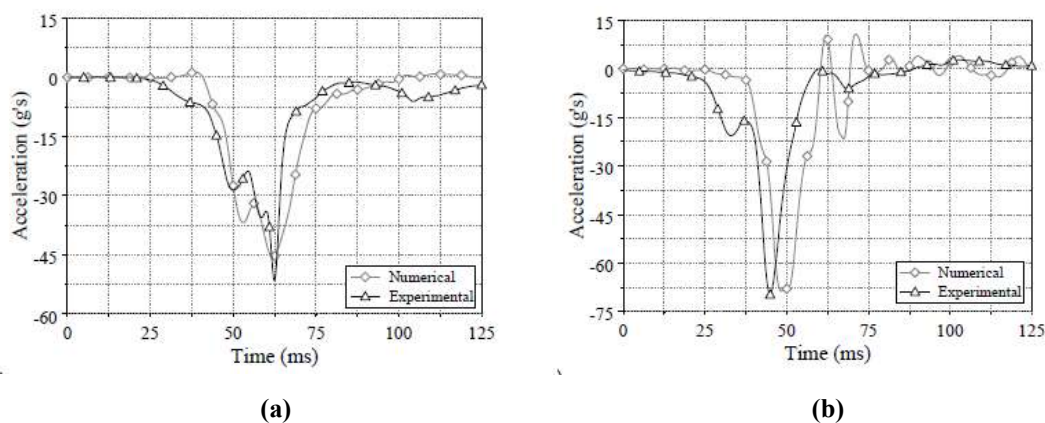
Figure 47 – Experimental and numerical head acceleration in local y-axis direction (a) and chest acceleration in local y-axis direction (b) as a function of time [92]

Afterward, the same model was used for analyzing and comparing the performance of a rigid ISOFIX system with two different cross-sectional geometries for the anchoring mechanism (rectangular and cross-shaped section). It was observed, this time without needing a correlation with experimental data, that the use of both solutions was effective in reducing resultant chest accelerations by approximately 40 percent.

Another process of quantitative validation is suggested by Oberkampf et al. [93], which recommends the use of two parameters: the validation metric *V* and the cumulative error *E*, which is the integral average of the relative error.

$$V = 1 - \frac{1}{L} \int_0^L tanh \left| \frac{y(x) - Y(x)}{Y(x)} \right| dx \tag{7}$$

$$E = \frac{1}{L} \int_0^L \left| \frac{y(x) - Y(x)}{Y(x)} \right| dx \tag{8}$$

Where $y(x)$ is the measured value, $Y(x)$ is the expected value and L is the range of the independent variable. When validating Finite Element Analysis results, $y(x)$ is the value numerically obtained, whereas $Y(x)$ is the experimental value.

The use of the validation metric has many advantages: it normalizes the difference between the computation results and the experimental data; secondly, the presence of the absolute value avoid that negative differences offset the positive ones and, lastly, when the difference between all computation and experimental results is zero, then the validation metric is unity, therefore it indicates perfect agreement between the computational results and the experimental data. On the other hand, if the relative error becomes large, the validation metric approaches zero. Figure 48 illustrates the validation metric V as a function of the relative error.
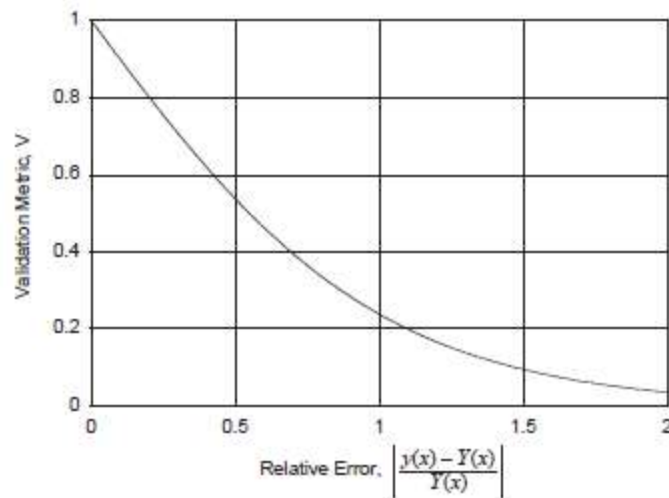
Figure 48 – Validation metric as a function of the relative error [93]

The main disadvantage of using this technique is that the normalization is inappropriate when $Y(x)$ is closer to zero. This can be overcome by introducing an error criterion: an upper and lower bound can be specified as $\pm 10\%$ of the maximum absolute expected value. Then, the error can be calculated as follows:

$$For\ lower\ bound\ \leq Y(x)\ \leq upper\ bound, error(x) = 0$$
$$else\ \ error(x) = \frac{y(x) - Y(x)}{Y(x)}$$

(9)

Therefore, within the window of the upper and lower bounds, the error is evaluated as zero; otherwise, the error is evaluated as the relative error between measured and expected values. This criterion avoids excessive overestimations of E and underestimations of V. The limit on the values of V and E to confirm the validation of an FE model varies as a function of the complexity of the analyzed case, marked by the number of elements and boundary conditions.

3. FOCUS OF RESEARCH

The last section of the literature review highlighted that simulations of sled tests for evaluating child safety have been already executed. This type of work often involved three or six-year-old child dummy models, placed in the proper CRS (usually Full Forward Facing), without the presence of the vehicle body. This project, instead, is aimed at simulating a full vehicle body sled test including all its components, and a ten-year-old child dummy, that needs a particular investigation: it is restrained by the vehicle seat belt, which must be routed over the booster seat to ensure the acceptable level of safety. The higher risk when verifying the safety of children placed on booster seats is the slipping of the belt webbing from the occupant's shoulder, as underlined in Section 2.6.2.1. Given its potential harm to the child, this event is highly penalized by both NCAP ad Euro NCAP, as described in Section 2.8.5, and it can be avoided with an effective belt pretensioning. On the other hand, the loads imposed by the seat belt on a ten-year-old child dummy have to be controlled to respect standardized levels of injury. Moreover, in this type of simulation, the acceleration pulse of the sled test is imposed on the vehicle body, which imposes inertial effects to the seat foam, booster and, lastly, to the child dummy, through the modelled contacts and constraints.

The simulations were executed using LS-DYNA Finite Element explicit code. The validation of the model was performed comparing the injury parameters registered by the numerical dummy with those monitored during an experimental sled test conducted with the physical Q10 and the same vehicle body, with the scope of reproducing the Euro NCAP Offset-Deformable Barrier crash test.

Therefore, this research purposes to focus on the following areas:

- To develop guidelines to perform a full vehicle body sled test FE simulation using a 10-year-old ATD. This procedure will be described in detail in the next Sections, including all phases of Finite Element Analysis (FEA), from the discretization (meshing) to the verification and validation of the model;
- The OEM utilizes a virtual restraint system provided by an external supplier. This research proposes to describe the generation and calibration of a numerical restraint system including belt webbing, retractor, pretensioner and DLT in the LS-DYNA environment;
- To consequently contribute to the understanding and improvement of injury risk of 10-year-old children and the safety performance of the booster seat and vehicle restraint system in their reciprocal interference during crash events.

4. DESCRIPTION OF THE MODELS

A detailed list of all models involved in this project is fundamental to understand every step of the research:

1. Vehicle body FE model (Figure 49), provided by the OEM, needed to position and eventually constrain all the other bodies in their correct positions and to prescribe the sled acceleration impulse in the final simulation;

2. Front passenger seat FE model (Figure 50a), provided by the OEM, needed to observe the likely impact of the child dummy lower leg against it, a higher risk event when assessing ten-year-old child safety, as already mentioned by Uphold, Harvey et al. [35];

3. Booster seat FE model (Figure 50b), provided by an external supplier, which has been positioned and fixed simulating the ISOFIX anchors in the FE environment. This model is essential to correctly simulate the seating position of the Q10 child dummy model;

4. 2nd-row seat foam and relative suspension frame FE model (Figure 51a and 51b), provided by the OEM. The CAD designs of both foam and frame were discretized using the preprocessor ANSA by BetaCAE in the first phase of the project, which will be described in the next chapter. These models are fundamental to place both booster seat and dummy models in the vehicle FE environment and to transmit the acceleration of the vehicle body to all the other entities;

5. Q10 child dummy FE model (Figure 52a), provided by Humanetics®, was positioned in the FE vehicle body to reproduce the same initial condition of the experimental sled test. This step of the work will be described in Section 7;

6. Restraint system CAD model (Figure 53a), was provided by the OEM and needed to generate the FE belt webbing (Figure 52b) with the correct anchorage points and routing, will be analyzed in more detail in Section 8;

7. Backrest foam CAD model (Figure 53b), provided by the OEM to increase the precision of the dummy initial position, knowing the relative position and distances between backseat and dummy. Usually, when simulating crash tests, the backseat foam is discretized and its relative FE model inserted in the final simulation. In the Euro NCAP frontal crash tests assessment, the rebound phase and the consequent deformation of the backrest are not considered, thus the backseat foam is needed only to correctly place the dummy model.
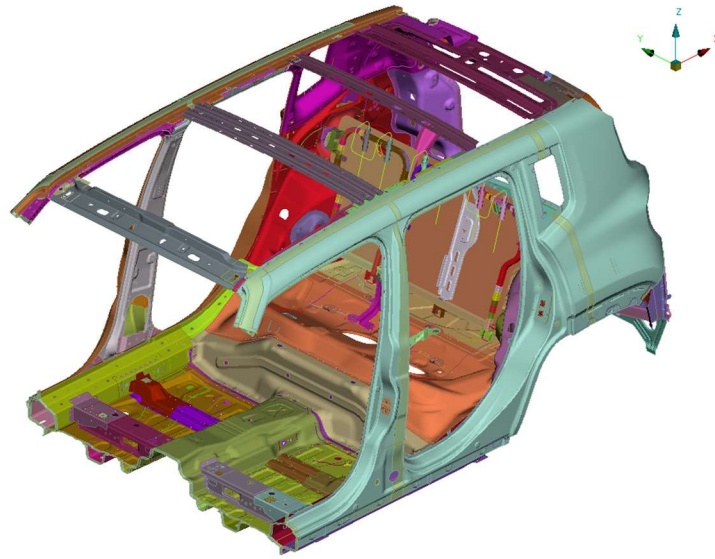
Figure 49 – Isometric view of the vehicle body FE model

| (a) | (b) |
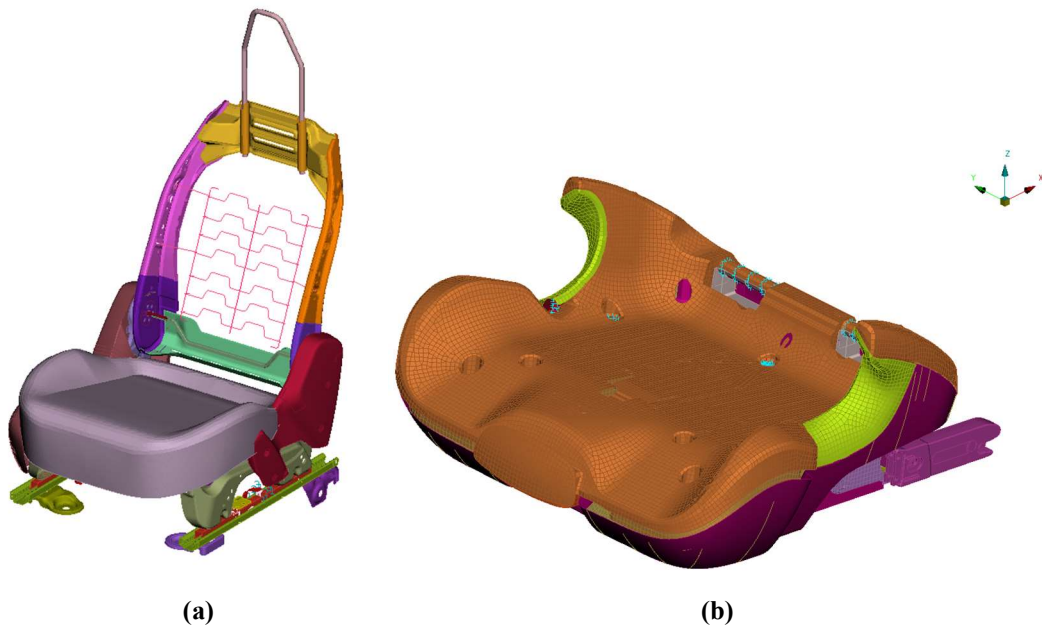
Figure 50 – Isometric view of front passenger seat (a) and booster seat (b) FE models

(a)   (b)
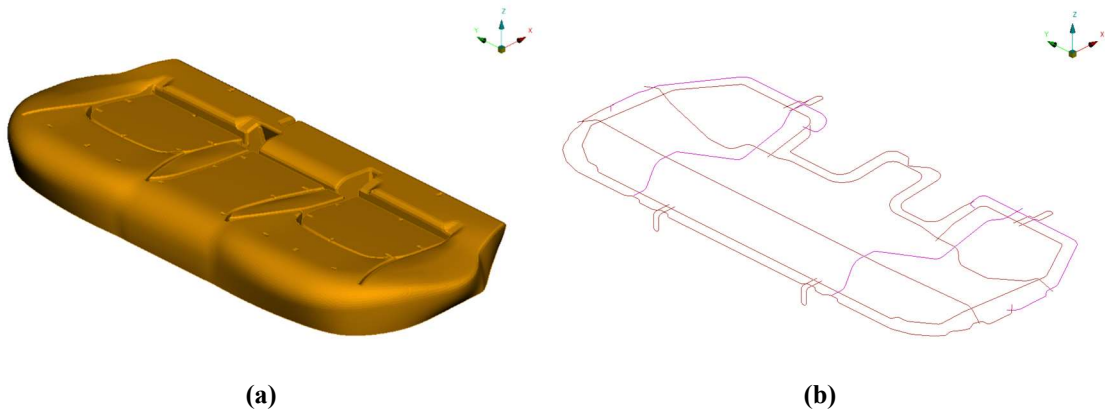
Figure 51 – Isometric view of the 2nd-row seat foam (a) and its relative suspension frame (b) FE models

(a)   (b)
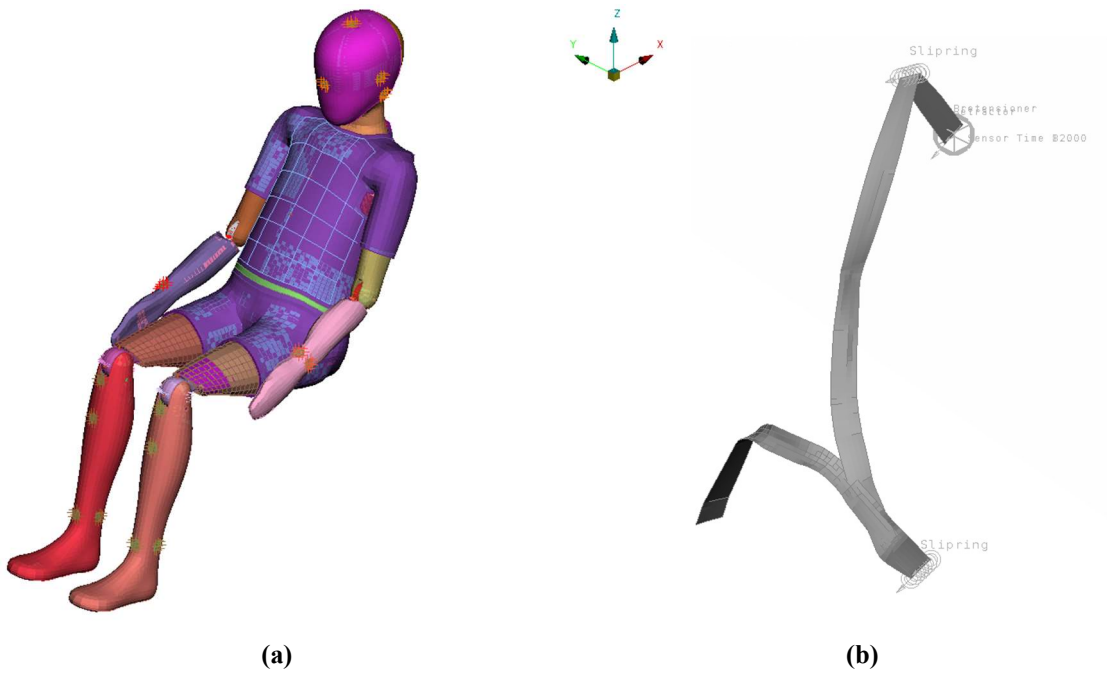
Figure 52 – Isometric view of the Humanetics® Q10 child dummy FE model (a) and of the virtual seatbelt (b)

(a)   (b)
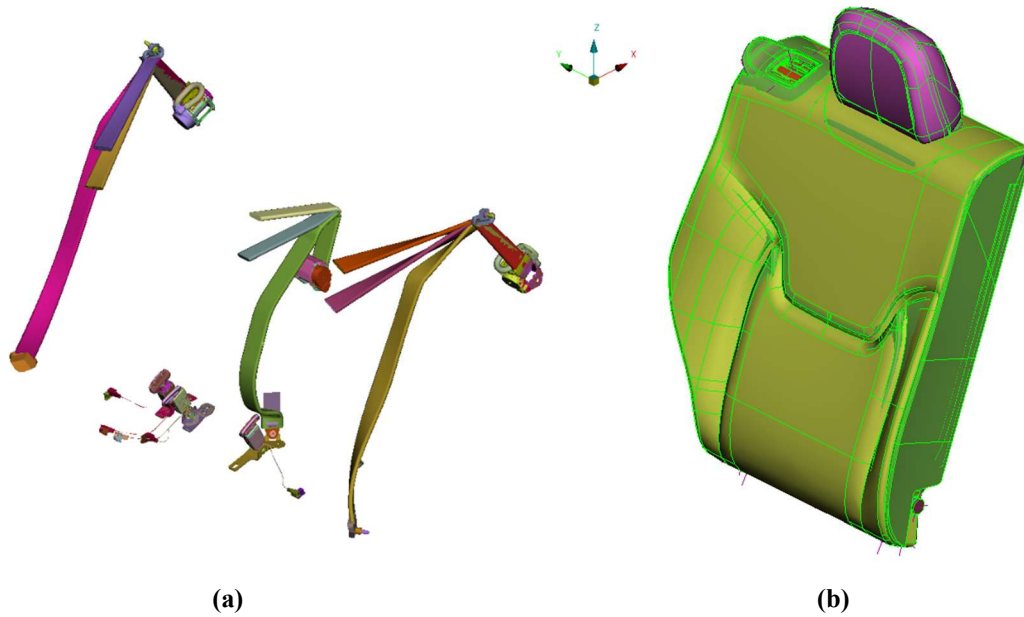
Figure 53 – Isometric view of the restraint system (a) and backseat foam CAD models

In addition, Table 5 shows the elements count for each FE model and the relative typology.

Entity	Elements count	Element
Vehicle Body	804,577	Beam, Shell, Solid
Front Passenger Seat	195,104	Beam, Shell, Solid
Booster Seat	220,046	Shell, Solid
2nd Row Seat Foam	921,760	Shell, Solid
2nd Row Seat Suspension Frame	2,242	Beam
Q10 Child Dummy	330,000	Beam, Shell, Solid
Restraint System	1,162	Shell
Total	2,474,891	

Table 5 – Element count and type of each FE model involved in the project

The total element count is very high: more than 2 million elements are involved in the sled test simulation and the running time is 200 ms, therefore the computational performance required by this assembly can not be obtained using a workstation. This is the reason why the

LS-DYNA simulations were executed on the cluster/supercomputer of the FCA US LLC Headquarters and Technology Center in Auburn Hills, MI.

Moreover, it is important to clarify that all material and section properties were provided by the OEM, since they are already available within the company, thus this research does not focus on the material characterization of any entity and they will not be described in this thesis so as to avoid the publication of confidential data.

Lastly, Figure 54 shows the assembled models, all placed and properly constrained in the FE vehicle environment. The way this preprocessing of the complete model was accomplished will be explained in the next chapters.
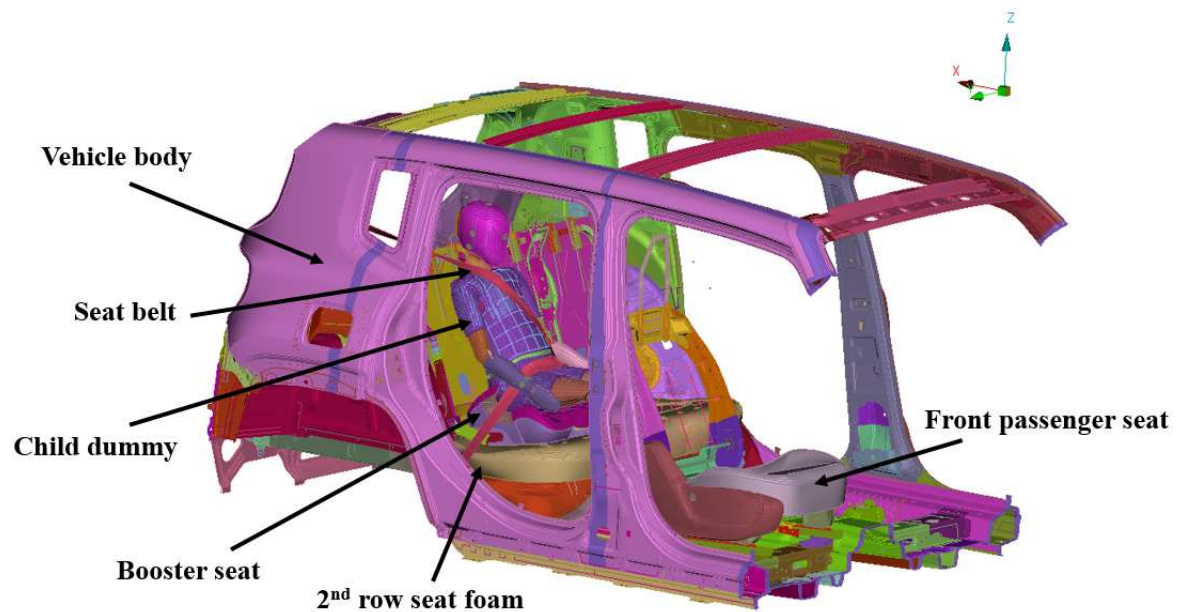
Figure 54 – Assembly of all FE models

5. MODELS UPGRADING FOR FE ANALYSIS

Some of the models provided by the OEM were not ready to perform the simulations required to complete this research, thus they needed to be upgraded through the preprocessor ANSA. In particular:

1. The 2nd-row seat foam and its suspension frame were discretized (meshed), developing a new input file for LS-DYNA code;
2. The new suspension frame model was fixed to the vehicle body, to simulate the fixing claps and screws used in the real vehicle to constrain these bodies;
3. The front passenger seat FE model was fixed to the vehicle body floor, reproducing the same type of attachments existing between the seat rails and the floor of the vehicle body.

5.1 Discretization of the 2nd-row seat

5.1.1 Discretization of the foam

5.1.1.1 Geometry cleaning

The CAD model of the foam was provided by the OEM and it is shown in Figure 55, which reports the representation of the original file from the software ANSA.
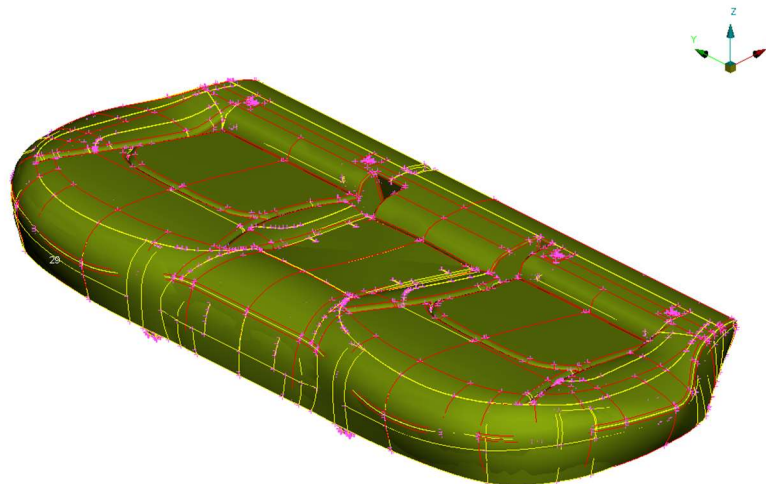
Figure 55 – Isometric view of the CAD model of the backseat foam

The geometry was not "ready-to-mesh"; in fact, the analysis of the CAD through the ANSA "Geometry check" interface reported different warnings which would cause failure of the meshing process, such as:

- Edge cracks (red borders in Figure 61);
- Overlaps of faces (yellow borders in Figure 61);
- Collapsed edges (red border in Figure 61);
- Unchecked faces.

These irregularities were mostly found on the bottom area of the model since it is characterized by holes and corridors needed to place the suspension frame, as shown in Figure 56.
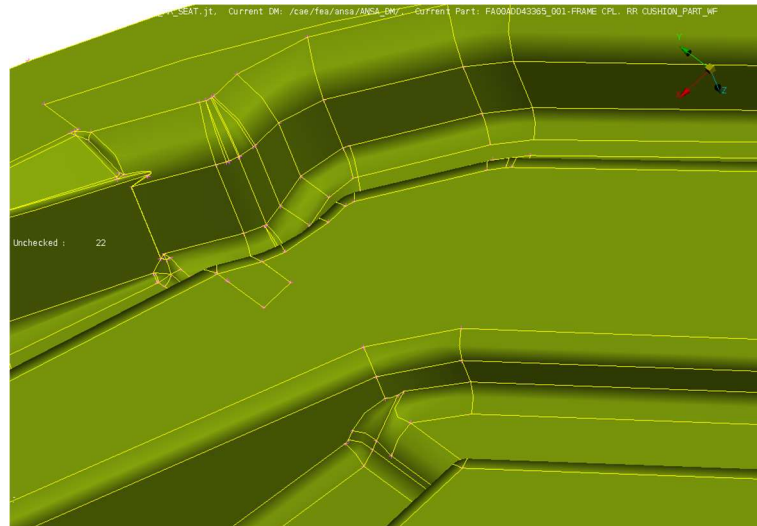
Figure 56 – Detail of the base of the foam CAD

The high number of edges, even very close to each other, indicates the complexity of this part of the model, that needed many fixing operations to ensure the success of the successive discretization phase. In this regard, the "Auto Fix" function of ANSA solved half of the abnormalities of the CAD, demonstrating the excellent performance of the preprocessor. A preliminary check of the geometry is a fundamental step to execute when trying to discretize a new CAD, mostly when the model is provided by an external designer. If the geometry is not too complex, the automatic fixing commands of most preprocessors could correct all its irregularities. On the other hand, when the geometry is characterized by areas with excessive numbers of edges and faces, manual corrections are necessary to stabilize the model.

In this case, the second half of the CAD irregularities was healed eliminating degenerated (unconnected, overlapped, cracked or simply too close) edges and faces and

building them again, preserving the shape of the seat foam. The cleaned geometry of the foam can be visualized in Figure 57: the green lines are called "Double cons" and they indicate a closed surface (ready-to-mesh).
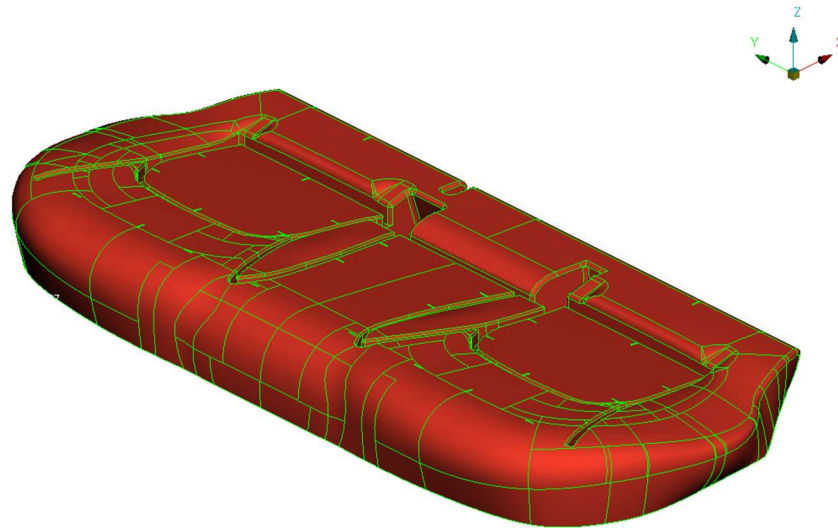
Figure 57 – Healed CAD of the seat foam

5.1.1.2   Foam surface and volume meshing

As in every volume meshing procedure, a 2D mesh was obtained from the cleaned CAD of the foam, through the "Mesh" interface of ANSA preprocessor.
Firstly, the type of elements and their average side target length was defined: triangular elements with edge length equal to 5 mm, since the other models of the assembly which will be in contact with the foam (vehicle body, booster, dummy) are characterized by elements with the same average dimension.

Successively, many quality criteria and parameters were set in ANSA, shown in Table 6 and in Figure 58; they influence the discretization algorithm, which tries to generate a mesh that respects these constraints.

Parameter	Value
Target side length	4.0 – 6.0 mm
Aspect ratio	1.0 – 2.0
Jacobian	0.8 – 1.0
Minimum angle	40° - 60°
Maximum angle	60° - 90°

Table 6 – Quality parameters for the surface mesh of the foam
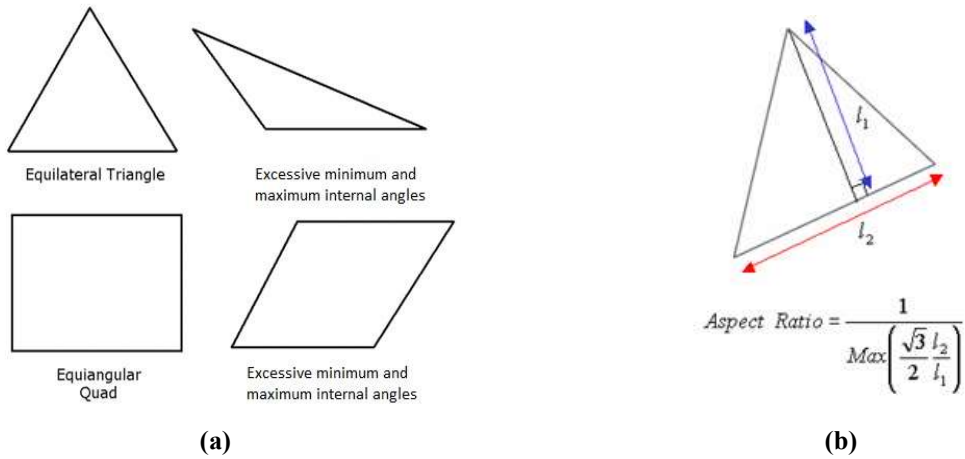
Figure 58 – Representations and definition of minimum and maximum internal angles (a) and aspect ratio (b)

After the first discretization process, the mesh needed several manual adjustments in some areas to be even and to respect the majority of defined parameters. The ANSA "Remesh" and "Reshape" interfaces were shown to be essential to reach the desired level of precision. The latter, for example, readjusted the shape of some complex zones of the model, to facilitate the meshing phase, without modifying the overall dimensions. Two details of the final surface mesh are shown in Figure 59.
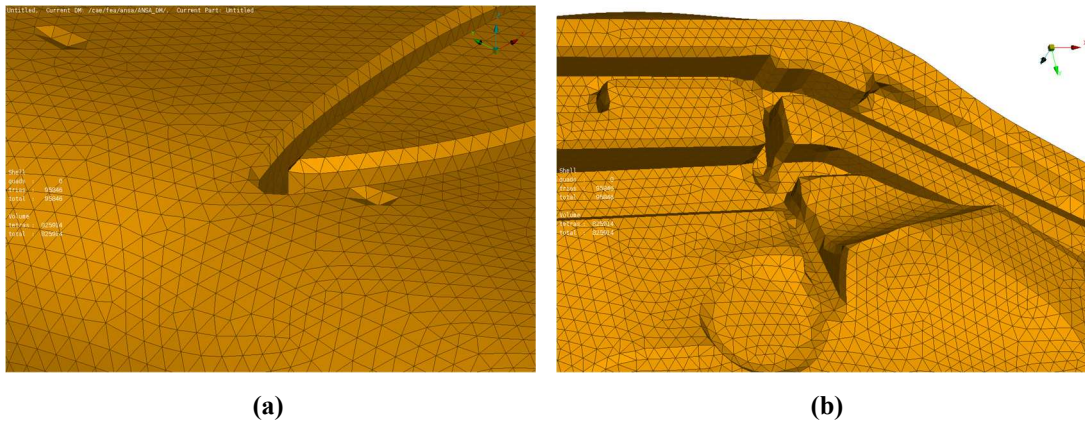
Figure 59 – Details of top (a) and bottom (b) of the final surface mesh

Once the 2D mesh had been defined, the volume discretization was executed through the "Volume Mesh" interface, using the automatic detection of an enclosed volume within the foam. Moreover, the same quality criteria used for generating triangular elements were used to create tetrahedrons, with the addition of two other constraints, specific for 3D elements, reported in Table 7 and Figure 60.

Parameter	Value
Maximum growth rate[5]	1.5
Tetra collapse	> 0.2

Table 7 – Additional quality parameters for generating the volume mesh

$$collapse = min\left(h_i / \sqrt{A_i}\right)/1.24$$

for perfect tetra
tetra collapse=1
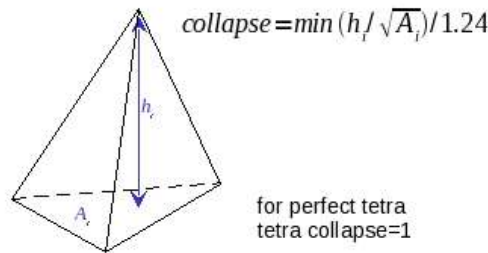
Figure 60 – Representation and definition of tetra collapse

The generation of a 3D mesh which respects these parameters always depends on the overall quality of the surface discretization, therefore it has been shown to be essential to define the optimal 2D mesh, through a "trial and error" approach: eliminating the volume mesh, improving the surface mesh, and repeating the process again. Figure 61 shows a cut of the final volume discretization. The regularity of the element shape and the low value of the growth ratio can be noticed.
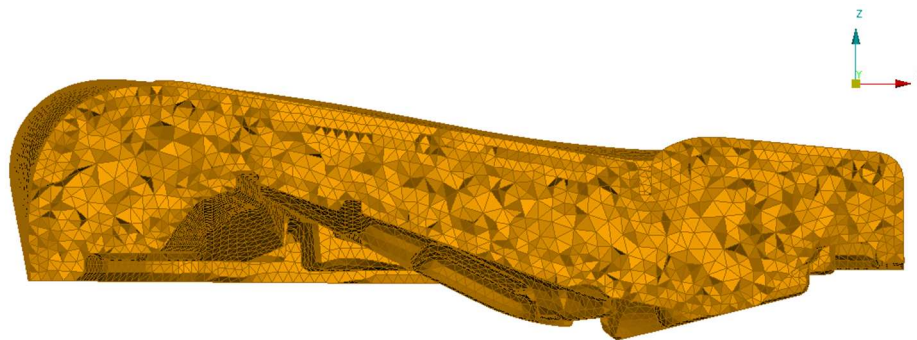
Figure 61 – Cut of the volume mesh on the *xz* plane

Lastly, a shell element "skin" of the foam was automatically generated through the "Mesh" and "Skin" interfaces of ANSA. The skin is characterized by shell elements placed on the external surface of the 3D mesh, exactly overlapping with the elements of the foam mesh, so

---

[5] It is the ratio between volumes of adjacent elements.

that to obtain an intrinsic tied contact. This new part will be used to regulate contact between the foam and every other external entity. Using the skin's 2D elements in the contact cards lightens the contact algorithm process: every nodal force (and subsequent deformation) on the solid foam will not be obtained by contact, but by the automatic transmission of the contact force on the skin elements (that are fewer than the solid elements), since they share the same external nodes with the foam itself. Moreover, the use of a shell skin contains the deformation of the solid elements, avoiding the occurrence of negative volume elements. The Young's modulus and Poisson's ratio of the skin shell elements are used for setting the contact stiffness, therefore reasonable values were set, according to the foam material properties.

5.1.1.3 Material and section characterization of the foam

After the definition of volume mesh and 2D mesh of foam and its skin respectively, the material and section properties of these two entities, provided by the OEM, were assigned to each part ID. The tetrahedral solid elements of the foam are characterized by:

- *SECTION_SOLID;
- *MAT_LOW_DENSITY_FOAM and a related curve for defining the nominal stress as a function of the strain.

The triangular shell elements of the skin, instead, are characterized by *SECTION_SHELL and *MAT_NULL. The details of material and section characterization of the foam cannot be provided in the body of this thesis document due confidentiality.

5.1.2 Discretization of the frame

5.1.2.1 Geometry extrapolation

The CAD of the suspension frame is reported in Figure 62.
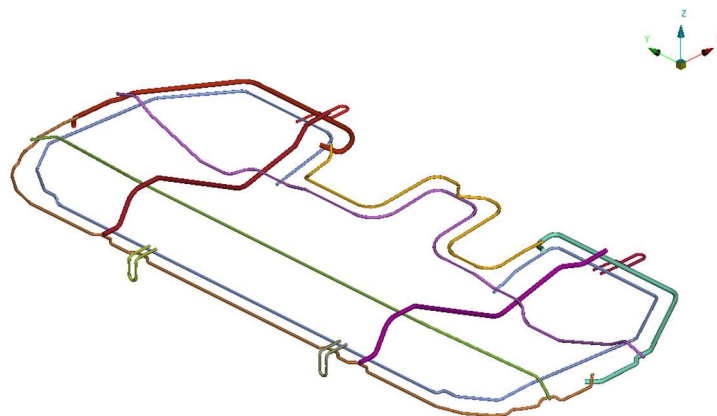
Figure 62 – CAD of the suspension frame of the 2ⁿᵈ-row seat foam

In this case, the CAD was utilized only to extrapolate the centerline of each frame tube, thus the lines which pass along the center of each tube, for their entire length and route. Consequently, these lines were used to generate beam elements that will represent the suspension frame in the FE environment. The centerlines of all tubes were already present in the CAD file of the frame, thus they were easily extrapolated, allowing to start the meshing phase.

5.1.2.2   Generation of the beam element mesh

The beam elements were generated through the "LS-DYNA" interface of the software ANSA, which includes the majority of the functions available within LS-PREPOST. The orientation node of the first beam element of each centerline was generated automatically and the average length was set to 5 mm, to guarantee congruent dimensions among elements of different models.

The new FE tubes were divided among two different PIDs, depending on the diameter of the CAD elements, 5 and 8 mm, which can be noticed in Figure 62.

The final mesh can be visualized in Figure 63.
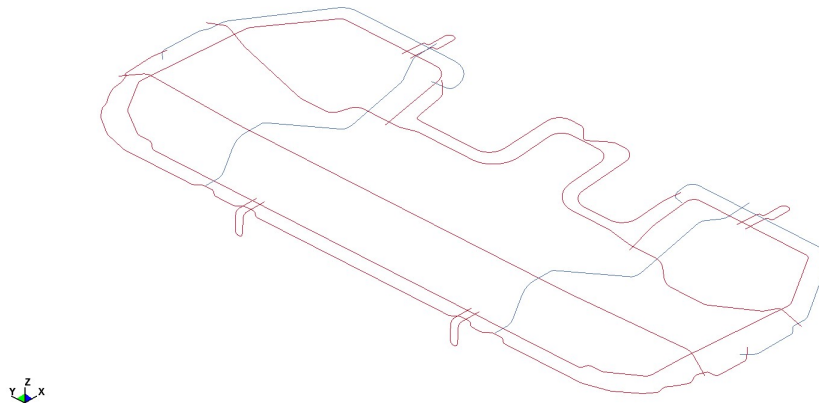
Figure 63 - Final beam elements mesh of the suspension frame

5.1.2.3   Material and section characterization of the suspension frame

The two PIDs were characterized with the same material ID, *MAT_PIECEWISE_LINEAR_PLASTICITY, with a related table collecting many effective flow stress versus plastic strain, to account for rate effects. Lastly, there are two different *SECTION_BEAM cards, depending on the diameter of the tubes, 5 or 8 mm.

5.2 Constraining of the 2nd-row-seat suspension frame

Once generated the suspension frame model, it needed to be upgraded to be used in the simulations regarding this research.

Front and rear areas of the frame were connected to the vehicle body floor, to simulate the fixing clamps and screws used in the real vehicle.

These connections were represented in the FE model using *CONSTRAINED_NODAL_RIGID_BODY, between nodes of the frame and nodes of the vehicle body.

Figure 64 shows the generated rigid bodies.
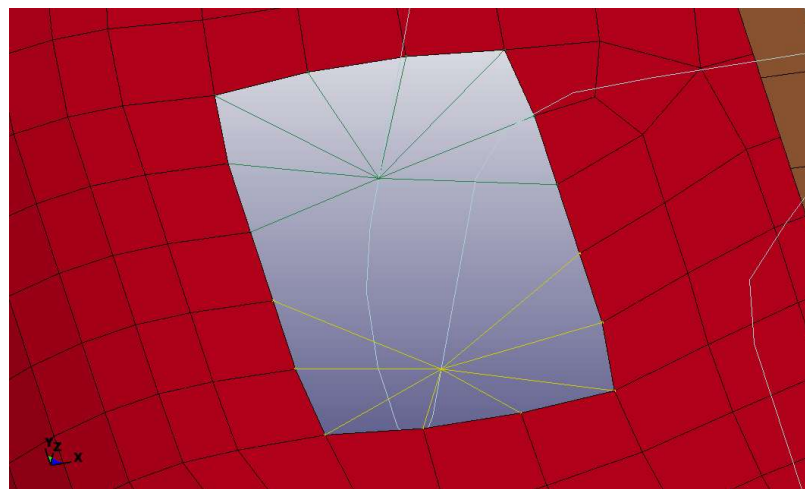
(a)
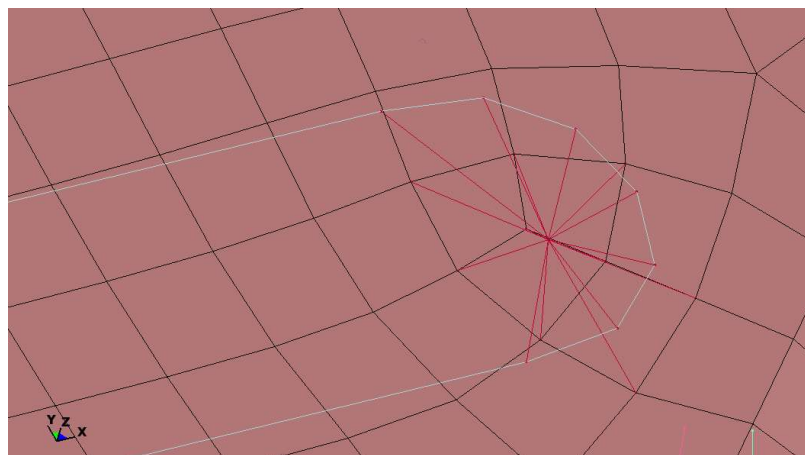
(b)

Figure 64 – Nodal rigid bodies simulating front clamps (a), rear screws (b) and tubes connection (c)

In Figure 64b, the absence of a hole for the screw in the vehicle body FE model is apparent. This omission is the reason why the connection was reproduced by connecting the nodes of the arc end of the frame tube to the closer nodes of the vehicle body elements, defining

a central master node. Instead, in the front connection (Figure 64a), the closer nodes of the connecting arcs of the frame were selected as master nodes, without the need to generate additional ones. These connections were replicated on both sides (left and right) of the model, due to the symmetry of the frame with respect to the *xz* plane, as can be noticed from Figure 62 and 63.

5.3 Constraining of the front passenger seat

The FE model of the front passenger seat needed to be fixed to the floor of the vehicle body. The seat model includes its rails and four fixing brackets, placed at the extremities of each rail.

Each bracket presents a screw hole, which coincides with another hole on the floor, where a bolt can be used to fix the passenger seat. As a matter of fact, a beam element is placed at the center of each hole, and is connected to all nodes of the bracket hole through a nodal rigid body. Figure 65a shows one of the four brackets and the respective beam nodal rigid body. Moreover, the vehicle floor includes a rigid washer in correspondence of the respective hole, underneath the fixing bracket of the seat, reported in Figure 65b.
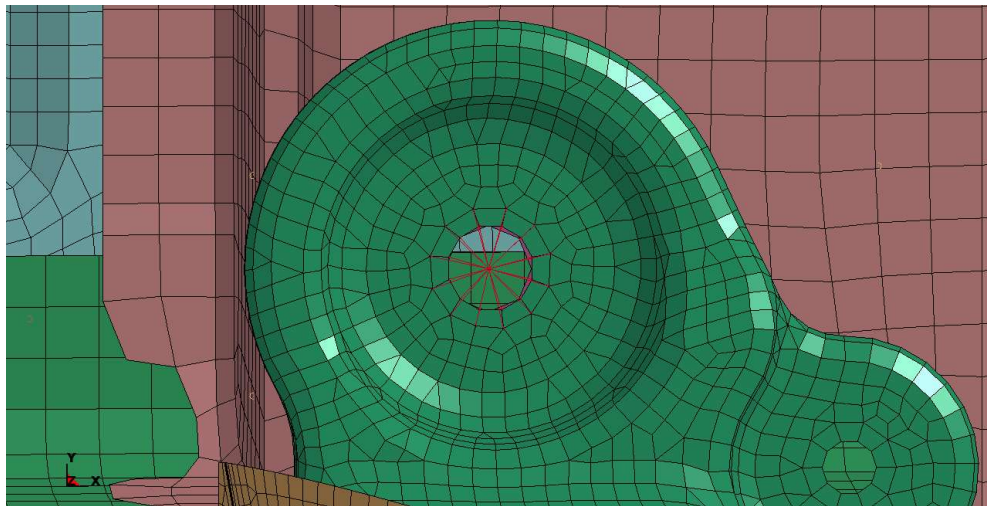
(a)
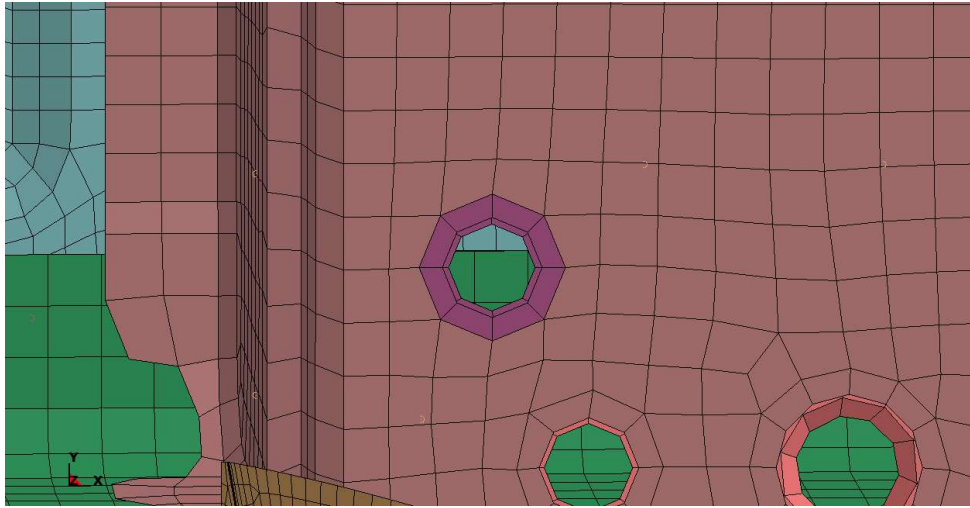
(b)

Figure 65 – Fixing bracket of the front passenger seat (a) and rigid washer of the vehicle body (b)

Therefore, it was decided to connect every seat bracket to the respective rigid washer of the vehicle body using four different *CONSTRAINED_EXTRA_NODES_NODE cards, thanks to which an additional and external node can be assigned to a rigid body. In this case, this node belongs to the beam element and it is the closest one to the rigid washer. Through this definition, one node of each beam is connected to the relative seat bracket using *CONSTRAINED_NODAL_RIGID_BODIES, whereas the opposite node is connected to the vehicle body rigid washer with *CONSTRAINED_EXTRA_NODES_NODE, ensuring the connection between the seat and the floor.

6. CRS INITIAL CONFIGURATION

The Finite Element booster seat was positioned on the 2nd-row seat, behind the front passenger seat, and fixed to the ISOFIX anchorage points.

Unfortunately, once its definitive position was defined, initial penetrations between the booster clamps and the seat foam were detected. This was an expected result since when a booster seat is placed in the vehicle body, the cushion foam undergoes a small deformation, which was not yet reproduced in the FE environment.

This section will describe:

1. The positioning of the booster seat in the vehicle cabin and the reproduction of the ISOFIX anchorages;
2. The LS-DYNA simulation executed to eliminate any initial penetration and predeform the seat foam, due to the defined initial position of the CRS.

6.1 Positioning the Child Restraint System

6.1.1 Positioning the booster seat FE model

The configuration of the booster seat was modified using the ANSA "Move" interface:

1. It was rotated with respect to the z-axis so as to obtain the proper orientation with respect to the vehicle body;
2. It was translated in z and x directions, with the aim to center the ISOFIX attachments (represented by beam elements and reported in Figure 66a) with the fixing holes of the booster clamps (Figure 66b);
3. It was centered in the 2nd-row seat in the y-direction so as to obtain the initial position of the clamps. Figure 67 shows the top view of the positioned booster seat with two symmetric measurements between a node of the ISOFIX beams and a node of the booster clamps chosen as references to obtain the optimal centering.
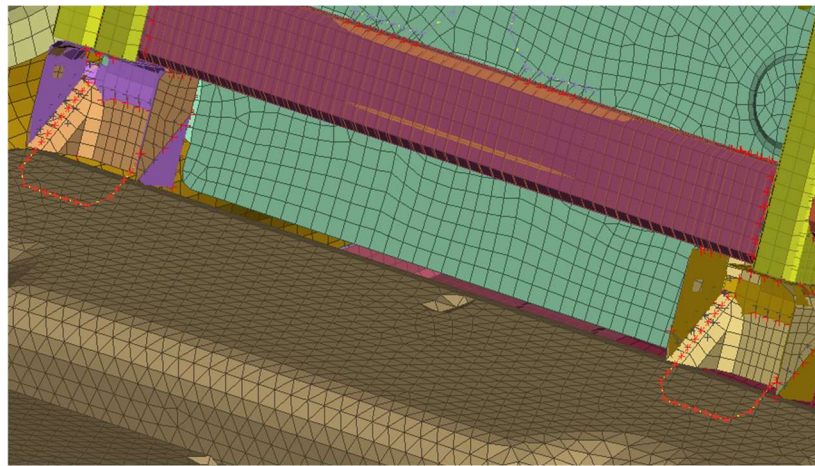
(a)
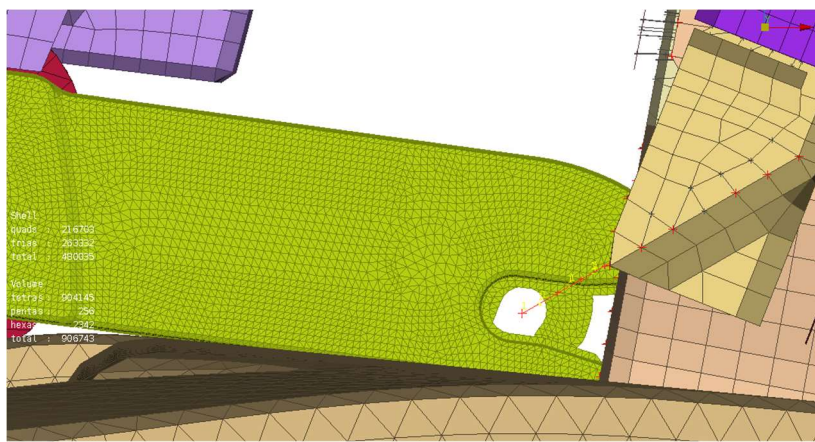
(b)

Figure 66 – FE ISOFIX anchors modeled with beam elements, in red (a) and centered booster clamps fixing hole

Figure 67 – Reference measurements defined to center the booster seat in the y-direction

Successively, the CAD of the backrest was used to correctly set the initial configuration of the CRS. In fact, Figure 68a shows the actual position of the CRS and the CAD model of the foam: a substantial penetration can be noticed, which indicates that the child seat needs to be extracted for obtaining a correct configuration for its use. Therefore, the "Move" interface was used to extract every entity of the booster seat, except for the clamps and their relative rails, to obtain the final configuration represented in Figure 68b.

(a)   (b)
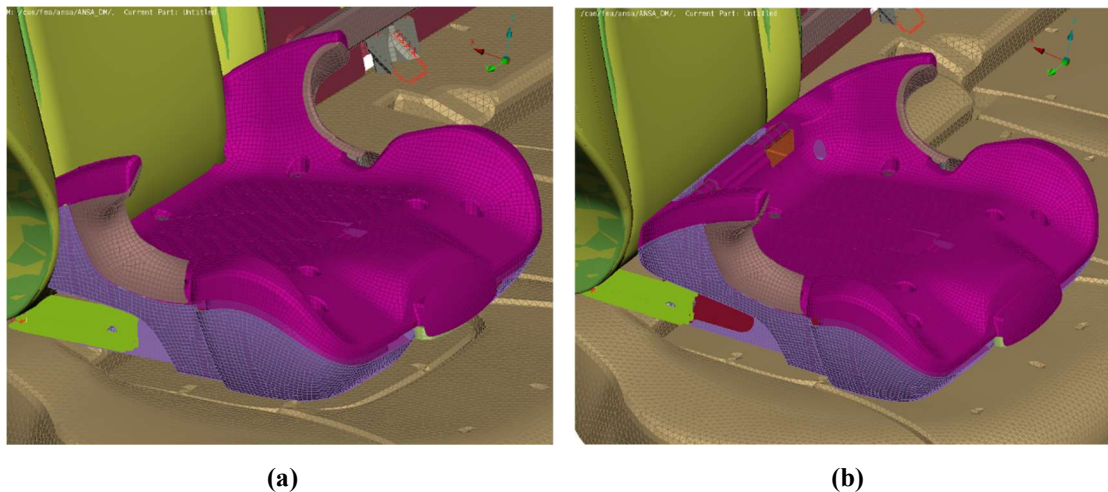
Figure 68 – Penetration of booster seat against the CAD of the vehicle backrest (a) and final configuration of the CRS (b)

From Figure 68b, the dark red rail of the clamps can be observed, since the seat was pulled out, reproducing its real setting. In the actual configuration, the booster does not touch the seat foam. The contact and predeformation of these two entities before the sled test FE reproduction will be achieved through a dummy seating simulation, which will be described in Section 7.3.

6.1.2 Finite Element reproduction of the ISOFIX anchorage

Once defined the CRS initial position, the ISOFIX anchorage needed to be modeled. Therefore, a revolute joint was defined between each booster clamp and the relative ISOFIX anchor of the vehicle body model. This construction was achieved using the LS-DYNA card *CONSTRAINED_JOINT_REVOLUTE, which needs the IDs of two pairs of nodes, belonging to two different rigid bodies, to define the joint rotation axis [94]. A drawing representing the definition of such a joint is reported in Figure 69.
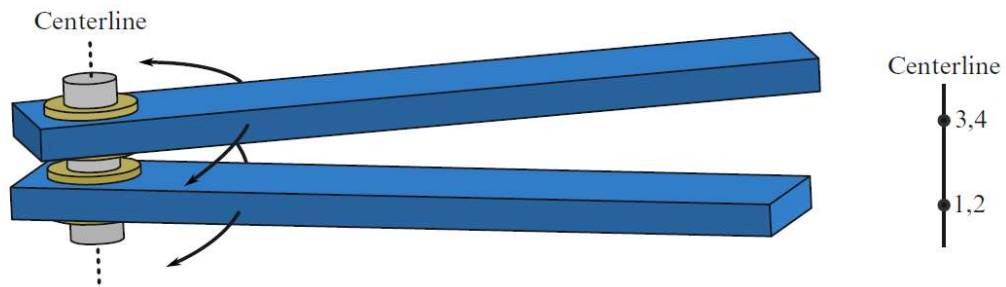
Figure 69 – LS-DYNA revolute joint scheme [94]

Nodes 1 and 2 and nodes 3 and 4 are coincident; nodes 1 and 3 belong to the first rigid body, whereas nodes 2 and 4 belong to the second one. Therefore, the relative motion of the two rigid bodies is restricted to rotations about the axis formed by these two pairs of coincident nodes.

In the booster seat FE model provided, the clamps are modeled as rigid bodies, thus two new nodes, coincident with two nodes of the beam elements modeling the ISOFIX anchors, were defined for each CRS clamp. Then, they were inserted in a *CONSTRAINED_EXTRA_NODES_SET card, to dictate their belonging to the respective rigid clamp. The other pairs of rigid nodes, instead, were defined with a *CONSTRAINED_NODAL_RIGID_BODY card collecting the coincident pair of nodes of the ISOFIX anchors. Thanks to this joint, the booster seat can rotate around the ISOFIX anchors, obtaining its downward motion that will cause the deformation of the foam due to the seating of the dummy model. At the same time, it will be fixed to the ISOFIX beam elements during the sled test simulation, avoiding its slipping from the vehicle seat. Modeling this interaction through a joint definition, rather than a contact card, surely leads to a more linear and realistic connection between the two entities.

6.2 Foam depenetration simulation

The position of both 2nd-row seat foam and suspension frame in the vehicle body were already set in their CAD models, thus the relative obtained FE models were not moved from their original coordinates. Therefore, once the initial configuration of the booster seat were set, the current FE assembly (vehicle body, foam, suspension frame, booster, and front passenger seat) was checked to detect initial penetrations.

Two different situations were noticed:

- A small portion of the CRS clamps penetrated the foam, near the ISOFIX anchors (Figure 70a);

- A considerable portion of the foam bottom area penetrated the vehicle body floor (Figure 70b). As the first situation, this condition was expected, since when a real foam is placed on the vehicle body, it surely deforms in the contact region.

(a)   (b)
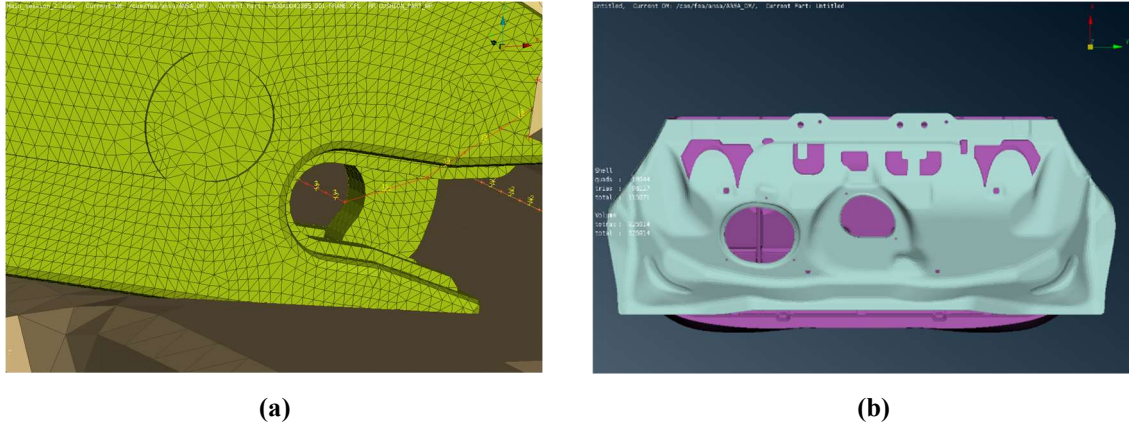
Figure 70 – Detected initial penetration of CRS clamps against the seat foam (a) and of foam the vehicle body (b, bottom view)

Therefore, since contact between these couples of models is fundamental for correctly seating the dummy and simulating the sled test, the first LS-DYNA simulation of this project regards the elimination of these initial penetrations and properly predeforming the seat foam.

6.2.1 Description of the input files

For running the predeforming LS-DYNA simulation, an Include structure was defined, and is shown schematically in Table 8.

FILENAME	FILE ROLE	INCLUDE OFFSET	INCLUDE TRANSFORMATION
MAIN.key	Master	0	
CRS_clamps.k	Include	10,000,000	TRANSL
Backseat_foam.k	Include	20,000,000	
Backseat_frame.k	Include	30,000,000	
Vehicle_body.k	Include	40,000,000	
Body_floor.k	Include	50,000,000	TRANSL
Connections.k	Include	0	
Contact.k	Include	0	
Control.k	Include	0	

Table 8 – Include structure of the foam predeforming simulation

The master file collects all the *INCLUDE and *INCLUDE_TRANSFORM cards, and two *DEFINE_TRANSFORMATION cards, needed to depenetrate both booster clamps and vehicle body floor. The former was translated by 4 mm in the negative *x*-direction and positive *z*-direction, whereas the latter was moved by 5 mm in negative *z*-direction, to eliminate all the initial penetrations. Moreover, the Table above underlines that all input files representing one of the bodies involved in the assembly was collected in the simulation using the option TRANSFORM, offsetting all entities IDs (nodes, elements, parts, sections, materials, and functions) using a gap of 10,000,000. This approach was used to avoid overlapped IDs during the launch of the simulation, which would lead to errors and incongruences of data. Lastly, three additional input files were generated, regarding connections card (*CONSTRAINED) in this case) between all entities, contact cards, and control (and database) cards.

The master file, visualized through ANSA, is shown in Figure 71.
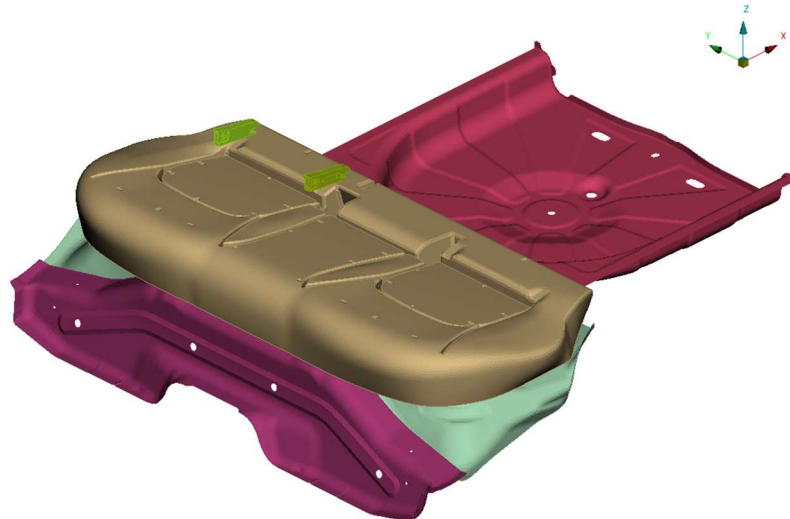
Figure 71 – Master file of foam depenetration simulation

Since the only parts of the booster seat to penetrate the foam after the positioning were its fixing clamps, this simulation was executed using only these components, so as to reduce the computational cost.

To avoid instabilities of the whole system and since its deformation and stress conditions are negligible during this run, the vehicle body was modeled as rigid in this simulation, using the material card *MAT_RIGID with the same properties of the original entity. The purple and pink bodies are collected in the include file ***Vehicle_body***, and are completely fixed in the space (CON1 = CON2 = 7) in the respective material card), whereas the light blue body (***Body_floor***) is not constrained in the *z*-direction since it has to move during the simulation.

Since the vehicle body is modeled as a rigid material in this simulation, the rigid connections to the foam suspension frame were substituted by *CONSTRAINED_EXTRA_NODES_SET, because a node can belong to only one rigid body when using LS-DYNA.

*CONTACT_AUTOMATIC_SURFACE_TO_SURFACE with SOFT = 2 (to improve contact forces stability) was used to regulate contact between the foam skin, the moving body floor and the moving booster clamps. The support of the suspension frame is needed in the simulation to avoid the downward displacement of the foam due to the motion of the CRS clamps.

The interaction between this body and the foam skin has been shown to be more difficult to define, due to the external diameter of the beam elements, that penetrates many areas of the foam skin, impeding the definition of a contact surface. Therefore, the tied contact algorithm *CONTACT_TIED_SHELL_EDGE_TO_SURFACE_BEAM_OFFSET was utilized to model the support provided by the frame. In this case, the BEAM option, which defines a penalty-based contact algorithm, was shown to be the more stable and suitable to realistically reproduce the interaction between the foam and the frame, whereas the OFFSET option was fundamental to preserve the original position of the nodes of the suspension frame.

In this card, the nodes of the frame are slave to the (master) skin of the foam. It is important to account that a selection of the only shell elements next to the frame was fundamental to obtain the desired behaviour and stability of such an algorithm. A sample portion of the model, with the evidenced contact entities, is reported in Figure 72.
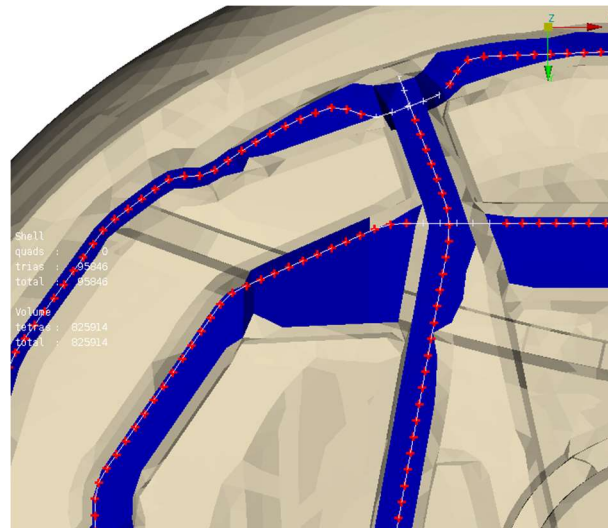
Figure 72 – Evidenced entities that define the contact between seat foam and suspension frame

Moreover, the optional card A with SOFT = 1, with SOFSCL = 0.1 and MAXPAR = 1.006 (as suggested by LSTC when using the BEAM_OFFSET option), was utilized. Every contact card is characterized by a viscous damping coefficient VDC equal to 20 percent. The *Control.k* include file contains *CONTROL_TERMINATION and *CONTROL_TIMESTEP cards, to set an explicit simulation with 23 ms of endtime with default value of TSSFAC, and *CONTROL_ENERGY to compute hourglass energy and sliding energy interface, required to verify the model.

*DATABASE_GLSTAT, MATSUM, RCFORC, SLEOUT, BINARY_D3PLOT, and EXTENT_BINARY cards were also inserted to obtain the desired output needed for verification of the results.

The motions of booster clamps and vehicle body were defined using the card *BOUNDARY_PRESCRIBED_MOTION_RIGID:

- During the first 10 ms of simulation, the CRS clamps move in the positive *x*-direction and in the negative *z*-direction of 4 mm, to return and stay in their original position, defined in the previous section.
- At *t* = 12 ms, the vehicle body floor starts to move in the positive *z*-direction, to return to its original position at the end of the simulation. To model this event, the BIRTH parameter of the *BOUNDARY card was used, to shift the beginning of the floor motion.

It was decided to obtain separated motions of the entities to minimize the kinetic energy of the system and to linearly deform the foam. Lastly, an *INTERFACE_SPRINGBACK_LSDYNA card was inserted in the input file, with a part set containing the solid foam part ID, to generate a new input file containing nodal coordinates, stress, and strain of all the elements of the cushion at the final instant of the simulation. Through this command, the first preloading condition of the foam can be obtained.

6.2.2 Discussion of the results

The energy balance of the simulation is reported in Figure 73.
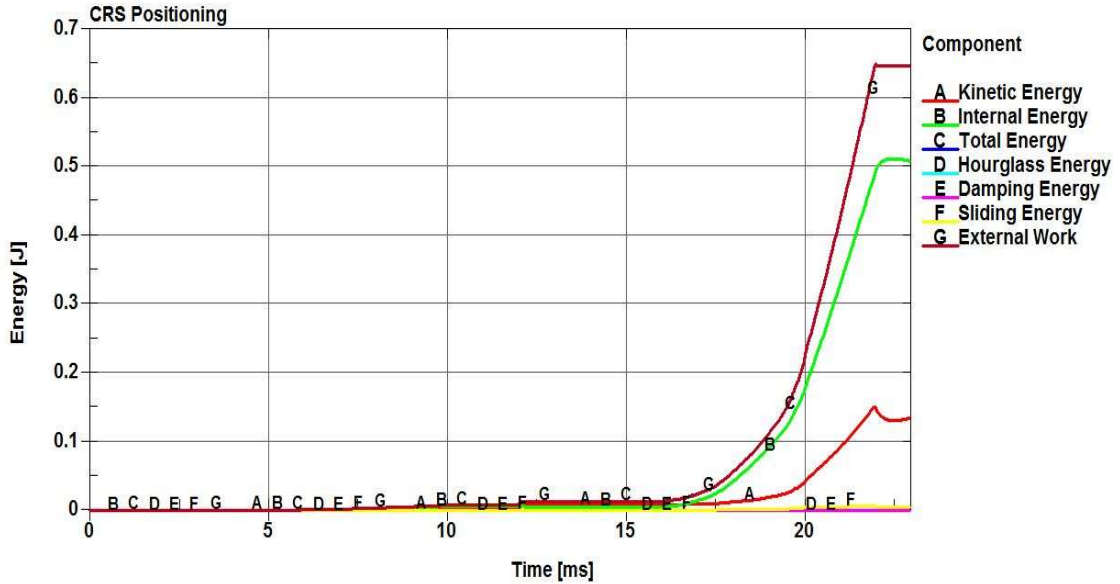
Figure 73 – Energy balance of the depenetration simulation

The first half of the simulation, where only the CRS clamps move, is characterized by very low energies with respect to the remaining part, where the vehicle body floor moves upward, increasing the kinetic energy of the system. The internal energy always constitutes the majority of the total energy of the system, defining an almost quasi-static simulation. Lastly, there is no hourglass energy, the sliding energy is always positive but very low (all friction coefficients are equal to 0 in this case), and the total energy curve coincides with that of the external work, both starting from 0, confirming the physical congruency of the simulation, represented by the following equation:

$$E_{kin} + E_{int} + E_{sli} + E_{rw} + E_{damp} + E_{hg} = E_{tot} = E_{kin}^0 + E_{int}^0 + W_{ext} \qquad (10)$$

The foam seat and the moving entities at the beginning and at the end of the simulation are shown in Figure 74.
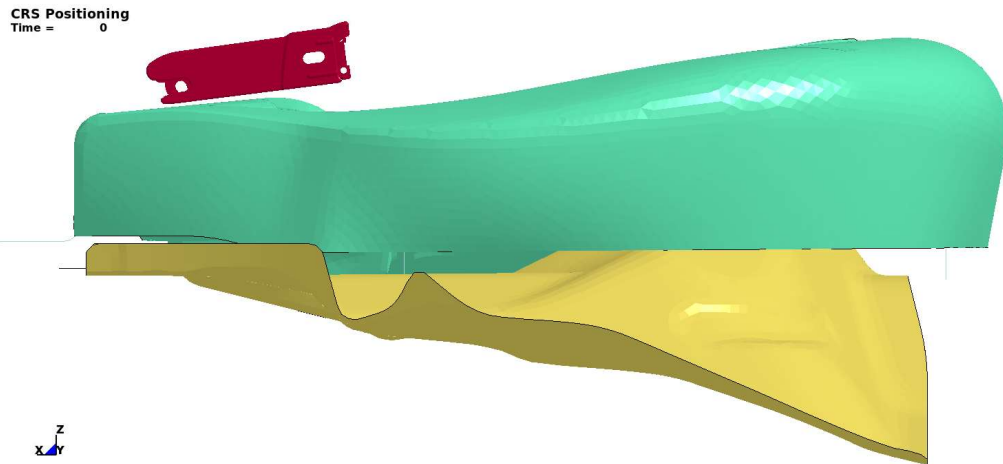
(a)
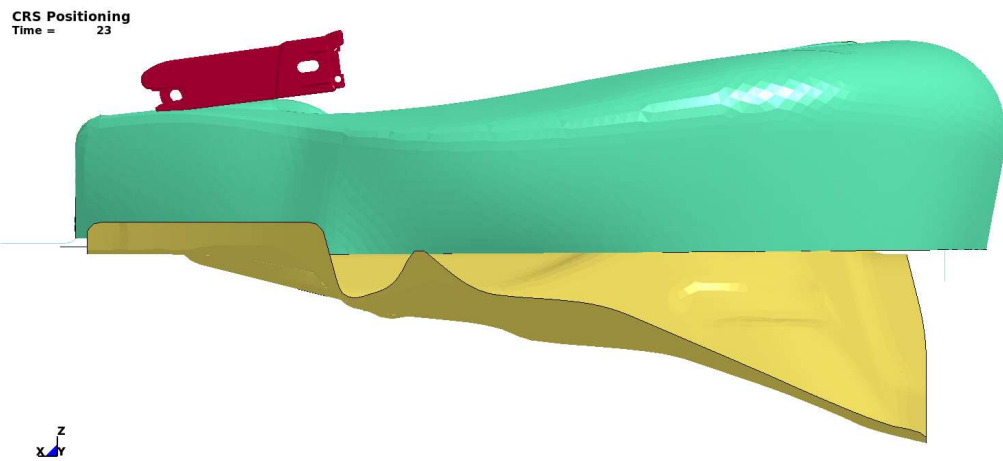
(b)

Figure 74 – Initial (a) and final (b) instants of the CSR clamps and body floor positioning

Figure 74 evidences the very small distances involved in the motions of the entities during this first simulation. Nodal coordinates, stress and strain conditions of the 2nd-row seat foam at the last instant of such simulation were used to update the model for the simulation of dummy seating, which will be described in the next section.

7. DUMMY POSITIONING

The Humanetics® Q10 virtual model was positioned in the vehicle FE environment in its initial configuration through three main steps:

1. Setting of its initial test position using the preprocessor (ANSA in this case);
2. Execution of an LS-DYNA presimulation, set by Humanetics®, to obtain the dummy nodal coordinates in the seating position;
3. Setting and running of an LS-DYNA simulation of dummy seating, to obtain booster, foam seat and suspension frame nodal coordinates and initial stress and strain at the starting instant of the sled test simulation.

The definition of the initial position of the dummy model and its integration in the vehicle cabin are crucial phases for crash test simulations using Finite Element Method, since they represent, along with the behavior of the FE restraint system, the greater influence to the final results, and the subsequent verification and validation of the overall model.

Therefore, this process is acutely described in this section, underlining every step considered necessary to obtain a reasonable initial configuration of dummy, booster seat, and cushion foam.

7.1 Definition of the Q10 initial position through the preprocessor

The Q10 FE model is initially positioned in the FE space with the H-point coordinates equal to (0,0,0), the pelvic angle at 0° and the dummy thorax spine box in vertical position. The software ANSA provides a dedicated interface for positioning an FE dummy model, called "Dummy articulation", which automatically detect the dummy H-point and all its joints, to improve the precision of its positioning and to simplify the setting (rotation and translation) of all dummy joints.

It is important to clarify that the experimental coordinates of the H-point were not available in this case since in the Euro NCAP procedure such coordinates are registered only for the adult dummies placed in the front seats. This lack of data made this process more difficult and less precise, since the only references to obtain the initial dummy position were:

- The Euro NCAP standardized measurements between different points of the dummy and of the vehicle cabin, collected in the report of the experimental sled test;

- Two lateral photos of the physical dummy placed in the vehicle cabin, before performing the test.

Moreover, the standard Euro NCAP dummy positioning procedure, described in Section 2.8.3.3, was reproduced in the FE environment, to ensure a suitable level of precision.

7.1.1 Setting of the Euro NCAP measurements in the FE assembly

First of all, the dummy H-point y and x coordinates were aligned with those of the center of the booster seat, already positioned and centered with vehicle foam and ISOFIX anchors. Afterward, three measurements from the experimental test report were virtually reproduced and stored in the virtual space, so that to be updated at every variation of position of the Q10:

1. Distance, along the z-axis, between the top of the dummy head and the closest point of the cabin roof;
2. Resultant distance between the front of the dummy head and the closest point of the front passenger seat backrest;
3. Internal y-distance between the dummy knee joints.

The experimental values of such measurements are collected in Table 9.

Measurement	Value [mm]
Head-to-roof	253
Head-to-front-seat	676
Knee-to-knee	130

Table 9 – Reference measurements from the experimental test

The correspondent virtual measurements are shown in Figure 75.
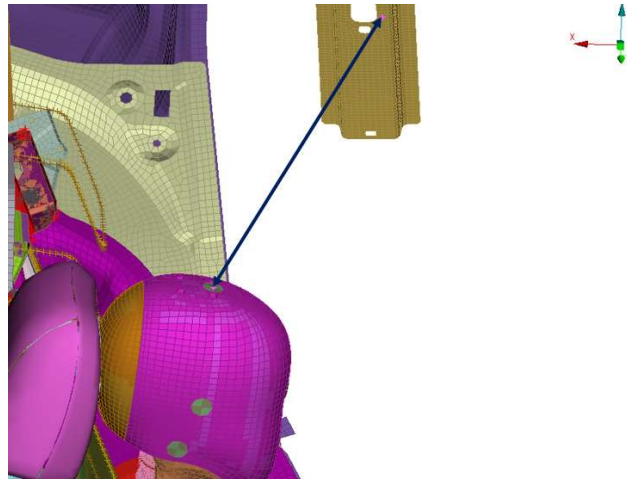
(a)
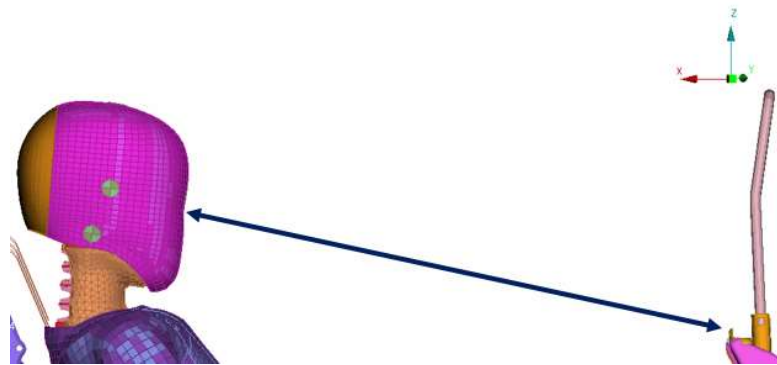
(b)
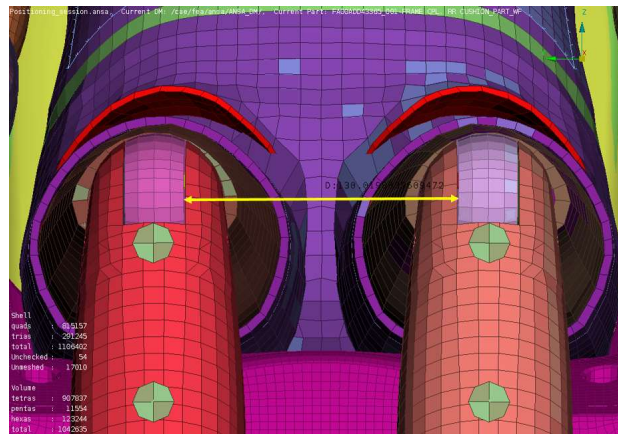
(c)

Figure 75 – Head-to-roof (a), head-to-front-seat (b) and knee-to-knee distances

Although the resultant head-to-roof distance is displayed in Figure 75a above, only its *z*-component was considered.

7.1.2 Virtual reproduction of the Euro NCAP dummy positioning

After the definition of the virtual measurements, the main steps of the Euro NCAP dummy positioning were reproduced in the FE vehicle cabin. The CAD of seatback was shown to be fundamental to reproduce such procedure:

- The dummy model was already aligned with the center of the respective CRS;
- The dummy torso was pushed toward the seatback until its back is in contact with the seatback itself. The penetration of the dummy head against the CAD of the head restraint was not considered since it is not in the same configuration as in the experimental test;
- The femurs were positioned straight forward, considering the gap between the knees described in the previous chapter;
- The lower legs were positioned in the natural rest position, the tibias are parallel to the vehicle centerline and they touch the seat foam;
- The upper arms were positioned parallel to the chest and the lower arms were positioned in a natural rest position, leaning on the booster armrests.

In addition, from the lateral photo captured during the experimental test, before the impact simulation, two important angles were measured, shown in Figure 76.

Figure 76 – Additional angle used for positioning the Q10

Their respective values are:

- $\alpha = 7°$;
- $\beta = 28.5°$.

Therefore, the head and pelvis rotations about the *y*-axis were modified, to obtain these configurations. Lastly, the dummy position was adjusted so that to fulfill both Euro NCAP measurements and positioning constraints, defining the initial position of the virtual dummy model. The final pretest configuration of the FE dummy is shown in Figure 87.
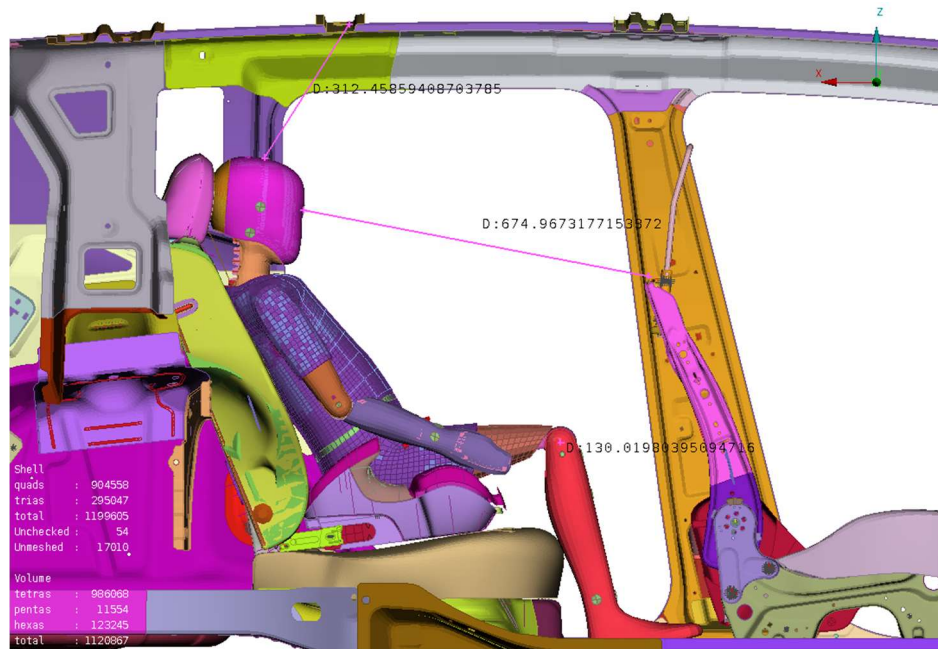
(a)

(b)

(c)

Figure 77 – Lateral (a), top (b) and front (c) view of the positioned Q10 dummy model

Before describing the next steps of dummy positioning, some considerations about its placement through the preprocessor must be made:

1. The absence of the H-point avoids reaching a very high level of correlation between dummy experimental and numerical initial position;

2. The booster seat is not realistically placed; in fact, it does not touch the seat foam and a presimulation is needed to obtain its initial configuration. Fortunately, this inaccuracy influences mostly the positioning of the dummy arms, which are not an important subject in this kind of study, since they represent the end of the child injury pattern, as described in Section 2.6.1;

3. Additional details about the points chosen to measure the Euro NCAP reference distances should be collected. The position of the front passenger seat reference point, for example, is not reported in the experimental test report. As a matter of fact, the respective virtual measurement (Figure 87a) does not perfectly coincide with the value reported in Table 9: a discrepancy of less than 2 mm was accepted, giving more weight and importance to the other measurements and constraints.

4. The measurements of standardized angles on the positioned experimental dummy would surely improve the precision of the virtual positioning. In this case, where the subject is a child and not an adult driver, the pelvis and neck angles are surely the most important, and the legs and arms angles can be neglected. To determine these angles from the photos of the real test could be a good method of estimation, but it will never be as accurate as experimental measures.

7.2 Dummy positioning presimulation

The Humanetics® dummy FE model is composed of many joints (neck, head, and torso) defined only to allow its positioning through a preprocessing software, but not suitable for an LS-DYNA simulation. In fact, when the dummy joints are rotated to obtain its desired position, many penetrations can be detected, mostly in the torso joint, as shown in Figure 78 and noticeable in Figure 77b and 77c.
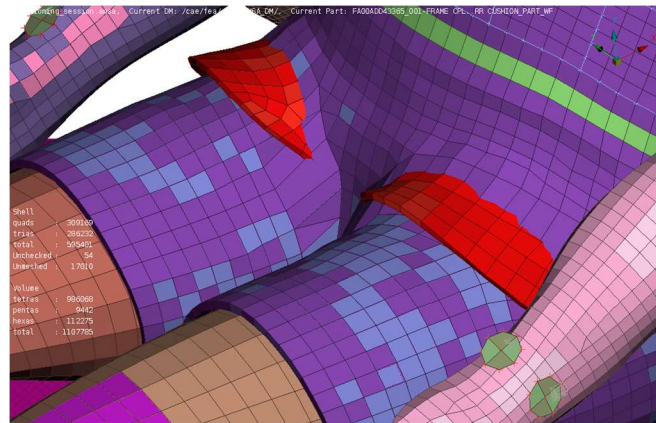
Figure 78 – Initial penetrations due to the rotation of the Q10 torso joint

Therefore, when the relative input file is updated and saved using ANSA, the model is not yet positioned in the vehicle FE environment, and a presimulation file is generated, containing the coordinates that selected reference points of the dummy have to reach to obtain its initial seated position. Consequently, such file needs to be properly tuned and launched using LS-DYNA, to obtain the input file of the Q10 model in its initial configuration, without undesired initial penetrations between the different joints.

7.2.1 Description and tuning of the presimulation input file

The input file needed to run the dummy positioning presimulation is the master file of an include structure, composing the whole dummy model. It contains the coordinates of different reference points placed on all joints and body parts of the dummy. Every point is the first extremity of a discrete element; the other extremity, instead, is connected to a node placed in the final position that every reference point has to meet to obtain the desired dummy setting. These coordinates were saved from the preprocessor when the Q10 model master file was saved using the ANSA "Output" interface, once the positioning phase described in the previous section was completed. The Q10 model in its presimulation setting is shown in Figure 79.
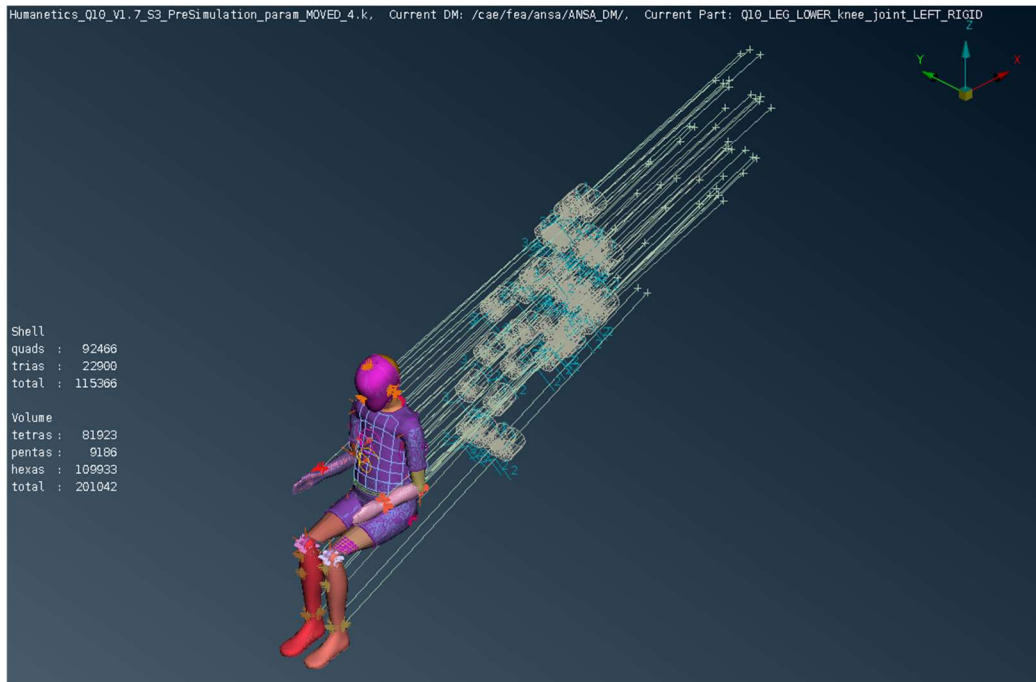
Figure 79 – Humanetics® Q10 presimulation file visualized through ANSA

Therefore, the model is connected to many discrete elements; in this case, called "positioning cables", that will drag it towards its initial seated configuration during the presimulation. The material properties of both the dummy model and the discrete elements can not be described since they are collected in an encrypted input file for confidentiality reasons.

Humametics® suggests the tuning of the cable characteristics and the simulation running interval to ensure the achievement of the desired dummy position in a reasonable computational time [95]. Hence, two *PARAMETER values were modified in the input file:

- Fcable - the magnitude of the force that drags the positioning cables;
- Tsim - the simulation end time.

In this case, Fcable was set equal to its maximum suggested value and the simulation end time in the *CONTROL_TERMINATION card was increased to 900 ms, due to the great distance between the dummy original position and its seated configuration. To find the proper values of these parameters, the launch of some presimulations was necessary, to quantify the time needed by the model to reach its final configuration.

Lastly, the presimulation input file includes a *DATABASE_BINARY_D3PLOT card to verify the displacement of the entire model and to allow the extrapolation of the new dummy nodal coordinates.

7.2.2 Presimulation launch and extrapolation of the dummy nodal coordinates

Once the dummy positioning parameters were defined, the presimulation file was ready to be launched. The displacement of the dummy model during the simulation is reported in Figure 80.

(a)
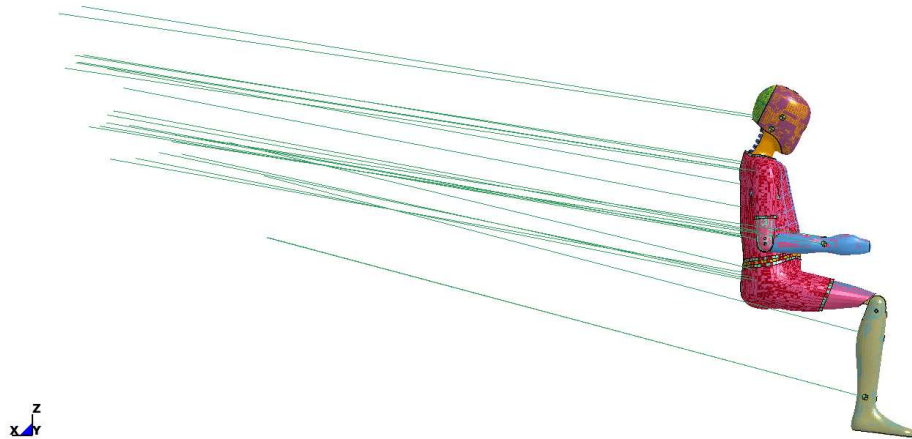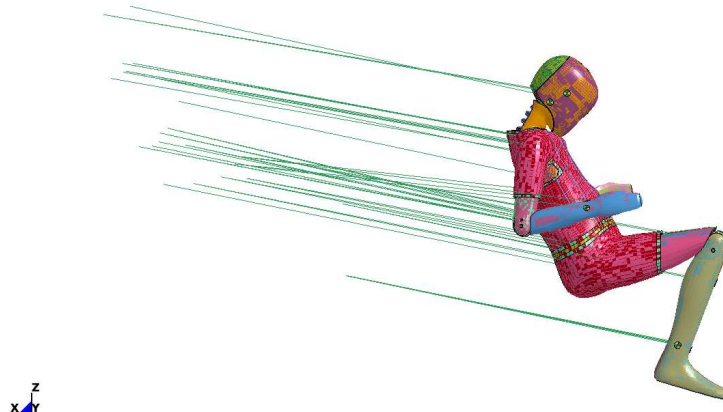
(b)

HUMANETICS Q10 CHILD DUMMY MODEL VERSION 1.7 S3 (MM, MS, KG)
Time =   750
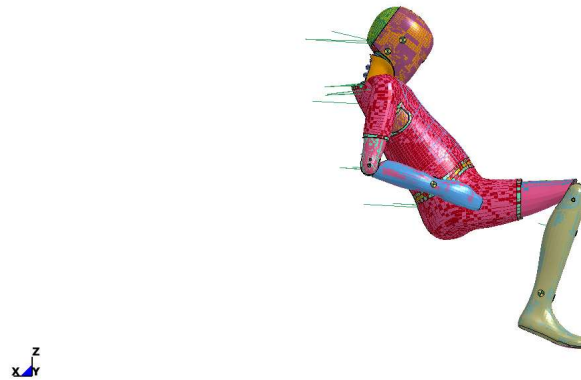
(c)

HUMANETICS Q10 CHILD DUMMY MODEL VERSION 1.7 S3 (MM, MS, KG)
Time =   900

(d)

Figure 80 – Displacement of the Q10 model at 0 (a), 400 (b), 750 (c) and 900 ms (d) of simulation time

The simulation terminates with the length of all discrete elements equal to 0, thus with the dummy model positioned in its seated configuration. Therefore, the nodal coordinates registered at the last instant of simulation were saved replaced in the original dummy model input file. The next chapter will describe the integration of the seated Q10 model in the FE vehicle body.

7.3 Dummy seating simulation

After obtaining the seated FE dummy model, a seating simulation was launched to obtain preloaded conditions of foam, booster seat and suspension frame, due to the weight of the dummy when placed on the respective CRS.

The simulation was defined in displacement control, extrapolating a rigid dummy from the Q10 model and defining its displacement so that to reach its initial position in the FE environment, reproducing a quasi-static seating event.

7.3.1 Description of the input files

The Include structure described in Section 6.2.1 was utilized as a baseline for composing the master seating simulation input file. The update Include structure is defined in Table 10.

FILENAME	FILE ROLE	INCLUDE OFFSET	INCLUDE TRANSFORMATION
MAIN.key	Master	0	
Booster_seat.k	Include	10,000,000	
Backseat_foam.k	Include	20,000,000	
Backseat_frame.k	Include	30,000,000	
Vehicle_body.k	Include	40,000,000	
Isofix.k	Include	50,000,000	
Dummy_rigid.k	Include	0	TRANSL
Springback_seating.k	Include	0	
Connections.k	Include	0	
Contact.k	Include	0	
Control.k	Include	0	

Table 10 – Include structure of the dummy seating LS-DYNA simulation

The positioned entire booster seat was included in the simulation, without facing any penetration against the foam, thanks to the previous simulation of foam preloading and to the subsequent update of the foam input file with new nodal coordinates and initial stresses and strains (collected in *Sprinback_seating.k*). Therefore, the input file *Vehicle_body* is composed of the three rigid bodies of the previous run, completely constrained (CON1 = CON2 = 7) and placed without any initial transformation.

The completely new input files needed in this simulation are:

- *Isofix* – the ISOFIX anchors, modeled as beam elements and connected to the booster using the revolute joint described in Section 6.1. It was extrapolated from the full

vehicle body model, to reduce the computation time. In addition, all nodes of the ISOFIX anchors were completely constrained using *BOUNDARY_SPC_NODE;

- ***Dummy_rigid*** – an input file composed by only the shell elements of the skin of the Q10 dummy model, with an assigned *MAT_RIGID free only in the *z*-direction, with material properties of steel to correctly compute the contact forces (as suggested by LSTC [94]). Moreover, all parts are constrained using *CONSTRAINED_RIGID_BODIES.

The extrapolation of the rigid dummy has many advantages: its displacement can be controlled without any deformation and its computational weight is very low, being composed of only rigid shells. The contact cards described for the first simulation were used again to regulate contact between foam, suspension frame, and vehicle body.

*CONTACT_AUTOMATIC_SURFACE_TO_SURFACE was used to model contact between foam seat, booster, and rigid dummy. In particular, the booster FE model was already provided with a *CONTACT_SINGLE_SURFACE card containing a set of all parts in contact in the CRS. Therefore, the same set was used to model contact with external entities. The values of VDC and of the optional card A described in Section 6.2.1 were again utilized. The rigid dummy needed an initial translation, obtained using *INCLUDE_TRANSFORM, to eliminate any initial penetration with the booster seat. Hence, it was translated in the positive *z*-direction of 30 mm. This distance will be retraced again during the whole simulation, in 600 ms, to preload and deform both booster and seat foam, using the command *BOUNDARY_PRESCRIBED_MOTION_RIGID in displacement control. The *DATABASE cards were not changed from the previous simulation. The simulation end time is equal to 700 ms so that to stabilize energies and contact forces with 100 ms of static condition after the motion of the rigid dummy. The dummy seating simulation master input file is shown in Figure 81.

| (a) | (b) |
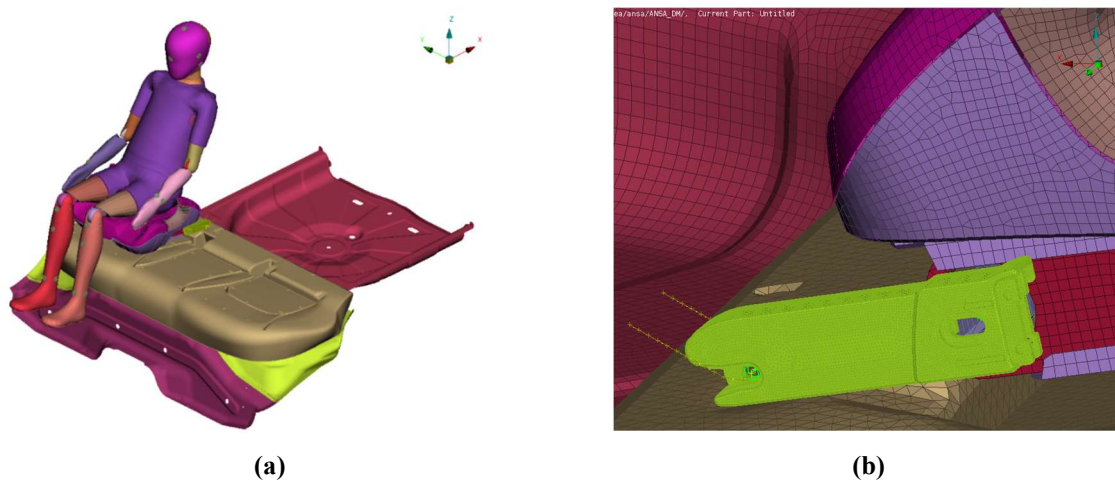
Figure 81 – Isometric view (a) of the LS-DYNA dummy seating simulation setting and detail of the extrapolated ISOFIX anchorage and the respective revolute joint (b)

7.3.2 Discussion of the results

Firstly, the energy balance of the simulation was verified, checking its congruency with Equation 10. It is reported in Figure 82.
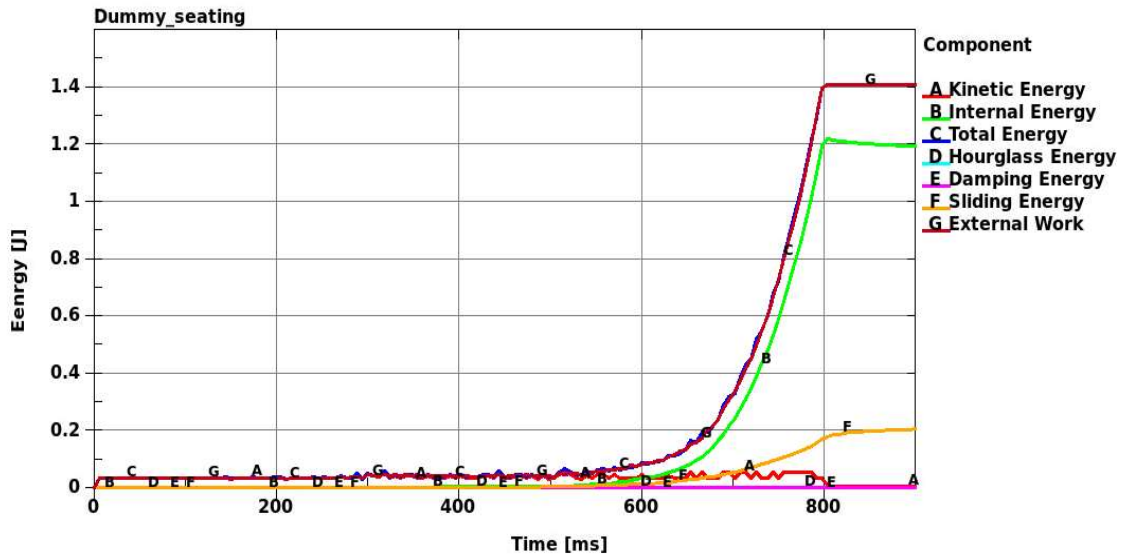
Figure 82 – Energy balance of the dummy seating LS-DYNA simulation

The initial energy of the system is equal to zero, and total energy and external work curves coincide over the whole duration of the event. Therefore, Equation 10 is again verified, confirming the consistency of the balance above.

The system at three instants of the simulation is visualized in Figure 83.

(a)

(b)

(c)
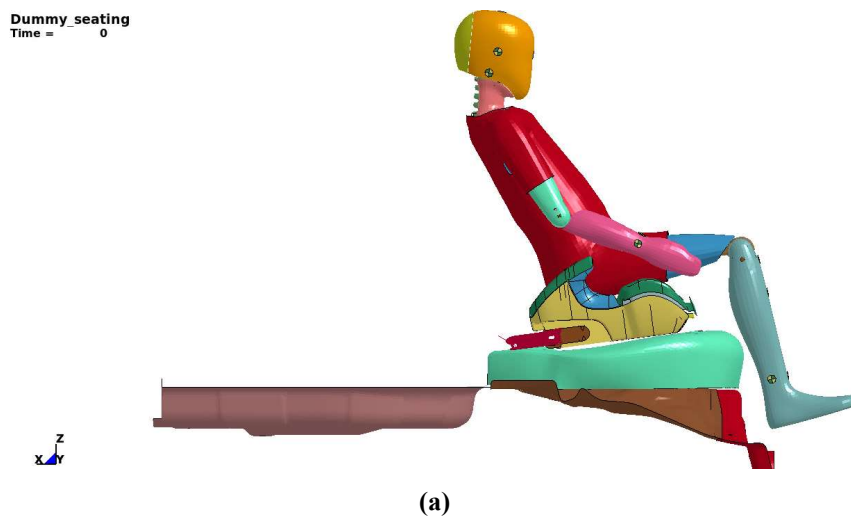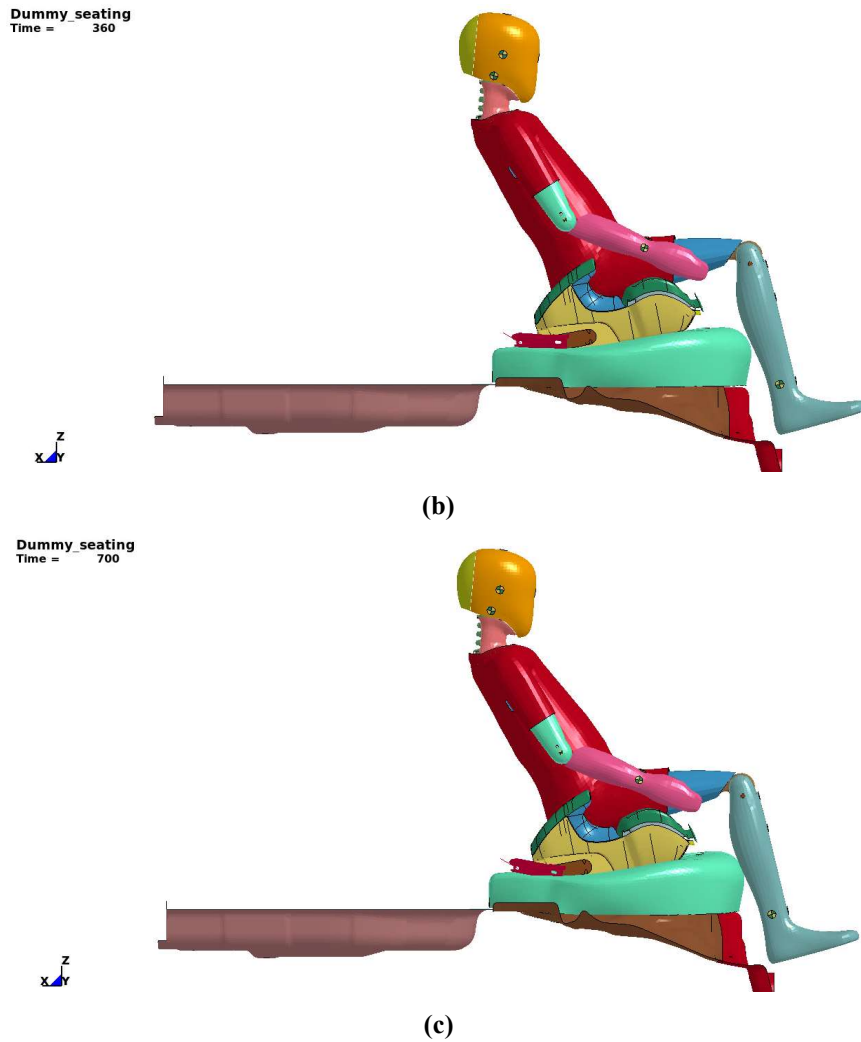
Figure 83 – Dummy seating simulation system at 0 (a), 360 (b) and 700 ms (c)

From the Figure above, the rotation of the booster seat clamps around the ISOFIX anchors can be noticed, and the consequent flattening of the foam seat is visualized.

The most important contribution of this simulation to the sled test simulation is the definition of the initial condition (preloading) of the booster seat, foam and suspension frame. Therefore, the loading forces acting on each element of the system at the end of the simulation were verified and compared to the expected ones. The latter is based on the mass (and consequent weight) of each FE component, which is reported in Table 11.

Component	Mass m	Weight ($m \cdot g$)
Dummy	35.93 kg	0.352 kN
Booster seat	2.35 kg	0.023 kN

Table 11 – Mass and weight of each component needed to preload the system

Consequently, all contact forces in the z-direction were analyzed through the output of *DATABASE_RCFORC, estimating to measure the following loads:

- The weight of the dummy w_{DUMMY} on the booster seat;
- The weight of dummy w_{DUMMY} and booster seat w_{CRS} distributed across the seat foam and ISOFIX anchors (as reaction load monitored through *DATABASE_SPCFORC);
- The weight of the dummy and booster seat (minus the load absorbed by the ISOFIX anchors r_{ISOFIX}) divided among foam suspension frame and vehicle body floor contact forces against the foam, to balance the system and consequently define a static condition.

A schematic of this load balance is shown in Figure 84.
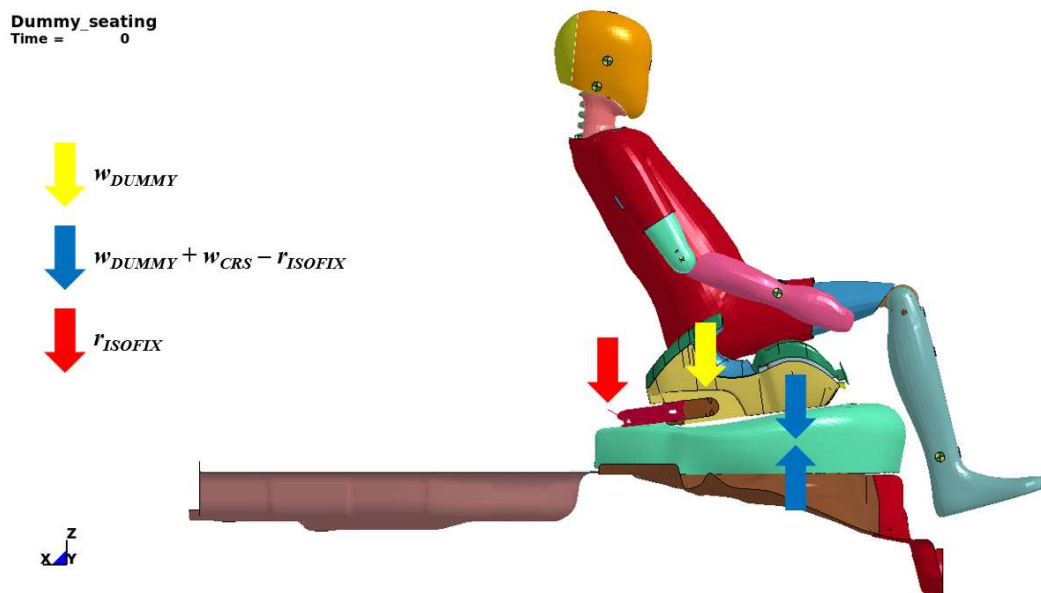
Figure 84 – Preloading of the dummy seating simulation

Therefore, the vertical load imposed by the rigid dummy during the simulation on the booster seat is visualized in Figure 85.
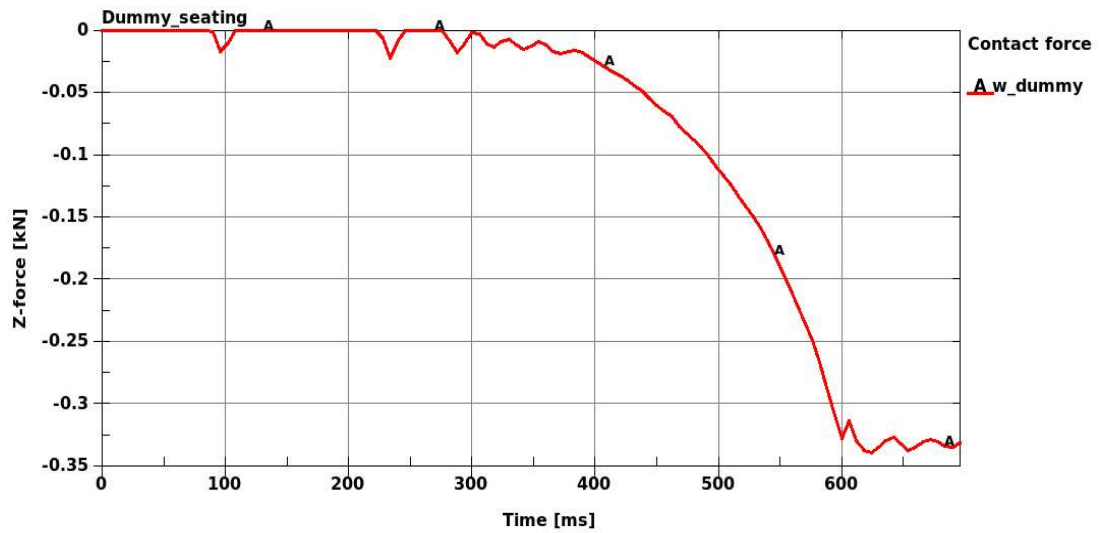
Figure 85 – Vertical contact force imposed by the rigid dummy on the CRS

At the end of the simulation, this load is equal to 0.335 kN. Subsequently, it is possible to compute the relative error between the expected and the numerical load:

$$\left|\frac{w_{DUMMY_{NUMERICAL}} - w_{DUMMY_{EXPECTED}}}{w_{DUMMY_{EXPECTED}}}\right| = \left|\frac{0.335 \, kN - 0.352 \, kN}{0.352 \, kN}\right| = 4.83 \, \% \qquad (11)$$

The relative error is lower than 10%, therefore the numerical value can be accepted. Furthermore, the vertical load on the foam seat imposed by the CRS is reported in Figure 86.
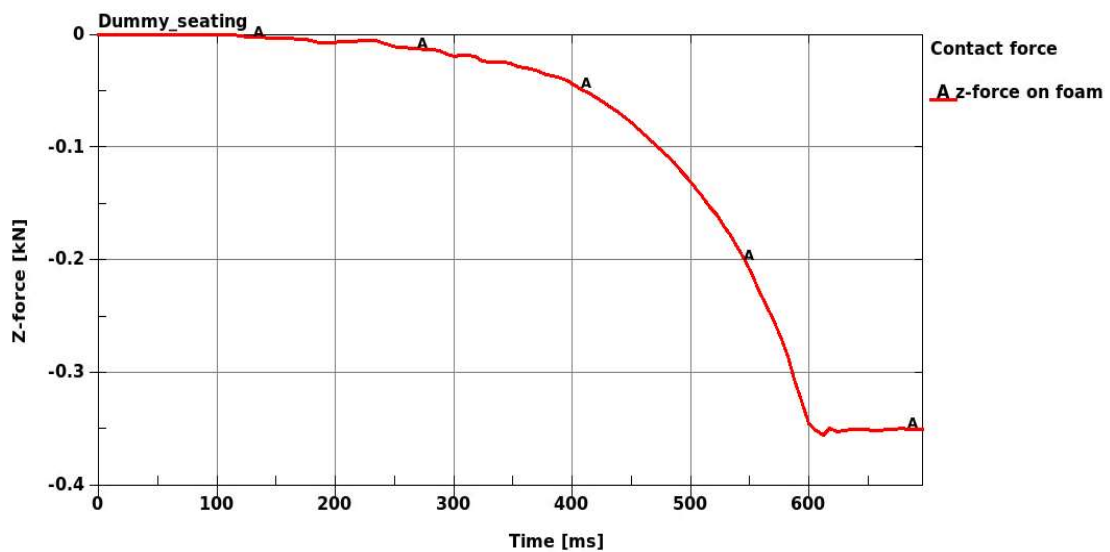
Figure 86 – Vertical contact force imposed by the CRS on the seat foam

At the end of the simulation, such load is equal to 0.351 kN. As mentioned before, a part of the weight of the dummy and booster seat is also absorbed by the constrained ISOFIX anchors, which oppose the clockwise rotation of the CRS clamps through a downward vertical reaction force r_{ISOFIX}, shown in Figure 87.
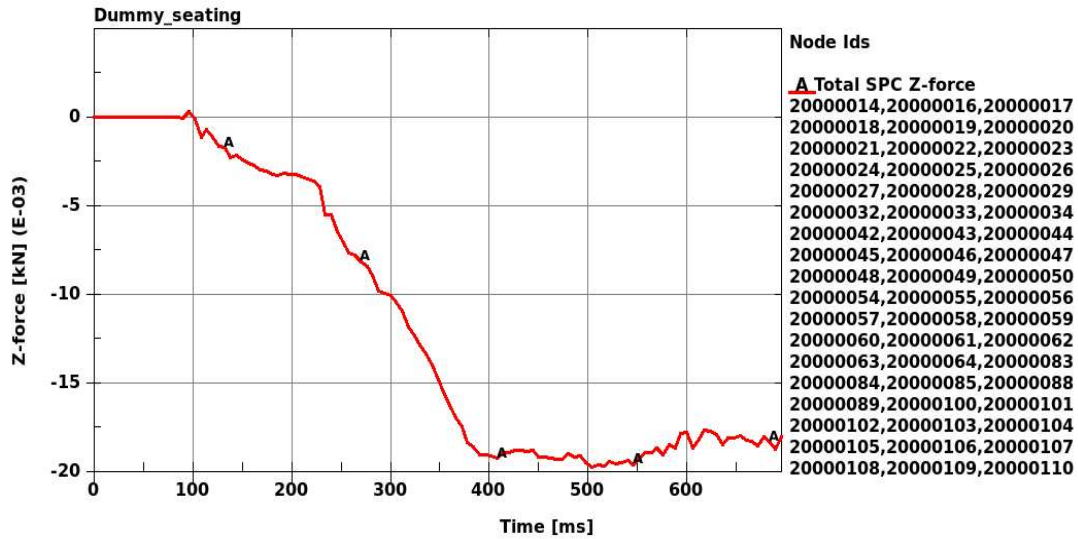
Figure 87 – Vertical reaction load of the constraints (*BOUNDARY_SPC) of the ISOFIX anchors

On the right, all the IDs of the constrained ISOFIX anchors nodes are visualized. At the last instant of simulation, the vertical reaction r_{ISOFIX} is equal to 0.018 kN. Summing such value to the load registered in Figure 96, the numerical estimation of the weights of dummy and booster seat can be computed, equal to 0.369 kN. The relative error with respect to the expected value is then equal to:

$$\left| \frac{(w_{DUMMY} + w_{CRS})_{NUMERICAL} - (w_{DUMMY} + w_{CRS})_{EXPECTED}}{(w_{DUMMY} + w_{CRS})_{EXPECTED}} \right| = \frac{0.369\ kN - 0.375\ kN}{0.375\ kN} = 1.6\ \% \quad (12)$$

Again, this value is lower than 10% and designates an acceptable preloading of the foam seat. Lastly, a balance of the vertical load on the foam was expected from the vehicle body floor and the suspension frame. Figure 88 shows the vertical load imposed by the booster seat on the foam (the same of Figure 86) compared to the sum of contact vertical forces distributed underneath the foam, among suspension frame and vehicle body.
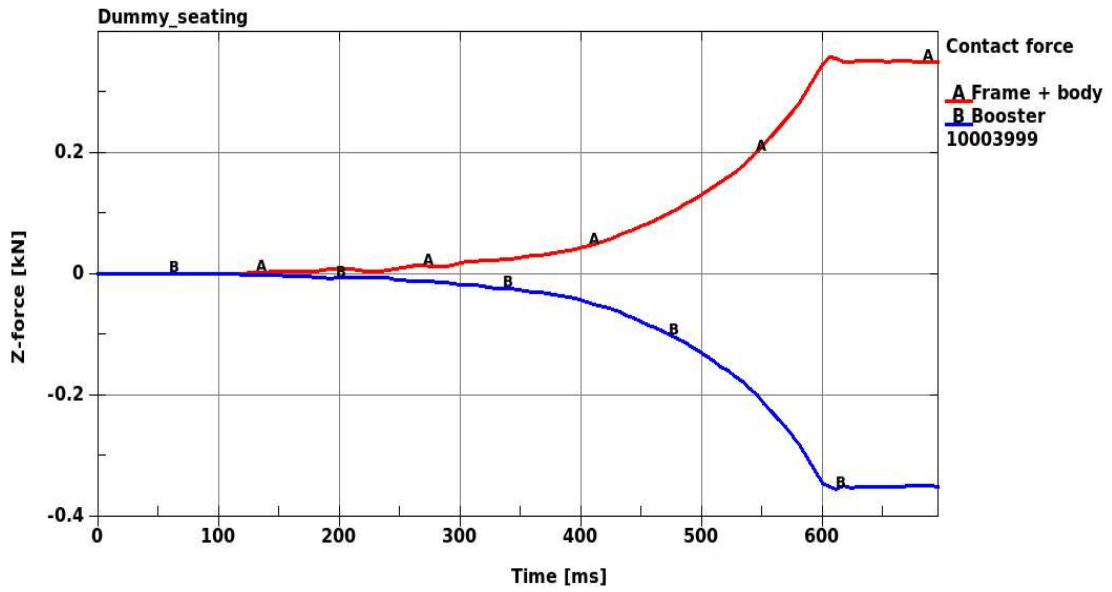
Figure 88 – Vertical contact forces of CRS (blue) and suspension frame and vehicle body (red) against the foam

The two curves are mirrored, and they report equal absolute values of contact force at the end of the simulation (0.351 kN), demonstrating the static balance of the system.

Contours of stress on both the booster seat and the foam seat, at the last instant of simulation, are visualized in Figure 89 and 90.

(a)

(b)
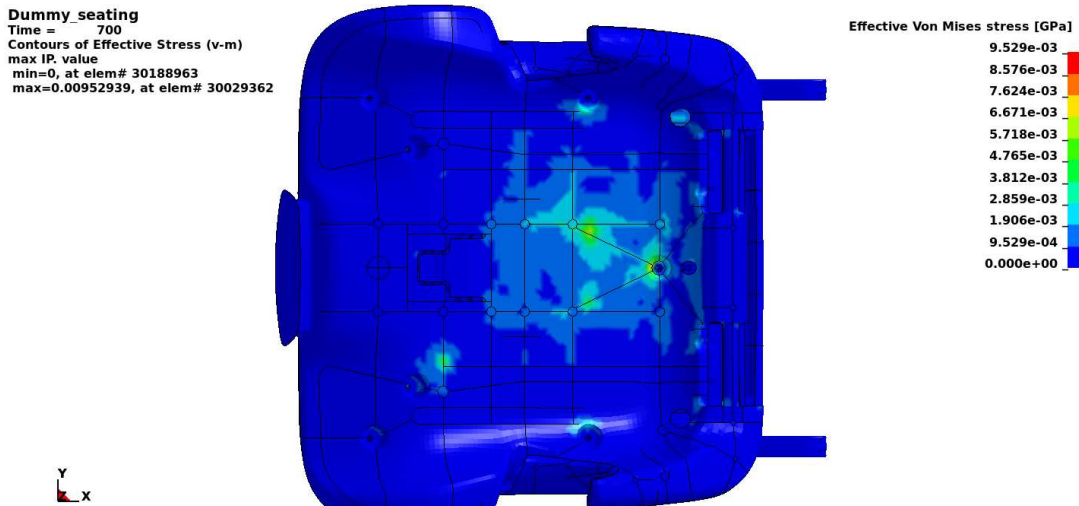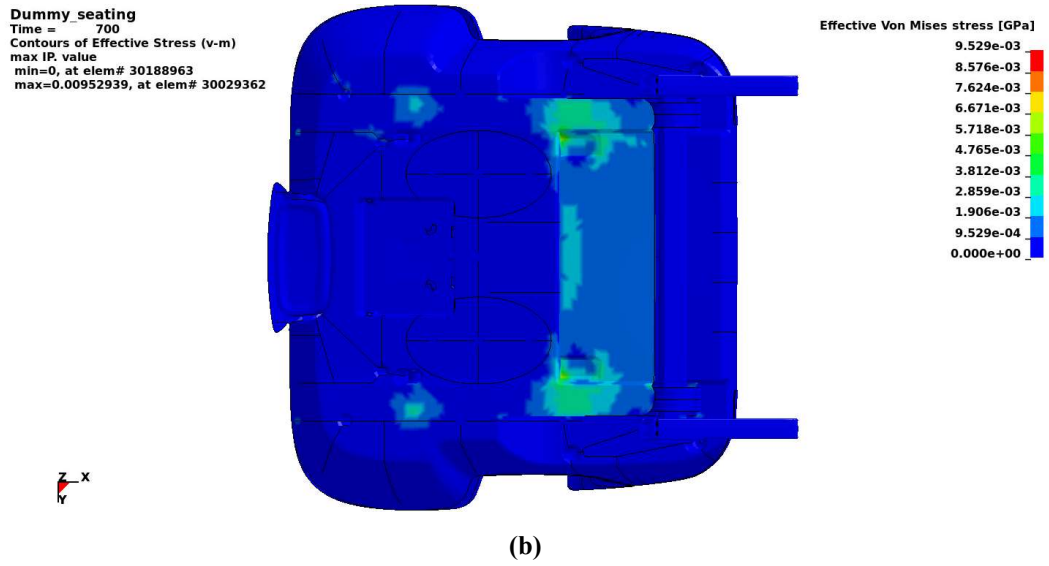
Figure 89 – Top (a) and bottom (b) view of contours of stress on the booster seat at 700 ms of simulation

(a)

Dummy_seating
Time = 700
Contours of Effective Stress (v-m)
max IP. value
 min=1.75529e-09, at elem# 40184805
 max=8.74069e-05, at elem# 40727337

Effective Von Mises stress [GPa]

8.741e-05
7.867e-05
6.993e-05
6.119e-05
5.244e-05
4.370e-05
3.496e-05
2.622e-05
1.748e-05
8.742e-06
1.755e-09
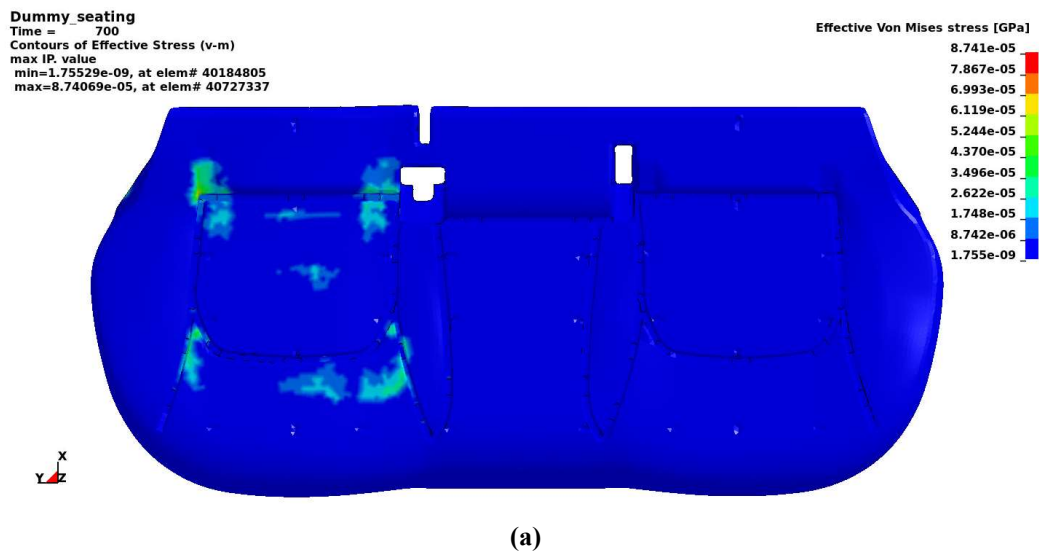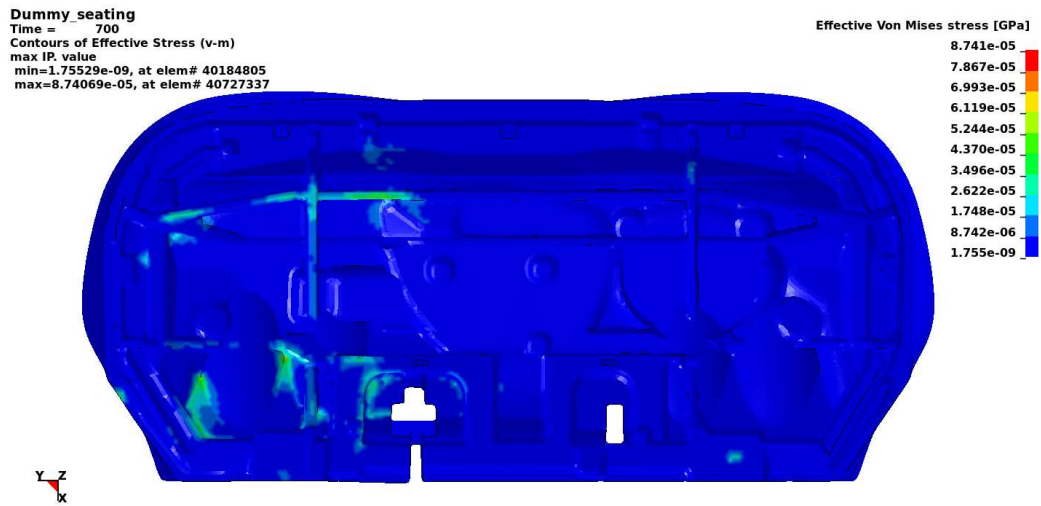
(b)

Figure 90 – Top (a) and bottom (b) view of contours of stress on the seat foam at 700 ms of simulation

Figure 90 evidences the loading of the seat foam in the only seating zone of the Q10 (top view) and the consequent support of both suspension frame and vehicle body in the bottom area.

To conclude, nodal coordinates and initial stress and strain of CRS, seat foam and suspension frame were collected in a new input file generated using the command *INTERFACE_SPRINGBACK_LSDYNA and utilized to update the three entities for defining their initial conditions in the sled test simulation.

8. GENERATION OF THE VIRTUAL RESTRAINT SYSTEM

The new assembly of FE models with updated foam seat, booster, and Q10 dummy was used to build the virtual seat belt needed to correctly constrain the dummy during the sled test simulation. A Finite Element seat belt generation can be divided into three main steps:

1. Belt routing – the definition of the path of the belt webbing along the body of the occupant and of the anchorage points;
2. Generation and constraining of the webbing mesh;
3. Implementation of the FE safety belt devices (retractor and pretensioner).

This process was completed using the ANSA "SeatBelt" interface, which assists the user during the generation of this entity. The definition of a suitable seatbelt LS-DYNA model, in fact, needs precise arrangements:

- The mesh of the belt webbing shall be as regular as possible, with elements of congruent and suitable dimensions with respect to the other FE entities;
- A precise belt routing, as close as possible to the experimental setting, is fundamental to obtain a satisfactory correlation between numerical and experimental conditions;
- For obtaining the correct functioning of the slip rings during the simulation, the exact order of nodes and element numbering must be accomplished in the model [94].

8.1 Belt routing

The CAD model of the restraint system, included in the virtual assembly, allowed to identify the position of retractor, slip rings and anchorage point with respect to the vehicle body. Such entities are shown in Figure 91.

(a)

(b)

(c)
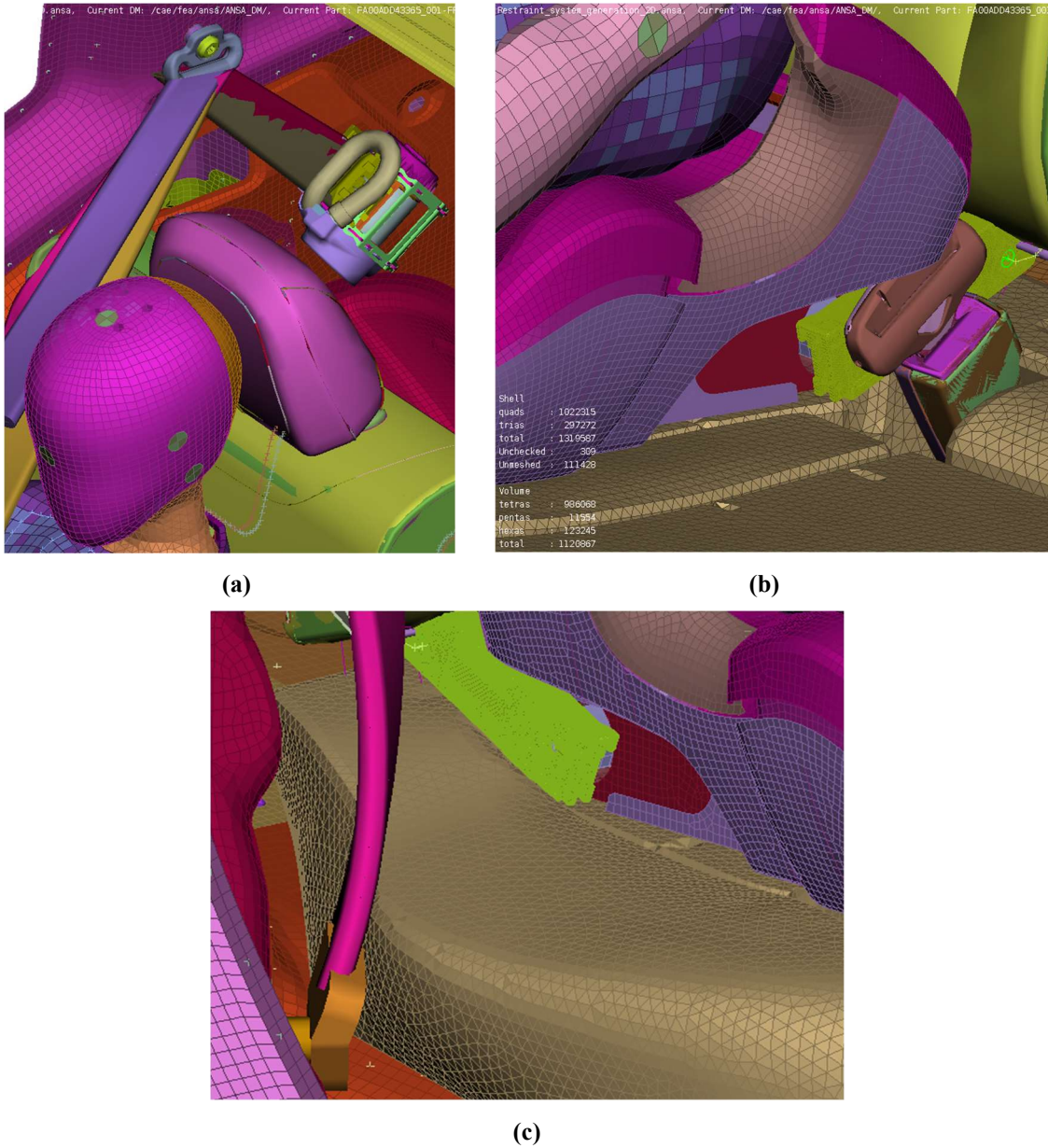
Figure 91 – Location of retractor and upper slip ring (a), locking tongue (b) and anchorage point (c)

Therefore, the FE belt webbing will be composed of three main entities:

1. Retractor belt – the first belt section, which connects the retractor to the upper slip ring (Figure 91a shows its CAD model);

2. Shoulder belt – the webbing that connects the upper slip ring to the locking tongue, enveloping the dummy torso;

3. Lap belt – the last article of the belt, defined from the locking tongue to the vehicle body fixing point.

In correspondence of the belt locking tongue, the second (lower) LS-DYNA slip ring will be generated, to obtain the same slipping of the belt as in the real vehicle. In addition, it is important to remember that the penetration of the locking tongue with the booster seat (Figure 91b) is not relevant for this type of process:

- A CAD model, if not meshed, is not included in a Finite Element Analysis;

- Usually, the locking tongues on the 2nd-row seats are attached to short webbings fixed underneath the seat, which can allow the passenger to move the tongue attachment, facilitating the belt buckling. Hence, the lower slip ring will be generated with an offset of 15 mm towards the central seat, to simulate the moved belt attachment due to the placement of a booster seat.

The first step of the belt routing process is the selection of the so-called "Parts to wrap", the FE entities that are going to be enveloped by the virtual seatbelt. In this case, they are constituted by seat foam, dummy vest, and booster seat. To ensure the absence of penetrations between belt webbing and wrapped parts during the mesh generation, an offset distance equal to 5 mm between the belt and all parts was defined through the "Seat belt" interface. This distance will be eliminated during the first instants of simulation, thanks to the action of the unlocked retractor, which applies a constant tension to the belt to reproduce the initial tightening and to eliminate any slack. Successively, the route of each seatbelt component was defined by selecting different points where the webbing will pass through. It is important to account that the ANSA generation algorithm of the LS-DYNA slip rings showed to work correctly only if these points are nodes belonging to FE entities. Therefore, the upper slip ring and the locking tongue CAD model were meshed and inserted in the virtual model as rigid bodies, needed to generate (and constrain afterward) the belt webbing. These FE models were collected in a dedicated input file (***Rigid_sliprings.k***) and are shown in Figure 92.

(a)   (b)
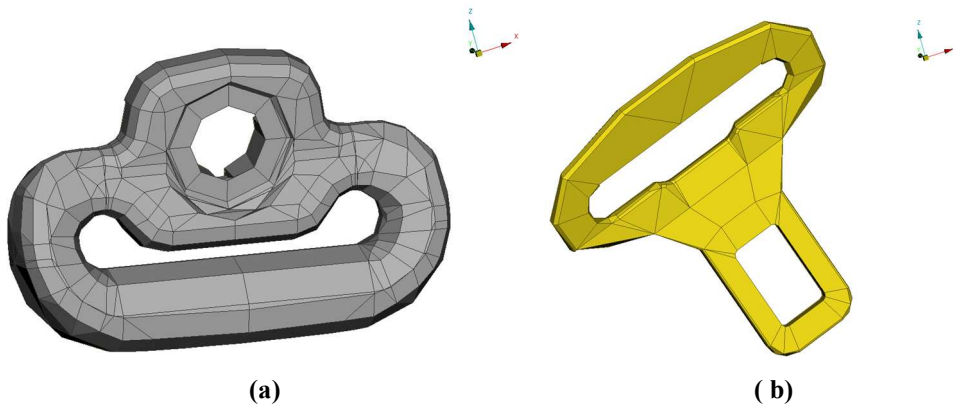
Figure 92 – Rigid slip ring (a) and locking tongue (b)

The mesh of these two entities was generated automatically, without particular quality requirements, since they are not deformable and they will only be used to fix the seatbelt to the vehicle body using *CONSTRAINED_EXTRA_NODE_SET, as described in Section 8.2.2.

After the placement of these bodies in the FE assembly, the first pair of nodes were selected to define the path of the retractor belt. This is the simplest region of the seat belt: a node on the vehicle body and another one on the rigid slip ring were chosen, evidenced in Figure 93.
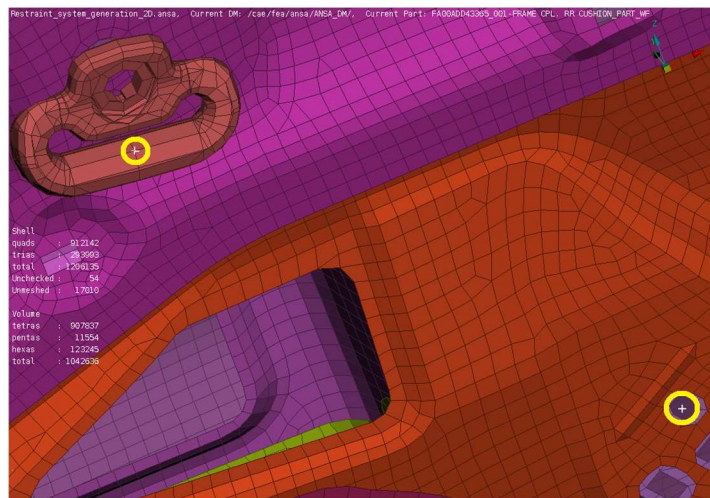
Figure 93 – Reference nodes of the retractor belt

The subsequent nodes to be selected are used to define the path of the shoulder belt: the first one is the last reference node of the retractor belt, to correctly generate the slip ring entity, a pair of nodes is positioned on the dummy vest, and the last one belongs to the rigid locking tongue. The dummy nodes are visualized in Figure 94.
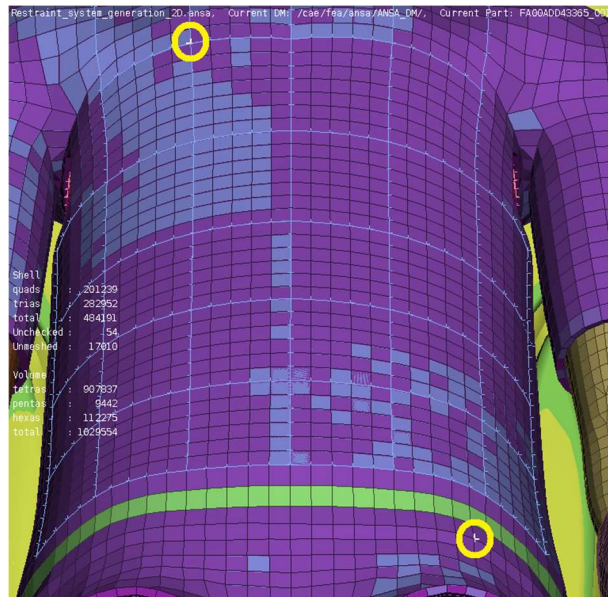
Figure 94 – Reference dummy nodes of the shoulder belt

Lastly, the last set of nodes was defined, to generate the lap belt:

- For correctly generating the lower LS-DYNA slip ring, the first node is equal to the last node of the previous set;
- Two symmetric nodes are placed on the dummy vest, around its hip;
- The last node is selected on the vehicle body, where the belt route and webbing terminate.

This node set is evidenced in Figure 95.
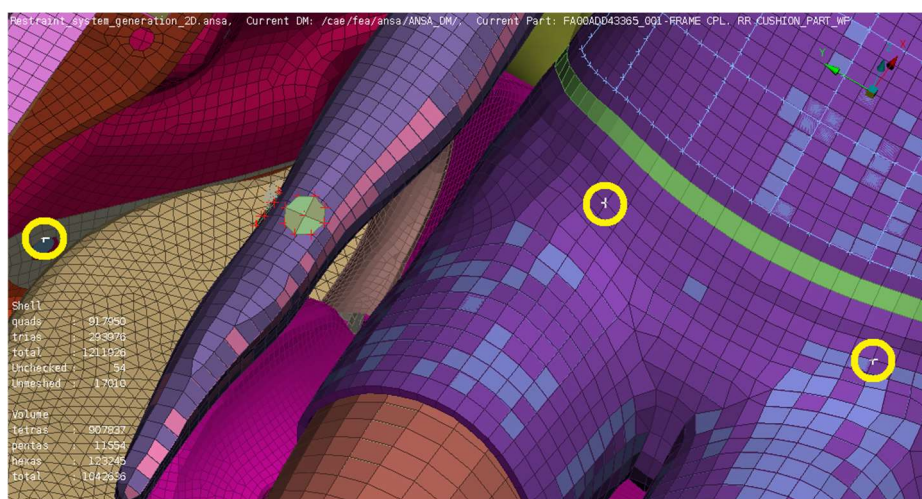
Figure 95 – Reference nodes of the lap belt

The selection of the nodes represented above concludes the phase of belt routing, which is followed by the definition of the belt webbing mesh.

8.2 Generation of the belt webbing

After the selection of all reference nodes needed for defining the path of each seat belt entity, the mesh of the belt webbing can be generated setting all its properties. This discretization has to be as regular as possible, with elements of even dimensions, to obtain stable contact of the webbing and functioning of the seat belt devices (retractor, pretensioner, and slip rings) during the simulation. Therefore, this phase is usually characterized by some iterations, where each belt section is generated and then adjusted in position and orientation to obtain the most suitable configuration.

8.2.1 Seat belt mesh definition

Firstly, the mesh characteristics of the virtual seat belt were inserted in the ANSA "Seat belt" interface: the webbing is discretized with 2D shell elements, with an average width equal to 50 mm, constituted by 5 quadrilateral elements with side length of 10 mm. All the elements of the seat belt will be LS-DYNA *ELEMENT_SEATBELT, the only element type suitable for using virtual retractor, pretensioner and slip rings.

The next important definition in the seat belt generation interface regards the anchor entities placed at the beginning and at the end of each belt, thus the devices connected to each extremity of the webbing, that allow to simulate the functioning of a real safety belt. Considering the same order the reference nodes were described in the previous chapter, the anchor entities of all three belts are collected in Table 12.

Belt entity	Starting anchor entity	Ending anchor entity
Retractor belt	Retractor	Slip ring 1
Shoulder belt	Slip ring 1	Slip ring 2
Lap belt	Slip ring 2	None

Table 12 – Anchor entities of each seat belt section

It can be noticed that all belts are connected through two FE slip rings, which will model the slipping of the real safety belt inside the upper slip ring and the locking tongue, and the lap belt end is fixed to the vehicle body without an anchor device. The entities in Table 12 are represented in LS-DYNA using the commands *ELEMENT_SEATBELT_RETRACTOR and *ELEMENT_SEATBELT_SLIPRING. Both these cards, when working with 2D seat belt elements, need the definition of a set of nodes and a set of elements (two for the slip rings), to identify the nodes that constitute the device itself and the belt entities which can be wrapped

around it. Moreover, these sets must be correctly ordered along the width of the webbing, and such orientation must be respected in the whole seat belt [94]. An example scheme is shown in Figure 96.
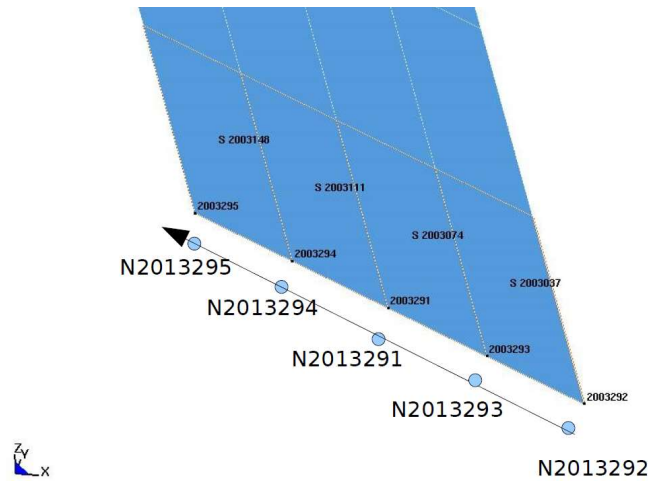
Figure 96 – Ordering rule of nodes of a slip ring/retractor and connected elements for LS-DYNA [94]

The Figure above also evidences that the nodes of a slip ring/retractor do not belong to any seat belt element. In addition, elements of two belt sections connected through a slip ring should share a set of nodes which is coincident with those of the FE slip ring, as shown in Figure 97. This rule is also valid for an LS-DYNA retractor but involves only one set of elements.
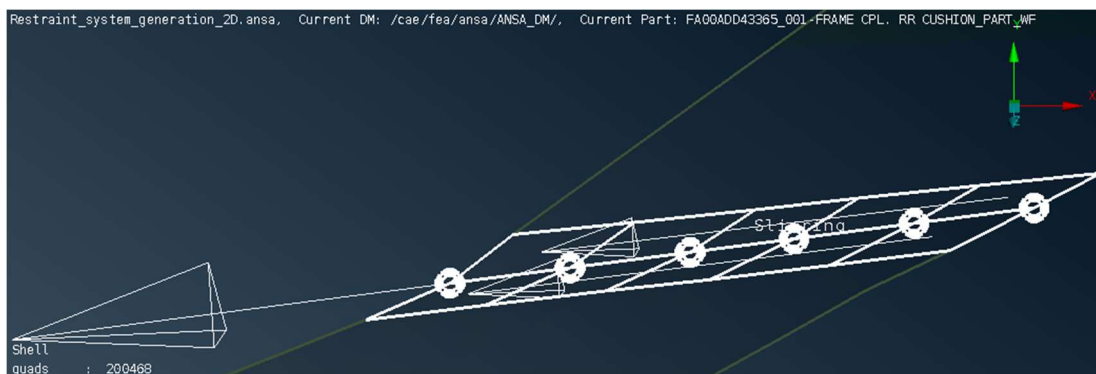
Figure 97 – Top view of an LS-DYNA slip ring. The two connected set of elements of shoulder and retractor belts and the coincident slip ring nodes are highlighted

The coincident set of nodes and the connected set of elements are automatically generated and ordered using ANSA, through the definition of a vector for each anchor entity. Such vectors indicate the ordering direction and they were always defined with the same

direction along the FE belt. The ending anchor entity vector of a belt section is the starting anchor entity vector of the next one, to correctly define sets of nodes and elements connected to the FE slip rings. The presence of the FE upper slip ring and locking tongue, shown in Figure 92, was revealed to be fundamental to correctly define the vectors and generate the LS-DYNA slip rings.

After the definition of mesh properties, anchor entities and vectors, the three belts can be generated. The first one, the retractor belt, is shown in Figure 98.
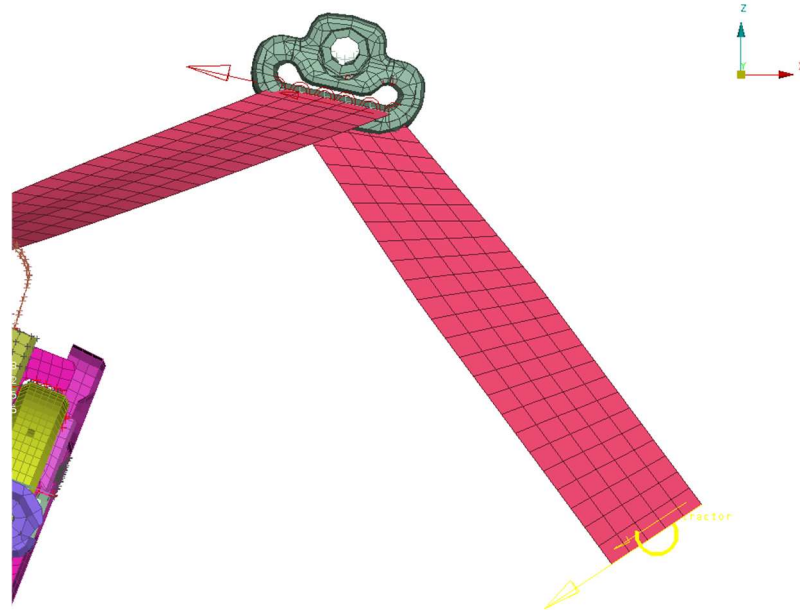
Figure 98 – FE retractor belt

The FE retractor (yellow arrow) can be noticed at the lower extremity of the belt, whereas the upper one is connected to the shoulder belt through an LS-DYNA slip ring (red arrow), coincident in position with the mesh obtained by the CAD model. This belt section, very linear and short, was simple to generate and has not needed an optimization of the routing to improve the mesh quality. On the contrary, the other two entities, more involved with the constraining of the FE dummy, have been shown to be more difficult to define. In fact, they both needed the utilization of the ANSA "Interactive Edit" interface, which allows the instantaneous modification of the belt route and the consequent variation of the respective mesh.

The shoulder belt, highlighted during the Interactive Edit, is reported in Figure 99.

Figure 99 – Interactive edit of the shoulder belt

Different points of the shoulder belt centerline are evidenced in light blue; these points can be moved, changing the route of the belt and stabilizing the mesh in the most difficult regions. In this case, the portion of webbing going under the booster armrest and then wrapping the left side of the child seat needed particular attention. A detailed image of this area is shown in Figure 100.
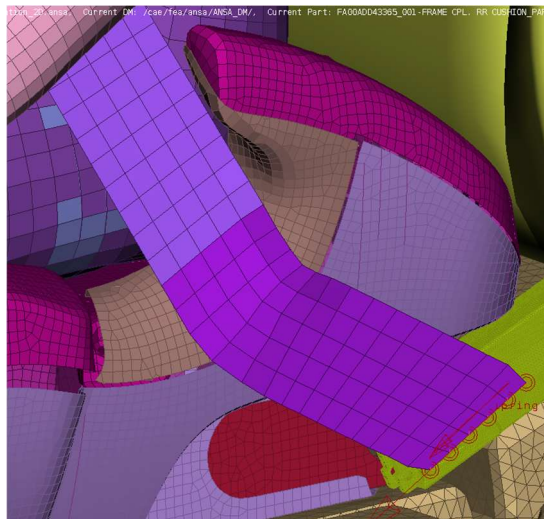
Figure 100 – FE shoulder belt wrapping the booster seat

One set of elements along the width of the belt is not characterized by a high mesh regularity as on the remaining parts of the webbing, but LS-DYNA can handle such localized irregularity, due to the change of direction in the belt path. Another important section of the shoulder belt is close to the dummy neck and chest; its correct reproduction is essential to obtain similar effects of displacement and forces on the FE dummy, compared to the experimental results. This portion of the shoulder belt is shown in Figure 101.
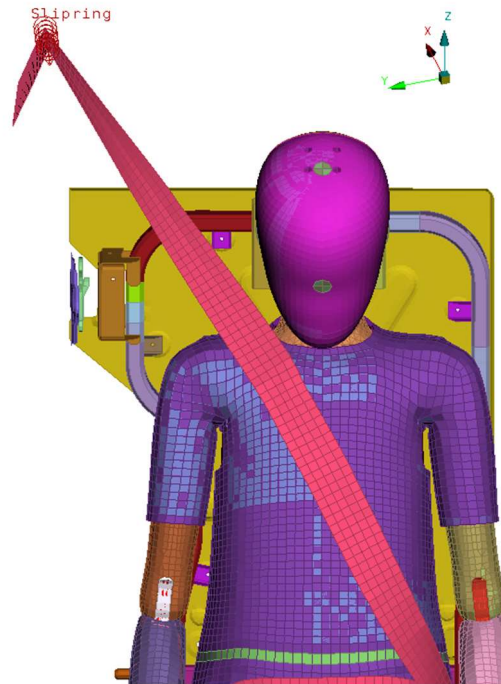
Figure 101 – Front view of the virtual shoulder belt

Therefore, the shoulder belt was generated between two slip rings, which connect it to both retractor and lap belt. The latter is the last entity that was created, wrapping the dummy pelvis, using the reference nodes previously defined. Figure 102 shows the virtual lap belt.
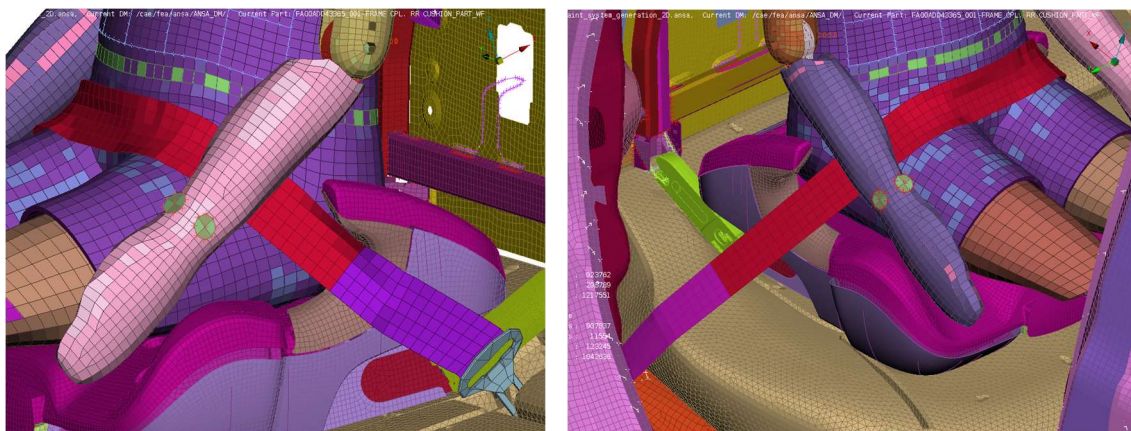
(a)   (b)

Figure 102 – Left (a) and right (b) view of the lap belt

Figure 102a evidences a small deformation of the webbing due to its route, under the booster armrest, whereas Figure 102b highlights the wrapping of dummy and foam seat, before the attachment to the vehicle body. As the shoulder belt, this entity needed an Interactive Edit as well, to respect its tensioning around dummy hip and booster seat and to obtain the most regular discretization. Consequently, Figure 103 reports the complete FE seat belt, with its anchor entities: a retractor and two slip rings.

(a)   (b)
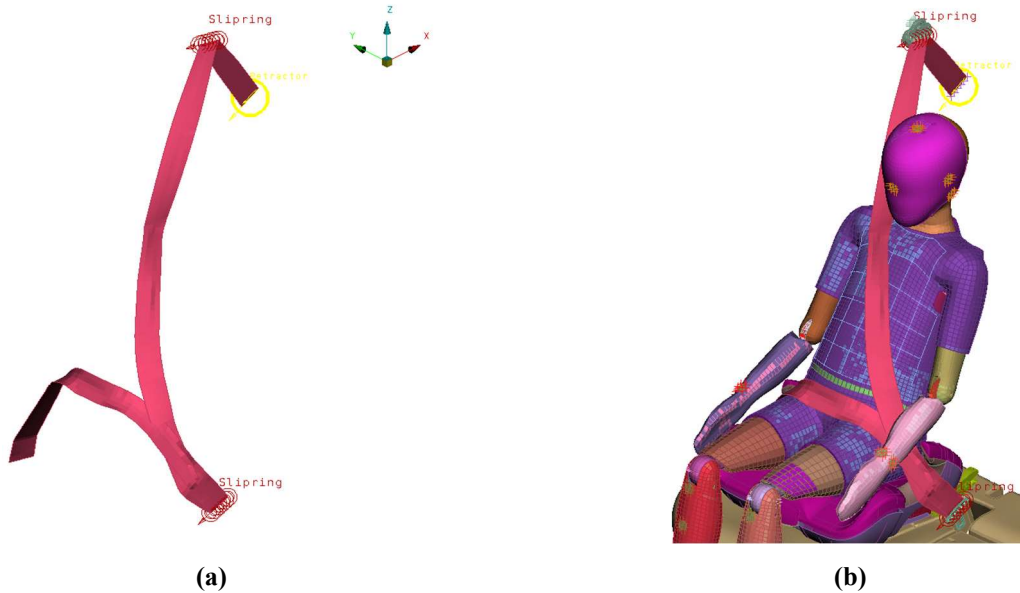
Figure 103 – Finite Element seat belt, slip rings, and retractor

A comparison with the experimental setting is visualized in Figure 104.

(a)   (b)
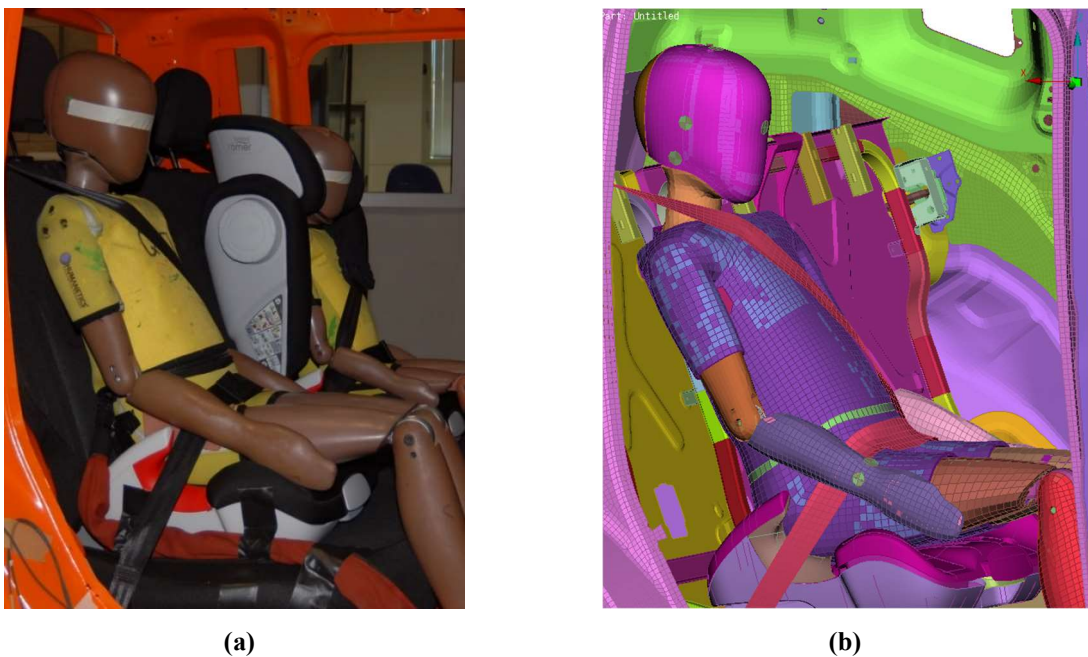
Figure 104 – Right view of experimental and numerical Q10 before the performing of the sled test

Comparing the seat belts reported above, the offset between the webbing and the wrapped parts can be noticed. This slack will be eliminated by the unlocked retractor during the first instants of simulation, as previously mentioned. The utilization of shell element seat belts is preferred when the webbing interacts with other entities of the FE environment. In this case, the contact between the belt, the dummy, and the booster seat is not negligible and needs to be considered. In fact, the most difficult part of this belt routing is represented by the encumbrance of the booster seat, which makes the belt generation near the locking tongue more difficult to achieve, as evidenced in Figure 111 and 113a.

The virtual seat belt is composed by a single PID and its material and section characteristics were provided by the OEM:

- *MAT_SEATBELT;
- *SECTION_SHELL – it is important to underline that, when characterizing an LS-DYNA seat belt, the EDGESET in the section card must be defined. This is the ID of a set of nodes on the transverse section of the webbing, called edge-nodes set. When there is a retractor, the belt nodes coincident with the retractor nodes at the beginning of the simulation must be used [94].

For confidentiality reasons, no further details about the material properties of the seat belt can be published. To conclude, a constant dynamic friction coefficient FC equal to 0.15 was inserted in both *ELEMENT_SEATBELT_SLIPRING cards, to simulate friction of the belt webbing against the physical upper slip ring and locking tongue.

8.2.2 Fixing of the belt webbing to the vehicle body

When simulating crash conditions using LS-DYNA, the Finite Element seat belt needs to be tethered to the vehicle body in all its four extremities:

1. The retractor nodes were connected to close rigid elements of the body using *CONSTRAINED_EXTRA_NODES_SET. Figure 105a evidences such connection, between the nodes circled in green and the purple (rigid) elements, behind the belt webbing;
2. The free extremity of the lap belt was fixed to a rigid section of the vehicle body, as for the retractor in point 1. The anchored nodes (yellow) and the rigid area of the body (cyan) are shown in Figure 105b.

(a)   (b)
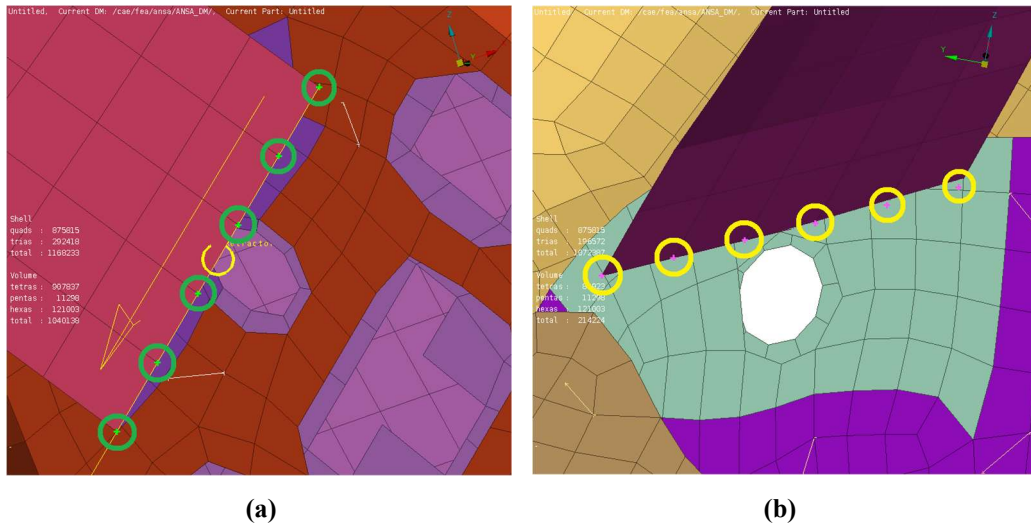
Figure 105 – LS-DYNA retractor and lap belt nodes connected to a rigid section of the vehicle body

3. The upper slip ring nodes were anchored to the vehicle body exploiting the rigid model of the slip ring previously defined. The nodes inserted in the new *CONSTRAINED_EXTRA_NODES_SET card are highlighted in yellow in Figure 106a;

4. The lower LS-DYNA slip ring nodes were connected to the vehicle body with the same method, using the rigid locking tongue. The chosen nodes are circled in yellow in Figure 106b.

(a)   (b)
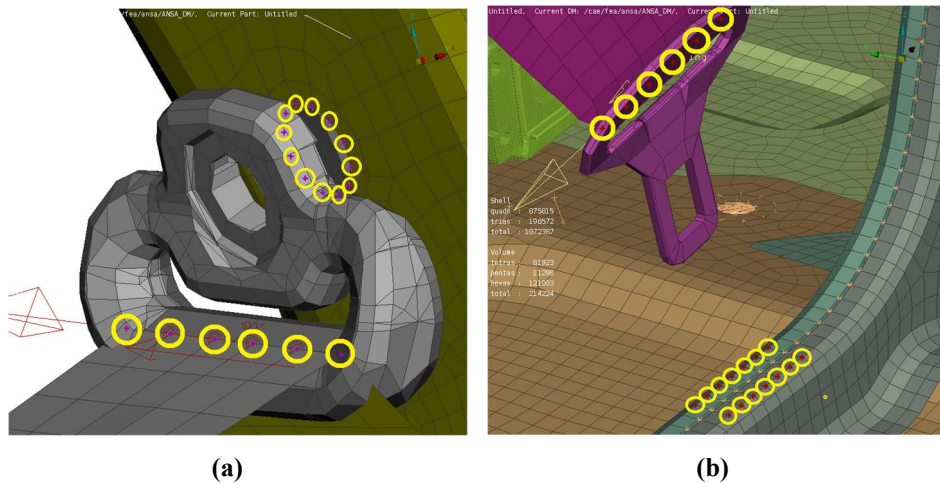
Figure 106 – Slip ring and locking tongue used to connect the LS-DYNA slip rings to the vehicle body

The use of *CONSTRAINED_EXTRA_NODES is preferred to tether the FE seat belt to the vehicle body. This command is known to be more stable when fixing 2D seatbelts, contrary to *CONSTRAINED_NODAL_RIGID_BODY, more utilized to connect hybrid 1D/2D seat belt entities.

8.3 Implementation of the FE safety devices

To work properly, a seat belt needs many devices acting directly on it during the event of a crash. The restraint system utilized during the experimental test regarding this research was equipped with:

1. Pretensioner;
2. Retractor;
3. Dynamic Locking Tongue.

These instruments and their functioning principle were already mentioned in Section 2.3.4. This chapter will describe their definition in LS-DYNA, to work with the virtual seat belt.

8.3.1 Pretensioner

The Finite Element pretensioner does not need the definition of any other elements or nodes since it is coupled with the virtual retractor, which ID is inserted in the *ELEMENT_SEATBELT_PRETENSIONER card. During the first instants of crash, the pretensioner pulls the FE belt in following a defined load curve (pull-in force as a function of time), after the following sequence of events has occurred:

1. Any one of up to four sensors must be triggered;
2. A user-defined time delay occurs before the definitive firing of the pretensioner.

In addition, LS-DYNA provides many types of pretensioner that can be used based on the functioning of the restraint system to simulate. Pretensioner type, sensor and loading curve are described in more detail in Section 9.2, which reports the calibration of all safety devices.

8.3.2 Retractor

The virtual retractor was already generated through ANSA and it is composed of a set of nodes coincident with the first line of nodes of the retractor belt, following the order defined in Table 11. The functioning of the retractor is based on the definition of two curves force vs pull-out, for loading and unloading conditions:

- The loading curve defines the amount of belt that is pulled out by the retractor as a function of the load registered on the belt webbing;
- The unloading curve describes the behavior of the retractor when the belt relaxes and is followed until the minimum tension is reached. The minimum tension is inserted at the first point of the loading curve, with abscissa (pull-out) equal to 0 mm.

A retractor can operate in one of two regimes:

- Unlocked, when the belt material is free to enter and exit the retractor, and when a constant tension is applied to the webbing, to eliminate any initial slack in the FE model. This tension is the minimum tension reported in the first point of the loading curve.
- Locked, when the user-defined force-pullout relationship (loading curve) applies.

At the beginning of the simulation, the retractor is unlocked, and the following sequence of events must occur for it to become locked:

1. Any one of up to four sensors must be triggered;
2. A user-defined time delay occurs;
3. An optional user-defined length of belt can be paid out before the definitive locked of the retractor. Once locked, this device remains locked.

The retractor sensor, curves and all other parameters needed to properly define the card *ELEMENT_SEATBELT_RETRACTOR will be described in Section 9.2.2.

8.3.3 Dynamic Locking Tongue

The Dynamic Locking Tongue (DLT) is the last safety device that was equipped on the restraint system used in the experimental test taken as a reference for this research. The DLT clamps the belt webbing in the locking tongue in the first instants of a crash event, to avoid excessive displacement of the occupant pelvis region. On the other hand, it avoids the generation of excessive loads on this area releasing the webbing when forces higher than a

certain limit are registered so that to distribute the belt force between the pelvis and the chest of the occupant.

Therefore, it was decided to model such a device using a set of nonlinear springs, defined between the locking tongue and the lap belt. To obtain a uniform behavior of the DLT over the belt webbing, 6 springs were created, to lock an entire set of nodes along the width of the FE belt. Such springs, modeled as *ELEMENT_DISCRETE, are reported in Figure 107.
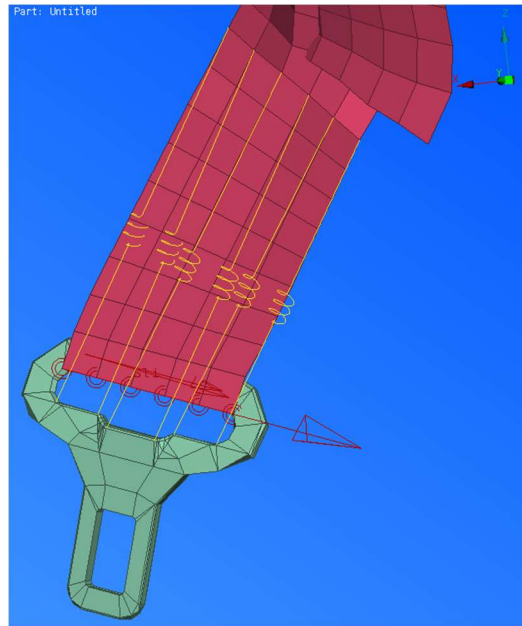
Figure 107 – FE model of the Dynamic Locking Tongue

Successively, a nonlinear force-displacement relationship was defined to obtain the action of the DLT, using *MAT_SPRING_GENERAL_NONLINEAR and the related loading and unloading curves. A stiffness relationship suitable for describing the behavior of the DLT using springs is visualized in Figure 108. The *y*-axis was removed to avoid the publication of confidential data.
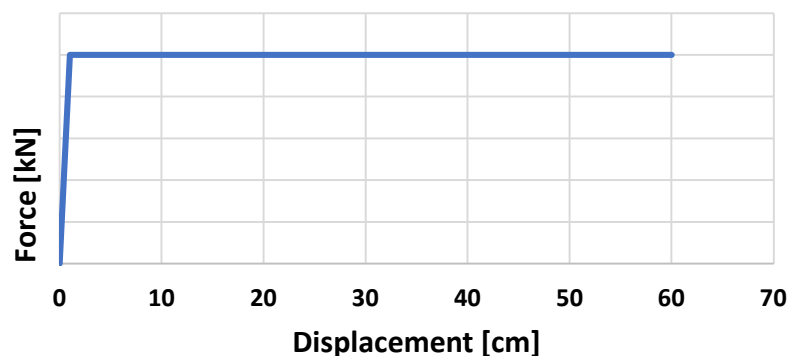
Figure 108 – Nonlinear stiffness of the DLT springs

Observing the curve of Figure 108, a spring has an elongation of only 1 mm for loads between 0 and the maximum limit. This part of the stiffness relationship is called unloading curve and it was inserted in the LS-DYNA material card using *DEFINE_CURVE. It simulates the locking of the DLT in the first instants of the crash, constraining the nodes on the lap belt to 1 mm of maximum displacement.

On the other hand, when the load on the DLT reaches the defined limit and is going to overcome it, the spring starts to stretch, to keep the load constant. This horizontal section of the relationship is called loading curve and simulates the release of the belt webbing from the locking tongue, to avoid excessive loads on the occupant pelvis. Therefore, the spring stays in the loading condition until the load becomes lower; at that point, the unloading curve describes again the behavior of the spring. It is important to notice that the values of the curve in Figure 108 were divided by the number of springs used in the FE environment, to obtain a uniform behavior of the DLT elements and the same load limiting behavior used in the experimental test.

Lastly, the choice of the lap belt nodes was fundamental to achieve the correct functioning of the FE Dynamic Locking Tongue: a safety length of 10 cm of the springs was set, to avoid the slipping of the spring nodes to the other belt side (shoulder).

8.3.4 Virtual tensiometers

During the experimental sled test, loads on the shoulder and lap belt were measured using two different tensiometers. Their location is shown in Figure 109.

Figure 109 – Location of lap and shoulder belt tensiometers

The utilization of these devices is fundamental to monitor the functioning of the safety devices previously described, during the whole sled test. In addition, this monitoring is essential to calibrate the Finite Element restraint system and reproduce the same functioning of pretensioner and retractor, as will be reported in Section 9.2. Therefore, two virtual tensiometers were reproduced in the FE belt webbing, using *DATABASE_CROSS_SECTION_PLANE: two cutting planes were generated using this command, to monitor the force acting on the virtual belt during the simulation and to correlate the performance of both the numerical and experimental restraint systems. The two cutting planes are visualized in Figure 110.

(a)   (b)
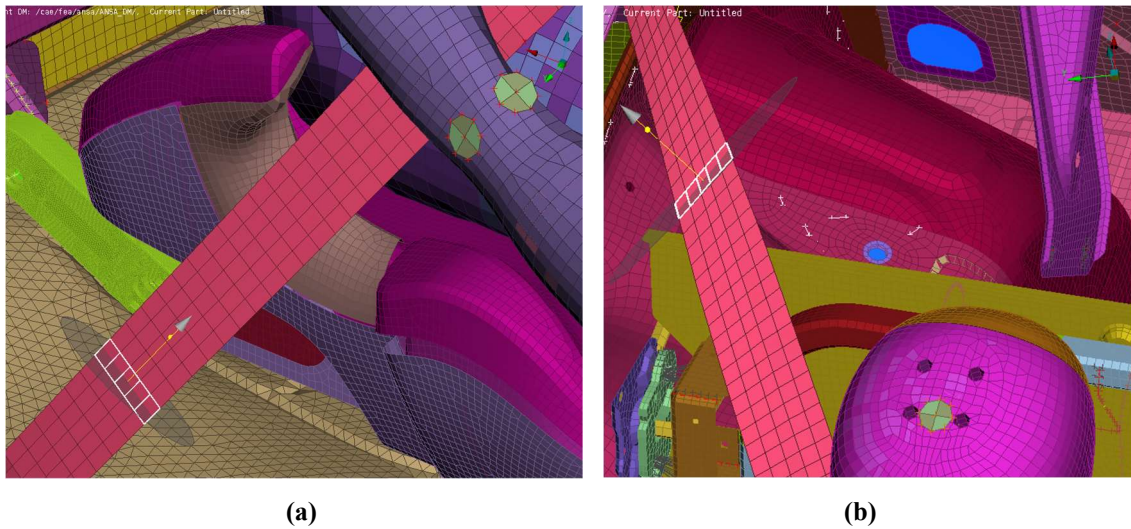
Figure 110 – Virtual tensiometers defined using *DATABASE_CROSS_SECTION_PLANE

When defining a cutting plane to measure the load on the belt elements, it is important to position such a plane in the central section of the elements, to avoid the registration of inaccurate data. All these devices were collected in a proper input file (*Safety_devices.k*), to facilitate their modification during the calibration phase.

9. SLED TEST SIMULATION

Once obtained the initial position of the virtual Q10 (Section 7.2), preloaded foam and booster seat models (Section 7.3) and generated the FE restraint system (Chapter 8), the master input file to launch the sled test LS-DYNA simulation can be defined. The additional important definitions to be included in the launch file regard contact control between all entities in the FE vehicle body and the acceleration imposed by the HYGE sled to simulate the Euro NCAP ODB test.

9.1 Description of the input files

The Include structure of the master input file of the sled test simulation is schematized in Table 13.

FILENAME	FILE ROLE	INCLUDE OFFSET
MAIN.key	Master	0
Booster_seat_ROT.k	Include	10,000,000
Backseat_foam_ROT.k	Include	20,000,000
Backseat_frame_ROT.k	Include	30,000,000
Vehicle_body_ROT.k	Include	40,000,000
Rigid_sliprings_ROT.k	Include	50,000,000
Seatbelt_ROT.k	Include	60,000,000
Springback_sled.k	Include	0
Belt_devices.k	Include	0
Q10_dummy.k	Include	0
Connections_sled.k	Include	0
Contact_sled.k	Include	0
Control_sled.k	Include	0

Table 13 – Include structure of the sled test simulation input file

The suffix ***ROT*** on the majority of the input files indicates that they were rotated of 18° with respect to the *z*-axis, to obtain the same configuration of the sled simulation of the Offset-Deformable Barrier Euro NCAP test, as described in Section 2.8.6.

Moreover, the suffix ***sled*** specifies that an already existing model was modified to perform this simulation:

- **Springback_sled** contains initial stresses and strain in the booster seat, seat foam and suspension frame. The nodal coordinates, instead, were inserted in their original input files and then rotated 18° about the *z*-axis;

- **Connections_sled** gathers the constraints of backseat foam suspension frame and front passenger seat described in Sections 5.2 and 5.3, the revolute joint that represents the ISOFIX anchorage (Section 6.1.2) and the FE seat belt tethering shown in Section 8.2.2;

- **Contact_sled** collects all the contact algorithm needed for correctly simulation the event:

  o *CONTACT_TIED_SHELL_EDGE_TO_SURFACE_BEAM_OFFSET is again utilized to model the interaction between seat foam and suspension frame;

  o *CONTACT_AUTOMATIC_SURFACE_TO_SURFACE models the contact of seat belt against dummy, booster and seat foam;

  o *CONTACT_AUTOMATIC_NODES_TO_SURFACE to control the likely impact of the dummy against the backseat frame of the front passenger seat (evidenced in yellow in Figure 111);
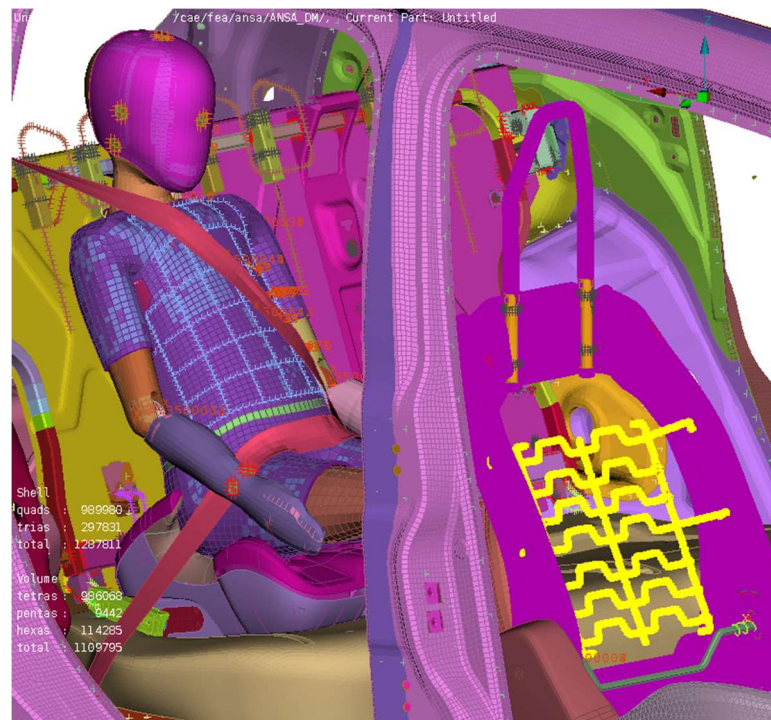
Figure 111 – Evidenced backseat frame of the front passenger seat

  o *CONTACT_AUTOMATIC_GENERAL was utilized to model the interaction between all other entities of the model.

  Static and dynamic friction coefficients were set equal to 0.2 in all contact cards, a reasonable low value often utilized in this type of simulation.

Moreover, it is important to underline that the seat belt has not been inserted in the automatic general contact algorithm since lap and shoulder belts penetrate each other near the locking tongue (as noticeable in Figure 103) and is always preferred to avoid initial penetrations in the definition of an LS-DYNA contact. Therefore, this entity was set as master side of another contact algorithm, to neglect penetration and rubbing of the two webbings.

Lastly, a part set was specified by Humanetics® to model contact between dummy and external entities, whereas internal contact between all dummy parts was already regulated by the manufacturer in the original dummy input file;

o *Control_sled* contains the termination time of the simulation, 200 ms, several database cards needed for verification and validation of the model and a *LOAD_BODY_Z command, to simulate gravity during the whole event.

In addition, this include file also contains the modeling of the sled motion, through a *BOUNDARY_PRESCRIBED_MOTION_RIGID command, which assigns a velocity/time curve to a rigid part of the vehicle body, specifically modeled to impose the sled speed. It was decided to model the sled motion using a velocity curve since it is more stable than the acceleration. This curve was obtained integrating the acceleration/time curve from the experimental sled test and is reported in Figure 112 (it is shown without the y-axis scale due confidentiality).
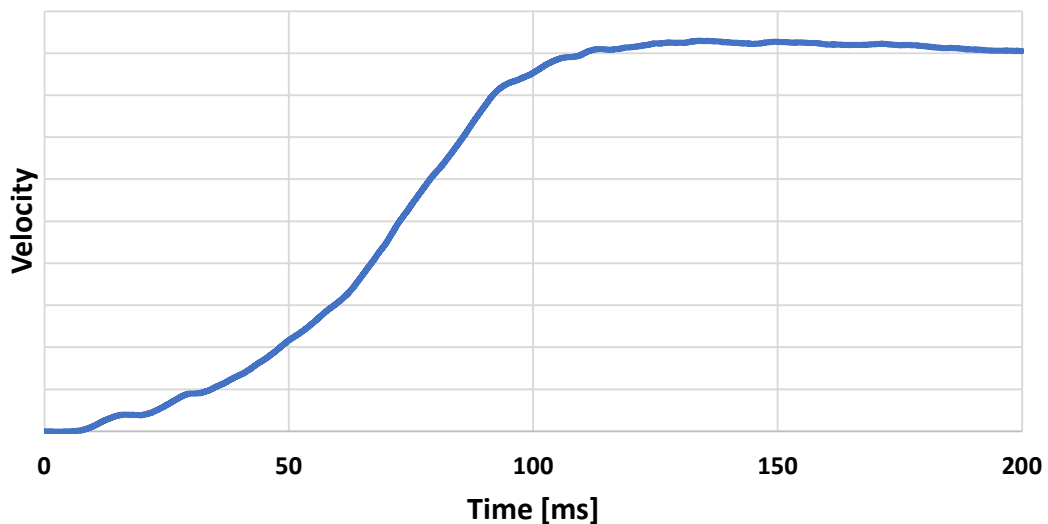
Figure 112 – Velocity/time curve imposed on the vehicle body to simulate the sled test

The completion of such LS-DYNA simulation required about 28 hours, thus it was decided to avoid the use of mass scaling and utilize the default time step defined with a TSSFAC equal to 0.9.

9.2 Calibration of the restraint system

The first sled test simulations were executed for verifying the proper contact interactions between all entities, the correct reproduction of the event and, successively, to calibrate the restraint system devices, to obtain the most precise correlation between numerical and experimental pretensioner and retractor. This objective was achieved using the experimental load/time curves from shoulder and lap belt tensiometers as reference, and following the information provided in the report of the experimental sled test about the equipped restraint system.

All curves in this section will be shown without the y-axis for confidentiality reasons.

9.2.1 Pretensioner

The virtual pretensioner was calibrated using a loading curve provided by the OEM as a starting model, and the experimental tensiometer curve of the shoulder belt as reference. These curves are shown in Figure 113 and 114.
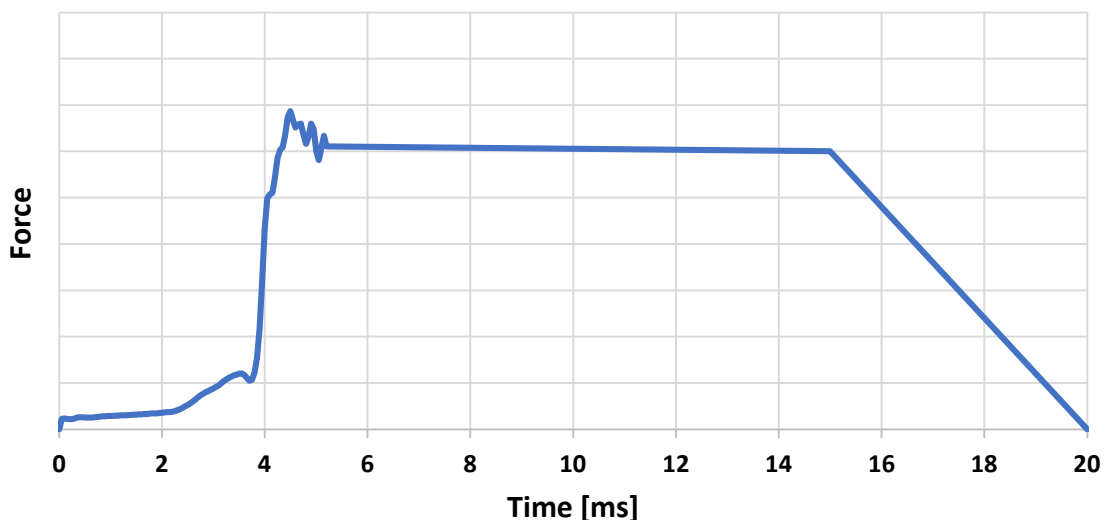
Figure 113 – Pretensioner starting loading curve
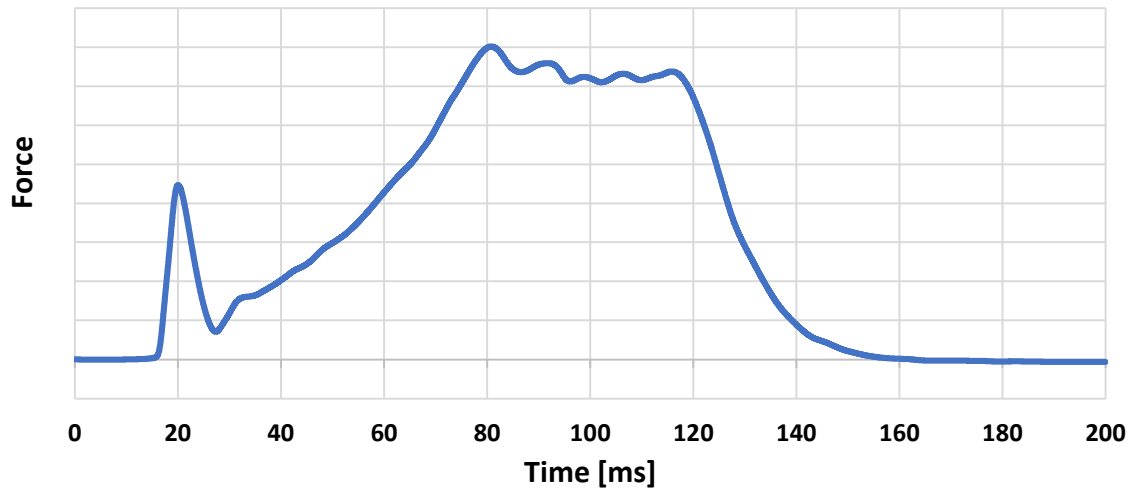
Figure 114 – Load on the shoulder belt registered during the experimental sled test

The first peak curve represented in Figure 114, between 0 and 30 ms, represents the influence of the pretensioner on the seat belt behavior. A load peak is reached at $t = 20$ ms, then the pretensioner stops loading the belt. Therefore, the curve in Figure 113 was modified, eliminating the constant load applied between $t = 5$ and $t = 15$ ms and dictating an instantaneous belt release. The definitive pretensioner curve is reported in Figure 115 and will influence the amount of belt material pulled in the virtual retractor. Its force peak was set coincident with the value registered by the tensiometer, using the scale factor in *DEFINE_CURVE.
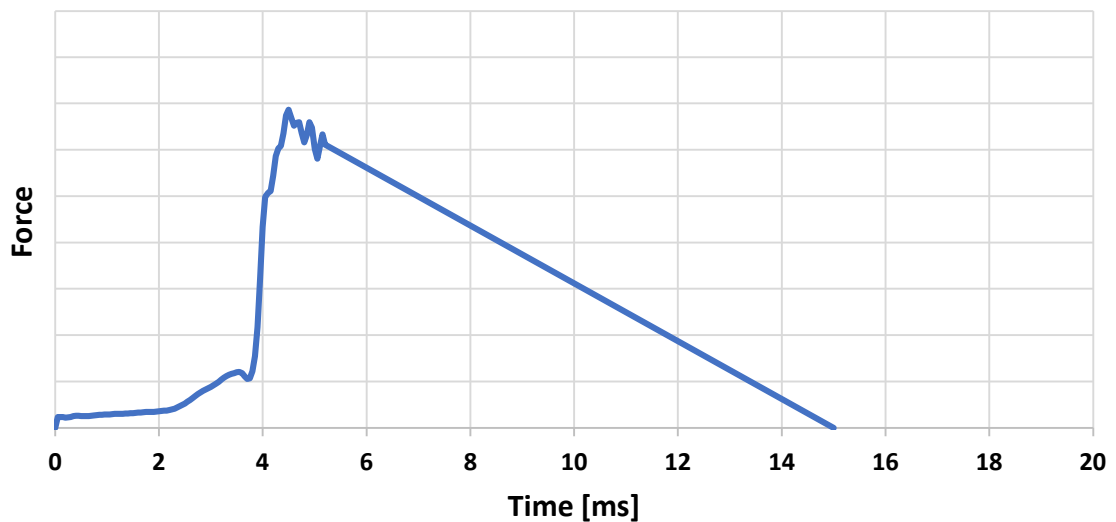
Figure 115 – Definitive pretensioner loading curve

Moreover, the experimental sled test report indicates the pretensioner firing time, equal to 12 ms. Consequently, the LS-DYNA sensor connected to this device was defined as a time-based sensor (*ELEMENT_SEATBELT_SENSOR type 3), with a coincident triggering time.

Lastly, to obtain the load decrease of Figure 114 after $t = 20$ ms, a certain amount of belt material must exit the retractor before it locks (the retractor locking is evidenced by the successive belt load rise). To do this, the pretensioner type must be properly chosen: in this case, type 6 is the most appropriate, since it dictates the locking of the retractor only after a certain belt length moves back out of it, defined through the PULL parameter (measured in mm) in the LS-DYNA retractor card. Once the retractor is locked, the pretensioner is disabled, and the retractor loading curve is utilized to match the current belt tension with the amount of belt to payout. The PULL parameter is the only connection between virtual retractor and pretensioner when using type 6 *ELEMENT_SEATBELT_PRETENSIONER, and it was set through a trial and error approach.

9.2.2 Retractor

The experimental test report describes the retractor as a Constant Load Limiter (CLL) type, with a precise force limit. Therefore, when the retractor locks the webbing, the belt load starts to increase until it reaches the maximum value. Successively, the retractor starts to pull belt material out, so as to maintain a constant load on the belt, equal to the designed limit. This behavior is intended to avoid injuries due to the excessive load of the locked belt on the occupant body. The retractor locking can be noticed in Figure 114, at about $t = 30$ ms, when the belt load starts again to increase. At $t = 80$ ms, the CLL activates and starts to pull out belt, to keep the load constant until the rebound phase, when the dummy moves rearward decreasing the force on the webbing.

Consequently, a CLL force/pull-out curve was defined as the retractor loading curve and is represented in Figure 116.
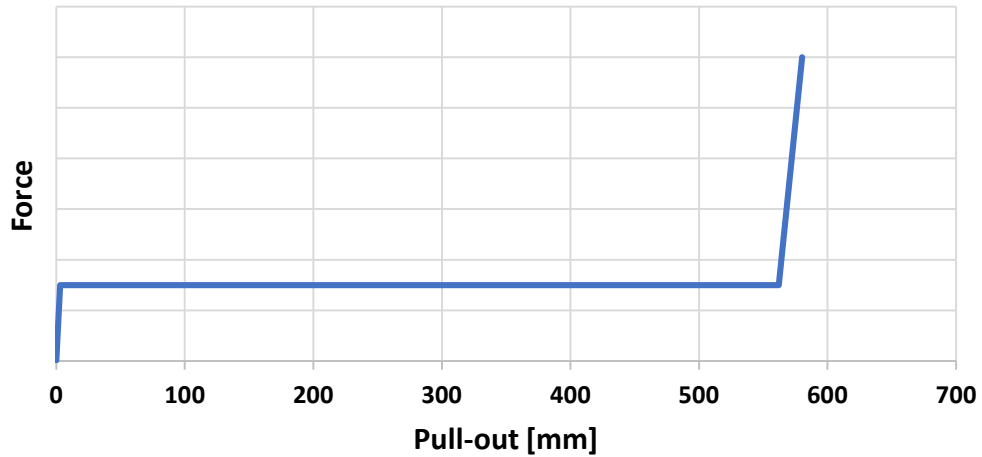
Figure 116- Constant Load Limiter retractor loading curve

Observing Figure 116, the insertion of a weblocker can be noticed: after 550 mm of pull-out, the load increases with a very steep characteristic, indicating the locking of the retractor due to excessive output of belt material. Usually, this characteristic does not influence the simulation since the retractor stops releasing belt material when the rebound phase begins, as can be noticed in Figure 114, at $t = 120$ ms.

When the belt relaxes due to the rebound phase, the retractor behavior is characterized by an unloading curve. This curve must start at null tension and increase monotonically. It is reported in Figure 117.
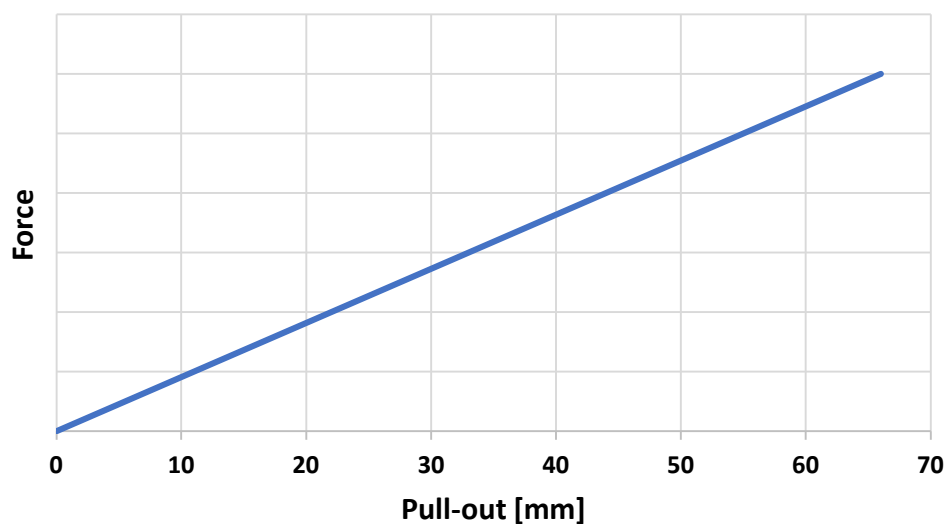
Figure 117 – Retractor unloading curve

In addition, an LS-DYNA retractor requires the definition of at least one virtual sensor to operate. In this case, since the locking of the retractor must be dictated by the PULL parameter, a time-based sensor with firing time at 0 ms was defined, to not influence the behavior of this device. To summarize the effects of retractor and pretensioner on the shoulder belt load and how this data was utilized to calibrate them, Figure 118 underlines each consequence on the tensiometer curve.
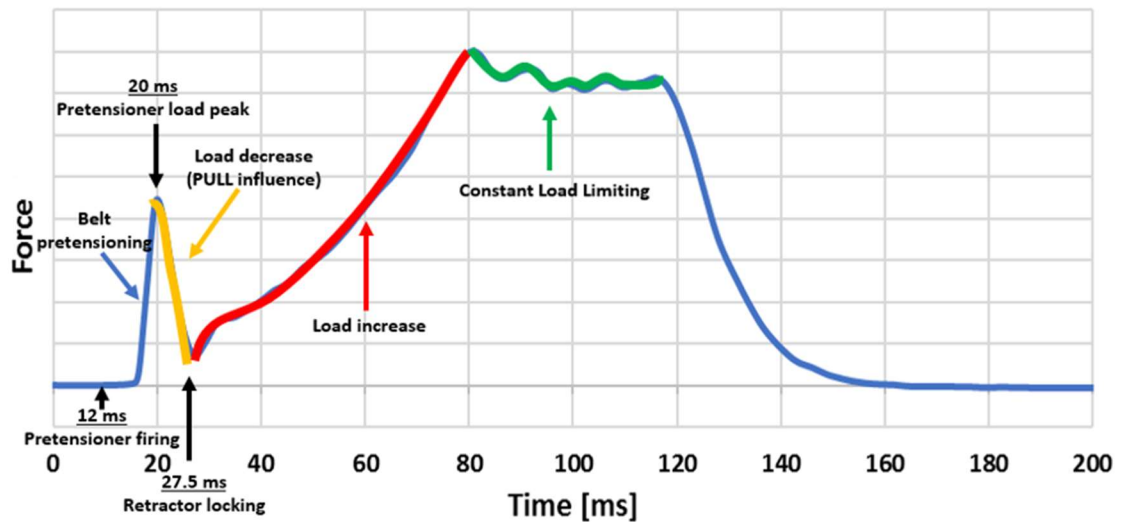
Figure 118 – Retractor and pretensioner effects on the shoulder belt load

9.2.3 Dynamic Locking Tongue

The influence of the DLT on the shoulder belt load is almost completely negligible since it is connected to the lap section. As described in Section 8.3.3, it acts as a load limiter on the lap webbing. Such limiting behaviour can be noticed on the experimental lap belt load measured through the second tensiometer and shown in Figure 119.
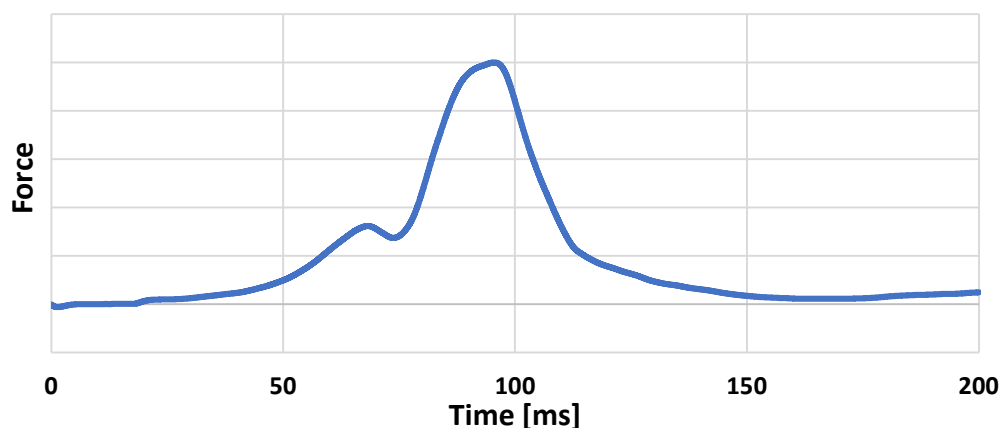
Figure 119 – Load on the lap belt measured during the experimental test

The imposition of this limit has already been described in the previous section, thus this device does not need an additional calibration. On the other hand, its functioning was monitored through *DATABASE_DEFORC, to observe the functioning of the virtual DLT discrete elements, and through the virtual lap belt tensiometer described in Section 8.3.4. In fact, during the validation of the model, numerical and experimental belt loads will be compared.

9.3 Model verification and validation

During the completion of the first simulations, needed to calibrate the virtual restraint system, the congruency of the energy balance was checked and verified. The model verification is necessary to approve the simulation as physically truthful and to successively validate its results. The model validation was executed comparing several injury parameters obtained from the virtual dummy with the experimental outputs.

9.3.1 Model verification

The energy balance of the sled test simulation is reported in Figure 120.
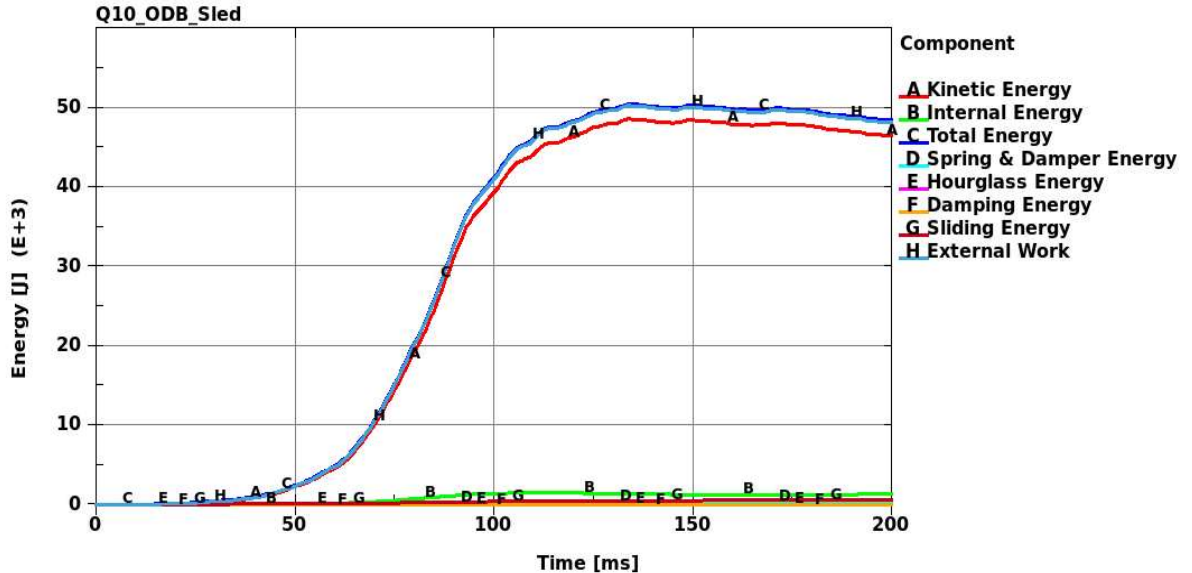
Figure 120 – Energy balance of the sled test simulation

Since the model simulates a crash, about 90% of the total energy of the system is kinetic energy. In addition, such parameter reports the same trend of the sled velocity plotted in Figure 112, an expected result from the definition of kinetic energy. Moreover, the Figure above evidences an overlap between total energy and external work curves, both starting from null

values, thus indicating the physical congruence of the model, and the observance of Equation 10, reported again below.

$$E_{kin} + E_{int} + E_{sli} + E_{rw} + E_{damp} + E_{hg} = E_{tot} = E_{kin}^0 + E_{int}^0 + W_{ext} \qquad (10 - \text{repeated})$$

Since their magnitude is much lower than those of total and kinetic energies, Figure 121 visualizes only the internal, sliding and hourglass energies.
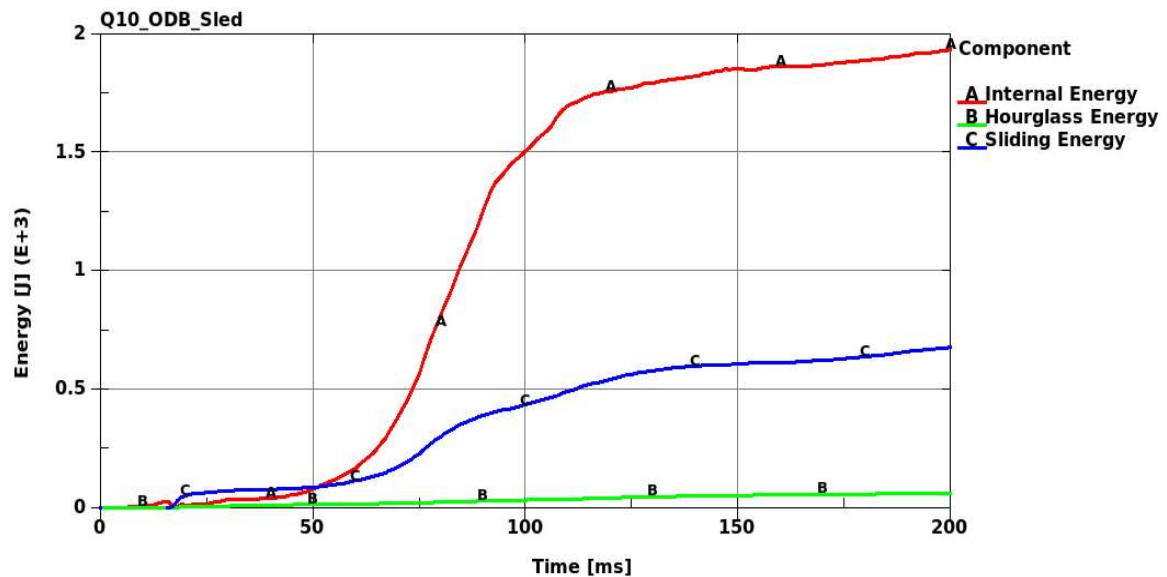
Figure 121 – Internal, sliding and hourglass energies registered during the sled test simulation

A crash simulation involves contact between several entities, sometimes characterized by really different materials (foam, plastic, aluminum, rubber, steel). Therefore, the presence of positive internal and sliding energy must be checked, to verify the correct functioning of all contact algorithms. Additionally, some elements might excessively deform during the most critical steps of the simulation, thus the magnitude of the hourglass energy must be controlled as well. In this case, during the second half of the simulation, the hourglass energy has a magnitude of 10 J, whereas the total energy is greater than 40,000 J. Consequently, the hourglass energy is equal to 0.025% (at the maximum) of the total energy during the entire event. Since this value is much lower than 10% over the whole simulation time, the result can be considered as acceptable.

9.3.2 Model validation

Once the physics of the simulation was verified, the model can be validated. This was executed comparing experimental and numerical data extrapolated from the dummy during the sled test and the numerical simulation. This data will be listed in the next chapter.

The indices used to quantify the level of accuracy of the FE model in the validation are the validation metric and the cumulative error, already described in Section 2.10.2.1. Their definitions (Equations 7 and 8) are repeated below.

$$V = 1 - \frac{1}{L} \int_0^L tanh \left| \frac{y(x) - Y(x)}{Y(x)} \right| dx \qquad (7 - \text{repeated})$$

$$E = \frac{1}{L} \int_0^L \left| \frac{y(x) - Y(x)}{Y(x)} \right| dx \qquad (8 - \text{repeated})$$

Additionally, the error criterion described in the same section was utilised as well, and is reported as follows, with upper and lower bound set equal to $\pm$ 10%, $\pm$ 15%, and $\pm$ 5% of the maximum absolute experimental value, to quantify the sensitivity to such bound in the model validation.

$$For\ lower\ bound\ \leq Y(x)\ \leq upper\ bound,\ error(x) = 0$$
$$else\ \ error(x) = \frac{y(x) - Y(x)}{Y(x)} \qquad (9 - \text{repeated})$$

9.3.2.1 Description of the experimental data

The experimental sled test conducted as reproduction of the Euro NCAP ODB test with the Humanetics® Q10 and the physical entities represented in the FE model described in the previous sections provided several output parameters. The monitoring of such factors is firstly fundamental to verify the satisfaction of the Euro NCAP safety requirements about the ODB test. Secondly, their comparison with the respective numerical output from the LS-DYNA simulation is necessary to validate the Finite Element model.

Therefore, the experimental output utilized for these purposes is described in Table 14.

Dummy region	Parameters	Euro NCAP Injury Criteria	Additional Injury Criteria
Head	Acceleration (x, y, z-components)	HIC_{15}	HIC_{36}
Upper neck	Force (x, y, z-components) Moment (x, y, z-components)	Tension F_z Extension M_y	Nij
Lower neck	Force (x, y, z-components) Moment (x, y, z-components)		
Chest	Acceleration (x, y, z-components)		
Pelvis	Acceleration (x, y, z-components)		

Table 14 – Injury parameters extrapolated from the experimental sled test

It is important to notice that these parameters were captured with a sampling time of 0.05 ms in both experimental and numerical tests, thus obtaining 4000 data points utilized to compute cumulative error and validation metric. In this regard, each data was properly filtered in accordance with the SAE J211-1 Recommended Practice [99], which also describes the orientation of the reference systems utilised for every dummy region.

The column "Euro NCAP Injury Criteria" of Table 14 lists the criteria exploited by Euro NCAP in the assessment of the Child Occupant Protection ODB test. The respective acceptable limits are reported in Table 3, in Section 2.8.5. The last column of the table above, "Additional Injury Criteria", reports further criteria that were computed for sake of completeness, since their monitoring is required by the other Vehicle Safety Standards mentioned in this research, FMVSS 213 and CMVSS 208. *HIC* and *Nij* were computed following the definitions described in Sections 2.3.2.1 and 2.3.2.2.

9.3.2.2 Data presentation

The OEM considers all the biomechanical outputs from the experimental test as strictly confidential. In addition, those data involve external companies (the dummy supplier and the sled owner), which believe that such parameters can not be published in its entirely.

Therefore, to publish this thesis complying with the agreements made with the OEM, both numerical and experimental biomechanical data presented throughout the next chapters were sealed. Such covering was applied normalizing all curves, dividing their points by the maximum experimental value of the respective measure. In this way, the effective and absolute values of each data have not been shown; at the same time, every plot shows a quantitative evaluation (in percentage) of the correlation between numerical and experimental outputs, without compromising the objectives of this research.

9.3.2.3 Belt loads

Before performing the actual validation of the model, comparing all injury parameters listed in Table 14, the forces registered on the virtual tensiometers were monitored during the first simulations, aimed at calibrating the LS-DYNA restraint system. Since the experimental retractor is a CLL type such a device did not require particular attention during this phase. On the other hand, the pretensioner curve needed to be modified, as stated in Section 9.2.1, and the PULL parameter needed to be properly set. The establishment of both these characteristics was achieved through a trial and error approach, leading to the launch of several pre-setting simulations.

The final numerical loads registered on both shoulder and lap belts are correlated to the experimental forces in Figure 122.
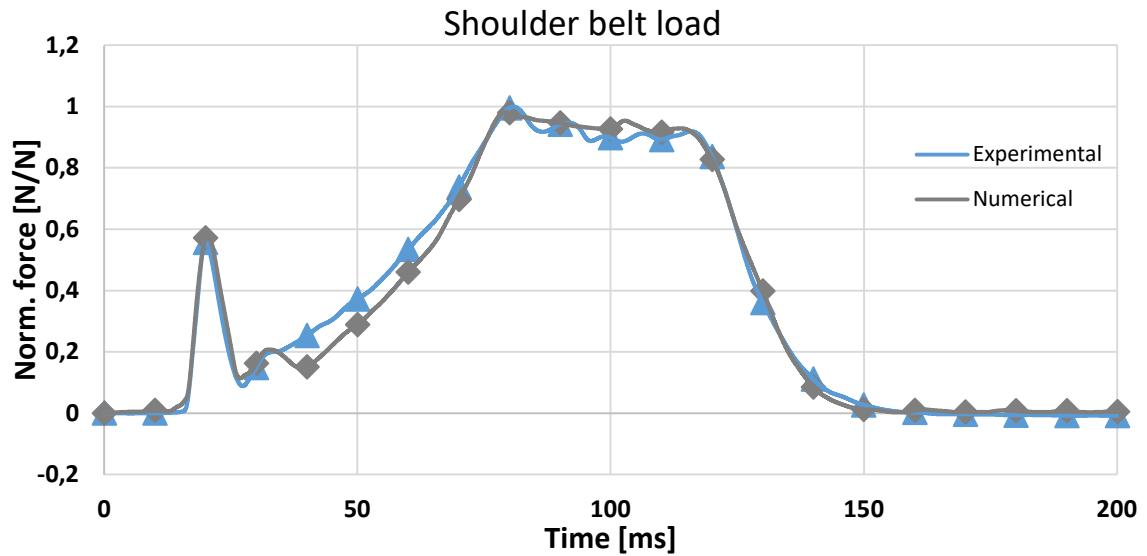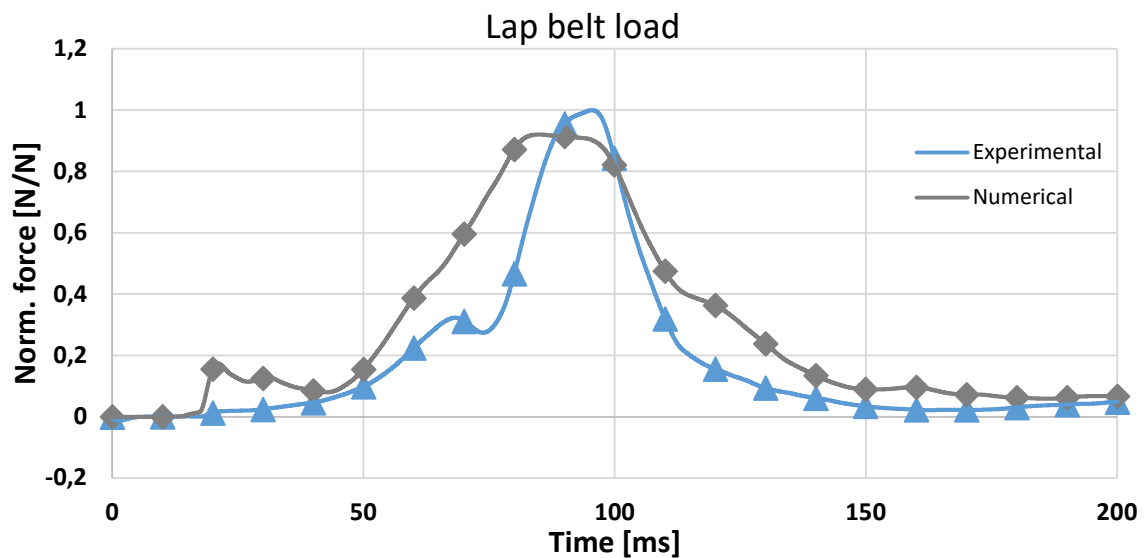
Figure 122 – Experimental and numerical loads on shoulder (a) and lap (b) belt

Figure 122a evidences a high level of correlation between the two curves. This result indicates the completion of the calibration of the virtual restraint system, which mostly influences the load on such a portion of the webbing since it is directly connected to pretensioner and retractor.

The PULL parameter was finally set equal to 24 mm to obtain the reported output, obtaining the same locking instant of the retractor in both experimental and numerical events. Lastly, the proper operation of the load limiter can be noticed, between $t = 80$ and $t = 120$ ms.

On the other hand, the load on the lap belt reported in Figure b shows a lower level of precision. This is caused by the presence of the DLT, which behavior can not be fully reproduced in the FE environment. Moreover, friction of the belt in the locking tongue has not been monitored during the experimental test, and it was reproduced with a constant dynamic friction coefficient. Also friction between the dummy and the belt or between the dummy and the booster seat can influence this curve. Although the variables that influence the lap belt are not easy to control, the numerical load trend visualized in Figure 122b respects the experimental result, with a load limiting behavior, produced by the DLT elements. The same Figure evidences a pretensioning of the virtual belt at $t = 20$ ms, when the physical belt remains relaxed. This probably causes the relaxation of the FE shoulder belt between $t = 30$ and $t = 40$ ms, since part of the pretensioner load acts on the FE lap belt.

9.3.2.4 Qualitative comparison

A qualitative comparison between experimental and numerical events is displayed in Figure 123.

(a)

(b)
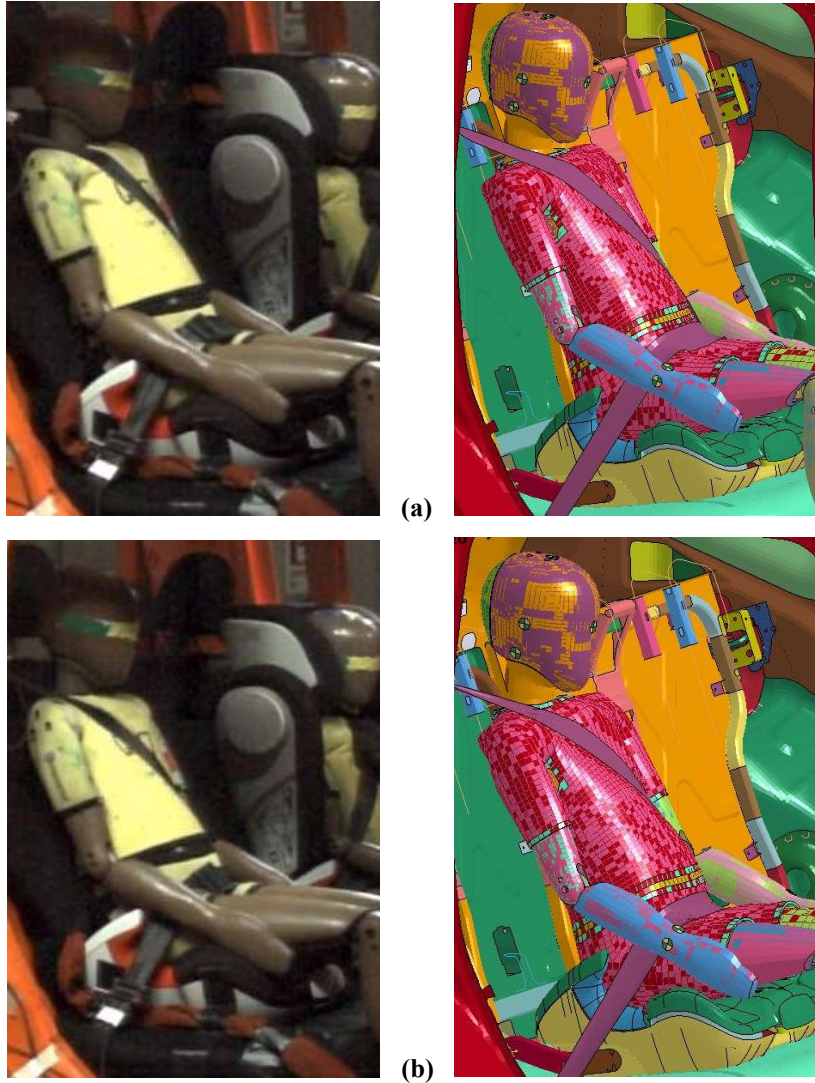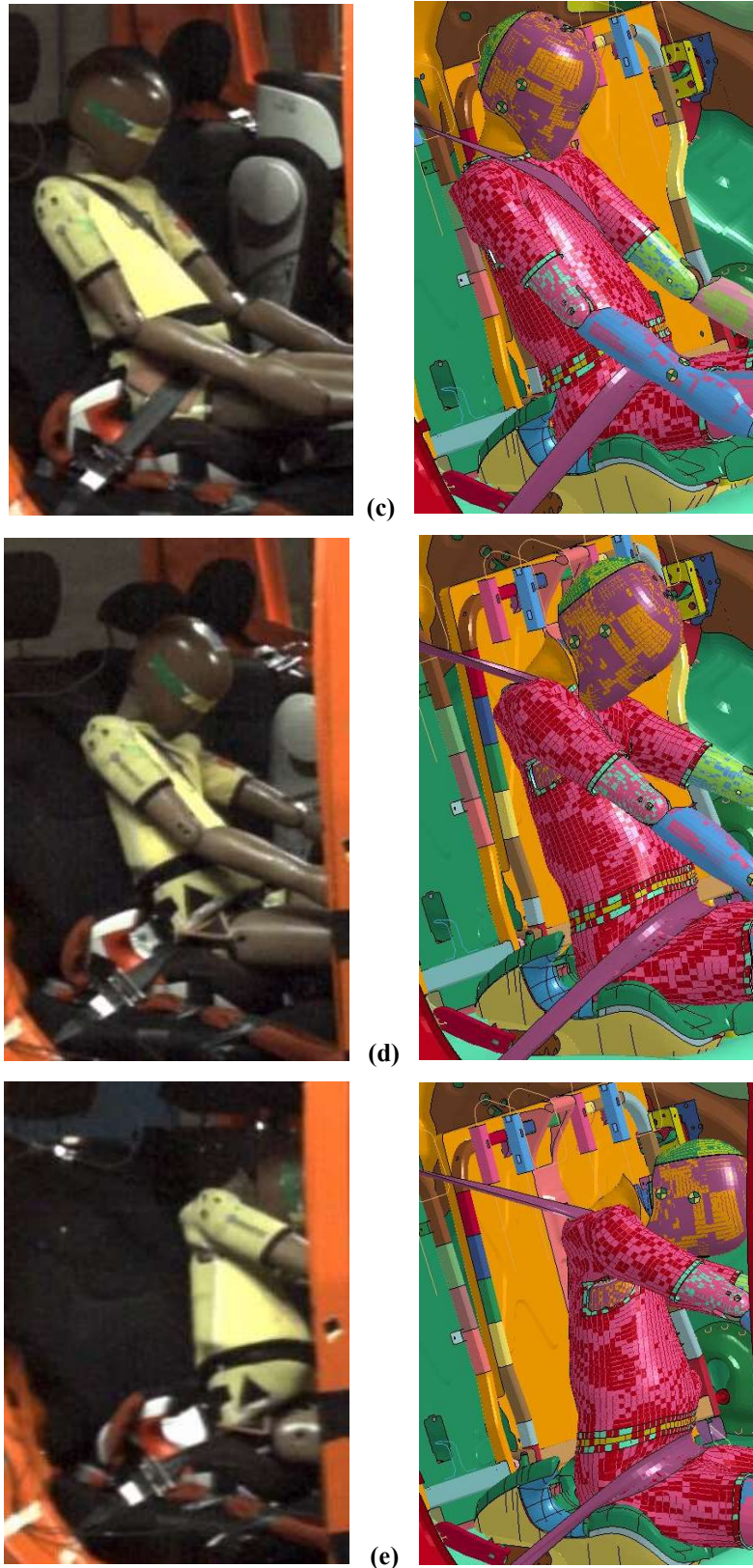
Figure 123 – Visual comparison between experimental (left) and numerical (right) sled test at 10 (a), 20 (b), 60 (c), 80 (d) and 100 (e) ms

The motion of the dummy during the experimental sled test was captured using a stationary high-speed camera. Thus, after 100 ms, the dummy is eclipsed by both B-pillar and front passenger seat. For this reason, the qualitative comparison of Figure 123 focuses only on pretensioning and impact phases:

- In the first 10 ms of the test, the sled is almost stationary and the only variation in the FE model from the initial instant of simulation is the application of the minimum tension to the belt. As mentioned in Section 8.3.2, the retractor applies a load, simulating the seat belt tightening, thus eliminating any offset between webbing and dummy defined in the pre-processing phase.

- At t = 20 ms, the pretensioning load on the belt reaches its maximum and the consequent deflection of the dummy chest can be noticed in both experimental and numerical events. At the same time, the forward displacement of the dummy neck and arms caused by the sled acceleration can be noticed;

- At t = 60 and 80 ms, the sled is still accelerating while the retractor is locked. Therefore, the dummy body continues to move forward, increasing the load on the locked belt. The forward excursion of the dummy head can be observed. Moreover, at t = 80 ms, the DLT limits the load on the lap belt, unlocking the lower slip ring. This causes a forward motion of the dummy pelvic region, which can be noticed in Figure 123d and e.

- After t = 80 ms, the CLL activates, releasing the webbing to ensure the load limitation. This releases the dummy torso, while the load on the pelvis decreases, causing the subsequent lock of the DLT after 20 ms. This cooperation of retractor and DLT leads to the rotation of the dummy torso with respect to the y-axis, exploiting the vehicle cabin space to reduce the load on the chest. Such a configuration can be observed in Figure e.

Although an acceptable tracking of the experimental Q10 after 100 ms is not available, the numerical model behavior during the second half of test is shown in Figure 124.

(a)

(b)

(c)

(d)
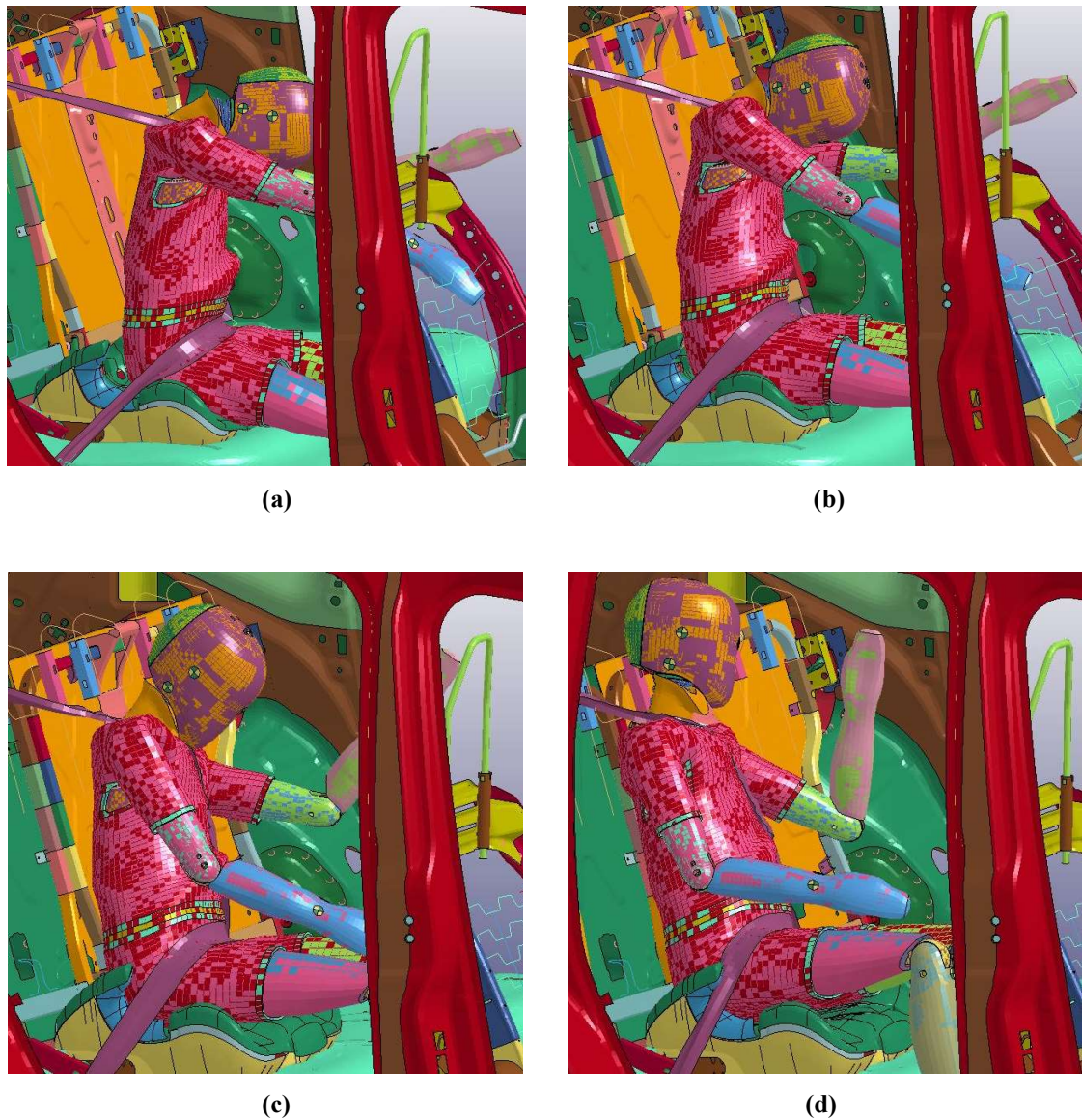
Figure 124 – Virtual dummy configuration at 120 (a), 140 (b), 170 (c) and 200 (d) ms of simulation

At t = 117 ms, the rebound phase begins, as shown by the reduction of the shoulder belt load. This an event is a consequence of the rearward movement of the vehicle after the impact against the barrier is completely absorbed, and it is simulated keeping the sled velocity equal to a constant value.

Figure 124a shows the maximum forward excursion of the virtual dummy, with downward-facing head and the right hand impacting the frontal backseat suspension frame. In the next figures, the Q10 moves towards the C-pillar, restoring the positions of neck, torso, and pelvis. During this phase, all injury parameters drop from the peaks reached during the first half of the test, in which the operation of the restraint system is fundamental to avoid serious injuries to the occupant.

9.3.2.5 Head

The first body region analyzed in the model validation is the head of the Q10, which accelerations (and related *HIC*) were compared. Since this simulation reproduces an offset frontal impact, all the three components of the head acceleration were analyzed and reported in Figure 125.

(a)

(b)

(c)
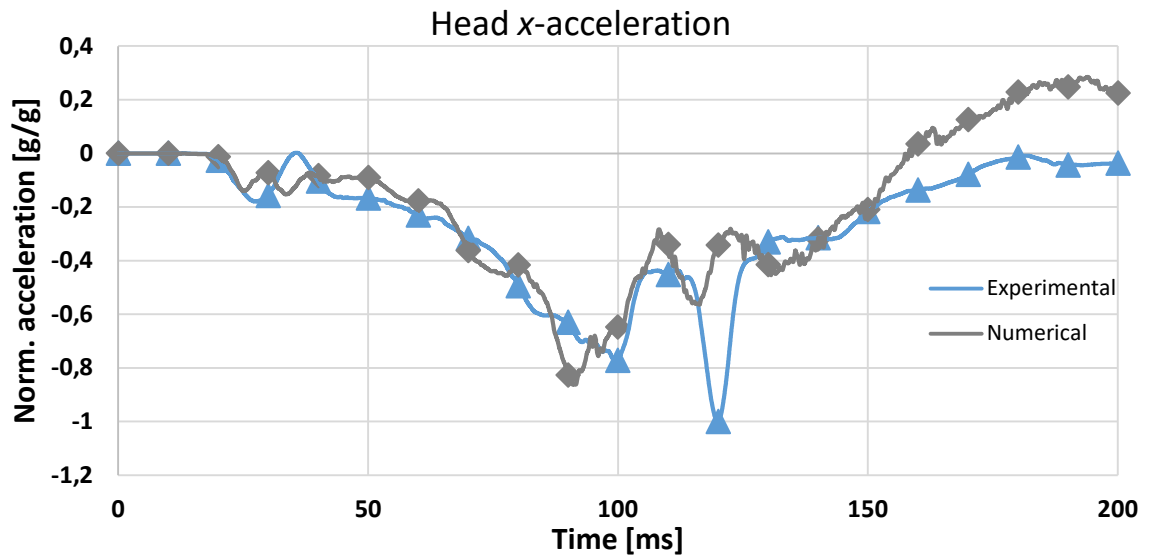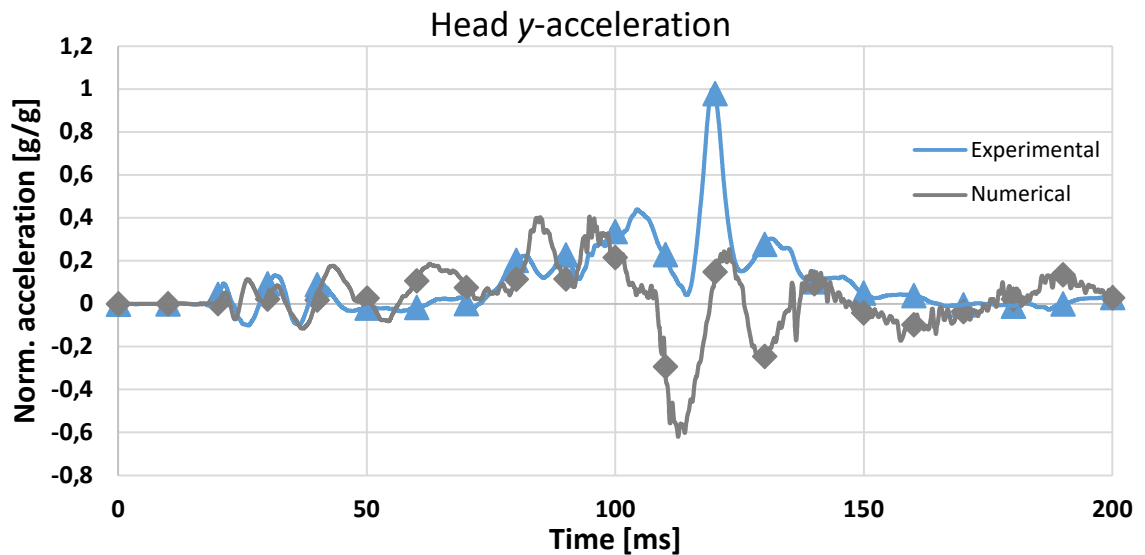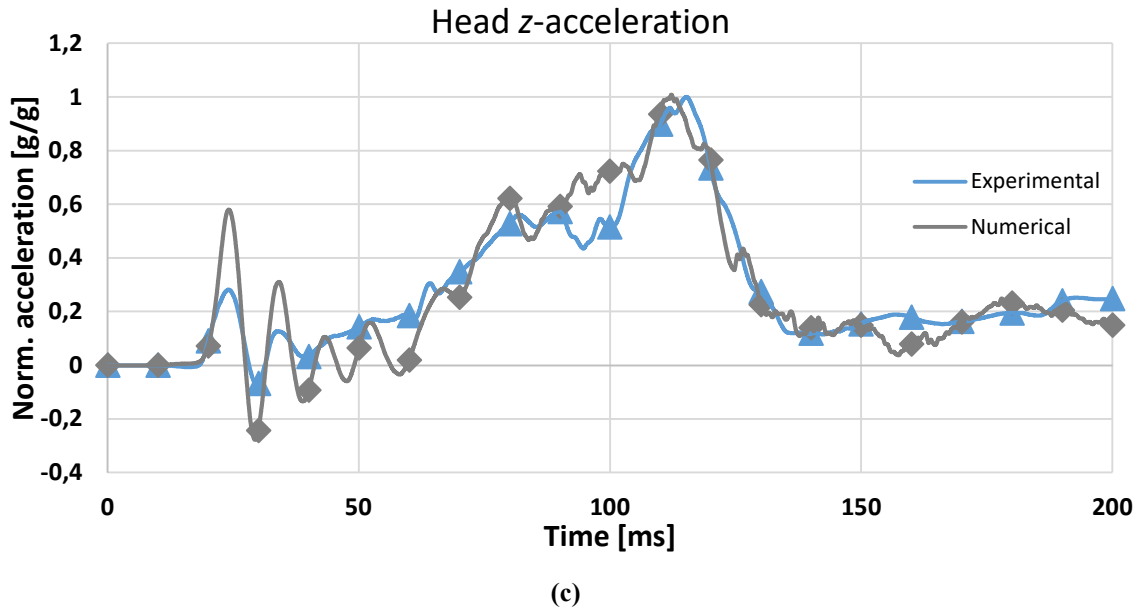
Figure 125 – Experimental and numerical head accelerations in *x* (a), *y* (b) and *z* (c) directions

The three curves show a good level of prediction during the loading phase (pretensioning and locking of the retractor), between $t = 0$ and $t = 100$ ms. All accelerations start to rise at the same time instant of the experimental ones, evidencing the aligned firing of the virtual pretensioner. At the end of the operation of the CLL ($t = 120$ ms), instead, the *x* and *y*-accelerations peaks are largely underestimated by the numerical model. Such misaligning can be caused by a different influence of the shoulder belt on the dummy neck and by a dissimilar motion of the booster seat during the event, which can influence the whole response of the Q10. The FE booster is constrained to the ISOFIX anchors through a revolute joint, which impedes the translation of the CRS clamps over the anchors, along the *y*-direction. Since this displacement would be less than 10 mm, it was decided to neglect it in the FE model, but it could cause a different locking of the booster motion, and affect the dummy reaction. The *x*-acceleration reports also a miscorrelation during the rebound phase, overestimating the values of approximately 15%. On the other hand, the *z*-acceleration shows really close experimental and numerical peaks, at $t = 116$ ms and $t = 112$ ms respectively, and the curve trend is followed in the rebound phase as well. Instead, in the pretensioning phase, higher loads are registered in the numerical model. This can be caused by different internal entities between experimental and numerical dummy, which can influence the load pattern within its body.

The good level of prediction of the *z*-acceleration, which is the predominant component, leads to a consequently reasonable estimation of the *HIC*, shown in Figure 126.
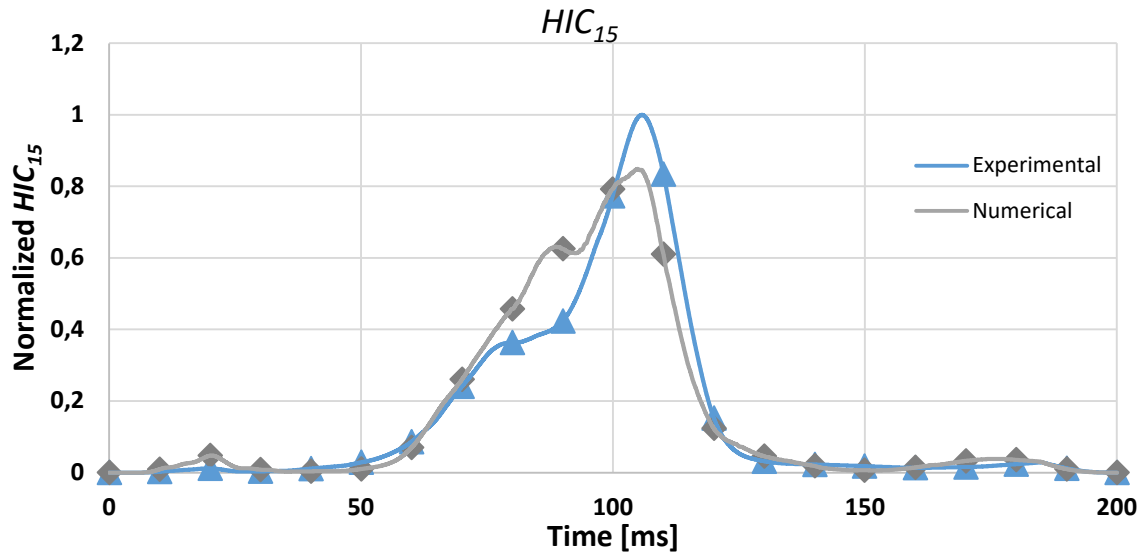
(a)
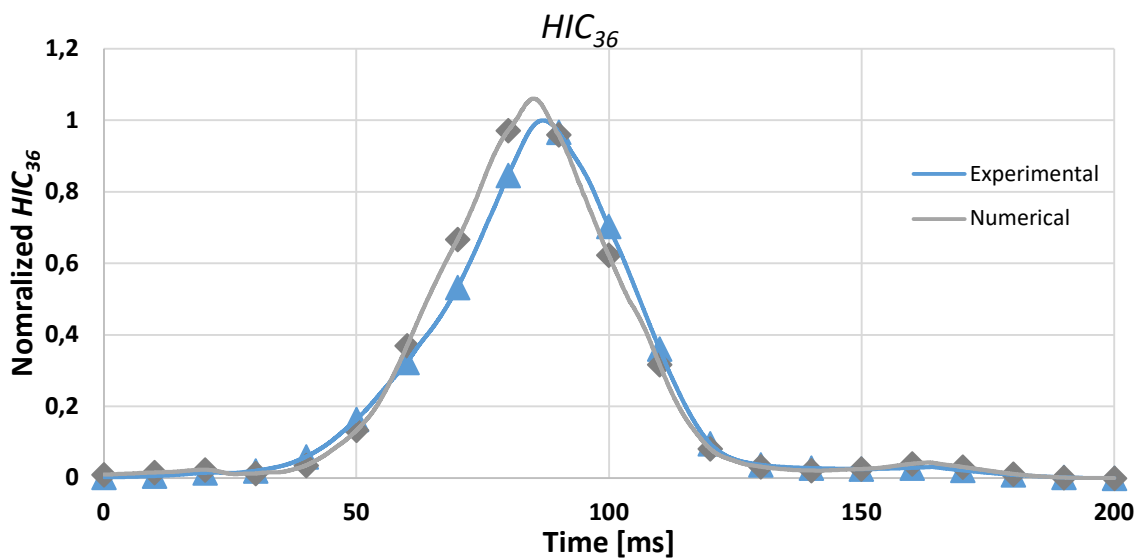
(b)

Figure 126 – Experimental and numerical *HIC₃₆*

As deducible from the comparison between experimental and numerical resultant accelerations, the trend of both *HIC* curves were well estimated. The HIC_{15} peak is slightly underestimated by the numerical model (Figure 126a), with an anticipated rise at $t = 70$ ms and an offset of 19%. The HIC_{36} (Figure 126b) is lightly overestimated by 2%, but the peak time instant is well predicted.

9.3.2.6   Chest

The dummy chest accelerations are one of the most influenced injury parameters by the pretensioner and load limiting devices since they are registered in the closest load cell to the shoulder belt. Chest *x*, *y,* and *z*-accelerations as a function of time are shown in Figure 127.

(a)

(b)

(c)
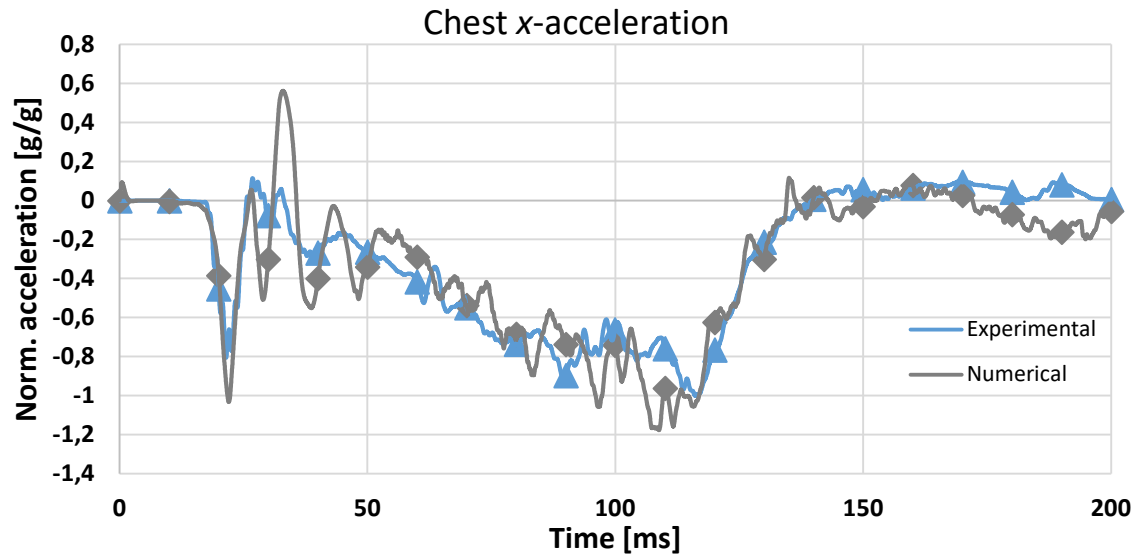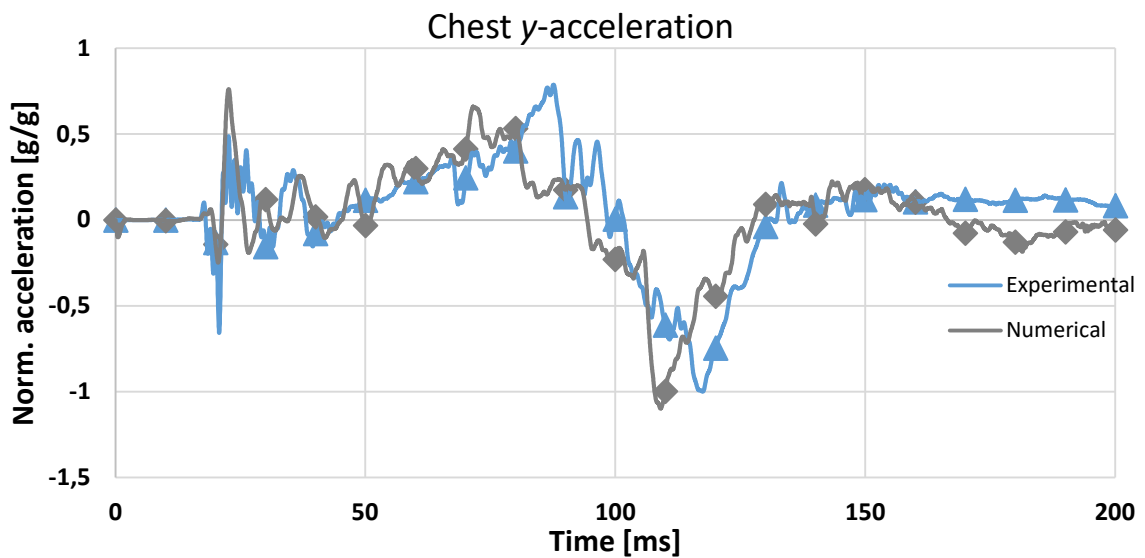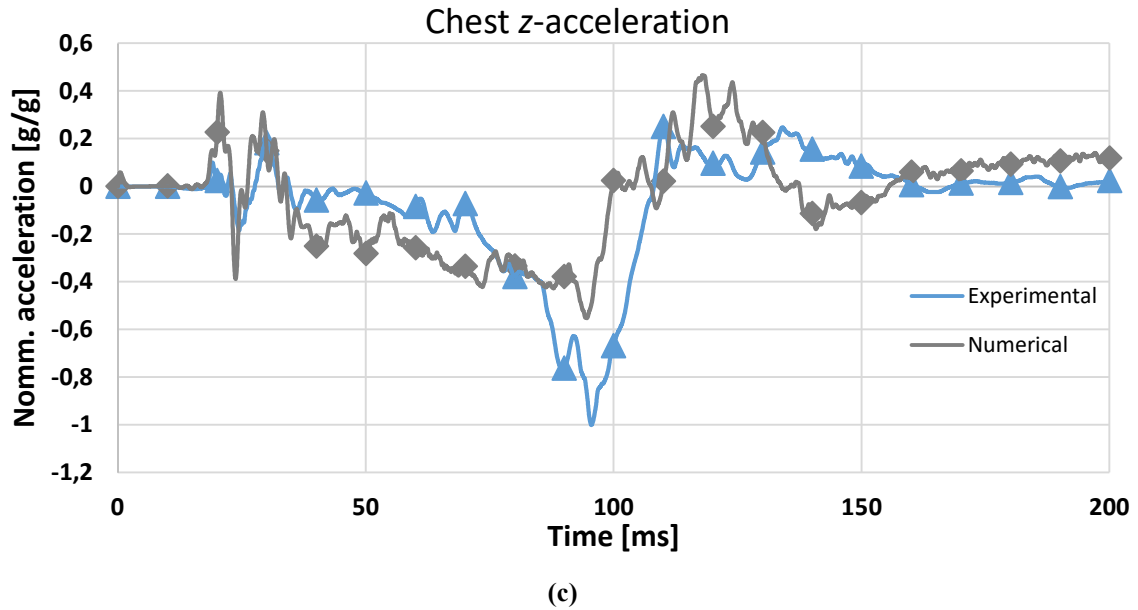
Figure 127 – Experimental and numerical chest *x* (a), *y* (b) and *z* (c) accelerations

The numerical model well predicts the overall trend and values of the chest *x*-acceleration registered during the experimental sled test, except for three excessive oscillations after the belt pretensioning. The numerical *y*-acceleration is correlated to the experimental output during the loading phase, with a subsequent underestimation of the positive peak value and an anticipation of approximately 8 ms of the negative peak, during the load limitation. Again, a dissimilar *y*-acceleration can be due to the displacement of the virtual CRS, and to slightly different position and behavior of the locking tongue in the numerical model. The *z*-component is the most miscorrelated, with alternate underestimations and overestimations of the load during the whole event. However, the overall trend of the curve is acceptably respected, with the numerical negative peak coincident in time instant with the experimental one. Such misaligning can be caused by the position of the seat belt on the dummy chest during the entire event, which can be different with respect to the experimental test. This difference can be due to a divergent path of the shoulder belt in the numerical model, which can be caused by a lower friction between belt webbing and dummy vest with respect to the real sled test. Lastly, the *x*-acceleration highlights the influence of the load limiter on the dummy, remaining within the same limit between *t* = 80 and *t* = 120 ms, the time window in which the CLL activates. Such limitation is acceptably predicted in the numerical model, but two higher peaks are registered in the last 20 ms of limiting event.

9.3.2.7 Pelvis

The Q10 pelvic region acceleration is mostly influenced by the operation of the lap belt. With 10-year-old children, the lap belt is in a higher condition of stress with respect to an adult occupant, due to the dimension of the booster seat summed to the height of the child's legs. For this reason, the DLT can be very helpful, acting as a load limiter on the dummy pelvis.

Experimental and numerical pelvis x, y and z-accelerations are displayed in Figure 128.

(a)

(b)

(c)
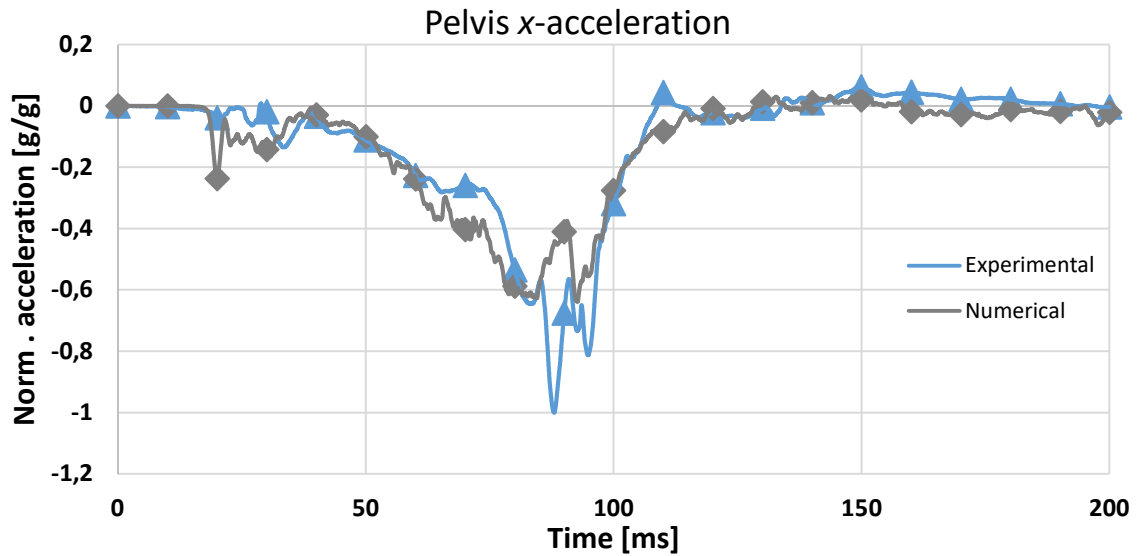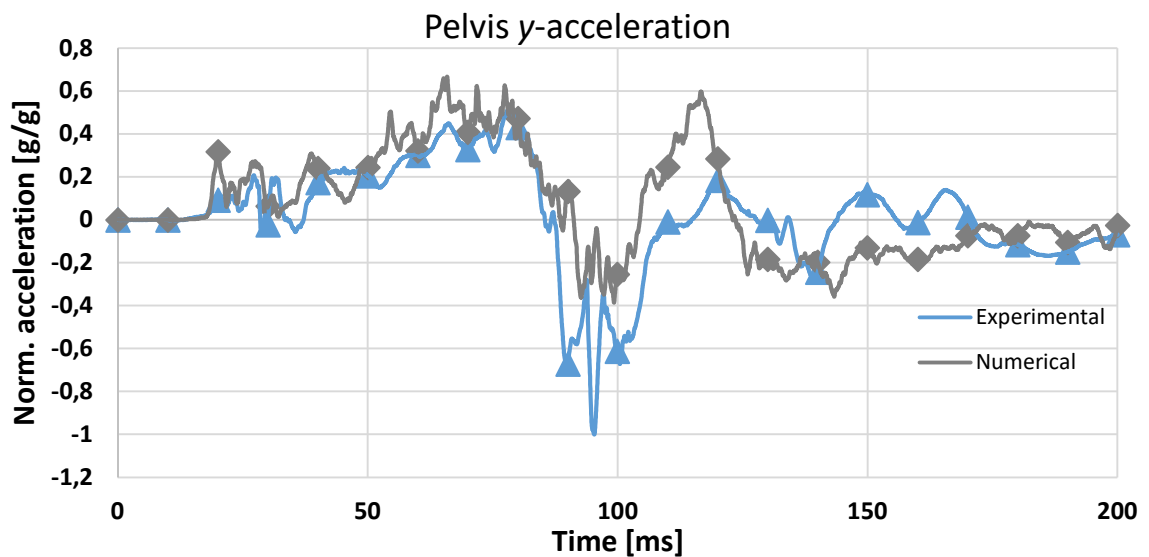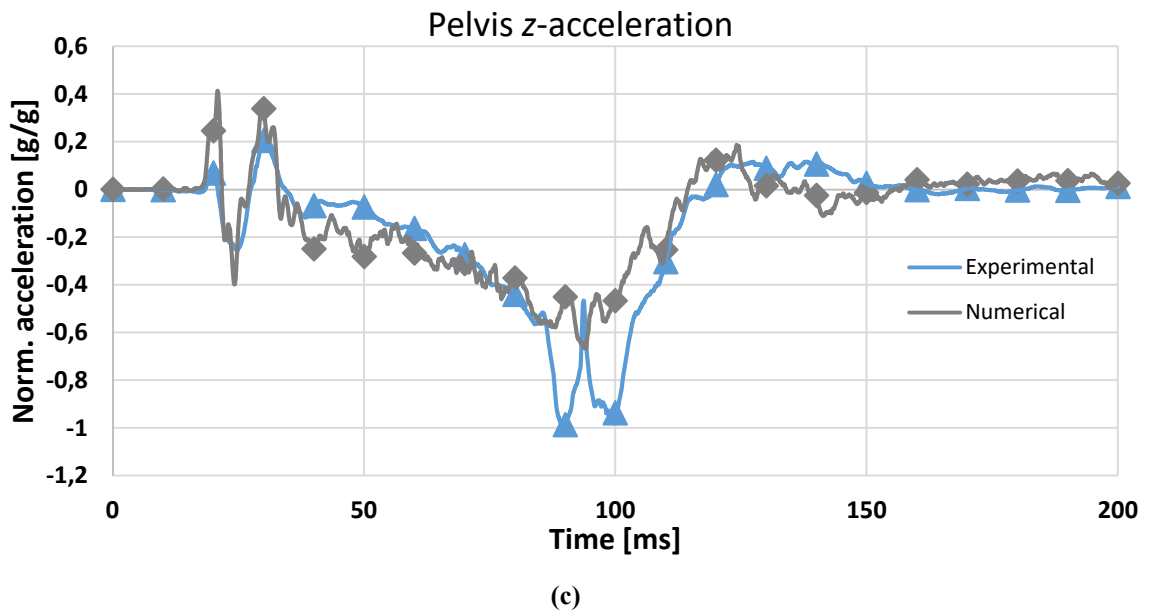
Figure 128 – Experimental and numerical pelvis *x* (a), *y* (b) and *z* (c) accelerations

The *x*-component of the pelvis acceleration is well predicted by the numerical model but presents some overestimation during the loading phase and a great underestimation of the acceleration peak at $t = 88$ ms. The virtual *z*-acceleration shows the characteristics of the first component, following the experimental curve and underestimating the peaks reached during the CLL operation. The *y*-component is the least correlated to the experimental output: it well predicts the pelvis acceleration during the loading phase and it underestimates the load when the CLL acts but also overestimates the physical values during the rebound phase.

To conclude, all components report lower values between $t = 80$ and $t = 100$ ms, the time interval within which the DLT unlocks and limits the load on the lap belt. Therefore, the numerical model is characterized by a stricter limiting behavior than the experimental locking tongue. Most likely, such a device is not yet perfectly operating during a high-speed real event, thus its numerical reproduction can overestimate its effects.

9.3.2.8 Upper neck

The upper neck is one of the three Q10 regions monitored by Euro NCAP for the final assessment in the ODB test, as well as head and chest. The *x*, *y*, and *z*-components of the force acting on this load cell during both experimental and numerical events are reported in Figure 129.
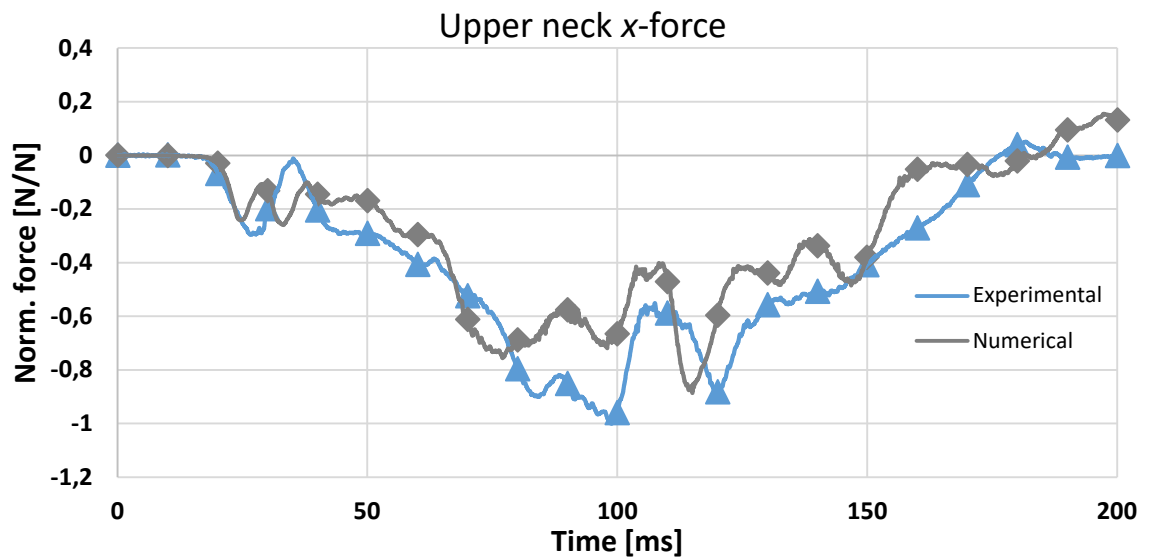
(a)
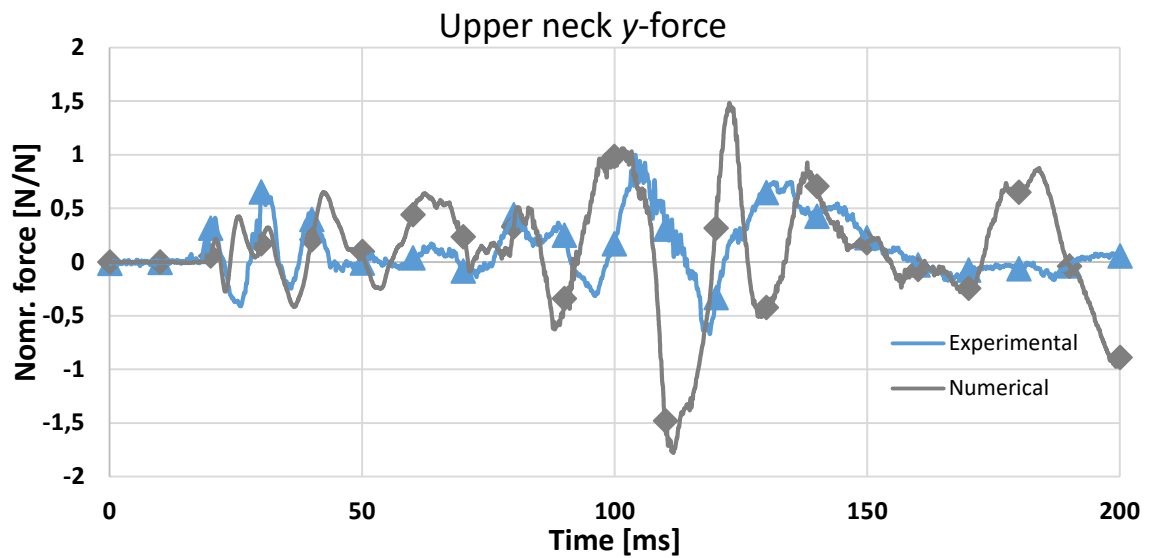
(b)
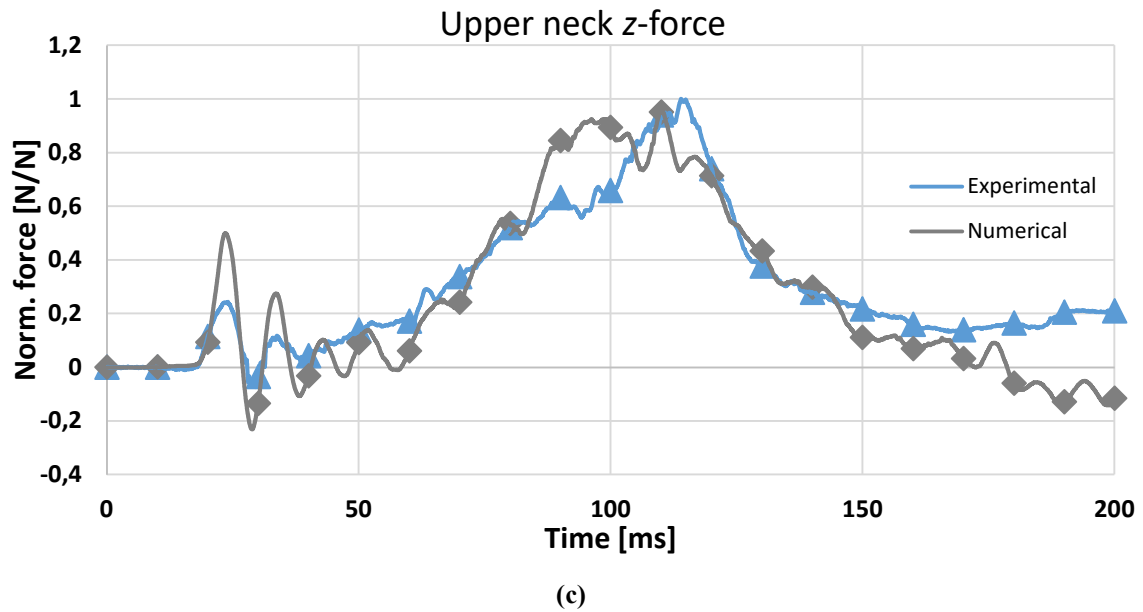
Figure 129 – Experimental and numerical upper neck *x* (a), *y* (b) and *z* (c) forces

The overall estimation of the *x*-component of the upper neck force in the numerical model is quite acceptable. The trend of the experimental curve is respected, but at the beginning of the load limiting phase (t = 80 ms) the load is underpredicted. The peak at t = 120 ms, instead, is well predicted in magnitude but occurs approximately 4 ms too early. During the loading phase, the load on the neck is generally underestimated. The *y*-component shows several misalignments between numerical and experimental results: mostly during the action of the CLL, the load peaks occur approximately 5 ms too early and are overestimated. Also, the numerical rebound phase reports an unexpected increase and decrease of the load during the last instants of the event. The trend of the *z*-component is well predicted by the FE model, with an overestimation of the load during the belt pretensioning and at the beginning of the CLL operation. The vertical load peak is almost coincident in both magnitude and time of emergence. The rebound phase again shows some misalignment.

Generally, the upper neck load is very similar in behavior to the head acceleration, and the performance of the former region influences the level of correlation of the latter. The three components of the upper neck moment are reported in Figure 130.
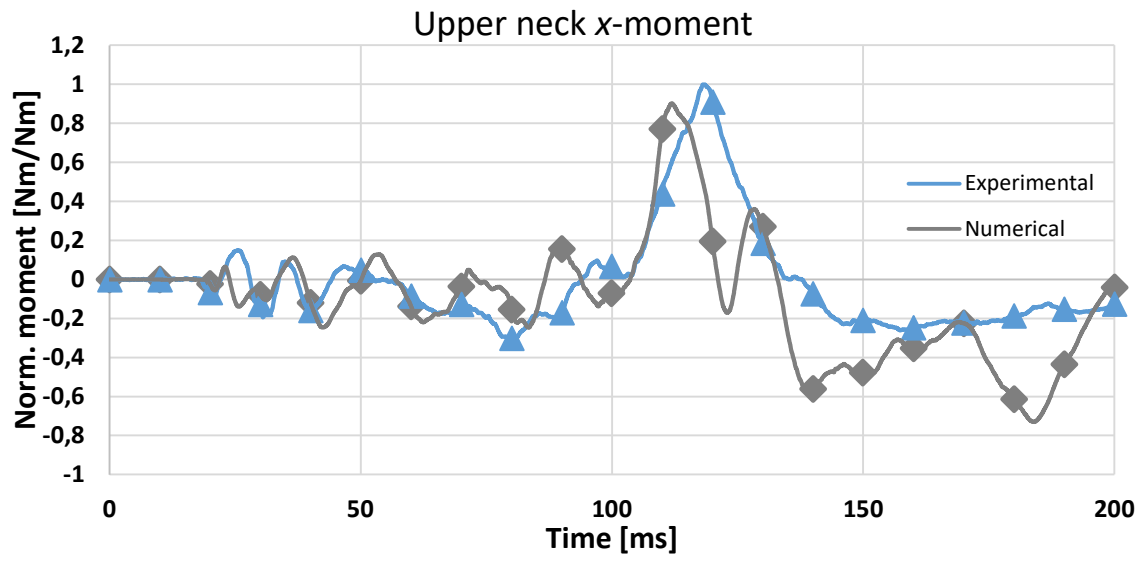
(a)
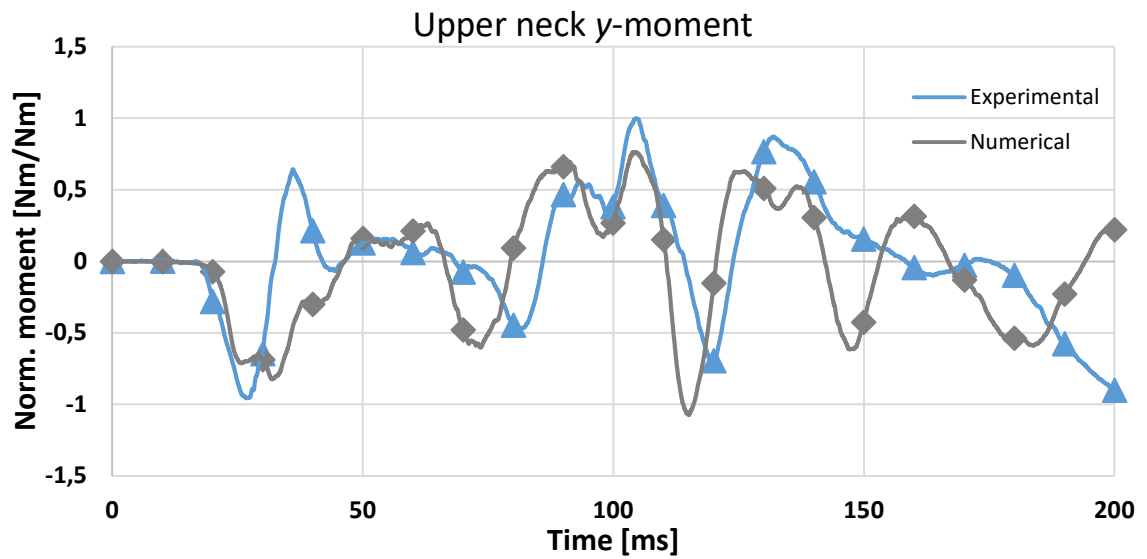
(b)
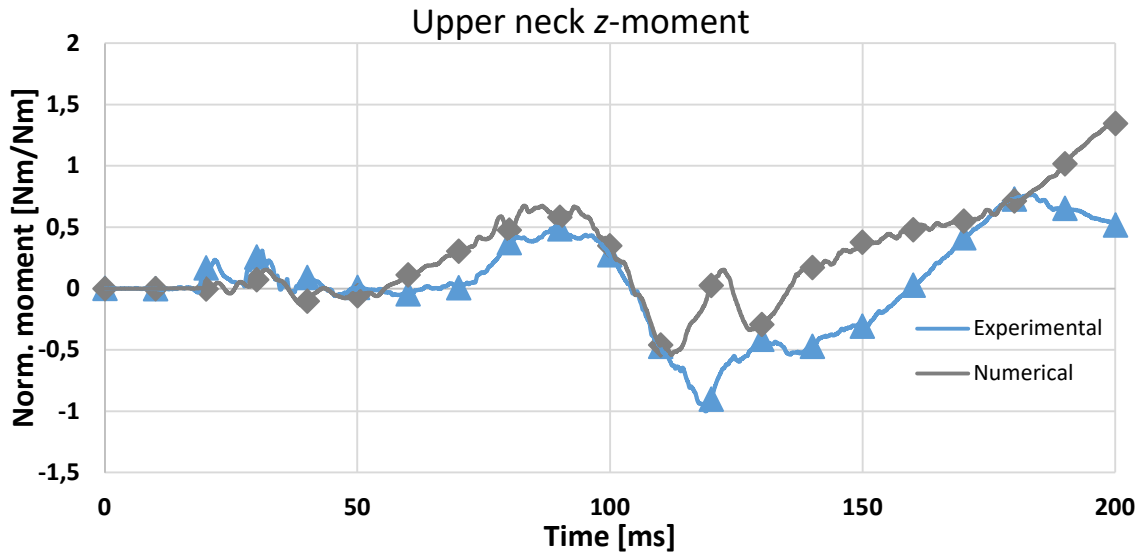
(c)

Figure 130 – Experimental and numerical upper neck *x* (a), *y* (b) and *z* (c) moments

The moments in the numerical models are always difficult to predict with high precision. Usually, the overall behavior can be respected but peaks and oscillations are anticipated or delayed. The overall trend of the *x*-moment is acceptably respected by the numerical output, except for the rebound phase. The peak at $t = 119$ ms occurs 5 ms too soon and is slightly underestimated. The same comment can be made for the *y*-moment (bending). This time, the load at $t = 120$ ms is overestimated. The *z*-moment, instead, displays a significant miscorrelation from the CLL operation to the end of the simulation.

North American Vehicle Safety Standards utilize the *Nij* criterion to evaluate the level of stress of the child neck generated by the combination of tension (F_z) and bending (M_y). The evaluation of this a parameter during real and virtual events is shown in Figure 131.
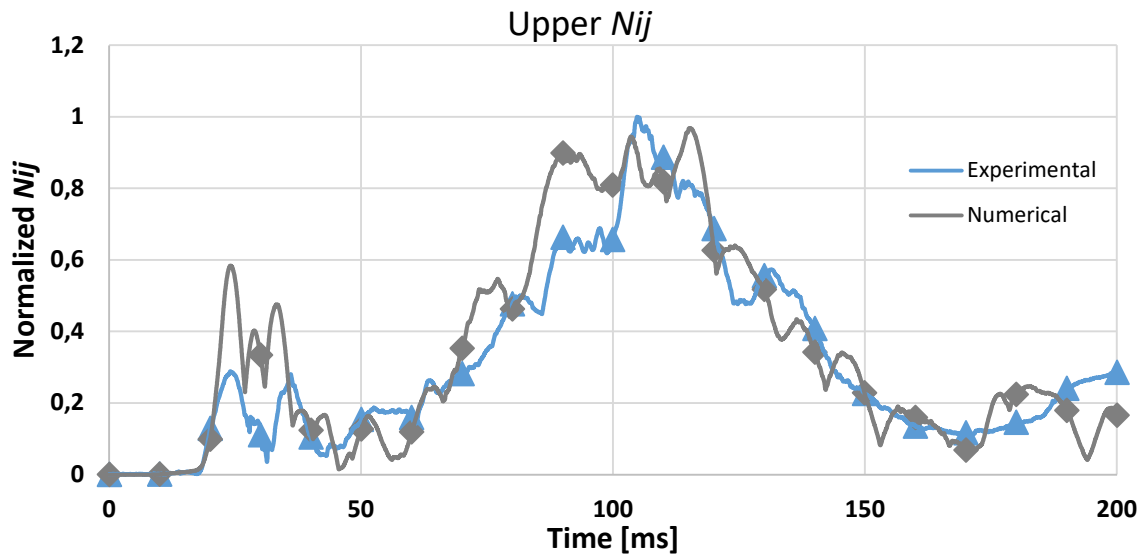
Figure 131 – Experimental and numerical *Nij*

The numerical model well predicts the neck stress condition, with an overestimation during the loading phase (as already noticed observing *z*-force and *y*-moment) and a realistic prediction of the load peak, during the operation of the CLL. This correlation demonstrates that the prediction of the upper neck injury risk following standardized parameters is quite realistic.

9.3.2.9 Lower neck

The lower neck cell is more influenced by the chest loading conditions during the test and for this reason, it is not considered in the Euro NCAP Child Occupant Protection test assessment. Nevertheless, its observation is useful for obtaining an additional parameters to validate the FE model. All components of the force acting on experimental and numerical lower neck are shown in Figure 132.
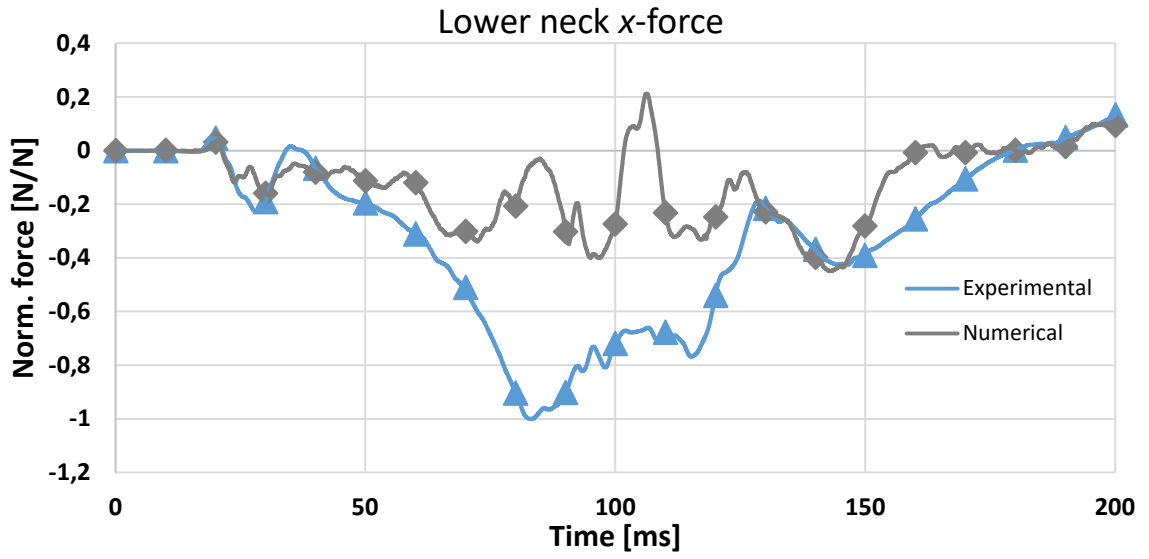
(a)
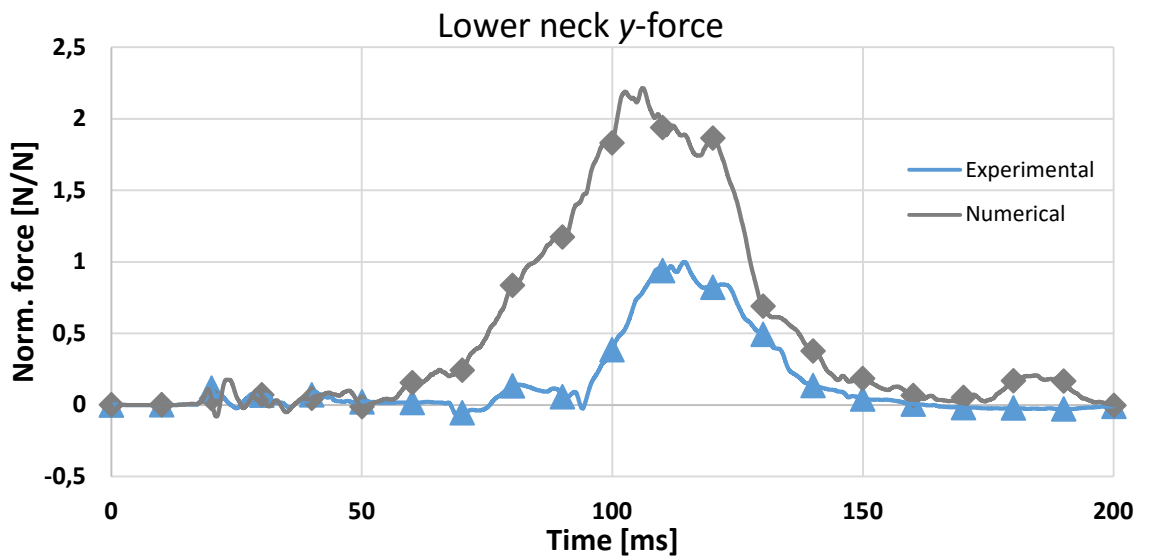
(b)
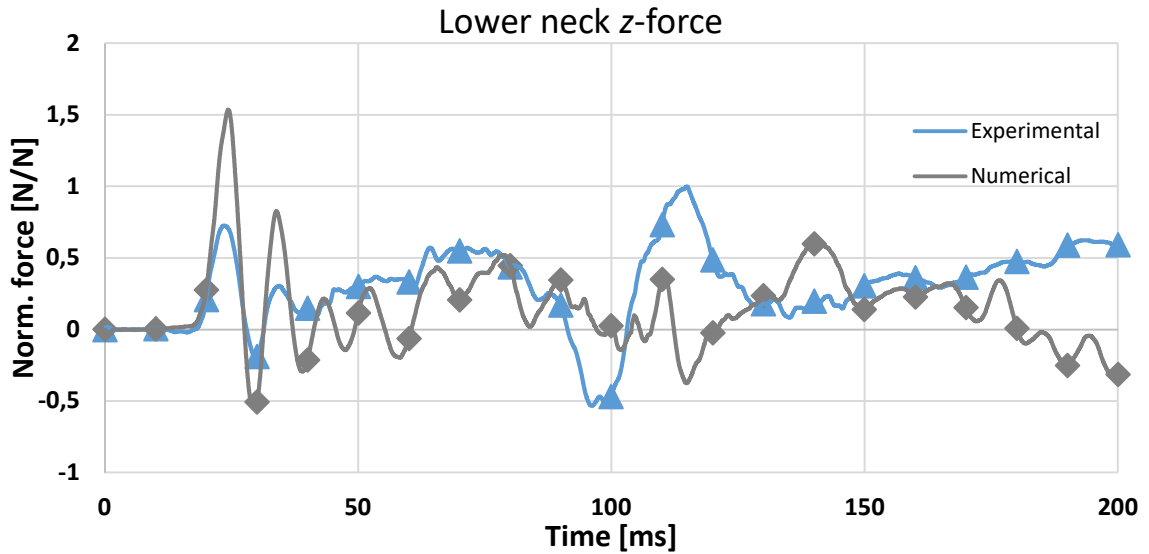
(c)

Figure 132 – Experimental and numerical lower neck *x* (a), *y* (b) and *z* (c) forces

The *x* and *y* numerical forces are respectively underestimated and overestimated during the load limiting phase. In the *y*-force, a similarity in the curve trends can be appreciated. The virtual z-component shows overestimated peaks during the pretensioning phase and does not predict the behavior of the experimental load. The lower neck virtual and experimental moments are displayed in Figure 133.
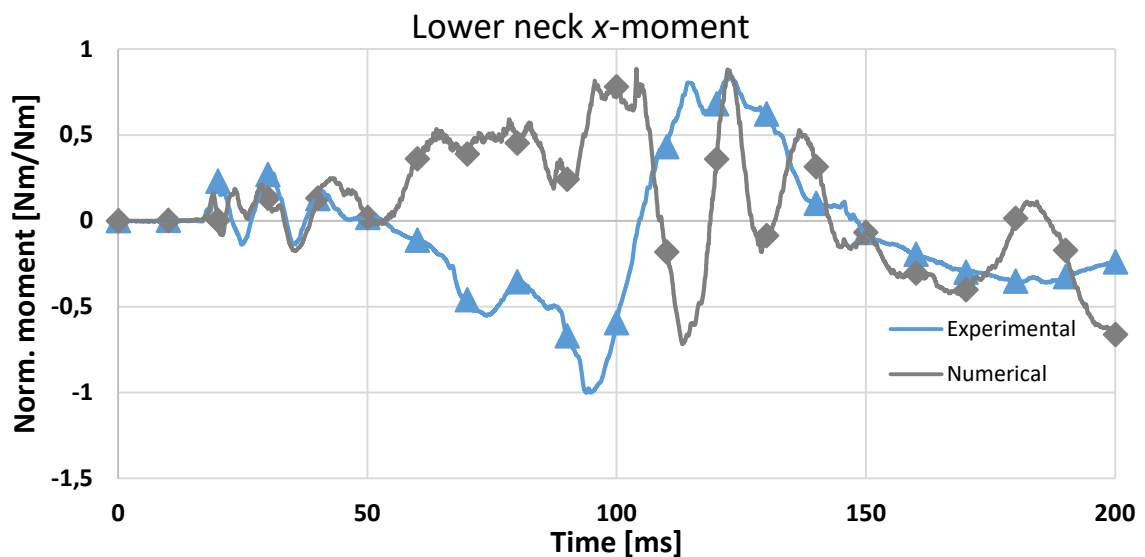
(a)
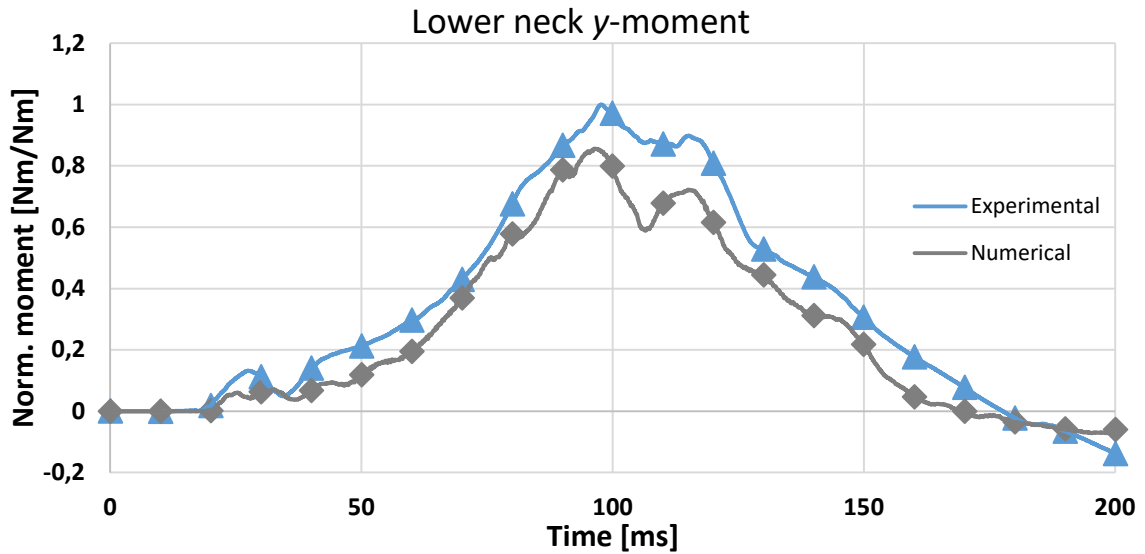
(b)
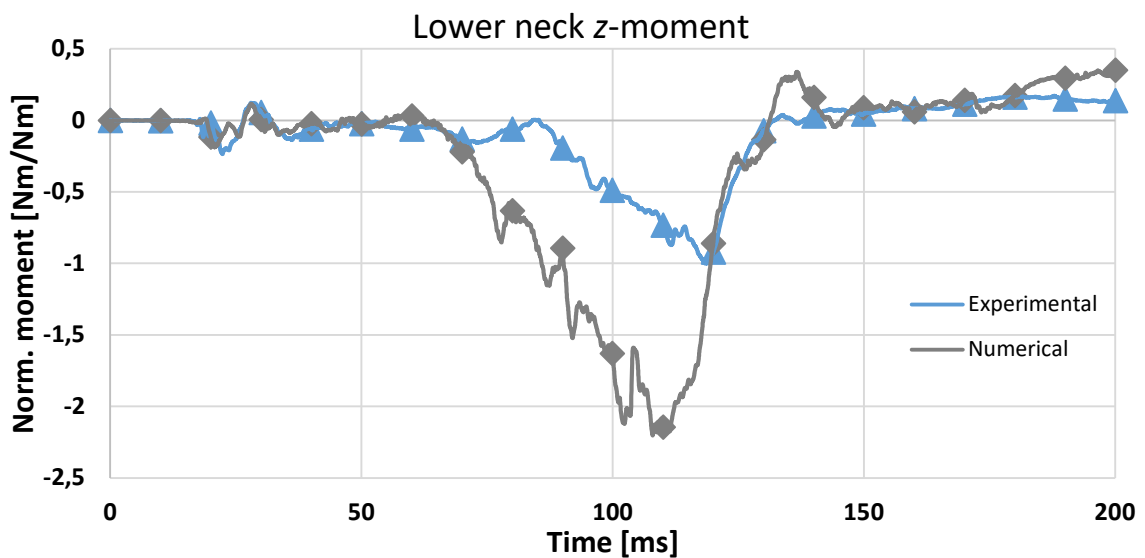
(c)

Figure 133 – Experimental and numerical lower neck *x* (a), *y* (b) and *z* (c) moments

The *x*-moment development is generally not predicted in the FE environment. The lowest peak is delayed by approximately 20 ms and slightly underestimated. The *y*-moment, instead, is very well predicted in behavior over the whole event, but always underestimated: the numerical peak at $t = 97$ ms coincides in time with the experimental curve but is underappreciated of about 15 Nm. Lastly, the *z*-moment is greatly overestimated during the load limiting phase. It is important to notice that the *y*-component is predominant in the lower neck resultant moment, thus its adequate prediction is a positive signal in terms of injury risk prediction.

9.3.2.10 Error analysis

Table 15 summarises cumulative error E and validation metric V computed for the injury parameters analyzed in the previous sections.

Injury parameter	$E_{5\%}$	$V_{5\%}$	$E_{10\%}$	$V_{10\%}$	$E_{15\%}$	$V_{15\%}$
Head *x*-acceleration	0.293	0.783	0.218	0.816	0.138	0.868
Head *y*-acceleration	0.507	0.728	0.344	0.791	0.234	0.849
Head *z*-acceleration	0.292	0.761	0.251	0.783	0.184	0.833
Chest *x*-acceleration	0.505	0.718	0.166	0.861	0.157	0.865
Chest *y*-acceleration	0.758	0.508	0.568	0.607	0.235	0.811
Chest *z*-acceleration	0.667	0.633	0.378	0.756	0.184	0.860
Pelvis *x*-acceleration	0.119	0.892	0.074	0.930	0.064	0.939
Pelvis *y*-acceleration	0.667	0.622	0.391	0.728	0.194	0.837
Pelvis *z*-acceleration	0.425	0.724	0.183	0.844	0.102	0.905
Upper neck *x*-force	0.253	0.773	0.226	0.790	0.210	0.804
Upper neck *y*-force	2.006	0.497	0.955	0.647	0.622	0.727
Upper neck *z*-force	0.453	0.659	0.395	0.697	0.317	0.761
Upper neck *x*-moment	0.790	0.560	0.587	0.647	0.378	0.740
Upper neck *y*-moment	1.266	0.519	0.730	0.642	0.572	0.689
Upper neck *z*-moment	0.732	0.598	0.549	0.655	0.462	0.688
Lower neck *x*-force	0.421	0.646	0.388	0.672	0.364	0.691
Lower neck *y*-force	1.333	0.665	0.767	0.754	0.376	0.828
Lower neck *z*-force	0.799	0.472	0.747	0.492	0.650	0.535
Lower neck *x*-moment	1.155	0.418	0.974	0.487	0.775	0.565
Lower neck *y*-moment	0.272	0.751	0.226	0.789	0.170	0.839
Lower neck *z*-moment	1.049	0.576	0.608	0.701	0.420	0.804

Table 15 – Cumulative error and validation metric computed with the Q10 experimental and numerical injury parameters

From the definition of cumulative error and validation metric, such indices are supposed to be approximately complementary to 1 when analyzing the same parameter, if the relative error is between 0 and 1. When calculated for experimental values closer to 0, the relative error overcomes the unity; in this situation, the hyperbolic tangent function in the computation of the validation metric approximates the error to 1, but the cumulative error is instead computed

without any rounding off. The proximity to 0 that affects the value of relative error is not universally quantifiable and depends on each observed parameter.

Head y-acceleration, chest x-acceleration, pelvis y, and z-accelerations, upper neck z-force and lower neck y-force $E_{5\%}$ and $V_{5\%}$ show a sum higher than 1, demonstrating that setting the error criterion limit on 5% of the maximum absolute experimental value to compute the validation indices is not congruent with the obtained results. Instead, when the error criterion bound is equal to 10%, the sum of E and V of these parameters is very close to 1, hence their computation properly represents the level of correlation between numerical and experimental outputs. In addition, if such indices are already complementary, $E_{15\%}$ and $V_{15\%}$ will indicate a better correlation only because additional relative errors in the time domain were set equal to 0, overestimating the level of prediction of the numerical model. On the other hand, chest y and z-acceleration, upper neck y-force, upper neck x, y and z-moment, and lower neck x and z-moments report values of $E_{10\%}$ and $V_{10\%}$ which sum overcomes the unity, thus the expansion of the error criterion window to $\pm$ 15% is necessary to obtain an optimal understanding of the correlation between the different sets of data.

Additionally, head x and z-accelerations, pelvis x-acceleration, upper neck x-force, and lower neck y-moment $E_{5\%}$ and $V_{5\%}$ are approximately complementary to 1, proving that narrowing the error criterion window avoids an excessive overestimation of numerical output precision.

Lastly, it is important to notice that lower neck z-force and x and z-moments report a sum of E and V much higher than 1 with every error criterion. Such miscorrelation is caused by the oscillation of the respective curves around 0, thus by the consequent presence of many points within the error criterion window. This leads to an improper estimation of the model precision for these parameters. Therefore, these factors can not correctly indicate the level of correlation of the considered FE model.

Such sensitivity analysis has been shown to provide a more accurate quantification of the prediction of the Finite Element model defined in this research. Since Section 11 will aim to observe the influence on the model precision given by the variation of a single friction coefficient, Table 16 lists the percentage on the error criterion bound calculation that will be utilized for each injury parameter. In this way, every single change in the model output will influence the validation indices in the most consistent mode.

Injury parameter	*Error criterion percentage*
Head *x*-acceleration	5%
Head *y*-acceleration	10%
Head *z*-acceleration	5%
Chest *x*-acceleration	10%
Chest *y*-acceleration	15%
Chest *z*-acceleration	15%
Pelvis *x*-acceleration	5%
Pelvis *y*-acceleration	10%
Pelvis *z*-acceleration	10%
Upper neck *x*-force	5%
Upper neck *y*-force	15%
Upper neck *z*-force	10%
Upper neck *x*-moment	15%
Upper neck *y*-moment	15%
Upper neck *z*-moment	15%
Lower neck *x*-force	10%
Lower neck *y*-force	15%
Lower neck *z*-force	15%
Lower neck *x*-moment	15%
Lower neck *y*-moment	5%
Lower neck *z*-moment	15%

Table 16 – Percentage utilized in the error criterion bound calculation for each injury parameter

To conclude, from Table 15, an acceptable prediction of the most relevant injury parameters can be quantified from the output of the Finite Element model. Therefore, the model reasonably simulates the kinematics and estimates the injury risk of the Q10, with higher correlations on head, chest and pelvis, acceptable errors on the upper neck, and a greater miscorrelation on the lower neck.

Generally, the dummy model has been shown to have higher performance in the prediction of the accelerations, rather than forces and moments. In fact, head, chest and pelvis numerical outputs report acceptable values of E and V to confirm the model as validated. Surely, they present some discrepancies with respect to the experimental data, which were already analyzed and justified in the respective sections. In addition, almost all numerical curves do not follow the respective experimental trends during the rebound phase. This can be caused by the

friction coefficient between the dummy vest and booster seat, which would need a further sensitivity study. Also, the operation of the slip ring elements, which is influenced by a dynamic friction coefficient, can affect the dummy kinematics.

Moreover, the overall incongruity between lower neck numerical and experimental outputs can have several causes, not only depending on the pre-processing steps:

- High-speed events, mostly a crash test involving hundreds of entities, are the most difficult to simulate, and there are numerous parameters (initial position, temperature, humidity, friction coefficient), that can influence the response of the model in every instant. Moreover, only one experimental test has been performed to validate the results. Therefore, a certain deviation of the outputs due to experimental variability must be considered during the validation;

- The dummy model, even being one of the most advanced FE reproductions of the Q10, is not validated with a sled test and can report many differences with respect to the physical counterpart. In addition, ten-year-old ATD virtual models are less developed than those which represent adult occupants and most Safety Standards focus on the upper load cell of the neck, neglecting the lower one. Therefore, the numerical load cell of the lower neck could not be as developed and precise as the other virtual sensors.

10. GUIDELINES SUMMARY

The guidelines and recommended practices to perform a Finite Element simulation of a full vehicle body sled test are described in detail from Chapter 5 to Chapter 9. This chapter contains the following summary with the most important advices for every phase.

MODELS UPDATE FOR FEA
- Similar level of discretization (average element dimension) for all models
- Preserving of the entities geometry while guaranteeing an optimal mesh quality
- Reproduction of all necessary connections and interactions between different bodies (*CONSTRAINED and *CONTACT)

CRS POSITIONING
- Centering of the CRS with the passenger seat
- Setting of its proper configuration (clamps length)
- Reproduction of the ISOFIX anchorages (a revolute joint has been shown to be stable and consistent with the experimental setting during the simulations)
- Check for initial penetrations and consequent correction through a pre-run

DUMMY POSITIONING
- Recommended measurement of the H-point coordinates during the experimental test
- In case the H-point is not available, center the dummy with the proper CRS and utilize the reference distances
- Recommended measurement of main joints angles (neck, pelvis, knees)
- Seating simulation to properly preload the CRS and the seat

SEAT BELT GENERATION
- To follow the same seat belt path of the experimental test
- To generate a full 2D seat belt when the webbing interacts with dummy, CRS and vehicle seat
- To set consistent mesh dimensions (5 to 10 mm average element dimension) and to obtain the most regular and even discretization

SLED TEST SIMULATION
- To define all necessary contact algorithms (a single surface algorithm is recommended for all entities which interaction does not need particular attention and without initial penetrations)
- To define an include structure when operating with several models
- To calibrate the restraint system utilising the information from the experimental test and to correctly choose the type of pretensioner based on its interaction with the retractor

11. SENSITIVITY ANALYSIS

The Dynamic Locking Tongue is one of the newest devices in the field of passive safety. It influences the slipping of the belt webbing through the locking tongue depending on the load applied to the lap belt. In addition, it has been shown to control the belt load from the first instants of a crash event, hence in the pretensioning phase, as well. Such behavior could not be easily reproduced in the FE environment. In fact, Figure 133 shows some miscorrelations on the belt loads during the first 30 ms of simulation. The numerical lap belt load increases during the pretensioning and this load transfer causes a subsequent relaxation of the shoulder belt, between $t = 30$ and $t = 40$ ms.

Therefore, it was decided to attenuate such occurrence modifying the dynamic friction coefficient FC in the *ELEMENT_SEATBELT_SLIPRING card of the locking tongue, analyzing the effect of the biomechanical parameters. Five different FC values were set: 0.05, 0.1, 0.3, 0.4 and 0.5. It is important to remember that the initial value of FC is 0.15. Successively, the cumulative error and validation metric of each output were calculated for each case, and the six cases were compared to quantify the influence of the DLT operation over the whole model.

11.1 Belt loads

The belt loads showed a more significant variation between $t = 0$ and $t = 80$ ms. Therefore, the forces registered on shoulder and lap belts in all cases during this time window are reported in Figure 134.
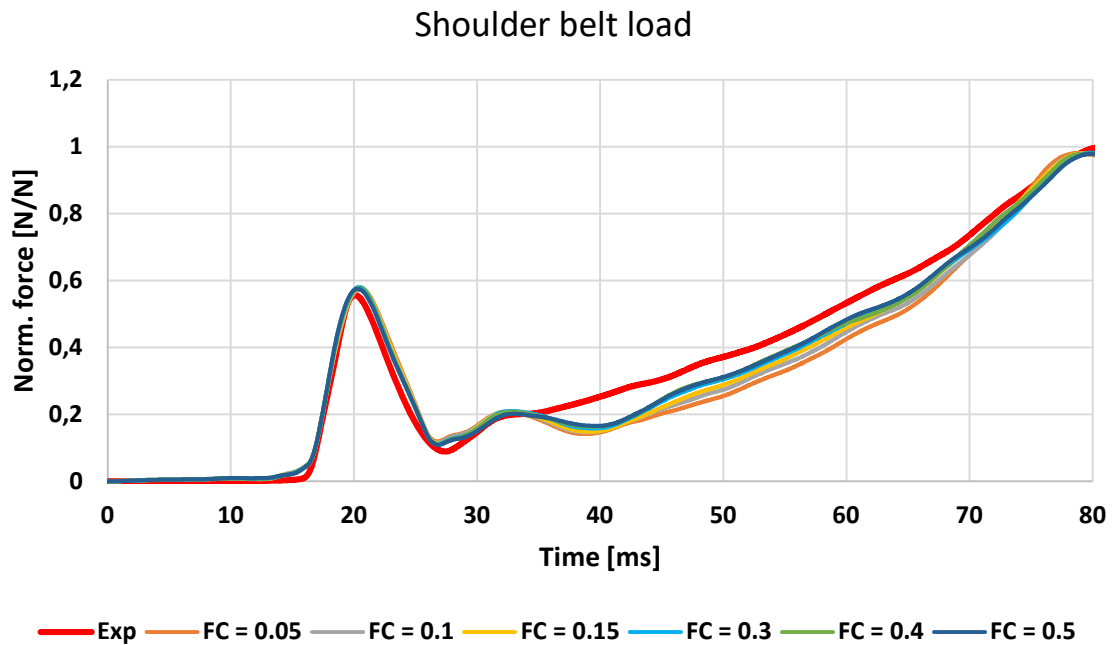
(a)
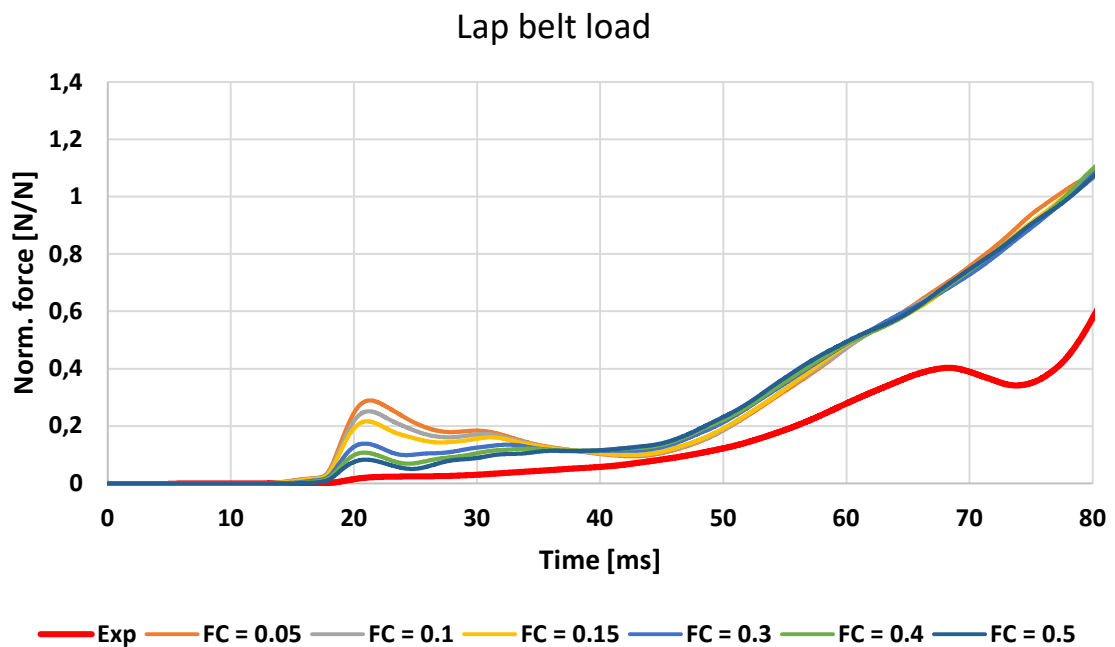
(b)

Figure 134 – Experimental and numerical loads registered on shoulder and lap belt varying FC

The expected result is shown in both Figures: Figure 134b reports the attenuation of the load increase on the lap belt due to the pretensioning, obtaining a higher correlation for higher values of FC. Figure 134a shows a consequent load increase on the shoulder belt since the high friction coefficient on the lower slip ring avoids the load transfer to the lap belt. Therefore, the numerical curve gets closer to the experimental output during the retractor locking with the increase of FC. A more realistic reproduction of the DLT was obtained in the numerical model, improving the prediction of the belt loads. The next sections will analyze the influence of such modification on every injury parameter.

11.2 Head

Cumulative error and validation metric computed in each case for head *x*, *y* and *z*-accelerations are displayed in Figure 135.

Head *x*-acceleration

(a)
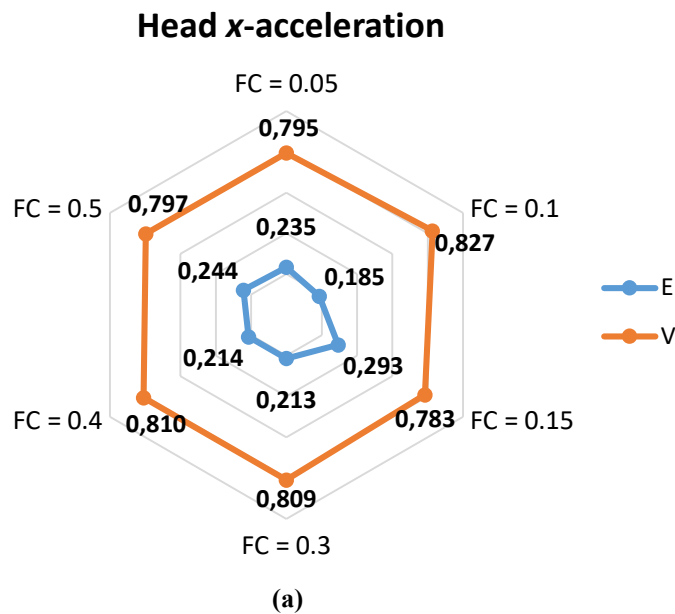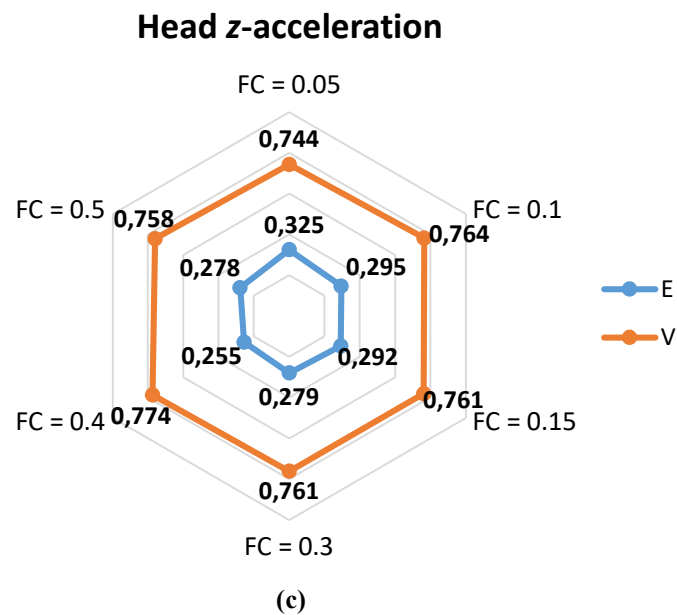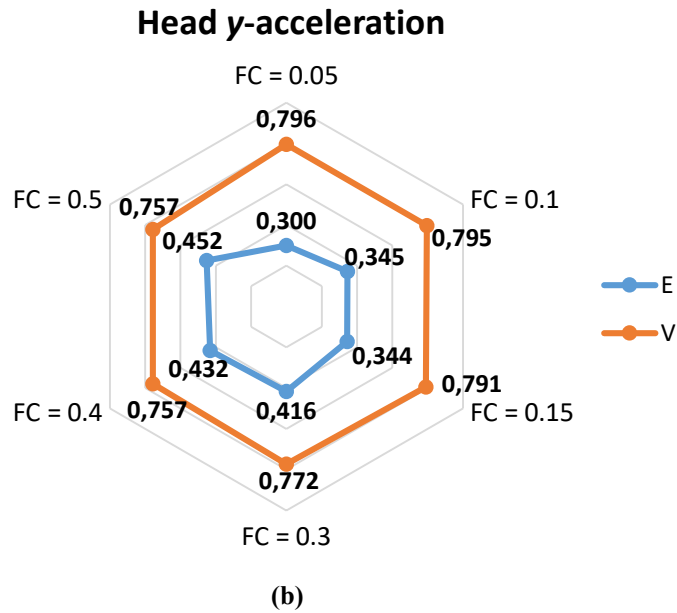
Figure 135 – Sensitivity analysis on head *x*, *y*, and *z*-accelerations

The head *x*-acceleration does not show a correlation improvement directly dependent on FC. The analysis with FC = 0.1 and FC = 0.4 shows the highest values of *V*, demonstrating that the grater prediction of this parameter can not be justified with the applied variation. The *y*-acceleration, instead, reports an increase of *V* and a decrease of *E* with lower values of FC. An almost frictionless locking tongue does not simulate the reality of the test; thus this performance improvement can not be accepted. The *z*-acceleration displays generally similar values of *V*, suggesting the low influence of the DLT operation on the predominant head acceleration. The miscorrelation between the variation of FC and head accelerations was expected since this body

extremity is not directly influenced by the DLT, but its behavior primary depends on dummy torso and neck.

11.3 Chest

E and *V* computed in each case for head *x*, *y* and *z*-accelerations are displayed in Figure 136.

Chest *x*-acceleration

(a)

Chest *y*-acceleration

(b)

(c)
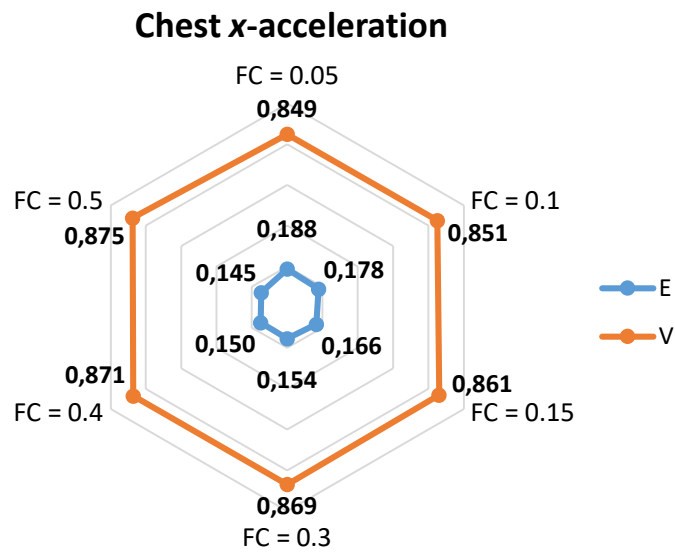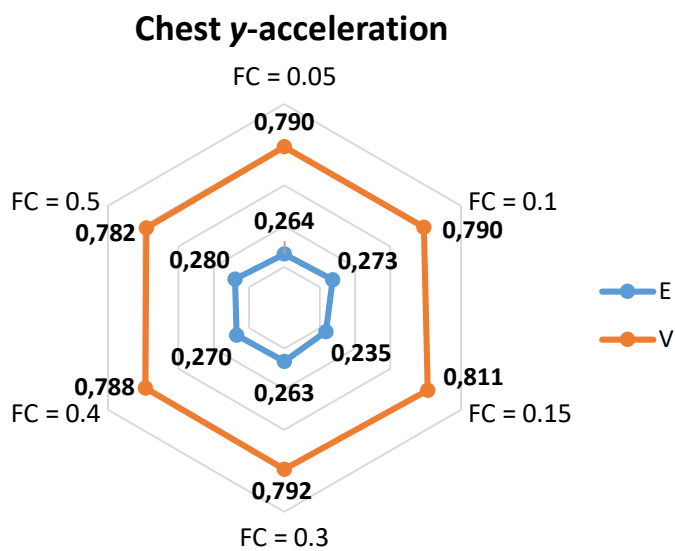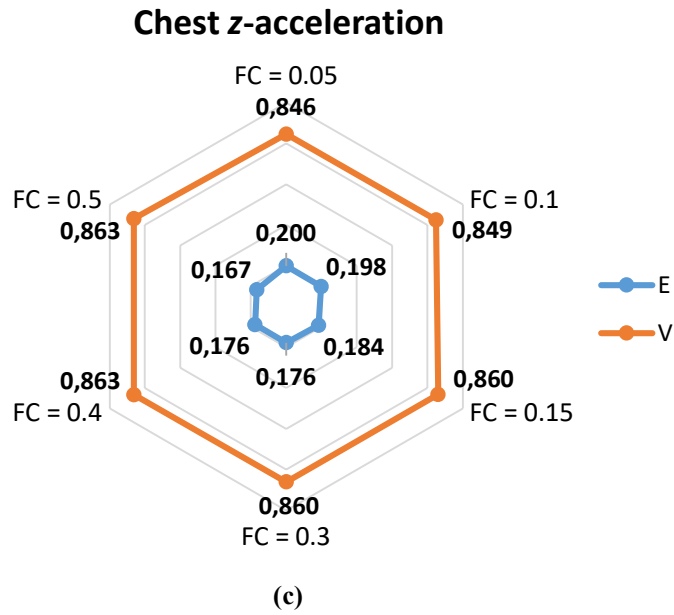
Figure 136 – Sensitivity study in chest *x, y,* and *z*-accelerations

The principal chest accelerations (*x* and *z*) display an increase in correlation with the experimental result directly dependent on the increase of FC. The *x*-acceleration is the most affected one, with an increase of *V* of 1.5% from FC = 0.15 to FC = 0.5. This slight variation demonstrates the influence of the DLT on the dummy chest, improving the correlation during the load limiting phase. The *y*-acceleration does not report deviations which can be correlated to the value of FC, suggesting that the behavior of the dummy along this direction is not associated with the DLT.

11.4 Pelvis

Figure 137 displays the sensitivity analysis performed on pelvis *x*, *y,* and *z*-accelerations.
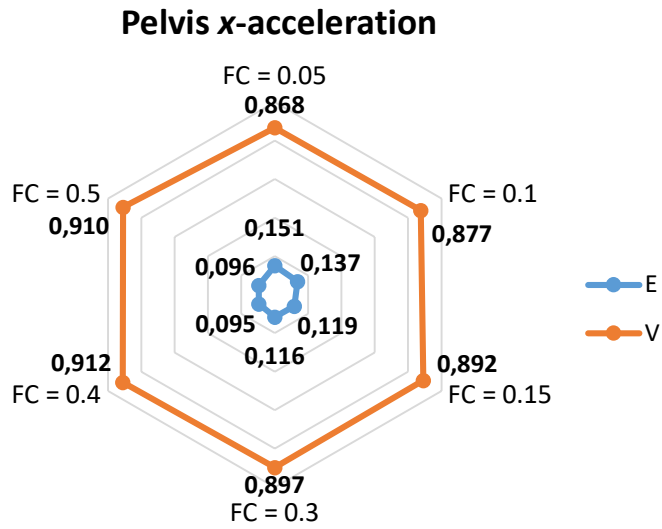
(a)
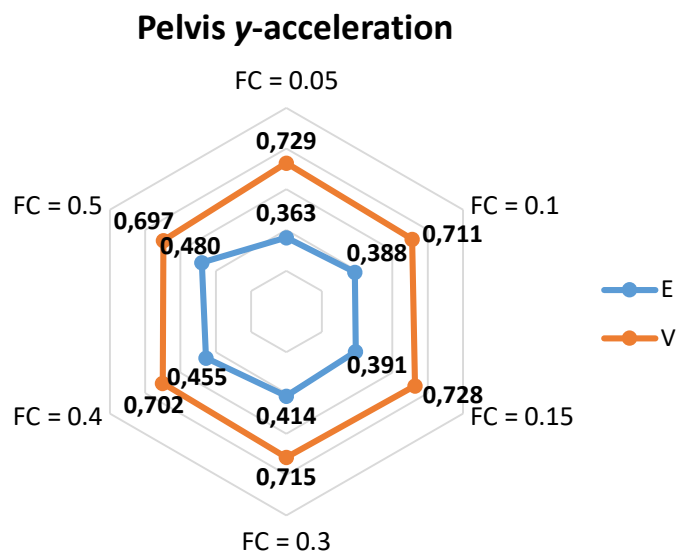
(b)
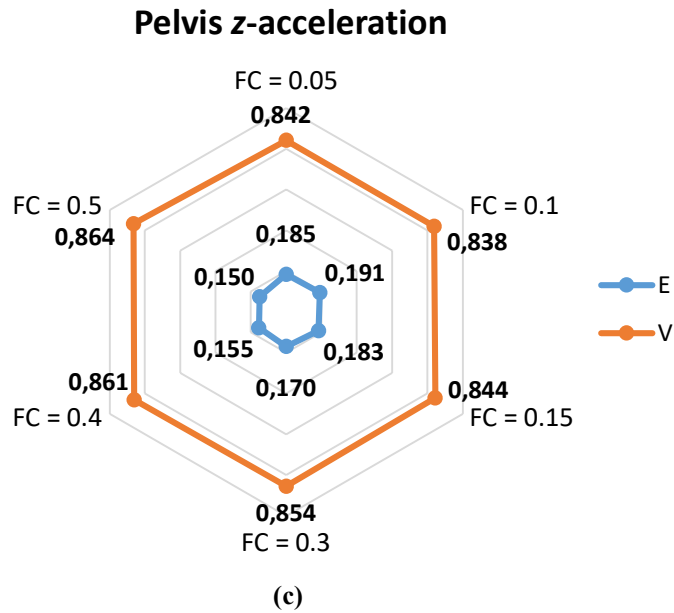
Figure 137 – Sensitivity analysis of pelvis *x*, *y* and *z*-accelerations

The pelvis accelerations evidence the same behavior underlined observing the chest ones: the validation metric slightly increases with the rise of FC in both *x* and *z*-accelerations. For this body region, the percentage of increase with respect to the default analysis is approximately equal to 2%. Such improvements and those registered on the chest prove the impact of the DLT on the dummy torso and pelvic region. In addition, they are consistent with the belt loads registered in Section 11.1, which are closer to the experimental trends with higher values of FC. The *y*-acceleration variations are instead not correlated with the friction coefficient, as concluded in the previous Sections. To conclude, head, chest and pelvis accelerations registered a slight upgrading of the correlation with the experimental data with the increase of FC. Moreover, observing Figure 135, 136 and 137, it can be concluded that the most balanced configuration has FC = 0.4, with the majority of progresses in all directions of motion.

11.5 Upper neck

The same sensitivity analysis was executed on the upper neck. Figure 138 reports it on *x*, *y,* and *z*-forces.

Upper neck *x*-force

(a)

Upper neck *y*-force

(b)

Upper neck *z*-force

(c)
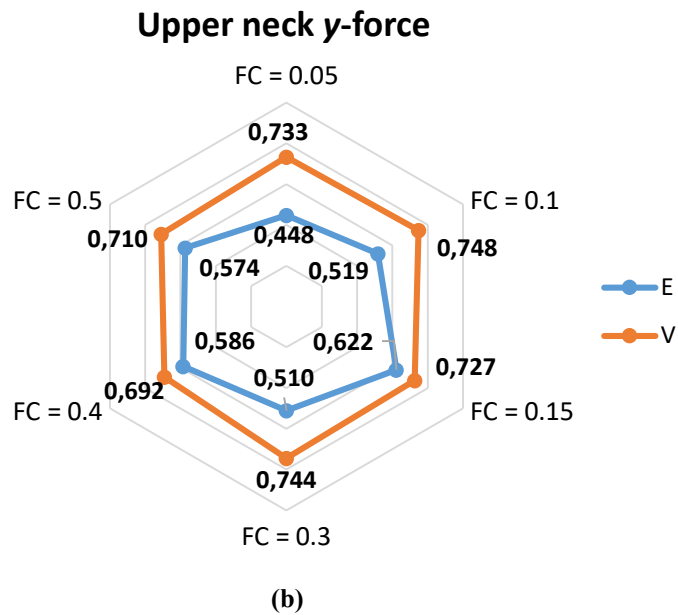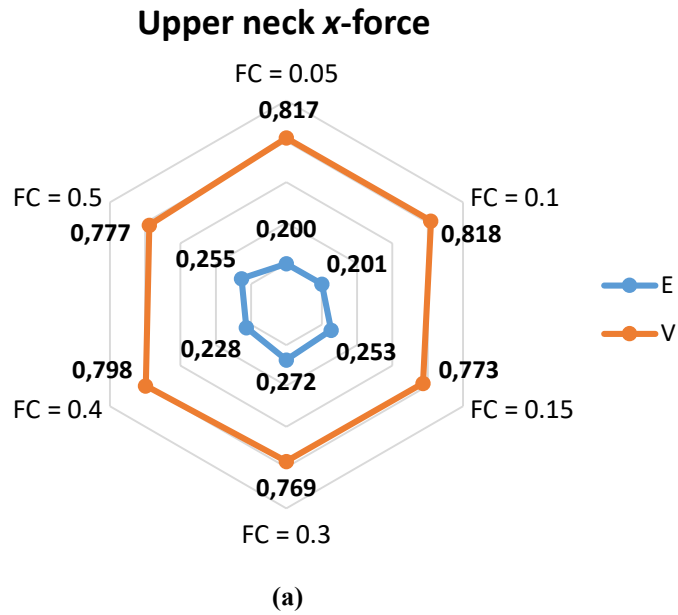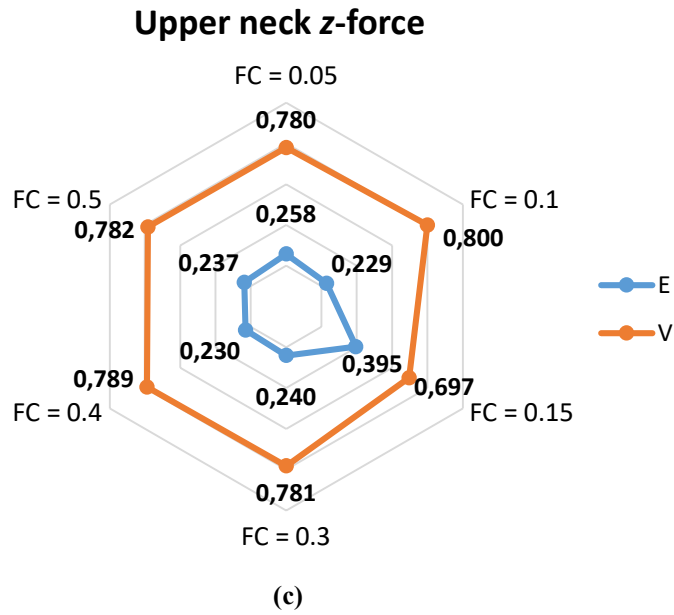
Figure 138 – Sensitivity analysis of upper neck *x*, *y*, and *z*-forces

The configuration with FC = 0.4 reports higher correlations for both *x* and *z*-forces. The neck *z*-force, which is the component with the highest order of magnitude, registered an improvement of more than 9%, which is a high value considering the slight variation implemented on the model. As already stated in the previous chapter, the upper neck force follows the head acceleration, thus the same conclusion can be made on the *y*-component. Figure 139 displays the sensitivity hexagons on the upper neck moment.

Upper neck *x*-moment

(a)
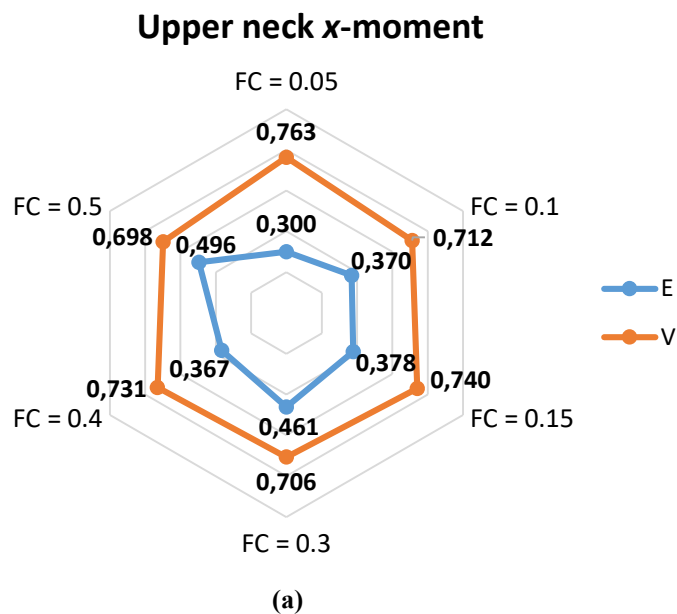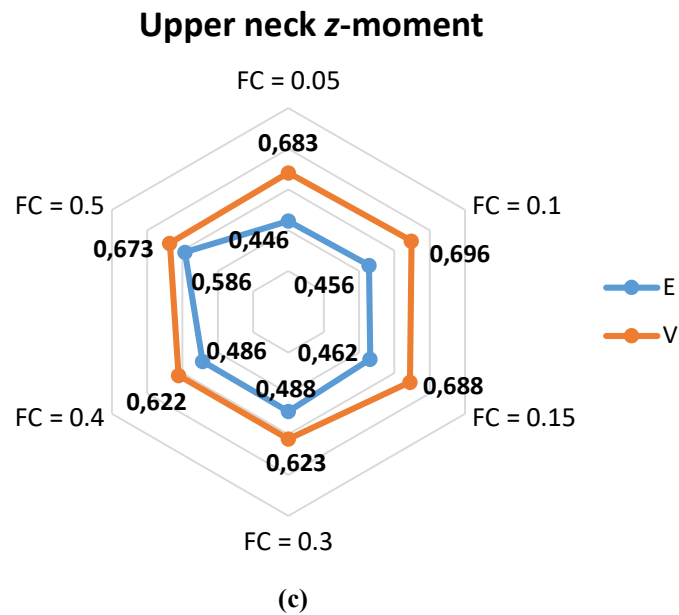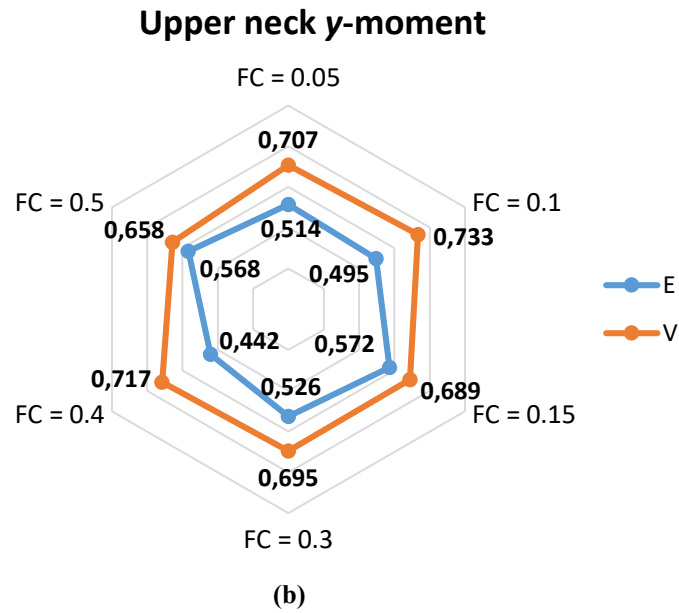
Figure 139 – Sensitivity analysis on the upper neck moment

The upper neck *y*-moment shows the lowest *E* with FC = 0.4, confirming the enhanced level of prediction of this configuration. The *x*-moment has the highest correlation with FC = 0.05, a situation that does not represent a consistent friction condition. The *z*-moment displays balanced results, except for FC = 0.5, where *E* increases by 10%, suggesting that this coefficient of friction may be excessive. Axial (*z*) force and bending (*y*) moment are the predominant components of force and moment acting on the upper neck, and they are also utilized by most of safety councils to compute the *Nij*. The configuration with FC = 0.4 shows a not negligible improvement in the correlation of these parameters.

11.6 Lower neck

The last region utilized to validate the model is the lower neck. Despite the low level of correlation with the experimental results, the same sensitivity analysis was performed and Figure 140 reports the force components.

Lower neck *x*-force

(a)
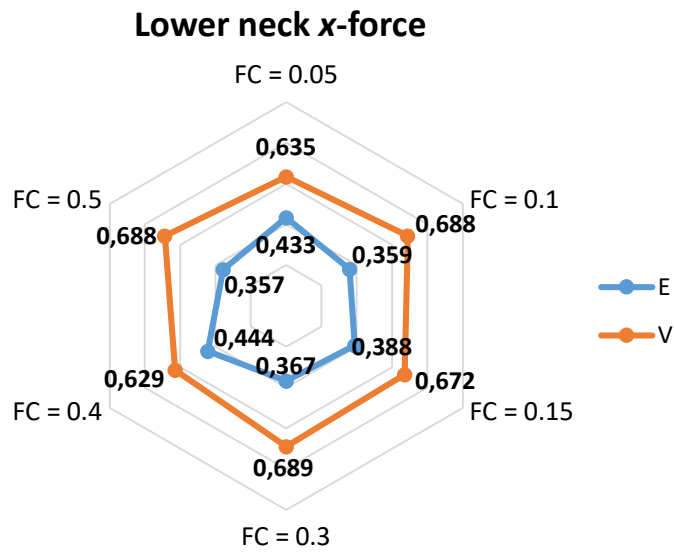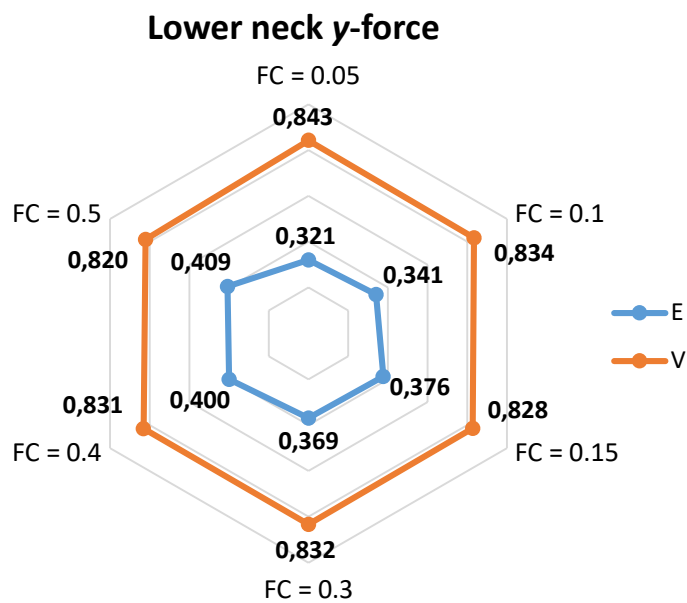
Lower neck *y*-force

(b)
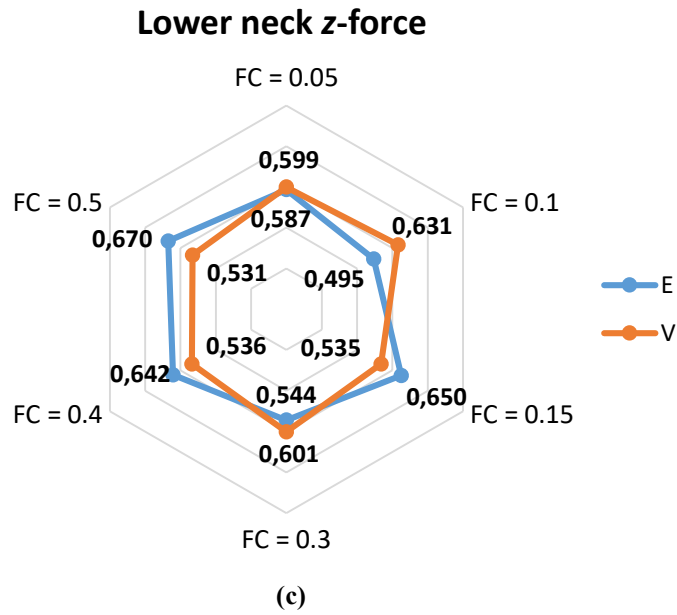
Figure 140 – Sensitivity analysis on the lower neck force

Lower neck x and y-forces do not show a direct dependency of E and V from the variation of FC, and the miscorrelation between E and V in the z-force described in Section 9.3.2.9 does not allow to perform a proper sensitivity study. Lastly, Figure 141 displays the sensitivity of the lower neck moment.

Lower neck *y*-moment

(b)

Lower neck *z*-moment

(c)
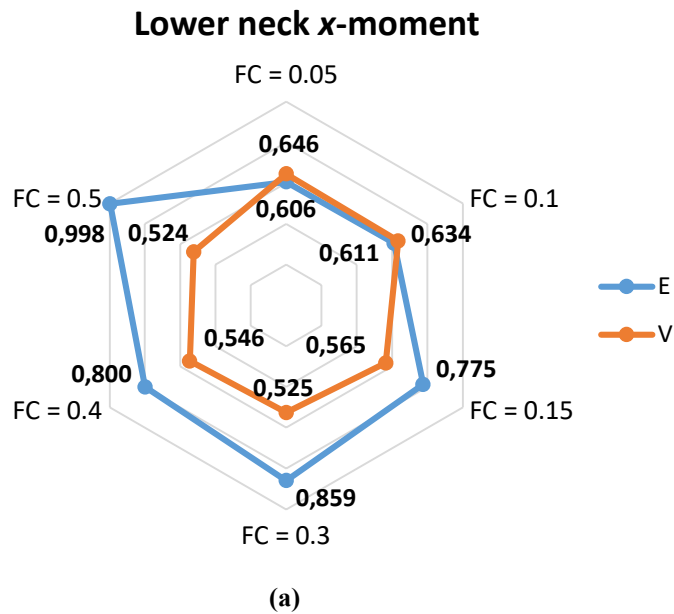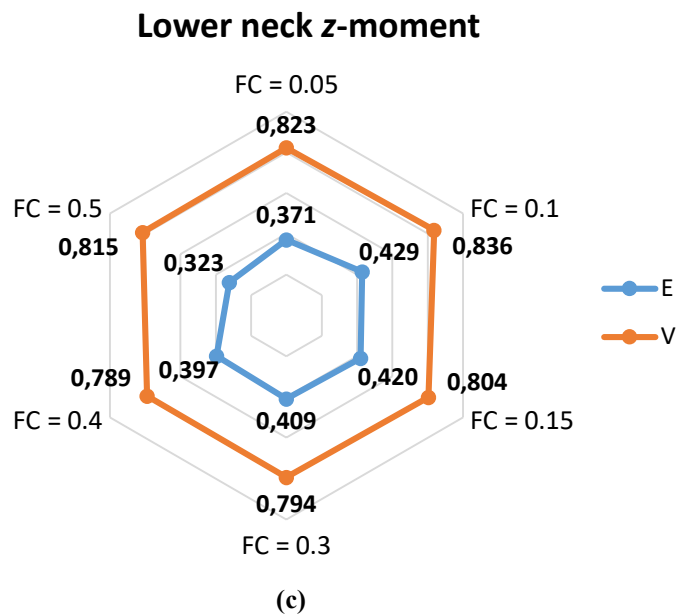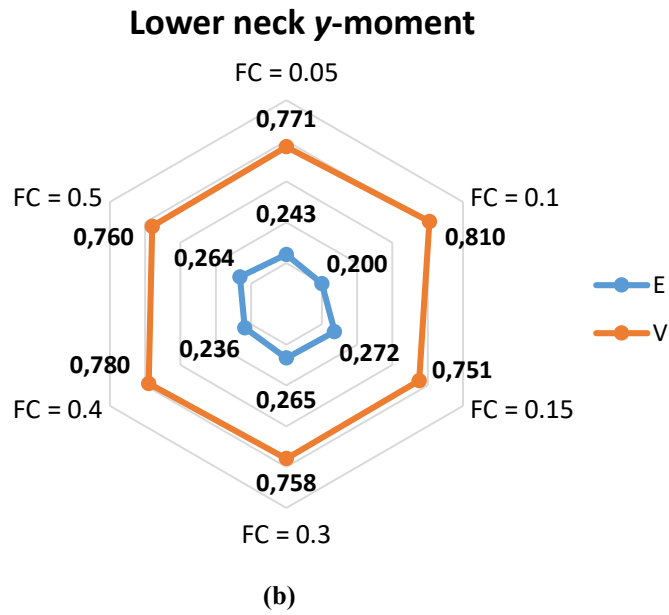
Figure 141 – Sensitivity analysis on the lower neck moment

A sensitivity analysis can not be performed on the *x*-moment, given its level of imprecision. The *y*-moment, instead, which reports consistent values of *E* and *V* and also constitutes the predominant component of this neck load, show the highest improvement for FC = 0.1 and FC = 0.4, with 3% and 6% of increase in the validation metric, respectively. The *z*-moment, lastly, maintains the same average prediction level for all values of FC. Therefore, the configuration with FC = 0.4 can be confirmed as the most balanced and performant in the prediction of the experimental results. Consequently, the biomechanical parameters, registered in this configuration, which evidence an increase of the correlation with respect to the default

setting will be displayed in Appendix D. Such plots, if compared with those of Section 9.3.2, displays a better prediction of the pretensioning loads, eliminating the overestimations observed in almost all parameters when using FC = 0.15. Moreover, they show a higher correlation during the retractor locking phase, with higher precision in the peaks correlation, and a greater correspondence during the rebound phase.

12. CONCLUSIONS AND FUTURE WORK

12.1 Conclusions

A full vehicle body FE model can require considerably more efforts to be completed and validated; for instance, this research focused only on the definition of the proper connections between different entities. However, front seat and vehicle body models are characterized by several internal connections, which have not been described in this thesis, since they are not subjects of the related research. Therefore, considering the complexity of the model and the number of FE entities involved, a guideline is surely needed to understand how to manage all interactions and to obtain a stable numerical environment. These guidelines are given in Chapters 5 to 9 and are summarized in Chapter 10, underlining the most important topics to consider.

The most significant contribution resulting from this part of the research is the description of the generation and consequent calibration of a virtual restraint system using LS-DYNA. The proper design of the retractor and pretensioner loading curves and the interpretation and tuning of the interaction of these two entities (carefully choosing the pretensioner type among the 9 alternatives provided by LSTC) has been shown to be fundamental to obtain the highest performance of the model in terms of validation. Additionally, in this particular case, the vehicle restraint system has to operate considering the interference of the booster seat, which makes its connection to the locking tongue harder. This leads to an increase of the initial tension of the seat belt, and its proper functioning must be guaranteed in this new condition, to ensure the correct level of safety for a ten-year-old occupant.

Once a definitive FE reproduction of the experimental sled test was obtained and its physical consistency was verified, the subsequent validation reported encouraging results with respect to the previous works studied during the Literature Review:

1. The head accelerations showed values of V equal to 78, 79 and 76% respectively, the trend of the experimental curves was reasonably predicted and the peak of the predominant component (z-direction) was completely predicted in magnitude and occur only 2 ms too early. Consequently, the *HICs* were well predicted, with coincident peak time instants and peaks relative error lower than 15%;

2. Chest and pelvis accelerations reported higher values of V, on an average of 85%, greatly predicting the experimental outputs, with a general underestimation of the acceleration peaks in the pelvic region;

3. Upper neck forces and moments displayed an acceptable level of prediction, with *V* at least equal to 70% and a consistent correlation of experimental and numerical *Nij*, properly estimating the upper neck level of injury during the event;

4. The lower neck region was shown to be the least accurate, with high overestimations of the forces and of *x* and *z*-moments. The *y*-moment, instead, which is the predominant component (10 times higher than the other ones) was well predicted, with *V* equal to 75%.

These results demonstrate a high performance of the model in the prediction the occupant injury risk, hence a general improvement in the estimation of biomechanical parameters utilising Finite Element Analysis can be appreciated in the last few years. Previous works analysed in the Literature Review reported average validation metrics equal to 70%. Additionally, considering the greater anthropometrics of a ten-year-old child with respect to three or six-year-old toddlers, the FE reproduction of all entities that interact with a Q10 during a crash event (booster seat, 2nd row seat foam, front passenger seat, vehicle body) was shown to be necessary to obtain the closest prediction of the dummy kinematics and injury risk.

In the last part of the research, a sensitivity study on the friction coefficient of the lower LS-DYNA slip ring was performed, to improve the FE modeling of the Dynamic Locking Tongue. It was concluded that the setting of a friction coefficient equal to 0.4 leads to an improvement of the majority of the validation metrics, with the highest increase (approximately 10%) in the upper neck region. This result suggests the level of detail required by a high-speed event reproduction, where the variation of a single parameter in the dummy pelvic region influenced also head and neck. In addition, the correspondence of all biomechanical signals during the rebound phase sensibly upgraded.

12.2 Future work

This research suggests an entire process to obtain a verified and validated FE model regarding sled test simulations. Once a numerical model was validated, it can be utilized for simulating a side impact event or for quantifying the influence and the effects of several entities. Focusing on the subject of this research, a sensitivity study could be performed on the friction coefficient between dummy and booster, to improve the model precision. In addition, the influence of the booster seat could be quantified, utilizing the same guideline to reproduce a sled test without the CRS, with the ATD directly seating on the 2nd-row seat. Higher loads on neck, chest, and pelvis should be expected, as described in Section 2.6.2.1. Moreover, the effects of load limiting and belt pretensioning in the field of ten-year-old children passive safety can be investigated.

Lastly, the presence of the Dynamic Locking Tongue is sometimes not considered when building a numerical model for crash events. Instead, a procedure to improve and validate the FE reproduction of the Dynamic Locking Tongue should be defined, to obtain a higher correlation between experimental and numerical restraint systems.

REFERENCES

1. Community database on Accidents on the Road in Europe (CARE). Last update: May 2017.

2. European Automobile Manufacturers Association Press Embargo, 19 September 2018, New passenger car registration in the European Union.

3. Canadian Motor Vehicle Traffic Collision Statistics: 2016, Transport Canada.

4. Sauber-Schatz E.K., Ederer D.J., Dellinger A.M., Baldwin G.T. Vital Signs: Motor Vehicle Injury Prevention — United States and 19 Comparison Countries. MMWR 2016;65. DOI: http://dx.doi.org/10.15585/mmwr.mm6526e1

5. Monroe brakes, Understanding Vehicle Dynamics. https://www.landmark-autoparts.com/shockabs/cardynamics.htm

6. Active and passive automotive safety systems, Atul Kumar, Team Lead (Automotive & Transportation Domain), MarketsAndMarkets, July/18/2017.

7. Active, Passive and Preventive safety of motor cars, Prof. Giovanni Belingardi, Dipartimento di Ingegneria Meccanica ed Aerospaziale, Politecnico di Torino, Research group on Vehicle Safety.

8. Transportation Today, Congressional highway freight report finds record amount of freight on US highway system, Chris Galford, July/10/2018.

9. L. Morello et al.: The Automotive Body, Vol. 2: System Design, MES, pp. 463–558. springerlink.com, Springer Science + Business Media B.V. 2011.

10. Henn, H Crash Tests and the Head Injury Criterion, Teaching Mathematics and its Applications, Vol 17, No 4, 1998.

11. Victoria Oţăt, Oana. (2015). Modeling The Frontal Collison In Vehicles And Determining The Degree Of Injury On The Driver. ACTA Universitatis Cibiniensis. 67. 10.1515/aucts-2015-0075.

12. NHTSA, Federal Motor Vehicle Safety Standard No. 213 Child Restraint Systems

13. Government of Canada, Motor Vehicle Safety Regulations, Occupant Protection In Frontal Impacts (Standard 208) [SOR/2013-9, s. 5].

14. McHenry R.R. Proc. Am. Assoc. Automot. Med. Annu. Conf. 1963; Analysis of the dynamics of automobile passenger-restraint systems 7: 207-249.

15. Yngve Håland, Autoliv Research, The Evolution Of The Three Point Seat Belt From Yesterday To Tomorrow, Vehicle Safety, Department of Applied Mechanics, Chalmers University of Technology, September 2006.

16. Jingwen Hu, Kurt Fischer, Angelo Adler, Rear Seat Occupant Protection: Safety Beyond Seat Belts, UMTRI, January 21, 2015.

17. Traffic Safety Facts 2015, DOT HS 812384, U.S. Department of Transportation, National Highway Traffic Safety Administration, pp. 1-6, 2017.

18. Statistiche Istat, Incidenti stradali 2017, pp. 1-7, 2017.

19. Child Restraint System Data Collection in NHTSA's Crash Investigation Programs, DOT HS 812645, 2018.

20. Hertz, E. (1996, December). Revised estimates of child restraint effectiveness. (Report No. DOT HS 96 855). Washington, DC: National Highway Traffic Safety Administration.

21. Kahane, C. J. (2000, December). Fatality reduction by safety belts for front-seat occupants of cars and light trucks. (Report No. DOT HS 809 199). Washington, DC: National Highway Traffic Safety Administration.

22. 12th Annual Road Safety Performance Index (PIN) Report, European Transport Safety Council.

23. Fatality Analysis Reporting System (FARS) Encyclopedia.

24. Mental Floss, A Brief History of 7 Baby Basics, March 2013.

25. K.B. Arbogast, Y. Ghati, and R.A. Menon, Field investigation of child restraints in side impact crashes, Traffic Injury Prev. 6 (2005), pp. 351–360.

26. National Highway Traffic Safety Administration, US Department of Transportation, Fatalities and injuries to 0–8-year-old passenger vehicle occupants based on impact attributes, Tech. Rep. DOT HS-809 410, US Department of Transportation, Washington, DC, 2002.

27. Zhanbiao Li, Wencheng Zhang, Tanya Kapoor & William Altenhof (2011) Crash analysis of a three-year-old human child model in side impacts considering normal and incorrect CRS usage, International Journal of Crashworthiness, 16:4, 457-467, DOI: 10.1080/13588265.2011.606998.

28. Anna Anund, Torbjörn Falkmer, Åsa Forsman, Susanne Gustafsson, Ylva Matstoms, Gunilla Sörensen, Thomas Turbell, Jan Wenäll, Child Safety in Cars – Literature Review, VTI rapport 489A, 2003.

29. A. Howard, A. M. McKeag, A. German, I Hale, W. Altenhof and R. Turchi, "Cervical Spine Injuries in Children Restrained in Forward Facing Child Restraints", Proceedings of the Canadian Multidisciplinary Road Safety Conference XIII, June 8- 11,2003, Banff, Alberta.

30. M. Prange, W. Newberry, T. Moore, D. Peterson, B. Smyth and C. Corrigan, "Inertial Neck Injuries in Children Involved in Frontal Collisions", SAE International 2007 World Congress Detroit, Michigan, April 16-19, 2007, SAE Technical Paper Series No. 2007-01-1170.

31. Yaek Jennifer L., Dibb Alan T., Prange Michael T., Sharpe Sarah S., Pediatric Biomechanics, Exponent, Engineering and Specific Consulting, 2017.

32. Arbogast, Kristy B.C., Rebecca A., Michael J.,Winston, Flaura K., Durbin, Injuries to children in forward facing child restraints, Association for the Automotive Medicine, 2002, Vol. 46, pp. 213-230.

33. Lukasz Mazurkiewicz, Pawel Baranowski, Hamid Reza Karimi, Krzysztof Damaziak, Jerzy Malachowski, Artur Muszynski, Andrzej Muszynski, Kjell Gunnar Robbersmyr, Dario Vangi, Improved child-resistant system for better side impact protection.

34. J. Brown, L. Bilston, M. McCaskill, and M. Henderson, Identification of injury mechanisms for child occupants aged 2-8 in motor vehicle accidents, Final Project Report for the Motor Accidents Authority o f NSW, pp. 1-71, June 2005.

35. Uphold, R., R. Harvey, et al. "Bilateral tibial fractures in properly restrained toddlers involved in motor vehicle collisions: case reports." Journal of Trauma-Injury Infection & Critical Care 31(10): 1411-1414; 1991.

36. Weber, K. Child Passenger Protection. Accidental Injury: Biomechanics and Prevention. A. Nahum and J. Melvin. New York, Springer-Verlag; 2002.

37. Yoganandan, N., S. Kumaresan, et al. Pediatric Biomechanics. Accidental Injury: Biomechanics and Prevention. A. Nahum and J. Melvin. New York, Springer-Verlag; 2002.

38. Arbogast K. B., Chen I., Durbin D. R. & Winston F. K. Injury risks for children in child restraint systems in side impact crashes. Proc. of International Research Conference on the Biomechanics of Impact (IRCOBI), 2004 Graz, Austria.

39. Isaksson-Hellman I., Jakobosson L., Gustafsson C. et al. Trends and effects of child restraint systems based on Volvo's Swedish accident database. SAE-973299. In Proceedings of Child Occupant Protection 2nd Symposium, P-316, Society of Automotive Engineers, Inc. Warrendale, PA 1997.

40. www.miltonnissan.ca/child-baby-seat-installation-milton-ontario.

41. K. Weber, Crash Protection for Child Passengers, UMTRI Research Review, Jul. - Sep., Vol. 31, No. 3, pp. 1-28, 2000, www.umtri.umich.edu/librarv/pdf7rr31 3.pdf.

42. National Highway Traffic Safety Administration, The 2017 National Survey of the Use of Booster Seats, U.S. Department of Transportation, DOT HS 812 617, September 2018.

43. C. Sherwood, S. Ferguson, and J. Crandall, Factors leading to crash fatalities to children in child restraints, Center for Applied Biomechanics, University of Virginia, pp. 1-17, 2003.

44. Sweatman P., Shope J., Schneider L., Seay-Ostrowski C., Romine F., Sweet B., Daniels J., Crash Protection for Child Passengers: Rationale for Best Practice, University of Michigan Transportation Research Institute, Volume 43, Number 1, 2012, ISSN 0739 7100.

45. Swedish Insurance Company Folksam.

46. Bendjellal, F., Nakhla, S., Maier, D., 2006. Investigation into children protection in side impact motor vehicle crashes. In: Proceedings of the 4th International Conference, Protection of children in cars.

47. Arbogast K.B., Moll E.K., Morris S.D., Anderko R.L., Durbin D.R.,Winston F.K., (2001) Factors influencing pediatric injury in side impact collisions. J Trauma Vol. 51, No. 3, pp. 469–477.

48. Kristy B. Arbogast, Yoganand Ghati, Rajiv A. Menon, Suzanne Tylko, Nicholas Tamborra & Richard M. Morgan (2005) Field Investigation of Child Restraints in Side Impact Crashes, Traffic Injury Prevention, 6:4, 351-360, DOI: 10.1080/15389580500255831.

49. Kallan MJ, Durbin DR, Arbogast KB. Seating patterns and corresponding risk of injury among 0- to 3-year-old children in child safety seats. Pediatrics. 2008; 121(5): e1342-7.

50. Starnes M, Eigen AM. Fatalities and Injuries to 0-8 Year Old Passenger Vehicle Occupants Based on Impact AttributesNHTSA report DOT HS 809 410. Washington, DC: National Highway Traffic Safety Administration; 2002.

51. Arbogast KB, Kallan MJ, Durbin DR. Front versus rear seat injury risk for child passengers: evaluation of newer model year vehicles. Traffic Inj Prev. 2009;10(3):297-301.

52. Stanford Children's Health, Air Bags: Not For Children.

53. Tanya Kapoor, William Altenhof, Andrew Howard, Jim Rasico, Fuchun Zhu, Methods to mitigate injury in toddlers in near-side impact crashes, Accident Analysis and Prevention 40 (2008), 1880-1892.

54. National Highway Traffic Safety Administration. National Standardized Child Passenger Safety Training Program Curriculum Instructor Guide. Washington, DC: National Highway Traffic Safety Administration; 2004.

55. Wittenberg E, Nelson TF, Graham JD. The effect of passenger airbags on child seating behavior in motor vehicles. Pediatrics. 1999;104 (6):1247-50.

56. Ediriweera Desapriya, Lionel Samayawardhena, Aruna Somasiri, and Ian Pike, Child Occupants and Side-impact Crashes: Commentary, Vancouver and Burnaby, British Columbia, Canada, 2011, doi: 10.1016/j.jen.2011.03.012.

57. ECE 44/04, Status of United Nations Regulation, Revised on February 2008.

58. www.etsc.eu/abouts.

59. Directive 2003/20/EC of the European Parliament and of the Council of 8 April 2003 amending Council Directive 91/671/EEC, Official Journal L 115, 2003-05-09 P. 63.

60. "Child car seat design and production regulations". Childseatcentre.com. Retrieved 27 May 2017.

61. www.etsc.eu, Latest UN child seat standard agreed for 2019.

62. Fitting safety as standard – Revision of the General Safety Regulation EC661/2009 and Pedestrian Protection Regulation EC78/2009 – May 2017.

63. Dovile Adminaite, Graziella Jost, Henk Stipdonk, Heather Ward, Theodora Calinescu, Reducing Child Deaths on European Roads, ETSC PIN Flash Report 34, February 2018.

64. National Highway Traffic Safety Administration, 49 CFR Part 571, Docket No. NHTSA-03-15351, RIN 2127-AI34, Federal Motor Vehicle Safety Standards; Child Restraint Systems.

65. Department of Transportation, National Highway Traffic Safety Administration, 49 CFR Part 571, Docket No. NHTSA–2014–0026, RIN 2127–AL35, Final rule; response to petition for reconsideration, Federal Register, Vol. 79, No. 37, Tuesday, February 25, 2014.

66. Department of Transportation, National Highway Traffic Safety Administration, 49 CFR Part 571, Docket No. NHTSA–2011–0176, RIN 2127–AL10 (Formerly RIN 2127–AJ44), Final rule, Federal Register, Vol. 77, No. 38, Monday, February 27, 2012.

67. U.S. Department of Transportation, National Highway Traffic Safety Administration, Laboratory Test Procedure for FMVSS 213, TP-213-10, February 16, 2014.

68. U.S. Department of Transportation, National Highway Traffic Safety Administration, Laboratory Test Procedure for FMVSS 208, 212, 219, 301F, TP208-14, April 16, 2008.

69. Transport Canada, Technical Standards Document No. 208, Revision 0R: Occupant Crash Protection, February 13, 2013.

70. The New Car Assessment Program Suggested Approaches for Future Program Enhancements National, Highway Traffic Safety Administration, January 2007.

71. Department of Transportation, National Highway Traffic Safety Administration, 49 CFR Parts 571 and 585, Docket No. NHTSA 2005–22323, RIN 2127–AI98, Final rule, Federal Register, Vol. 71, No. 169, Thursday, August 31, 2006.

72. Pernille Larsen (2011-05-25). "FIA Region I . Euro NCAP's standard set for upcoming electric and range-extender cars". Fiabrussels.com. Retrieved 2011-11-02.

73. Michiel van Ratingen, Aled Williams, Anders Lie, Andre Seeck, Pierre Castaing, Reinhard Kolke, Guido Adriaenssens, Andrew Miller, The European New Car Assessment Programme: A historical review, Chinese Journal of Traumatology 19 (2016) 63-69, 2016.

74. www.euroncap.com.

75. Euro NCAP, Offset Deformable Barrier Frontal Impact Testing Protocol, Version 7.1.3, November 2018.

76. Euro NCAP, Child Occupant Protection Testing Protocol, Version 7.2.2, September 2018.

77. Euro NCAP, Full Width Frontal Impact Testing Protocol, Version 1.1, September 2018.

78. Euro NCAP, Side Impact Mobile Deformable Barrier Testing Protocol, Version 7.1.3, November 2017.

79. Euro NCAP, Child Occupant Protection Assessment Protocol, Version 7.2.2, September 2018.

80. Nahum Alan M., Melvin John W., Accidental Injury: Biomechanics and Prevention, Springer-Verlag New York 2002, DOI: https://doi.org/10.1007/978-0-387-21787-1.

81. K. Jager, M. Ratingen, P. Lesire, H. Guillemot, C. Pastor, B. Schnottale, G. Tejera, and J. Lepretre, Assessing new child dummies and criteria for child occupant protection in frontal impact, TNO Science and Industry (The Netherlands), Paper no. 05-0157,

www.eevc.org/publicdocs/ESV2005 WG12+18 05-0157-Q.pdf. pp. 1-15, Accessed Jan 2006.

82. Masami Iwamoto, Yoshikatsu Kisanuki, Isao Watanabe, Katsuya Furusu, Kazuo Miki, Development of a Finite Element model of the total human model for safety (THUMS) and application to injury reconstruction, Toyota Central R&D Labs., Inc., 2002.

83. Koji Mizuno, Kazuya Iwata, Takashi Deguchi, Takashi Ikami & Masami Kubota (2005) Development of a Three-Year-Old Child FE Model, Traffic Injury Prevention, 6:4, 361-371, DOI: 10.1080/15389580500255922.

84. LS-DYNA model of the Hybrid III 3-year-old child dummy – version 2.3B2. (2000). User's Manual, First Technology Safety Systems, Plymouth, MI.

85. R. Turchi, W. Altenhof, T. Kapoor, and A. Howard, An investigation into the head and neck injury potential of three-year-old children in forward and rearward facing child safety seats, International Journal of Crashworthiness, Vol. 10, pp. 1-14, 2004.

86. Ramaswamy, K., Patham, B., Savic, V., and Tripathy, B., "Stable and Accurate LS-DYNA Simulations with Foam Material Models: Optimization of Finite Element Model Parameters," SAE Int. J. Mater. Manf. 10(2):2017, doi:10.4271/2017-01-1338.

87. Erhart T., "Review of Solid Element Formulations in LS-DYNA: Properties, Limits, Advantages, Disadvantages," 2011 Developers' Forum, Stuttgart, Germany, October, 2011.

88. Tanya Kapoor, William Altenhof, Qian Wang, Andrew Howard, "Injury potential of a three-year-old Hybrid III dummy in forward and rearward facing positions under CMVSS 208 testing conditions", Accident Analysis and Prevention 38 (2006), pp. 786-800. https://doiorg.ledproxy2.uwindsor.ca/10.1016/j.aap.2006.02.005.

89. Tanya Kapoor, William Altenhof, Anne Snowdon, Andrew Howard, Jim Rasico, Fuchun Zhu, Daniel Baggio, A Numerical investigation into the effect of CRS misuse on the injury potential of children in frontal and side impact crashes, Accident Analysis and Prevention 43 (2011), 1438-1450.

90. Tanya Kapoor, William Altenhof, Andrew Howard, Anne Snowdon, Jim Rasico, Fuchun Zhu & Koji Mizuno (2010) Countermeasures to mitigate head and neck injuries to toddlers in frontal and lateral vehicle crash conditions, International Journal of Crashworthiness, 15:1, 17-37, DOI: 10.1080/13588260902986010.

91. Tanya Kapoor, William Altenhof, Miroslav Tot, Wencheng Zhang, Andrew Howard, Jim Rasico, Fuchun Zhu & Koji Mizuno (2008) Load Limiting Behavior in CRS Tether Anchors as a Method to Mitigate Head and Neck Injuries Sustained by Children in Frontal Crash, Traffic Injury Prevention, 9:3, 243-255, DOI: 10.1080/15389580801975210.

92. Tanya Kappor, William Altenhof and Andrew Howard, The Effect of using Rigid ISOFIX on the Injury Potential of Toddlers in Near-side Impact Crashes, 10th International LS-DYNA Users Conference, 2008, Dearborn, MI.

93. Oberkampf W. and Trucano T. (2002). Verification and validation in computational fluid dynamics. Progress in Aerospace Sciences. Vol. 38, pp. 209 - 272.

94. Livermore Software Technology Corporation (LSTC), LS-DYNA Keyword User's Manual Volume 1, 07/27/17.

95. Humanetics Innovative Solutions, Inc. Q10 Child Dummy LS-DYNA model User's Manual, Release Version 1.7, July 2017.

96. Belytschko, T., Liu, W.K., Moran, B.: Nonlinear Finite Elements for Continua and Structures. Wiley, New York (1997).

97. Belingardi G., Il Metodo degli Elementi Finiti nella Progettazione Meccanica, Libreria Editrice Universitaria "Levrotto & Bella", Torino.

98. Klaus-Jürgen Bathe, Finite Element Procedures, Second Edition.

99. SAE International, SAE J211-1 Surface Vehicle Recommended Practice, Revised March 1995.

APPENDICES

APPENDIX A – Speed time diagrams

Diagrams that represent the speed during the crash as a function of the time have proven to be a useful tool to understand the role of different elements involved such as the restraint system and the shock absorption structure. Apart from the speed, other quantities can be represented in these diagrams, such as the acceleration and the distance. If the speed is measured with respect to a reference system fixed to the ground, the acceleration is the slope of the diagram, while the distance relative to the ground is represented by the area between the time axis and the speed curves. Additionally, in the case of objects in relative motion, the relative displacement is the area between their speed curves.

Figure 142 shows the speed time diagram for the case of a normal braking with no crash. At time $t = 0$ the speed is 14 m/s (~50 km/h) and the braking action starts. The intensity of the braking action is enough to produce a constant 5 m/s2 (0.5 g) deceleration that leads to a full stop in

$$\frac{14 \; m/s}{5 \; m/s^2} = 2.8 \; s$$

The braking distance is represented by the area under the speed diagram. As the deceleration is constant, this area is that of a triangle:

$$\frac{14 \; m/s \cdot 2.8 \; s}{2} = 19.6 \; m$$

If the restraint system was rigid, the speed of the occupant during the deceleration would be the same as that of the vehicle and the two speed-time curves will overlap. Conversely, if the restraint system acts with a delay of 0.01 s, the speed curve of the occupant and that of the vehicle would not overlap. The area between the two curves is the displacement d that the restraint system allows the occupants to have with respect to the vehicle frame.
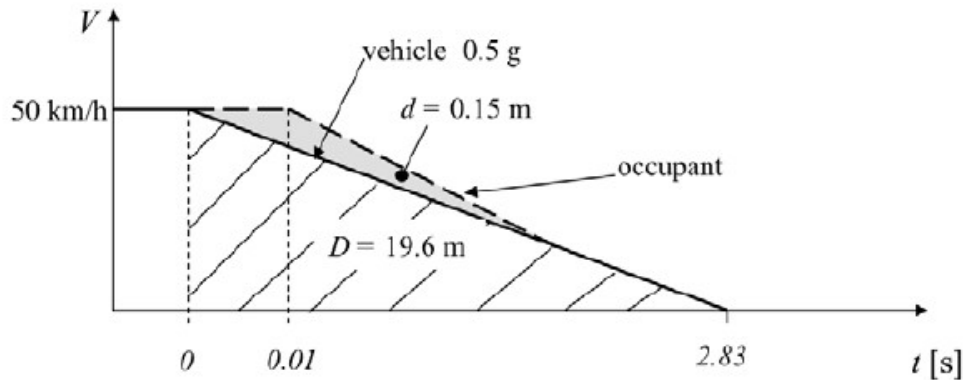
Figure 142 – Speed-time diagram during braking

Instead, Figure 143 shows the speed-time diagram for a crash against a rigid barrier with an unrestrained occupant. If the deformation involves only the front part of the car body structure, the displacement of the central portion (safety cell) will be equal to the amount of deformation of the front part itself, for example, 0.625 m.

Additionally, if: 1) the same speed before the impact of 50 km/h as for the previous case, and 2) the deceleration during the crash is constant, the deceleration during the crash can be determined by letting the area under the speed-time diagram equal to the amount of deformation of the front part

$$\frac{14 \, m/s \cdot \Delta t}{2} = 0.625 \, m$$

Thus, the duration Δt of the impact can be computed and, in this case, it is equal to 0.09 s, leading to an acceleration of

$$a = \frac{14 \, m/s}{0.09 \, s} = 157 \, m/s^2 = 16 \, g$$

The solid line in Figure 154 represents the speed of the central portion. The unrestrained occupant (dashed line) maintains its speed of 14 m/s until it strikes against the steering wheel or the dashboard. If the initial distance between the occupant and the steering wheel (or dashboard) is the same as the deformation of the front part of the vehicle (0.625 m), the occupant will impact these elements when the vehicle speed is null. The total distance covered by the occupant relative to the ground is 1.25 m (0.625 m + 0.625 m).
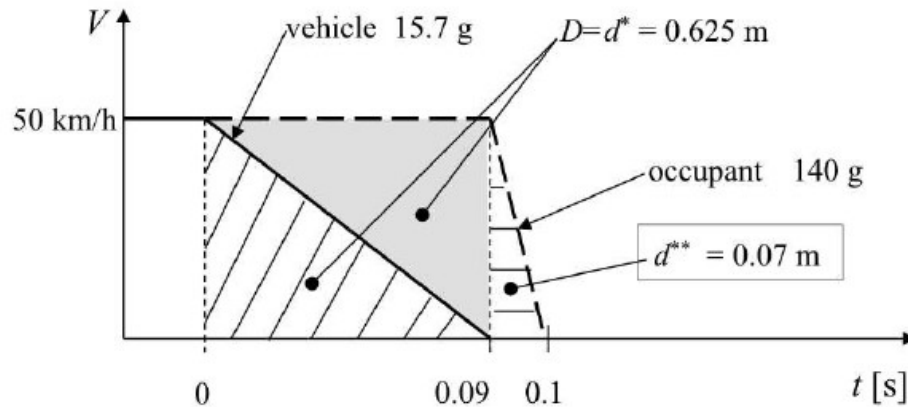
Figure 143 – Speed-time diagram during a crash against a rigid barrier with unrestrained occupant

The same considerations used to estimate the deceleration of the vehicle can be repeated now for the occupant. The assumption is that the surface hit by the occupant is rigid and that the deformation of the body is 7 cm. The result is that the time required to stop the occupant is 0.01 s, corresponding to an average acceleration of 140 g. This amount of deformation, together with the short time and the very high acceleration, implies very severe or fatal injuries.

Figure 144 shows the speed-time diagram for the same crash with a restrained occupant. If the restraint system allows a backlash distance of $d^* = 0.156$ m the occupant continues to travel at a constant speed for 0.045 s from the beginning of the crash. If the restraint system can stop the occupant in the following 0.045 s, the acceleration is

$$\frac{14 \, m/s}{0.045 \, s} = 280 \, m/s^2 = 28.5 \, g$$

In this case, the occupant and the vehicle stop at the same time, after 0.09 s from the start of the crash. During the phase when the restraint system is active, the occupant moves relative to the vehicle by 0.156 m (distance d^{**} of Figure 144); the total displacement of the occupant relative to the ground is then 0.937 m (0.625 m is the deformation of the vehicle, 0.156 m backlash distance, 0.156 m restraint phase).

If at the beginning the distance between the occupant and the steering wheel (or the dashboard) is 0.625 m, at the end of the crash a distance of 0.312 m remains. This can be exploited to reduce the occupant acceleration, as shown by the dotted line in Fig. 144. The result is a significant reduction of the forces applied by the restraint system and, consequently, of the potential injuries to the occupant.
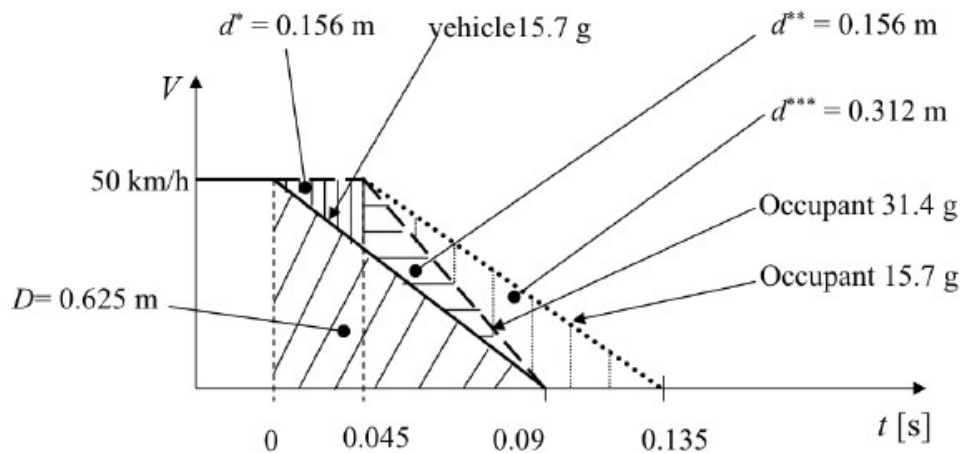
Figure 144 – Speed-time diagram of a crash against a rigid barrier with a restrained occupant

In conclusion, with this knowledge regarding the role of the restraint system, together with some considerations about the injury criteria, it is possible to outline some general guidelines regarding the restraint system itself which should be designed to:

- Maximize the distance traveled by the occupant under the action of the restraint system;
- Minimize the backlash, enabling the occupant acceleration to be reduced;
- Minimize the movement of the occupant body joints, the deformation and the deformation speed since the severity of injuries increases as these parameters increase;
- Maximize the interface area with the restraint system so as to reduce the interface pressure and, hence the extent of injury;
- Apply the restraint forces on bones (femur, hip, chest, shoulders, head) rather than soft tissue areas since higher loads can be resisted and such areas of the body are less affected by the deformation speed that is potentially very harmful to softer tissue.

APPENDIX B – Nonlinear Finite Element Analysis

To describe a dynamic system, it is possible to write a nonlinear general equation, where the equilibrium between internal F and external R forces is guaranteed by the presence of inertial forces. Inertial forces can be written as a product between mass matrix $\boldsymbol{M}$ and the acceleration vector $\ddot{q}$. Hence, this product is equal to the equilibrium between internal and external forces [96].

Internal forces depend on the stiffness and damping characteristics of the material, as a function of time t, and on the values of displacements and speeds (vectors q and $\dot{q}$):

$$\boldsymbol{M}\ddot{q} = R(q, \dot{q}, t) - F_{internal}(q, \dot{q}, t) \tag{12}$$

Furthermore, functions that link the expression of internal forces to the variables q, $\dot{q}$ and t are, generally, nonlinear and even the mass matrix $\boldsymbol{M}$ can be a function of the system evolution.

On the other hand, when the system behavior can be considered as linear, Equation 12 can be written as:

$$\boldsymbol{M}\ddot{q} + \boldsymbol{C}\dot{q} + \boldsymbol{K}q = \boldsymbol{R}(t) \tag{13}$$

where the internal forces are represented by the sum of the elastic and damping forces; with much simpler functions, forces are linked to the values of displacements and speeds, through matrices $\boldsymbol{C}$ and $\boldsymbol{K}$ that, in the simplest case are constant over time, and represent linear functions (thus, not function of q) [97].

In a nonlinear problem, the material stiffness is not constant with deformation. If the stiffness matrix is always equal with the variation of material deformation, in each tension and deformation condition it is possible to treat the problem as a linear one and obtain a linearization of the stiffness characteristic valid for a limited range of considered conditions. For each operation of this type, a matrix of stiffness $\boldsymbol{K}_t$, called matrix of tangent stiffness, is obtained. The $\boldsymbol{K}_t$ matrix in the nonlinear field has to be recalculated for each condition of tension and deformation of the material that generates modifications in the stiffness characteristics and depends on the instant t considered.

Therefore, to obtain the material behavior at a certain point of the characteristic, the following expression can be used:

$$F(q, t) = \boldsymbol{K}_t \cdot q \tag{14}$$

that, as already mentioned, is valid only for t assigned.

The search of the solution to a problem of this type reduces to the determination of a vector q that satisfies the equilibrium equation

$$R_t(q,t) - F_t(q,t) = 0 \tag{15}$$

obtained setting the acceleration vector equal to 0 in Equation 12. Therefore, the vector q at the instant t can be determined. A typical incremental approach assumes that the solution for certain instant t is known and that the objective is to calculate the solution for another instant $t + \Delta t$, where Δt is the time increment, appropriately selected.

For the instant $t + \Delta t$, it can be written:

$$R_{t+\Delta t} - F_{t+\Delta t} = 0 \tag{16}$$

Assuming that the external forces vector R is independent of deformations since the solution at time t is known, it is possible to express:

$$F_{t+\Delta t} = F_t + F \tag{17}$$

where F is the increment in the nodal forces between t and $t + \Delta t$. This vector can be approximated with the tangent stiffness matrix, calculated with a linearization at time t:

$$F = \boldsymbol{K_t} \cdot q \tag{18}$$

where q is a nodal displacements vector and $\boldsymbol{K_t}$ is the tangent stiffness matrix

$$\boldsymbol{K_t} = \frac{dF_t}{dq_t} \tag{19}$$

Substituting the last two equations in Equation 1, it is possible to obtain

$$\boldsymbol{K_t} \cdot q = R_{t+\Delta t} - F_t \tag{20}$$

and, making q explicit:

$$q_{t+\Delta t} = q_t + q \tag{21}$$

which is an approximation since the tangent stiffness was used.

Evaluating only an approximation of displacements at time $t + \Delta t$ it is possible to obtain only an approximation of stresses and corresponding nodal forces and then proceed to the next interval. However, because of the approximations induced by the use of a tangent mass matrix, the solution will be subject to errors and could give rise to numerical instability depending on the load type. To reduce the error is necessary to iterate until Equation 12 is satisfied with sufficient accuracy. Different iterations methods exist; an example is the Newton – Raphson method, that comes from the incremental technique. This method is based on the calculation of an increment in the nodal displacements to define a new vector of total displacements and repeat the incremental solution using the calculated displacements as starting point, and not anymore those at the first instant t. Therefore, the $R_t – F_t$ vector, called vector of unbalanced loads by elements tensions, is balanced in this way with an error that reduces itself at each iteration.

The solution to nonlinear dynamic problems necessarily necessitates the treatment of all model parameters as time-dependent requiring the time integration of all the FEM model degrees of freedom. The speed which the parameters on the model vary is very important and distinguished between the various types of models and integration time interval dimensions to be used. As concerns structural components, Belitschko [96] states that problems related to reflection and diffraction are not important; structural problems are called "inertials" because the time response is long compared with the time taken by pressure waves to cross the structure. There are various approaches for the integration technique depending on the method used to write the dynamic equations: sometimes it is possible to express the speed and the position value in a time instant as a function of the previous instant, while in other cases it is not.

Integration techniques are therefore divided into explicit and implicit. An equation for a dynamic system, neglecting the damping matrix effect, can be written as follows

$$\boldsymbol{M}\ddot{q}_t = R_t - F_t \tag{22}$$

The explicit method involves imposing the equilibrium in such a system at the instant $t + \Delta t$ to calculate displacements at instant t. The central difference method is usually used in this case; the derivatives of q and $\dot{q}$ are written as function of themselves at the previous instant, using an expression at the instant t, or rather as a function of $q_{t+\Delta t}$ and $\dot{q}_{t+\Delta t}$ besides q_t and $\dot{q}_t$. Consequently, it is obtained a system of two equations with $\dot{q}_{t+\Delta t}$ and $q_{t+\Delta t}$ as only unknowns. Thus, it is possible to calculate the system behavior at the instant $t + \Delta t$ as function of the conditions at instant t.

Furthermore, operating explicitly it is possible to calculate the accelerations $\ddot{q}$ for each instant as a function of the previous instant only if the mass matrix $\boldsymbol{M}$ is inverted. Fortunately, such inversion is often easily achievable since it is possible to assume the mass to be

concentrated (*lumped*), and the mass matrix **M** to be diagonal, making matrix inversion more straightforward.

The main disadvantage of using the explicit technique and the central difference method concerns the restrictions on the time interval dimensions (*time step*) since the time interval must be smaller than the critical value to obtain a stable algorithm:

$$\Delta t_{cr} = \frac{T_n}{\pi} \tag{23}$$

where T_n is the smallest period in the finite element model [98].

This interval is often defined as the one needed by an elastic wave (of pressure) to cross the smallest element inside the model. Therefore, the stability of explicit techniques is subordinated to the characteristic length of the smallest element, which influences the integration step Δt.

With the implicit method, the dynamic equation is again written at time $t + \Delta t$, but this time to calculate displacements at instant $t + \Delta t$. This method always requires the inversion of the stiffness matrix **K** and the use of an iteration solution as for nonlinear static systems, using, for example, the Newton – Raphson method. Moreover, implicit schemes remove the constraint of maximum dimension of time interval, calculating the dynamic quantities at time $t + \Delta t$, not only by their values at instant t but also on their values at instant $t + \Delta t$.

In structural problems, the implicit integration usually produces acceptable solutions with time interval values one or two orders of magnitude higher than the stability limit of the explicit method.

APPENDIX C – Contact algorithms

1. Contact algorithms utilized in the foam depenetration simulation

```
*CONTACT_TIED_SHELL_EDGE_TO_SURFACE_BEAM_OFFSET_ID
$#     CID                                                          TITLE
         1CONTACT BACKSEAT_FRAME-FOAM
$#    SSID      MSID     SSTYP     MSTYP     SBOXID    MBOXID       SPR       MPR
   9999949  40000425         4         3         0         0         0         0
$#     FS        FD        DC        VC       VDC    PENCHK        BT        DT
      0.0       0.0       0.0       0.0      20.0         0       0.0       0.0
$#    SFS       SFM       SST       MST      SFST      SFMT       FSF       VSF
      1.0       1.0       0.0       0.0       1.0       1.0       0.0       0.0
$#   SOFT    SOFSCL    LCIDAB    MAXPAR     SBOPT     DEPTH     BSORT    FRCFRQ
        1      0.10                1.006
*CONTACT_AUTOMATIC_SURFACE_TO_SURFACE_ID
$#     CID                                                          TITLE
         2CONTACT FOAM-VEHICLE BODY
$#    SSID      MSID     SSTYP     MSTYP     SBOXID    MBOXID       SPR       MPR
 101000107  40000425         3         3         0         0         0         0
$#     FS        FD        DC        VC       VDC    PENCHK        BT        DT
      0.0       0.0       0.0       0.0      20.0         0       0.0       0.0
$#    SFS       SFM       SST       MST      SFST      SFMT       FSF       VSF
      1.0       1.0       0.0       0.0       1.0       1.0       0.0       0.0
$#   SOFT    SOFSCL    LCIDAB    MAXPAR     SBOPT     DEPTH     BSORT    FRCFRQ
        2                        1.025                  13
*CONTACT_AUTOMATIC_SURFACE_TO_SURFACE_ID
$#     CID                                                          TITLE
         3CONTACT CRS_CLAMPS-FOAM
$#    SSID      MSID     SSTYP     MSTYP     SBOXID    MBOXID       SPR       MPR
         1  40000425         2         3         0         0         0         0
$#     FS        FD        DC        VC       VDC    PENCHK        BT        DT
      0.0       0.0       0.0       0.0      20.0         0       0.0       0.0
$#    SFS       SFM       SST       MST      SFST      SFMT       FSF       VSF
      1.0       1.0       0.0       0.0       1.0       1.0       0.0       0.0
$#   SOFT    SOFSCL    LCIDAB    MAXPAR     SBOPT     DEPTH     BSORT    FRCFRQ
        2                        1.025                  13
```

2. Contact algorithm utilized in the dummy seating simulation

```
*CONTACT_TIED_SHELL_EDGE_TO_SURFACE_BEAM_OFFSET_ID
$#     CID                                                          TITLE
        1CONTACT_BACKSEAT_FRAME-FOAM
$#    SSID      MSID     SSTYP     MSTYP    SBOXID    MBOXID       SPR       MPR
   9999949  40000001         4         1         0         0         0         0
$#     FS       FD        DC        VC       VDC    PENCHK        BT        DT
      0.0      0.0       0.0       0.0      20.0         0       0.0       0.0
$#    SFS      SFM       SST       MST      SFST      SFMT       FSF       VSF
      0.0      0.0       0.0       0.0       1.0       1.0       0.0       0.0
$#   SOFT    SOFSCL    LCIDAB    MAXPAR     SBOPT     DEPTH     BSORT    FRCFRQ
        1      0.10               1.006
*CONTACT_AUTOMATIC_SURFACE_TO_SURFACE_ID
$#     CID                                                          TITLE
        2CONTACT DUMMY-FOAM
$#    SSID      MSID     SSTYP     MSTYP    SBOXID    MBOXID       SPR       MPR
       10  40000425         2         3         0         0         0         0
$#     FS       FD        DC        VC       VDC    PENCHK        BT        DT
      0.0      0.0       0.0       0.0      20.0         0       0.0       0.0
$#    SFS      SFM       SST       MST      SFST      SFMT       FSF       VSF
      1.0      1.0       0.0       0.0       1.0       1.0       0.0       0.0
$#   SOFT    SOFSCL    LCIDAB    MAXPAR     SBOPT     DEPTH     BSORT    FRCFRQ
        2               1.025                13
*CONTACT_AUTOMATIC_SURFACE_TO_SURFACE_ID
$#     CID                                                          TITLE
        3CONTACT DUMMY-BOOSTER
$#    SSID      MSID     SSTYP     MSTYP    SBOXID    MBOXID       SPR       MPR
  30000081        10         2         2         0         0         0         0
$#     FS       FD        DC        VC       VDC    PENCHK        BT        DT
      0.0      0.0       0.0       0.0      20.0         0       0.0       0.0
$#    SFS      SFM       SST       MST      SFST      SFMT       FSF       VSF
      1.0      1.0       0.0       0.0       1.0       1.0       0.0       0.0
$#   SOFT    SOFSCL    LCIDAB    MAXPAR     SBOPT     DEPTH     BSORT    FRCFRQ
        2               1.025                13
*CONTACT_AUTOMATIC_SURFACE_TO_SURFACE_ID
$#     CID                                                          TITLE
        4CONTACT FOAM-BOOSTER
$#    SSID      MSID     SSTYP     MSTYP    SBOXID    MBOXID       SPR       MPR
  30000081  40000425         2         3         0         0         0         0
$#     FS       FD        DC        VC       VDC    PENCHK        BT        DT
      0.0      0.0       0.0       0.0      20.0         0       0.0       0.0
$#    SFS      SFM       SST       MST      SFST      SFMT       FSF       VSF
      1.0      1.0       0.0       0.0       1.0       1.0       0.0       0.0
$#   SOFT    SOFSCL    LCIDAB    MAXPAR     SBOPT     DEPTH     BSORT    FRCFRQ
        2               1.025                13

*CONTACT_AUTOMATIC_SURFACE_TO_SURFACE_ID
$#     CID                                                          TITLE
        5CONTACT FOAM-VEHICLE BODY
$#    SSID      MSID     SSTYP     MSTYP    SBOXID    MBOXID       SPR       MPR
        3  40000425         2         3         0         0         0         0
$#     FS       FD        DC        VC       VDC    PENCHK        BT        DT
      0.0      0.0       0.0       0.0      20.0         0       0.0       0.0
$#    SFS      SFM       SST       MST      SFST      SFMT       FSF       VSF
      1.0      1.0       0.0       0.0       1.0       1.0       0.0       0.0
$#   SOFT    SOFSCL    LCIDAB    MAXPAR     SBOPT     DEPTH     BSORT    FRCFRQ
        2               1.025                13
```

3. Contact algorithms utilized in the sled test simulation

```
*CONTACT_TIED_SHELL_EDGE_TO_SURFACE_BEAM_OFFSET_ID
$#     CID                                                              TITLE
         1CONTACT_BACKSEAT_FRAME-FOAM_SKIN
$#    SSID      MSID     SSTYP     MSTYP    SBOXID    MBOXID       SPR       MPR
   9999949  40000001         4         1         0         0         0         0
$#      FS        FD        DC        VC       VDC    PENCHK        BT        DT
       0.0       0.0       0.0       0.0       0.0         0       0.0       0.0
$#     SFS       SFM       SST       MST      SFST      SFMT       FSF       VSF
       0.0       0.0       0.0       0.0       1.0       1.0       0.0       0.0
$#    SOFT    SOFSCL    LCIDAB    MAXPAR     SBOPT     DEPTH     BSORT    FRCFRQ
         1       0.1         0     1.006       2.0         2         0         1
*CONTACT_AUTOMATIC_SURFACE_TO_SURFACE_ID
$#     CID                                                              TITLE
         2CONTACT SEATBELT-DUMMY_BOOSTER_FOAM
$#    SSID      MSID     SSTYP     MSTYP    SBOXID    MBOXID       SPR       MPR
         9  60000016         2         2         0         0         0         0
$#      FS        FD        DC        VC       VDC    PENCHK        BT        DT
       0.2       0.2       0.0       0.0       0.0         0       0.01.0000E+20
$#     SFS       SFM       SST       MST      SFST      SFMT       FSF       VSF
       1.0       1.0       0.0       0.0       1.0       1.0       0.0       0.0
$#    SOFT    SOFSCL    LCIDAB    MAXPAR     SBOPT     DEPTH     BSORT    FRCFRQ
         1       0.1         0      1.05       0.0         1         0         1
*CONTACT_AUTOMATIC_SINGLE_SURFACE_ID
$#     CID                                                              TITLE
         3GENERAL SLED TEST CONTACT
$#    SSID      MSID     SSTYP     MSTYP    SBOXID    MBOXID       SPR       MPR
         3         0         2         0         0         0         0         0
$#      FS        FD        DC        VC       VDC    PENCHK        BT        DT
       0.2       0.2       0.0       0.0       0.0         0       0.01.0000E+20
$#     SFS       SFM       SST       MST      SFST      SFMT       FSF       VSF
       1.0       1.0       0.0       0.0       1.0       1.0       0.0       0.0
$#    SOFT    SOFSCL    LCIDAB    MAXPAR     SBOPT     DEPTH     BSORT    FRCFRQ
         2                         1.025                  13
*CONTACT_AUTOMATIC_NODES_TO_SURFACE_ID
$#     CID                                                              TITLE
         4CONTACT DUMMY-FRONT_PASSENGER_SEAT_BEAMS
$#    SSID      MSID     SSTYP     MSTYP    SBOXID    MBOXID       SPR       MPR
  10005000   3500239         4         2         0         0         0         0
$#      FS        FD        DC        VC       VDC    PENCHK        BT        DT
       0.2       0.2       0.0       0.0       0.0         0       0.01.0000E+20
$#     SFS       SFM       SST       MST      SFST      SFMT       FSF       VSF
       1.0       1.0       0.0       0.0       1.0       1.0       0.0       0.0
$#    SOFT    SOFSCL    LCIDAB    MAXPAR     SBOPT     DEPTH     BSORT    FRCFRQ
         1       0.1         0      1.05       0.0         1         0         1
```

APPENDIX D – Injury signals registered with FC = 0.4

Chest *x*-acceleration

Chest *z*-acceleration

Pelvis *x*-acceleration

Pelvis *z*-acceleration

Upper neck *x*-force

Upper neck *z*-force

Upper neck *y*-moment

Lower neck *y*-moment
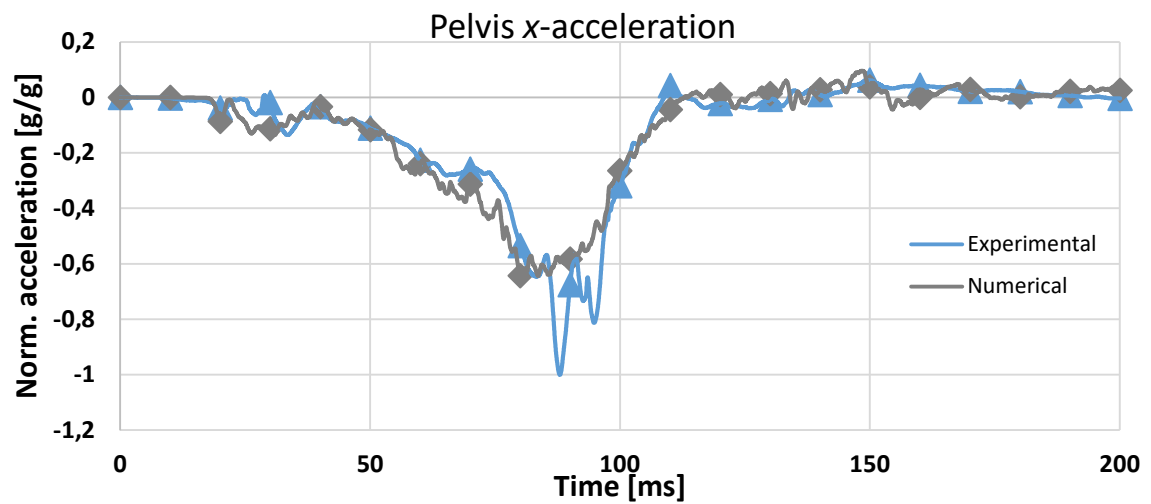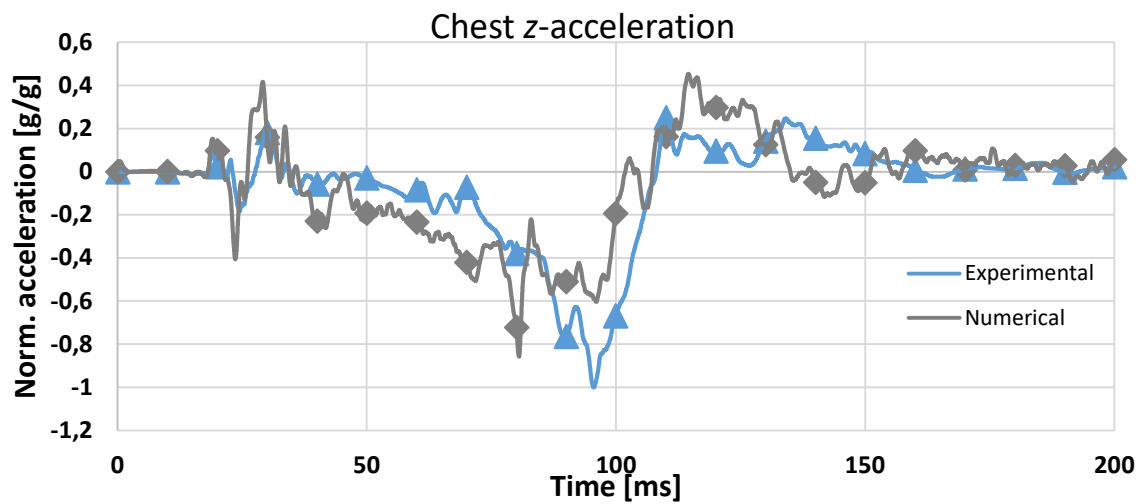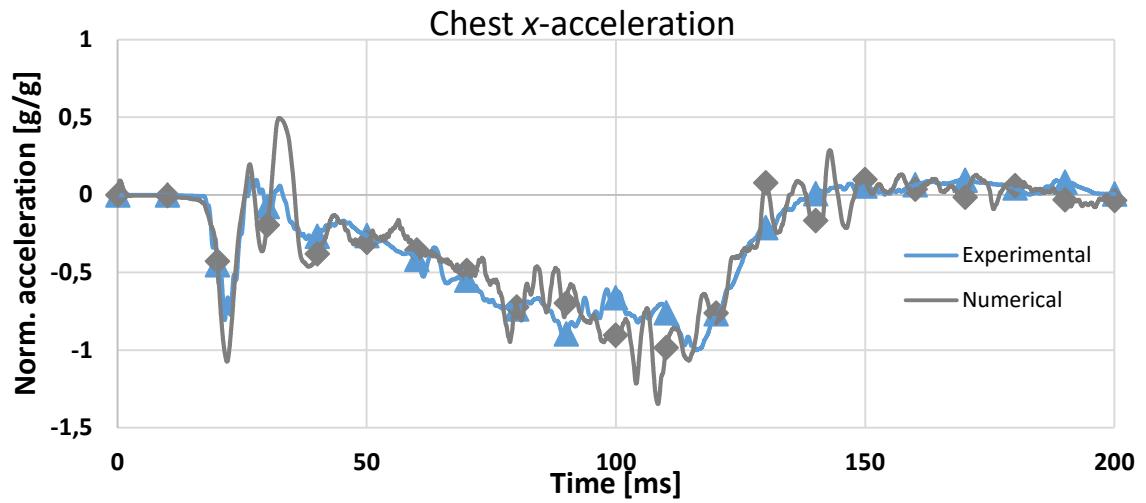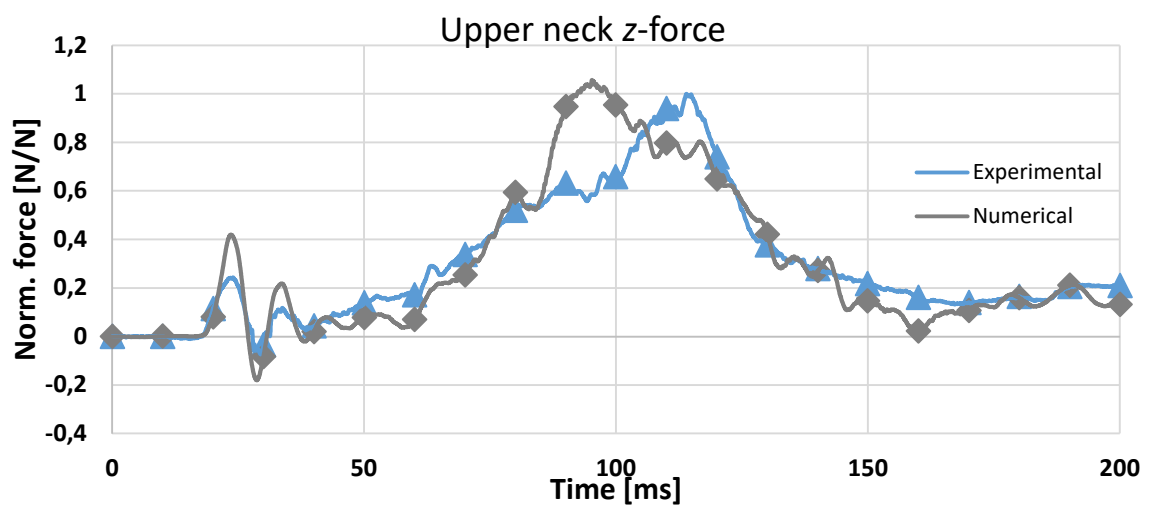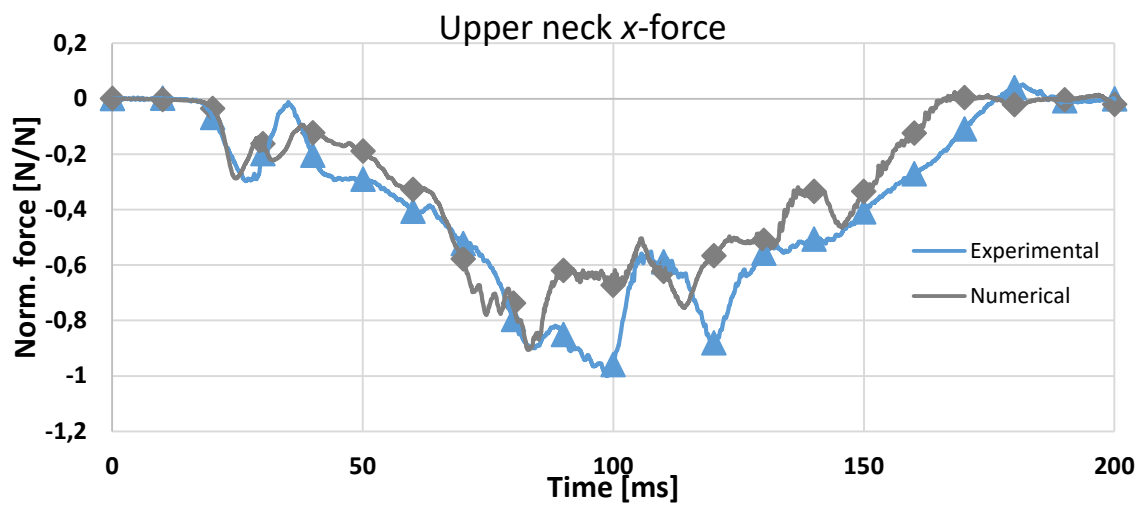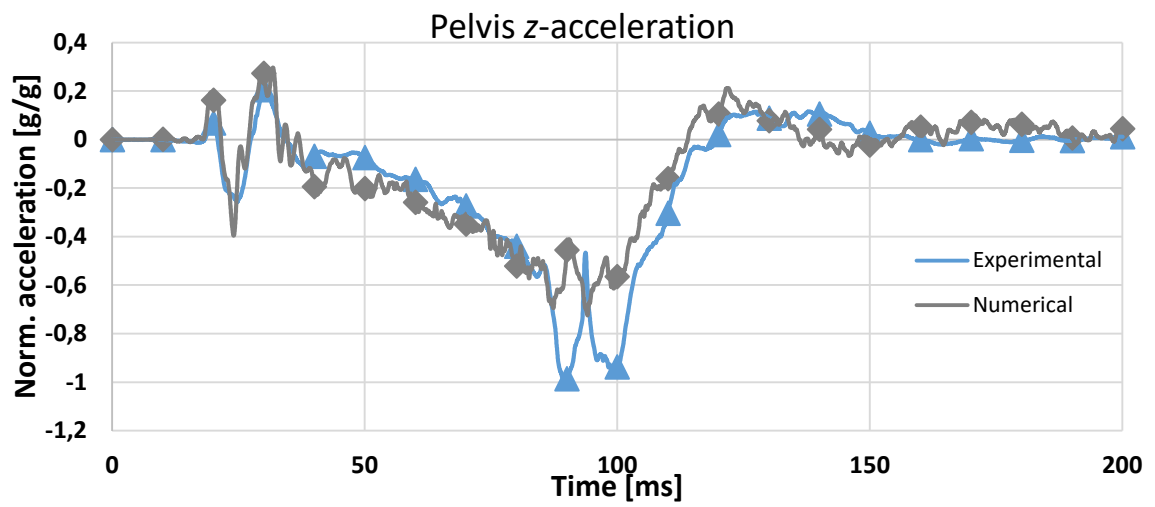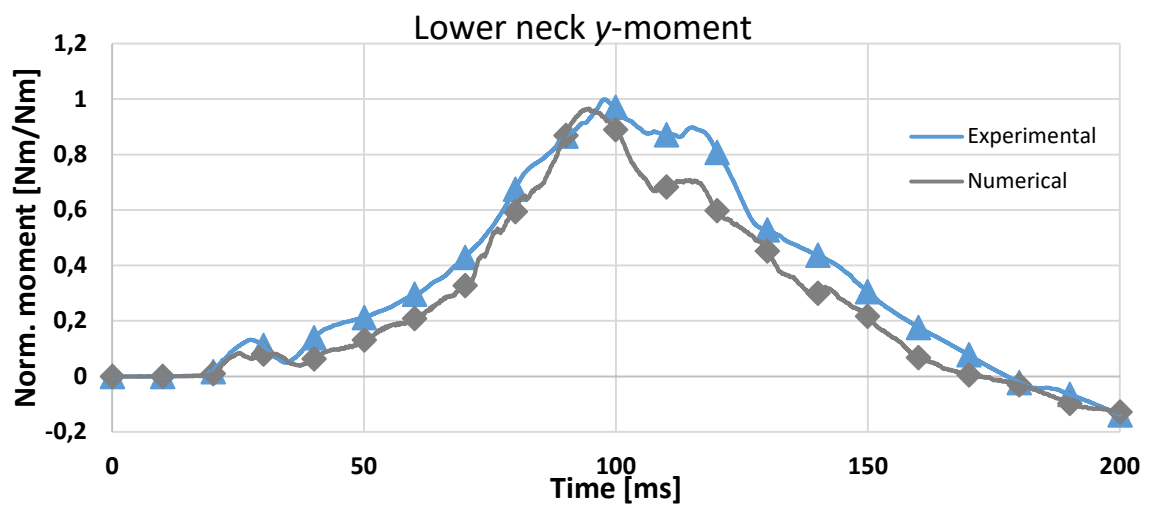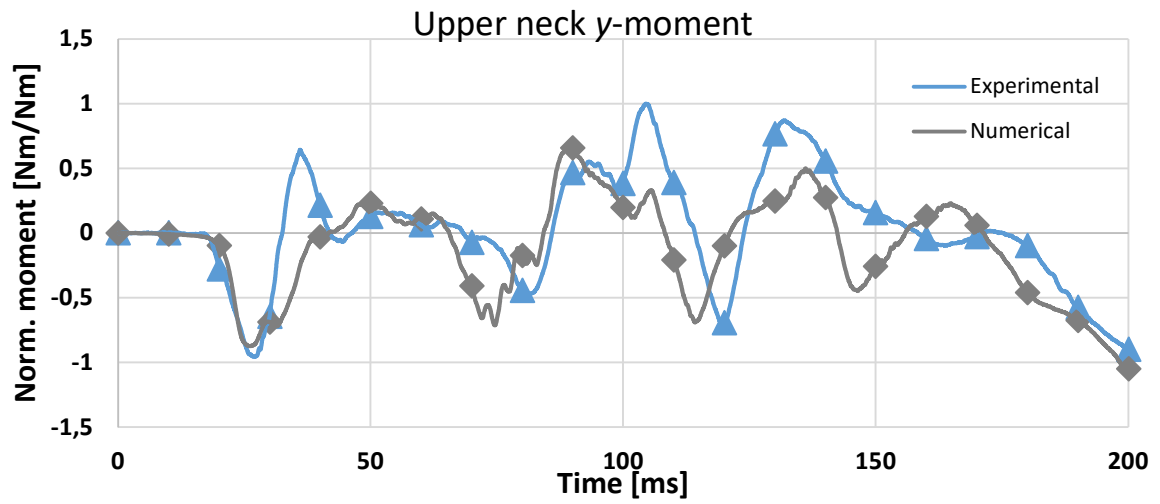
VITA AUCTORIS

Paolo Lorusso was born in 1995 in Bari, Italy. He graduated from Liceo Scientifico E. Majorana in 2014. After that, he went on to Politecnico di Bari where he obtained a Bachelor's degree in Mechanical Engineering in 2017, with a final grade of 105/110. He presented a thesis on "Aerodynamic study of a MotoGP prototype", working with Pointwise and ANSYS Fluent.

The same year, he enrolled for the course of Master's degree in Automotive Engineering at Politecnico di Torino, and the year after he joined a dual degree program between Politecnico and the University of Windsor.

He is currently a candidate for both the Master of Applied Science in Automotive Engineering at the University of Windsor, hoping to graduate in Fall 2019, and the Master's degree in the same field at Politecnico di Torino.